2022

Ironing out ferric-siderophore reduction in Gram-negative bacteria

Inês de Brito Trindade

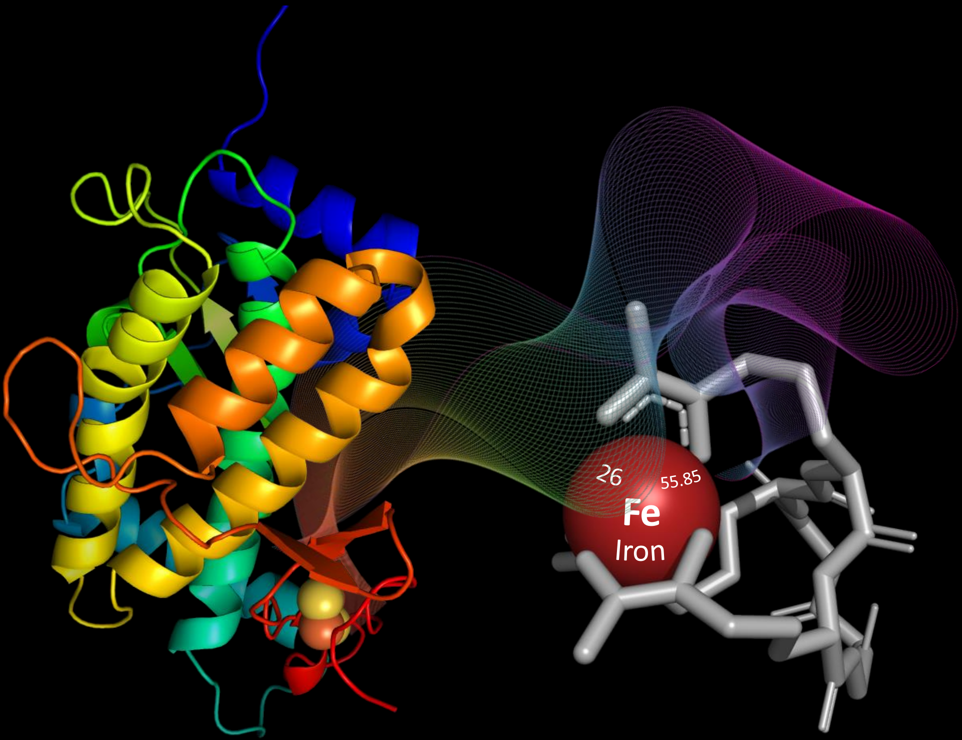

Dissertation presented to obtain the **Ph.D degree in**

Molecular Biosciences

Oeiras, November2022

INSTITUTO DE TECNOLOGIA QUÍMICA E BIOLÓGICA ANTÓNIO XAVIER | UNIVERSIDADE NOVA DE LISBOA

Ironing out ferric-siderophore reduction in Gram-negative bacteria

Inês de Brito Trindade

Dissertation presented to obtain the Ph.D. degree in Molecular Biosciences.

Instituto de Tecnologia Química e Biológica António Xavier
Universidade Nova de Lisboa

Oeiras, November 2022

From left to right: Cecília M. Arraino, Roland Sigel, Robert Crichton, Elin Moe, Inês B. Trindade, Ricardo O. Louro, João B. Vicente together with Darcy McRose and Mario Piccioli (projected on the screen via Zoom) – 7th December 2022

President of the Jury:

- Dr. Cecília M. Arraiano, Investigadora Coordenadora do Instituto de Tecnologia Química e Biológica António Xavier da Universidade NOVA de Lisboa, por delegação;

Members of the Jury:

- Dr. Robert Crichton, Full Professor Emeritus, Université Catholique de Louvain la Neuve, Belgium;
- Dr. Roland Sigel, Full Professor, University of Zurich, Switzerland;
- Dr. Darcy McRose, Assistant Professor, Massachusetts Institute of Technology, United States of America;
- Dr. João B. Vicente, Investigador Auxiliar no Instituto de Tecnologia Química e Biológica António Xavier na Universidade NOVA de Lisboa, Portugal.

Research work performed within the Nuclear Magnetic Resonance Applied to Chemistry, Materials and Biosciences PhD Program (PD/00065/2013), supported by Fundação para a Ciência e a Tecnologia (PD/BD/135187/2017).

The research described in this thesis was performed under the supervision of:

Professor Ricardo O. Louro (supervisor)

Instituto de Tecnologia Química e Biológica António Xavier, Universidade Nova de Lisboa, Avenida da República, 2780-157 Oeiras, Portugal;

Professor Mario Piccioli (co-supervisor)

Magnetic Resonance Center (CERM) and Department of Chemistry, University of Florence, Via L. Sacconi 6,50019 Sesto Fiorentino, Italy;

Consorzio Interuniversitario Risonanze Magnetiche Di Metallo Proteine (CIRMMP), Via L. Sacconi 6, 50019 Sesto Fiorentino, Italy;

Doctor Elin Moe (co-supervisor)

Instituto de Tecnologia Química e Biológica António Xavier, Universidade Nova de Lisboa, Avenida da República, 2780-157 Oeiras, Portugal.

"…I hear the music, I feel the beat,
and for a moment when I am dancing, I am free."
Florence and the Machine

To the loves of my life.

Acknowledgments

The path to knowledge pursuit can be lonely and frightening. Like a sailor in the ocean, sometimes we lose sight of the shore for a very long time. Luckily for us, stars are there to guide us as we adjust our sails and learn how to navigate through the unpredictable winds. Foremost, I would like to express my sincere gratitude to everyone that accompanied me throughout my time as a Ph.D. student and I could not have done it without you!

I would like to start by acknowledging my supervisor Dr. Ricardo O. Louro. It was a pleasure to be part of your team. You were my mentor and my friend. I am very grateful for all the challenges you threw at me and for all the things you taught me. Thank you for your patience and support. Also thank you for the freedom, you always gave me all the space and support that I needed. I could safely fly to great heights without the risk of injury. This was very precious and for that, I will be forever grateful.

To my co-supervisor Dr. Mario Piccioli that “blindly” accepted the challenge of having me as a Ph.D. student. Thank you for making it so easy to be your Ph.D. student. Thank you for all your support! My time at CERM was very special for me and I thank you very much for that!

To my co-supervisor, Dr. Elin Moe, which gave me a “second” home (lab) and together with me never gave up on the quest for obtaining the structure of FhuF. After 5 years of trying, we made it! Thank you so much! It was a blessing to work with you, I am very fortunate. You also always acted as a supervisor for me, even when you were not! Thank you so much for the bright crystals. They made “my days” many days! I feel very grateful for your presence!

I would like to acknowledge the IBN team, past and current members. Starting by thanking Dr. Catarina Paquete. For the best advice! You were crucial for my growth as a PhD student and a researcher. You also showed me that even though our scientific passion sometimes fades, it is possible to nurture it. Thank you so much. To Dr. Bruno Fonseca, my first "supervisor", and the pioneer of the iron uptake pathways at the IBN lab, you were crucial for my entrance into this field, and you were always the best person to work with. To the lab colleagues that also became my friends, which made "life" at the lab more enjoyable: Marisa, my marathon companion, my companion in purifying proteins from spinach! Your innocence and purity were the best thing I could encounter through the time I spent at ITQB; To Anaísa, my ptNMR companion, we "started from the bottom and now we are here", and somehow, I knew it from the beginning! Thank you for being such a good spirit (pimba will always remind me of you now) and thank you for taking care of me, your organization skills are an outstanding example! To Ricardo Soares, or "Ricardinho", my all-time favorite, my journal club companion, you were a fresh breeze to have around! To Alexandra Alves, who made a great return to the lab, and helped me out in finishing the work of PioC. It was a great pleasure to work with you and you always took care of me, riding along with my crazy ideas! And to Ana Silva, that kept everything in order! Making sure that the good practice in the lab was kept to a high standard. Thank you so much, I learned a lot from you, and we can only evolve when we have great people around us, so thank you so much for that!

Then a great deal of my thesis was spent on building collaborations outside of the IBN lab, which also taught me the great lesson that Science has more to do with people than with resources or logical thinking. To Dr. Teresa Catarino, my companion in the stopped-flow experiments, and my favorite person to work with. I wish everyone would have as much fun as we did while doing great experiments. To Dr. Dianne K. Newman that opened her lab for me. You gave me a scientific shelter when I needed it the most. It was a pleasure to work with you. You are truly inspirational! But also, without any particular order: ptNMR friends, Dr. Francesca Cantini, Dr. Darcy McRose, Dr. Smilja Todovoric, Dr. Célia Silveira, Dr. Zach Hensel, Dr. Pedro Matias, Dr. João Vicente, Dr. Tiago

Cordeiro, Guillem Hernandez, Filipe Rollo, Paula Chicau, Cristina Timóteo, João Carita, Helena Matias, Pedro Lamosa, Dr. José Pedro Silva, Dr. Michelle Invernici, Steven Hilbert, Dr. Roxana Shafiee, John Ciemniecki, Dr. Georgia Squyres, Lev Tsypin, and many others which I am likely forgetting the names.

To my friends, especially Sara Costa, my shoulder at ITQB, and my companion in the good and bad moments! Thank you so much for everything! You always had my back! Also, thanks to you this thesis will have less-to-no typos! Thanks a lot! And to Delfim Ferreira, for the amazing geek gaming group club which was crucial for keeping us all sane throughout this journey! Carcassonis! To my Master in Biochemistry friends who kept me young and happy every time we were together, Gémea Ana Rodinha, Khrystyna Kucheryava and Diana Silva! And of course, their soul mates!

To Fatima, my guardian angel, which always helped me when I needed it the most. You gave me the best but also the hardest pieces of advice but that were crucial for my success, as a scientist, as a woman, as a friend and now as a mother. I will be forever grateful!

To my family which allowed me the path to reach the person that I am today. You gave me the basis for my foundation. Thank you so much.

Last, but not least, to Paulo Oliveira, the love of my life, that always believed in me and always reminded me of my scientific flame when cold periods were hard to go by. You have always been by my side. And all the success I have belongs to you. I love you.

To my daughter, Matilde Oliveira, who showed me that we always have more time than we think and that life is beautiful, and we should definitely make a serious effort to save this world so that you can grow up healthy and happy. I love you.

And to the ones reading this thesis. Thank you very much!

Inês B. Trindade

Thesis Publications

1) **Trindade I.B.**, Invernici M, Cantini F., Louro, R.O. & Piccioli, M. (2020) ^{1}H, ^{13}C and ^{15}N assignment of the paramagnetic high potential iron–sulfur protein (HiPIP) PioC from *Rhodopseudomonas palustris* TIE-1. Biomol NMR Assign 14:211–215.

2) **Trindade I.B.**, Invernici M., Cantini F., Louro, R.O. & Piccioli, M. (2021) Sequence-specific assignments in NMR spectra of paramagnetic systems: A non-systematic approach. Inorganica Chim. Acta 514:1-8.

3) **Trindade I.B.**, Invernici M., Cantini F., Louro, R.O. & Piccioli, M. (2021) PRE-driven Protein NMR Structures: an Alternative Approach in Highly Paramagnetic Systems. FEBS Journal. 288: 3010–3023.3.

4) **Trindade I.B.**, Hernandez, G., Lebègue, E., Barrière, F., Cordeiro, T., Piccioli, M. & Louro, R.O. (2021) Conjuring up a ghost: structural and functional characterization of FhuF, a ferric siderophore reductase from *E . coli*. JBIC 26: 313–326.

5) **Trindade I.B.**, Rollo, F., Todorovic, S., Catarino, T., Moe, E., Matias, P.M., Piccioli, M., Louro, R.O. (2022) The structure of a novel ferredoxin – FhuF, a ferric-siderophore reductase from *E. coli* K-12 with a novel 2Fe-2S cluster coordination **(to be submitted).**

6) **Trindade, I.B.,** Fonseca, B.M., Catarino, T., Matias, P.M., Moe, E., Louro, R.O. (2022) Ferric-siderophore reduction in Shewanella *bicestrii*:

Structural and functional characterization of SbSIP reveals an overlooked specificity of siderophore-interacting proteins **(to be submitted).**

7) **Trindade, I.B.**, Firmino, M. O., Noordam, S., Alves, M.A., Fonseca, B.M., Piccioli, M., Paquete, C.M., Louro, R.O. (2022) Protein interactions in *Rhodopseudomonas palustris* TIE-1 reveal the molecular basis for resilient photoferrotrophic iron oxidation **(to be submitted).**

Other publications

1) **Trindade IB**, Coelho, A., Cantini, F., Piccioli, M. & Louro, R.O. (2022) NMR of paramagnetic metalloproteins in solution: *Ubi venire*, *quo vadis*? J. Inorg. Biochem 234: 1-15.

2) Invernici M, **Trindade I.B.**, Cantini F, Louro, R.O & Piccioli, M. (2020) Measuring transverse relaxation in highly paramagnetic systems. J Biomol NMR 74:431–442.

3) Fonseca, B. M., Silva, L., **Trindade, I.B.**, Moe, E., Matias, P. M., Louro, R. O., & Paquete, C. M. (2019). Optimizing Electroactive Organisms: The Effect of Orthologous Proteins. Front. Energy Res, 7, 1–13.

4) **Trindade, I.B.**, Silva, J. M., Fonseca, B. M., Catarino, T., Fujita, M., Matias, P. M., Moe, E. & Louro, R. O. (2019). Structure and reactivity of a siderophore-interacting protein from the marine bacterium *Shewanella* reveals unanticipated functional versatility. JBC, 294(1) 157–167.

5) **Trindade, I.B.**, Paquete, C.M. & Louro, R. O., (2021) Chapter 8: Extracellular Redox Chemistry in Metals, Microbes, and Minerals: The biogeochemical side of life. De gruyter.(ed) Sigel, A., Freisinger, E. & Sigel, R.K.O.

6) **Trindade I.B.**, Moe E, Louro RO (2020) Siderophore-Interacting Protein. Encycl Inorg Bioinorg Chem 1–12.

7) **Trindade, I.B.** & Louro, R. O., (2019). Chapter: 5: Introduction to biomolecular nuclear magnetic resonance and metals in Practical Approaches to

Biological Inorganic Chemistry. Elsevier. (2nd edition) Crichton, R.R. & Louro, R.O.

8) Louro, R.O, Costa, N.L., Fernandes, A.P, Silva, A.V., **Trindade, I.B.**, Fonseca, B.M. & Paquete, C.M., (2018). Chapter 2.2: Exploring the Mechanisms of Electron transfer for harnessing reducing power in METs: Methodologies and Approaches in Microbial Electrochemical Technology: Sustainable platform for fuels chemicals and remediation. Elsevier. (ed) Mohan, V., Varjani, S. & Pandey, A.

Abbreviations

ABC- ATP-Binding Cassette
AMP- Adenosine MonoPhosphate
CD- Circular Dichroism
CCR- Crosscorrelation rates
EPR- Electron Paramagnetic Resonance
FAD- Flavin Adenine Dinucleotide
Fes- Ferric-Esterase from *E. coli*
FhuF- Ferric hydroxamate utilizer F protein
FSR- Ferric-Siderophore Reductase
FSE- Ferric-Siderophore Esterase (generic)
FUR- Ferric-Uptake Regulator
GOE- Great Oxidation Event
HiPIP- High Potential Iron-Sulfur Protein
HSQC- Heteronuclear Single Quantum Coherence spectroscopy
IEPs- Inner membrane Efflux Proteins
LH-RC- Light Harvesting Reaction Center
MDR- Multidrug Resistance
MFS- Major Facilitator Superfamily
MR- Molecular Replacement
NADH- Nicotinamide Adenine Dinucleotide (reduced)
NADPH- Nicotinamide Adenine Dinucleotide Phosphate (reduced)
NHE- Normal Hydrogen Electrode
NIS- NRPS-Independent Siderophore
NMR- Nuclear Magnetic Resonance
NOE- Nuclear Overhauser Enhancement
NRPS- Non-Ribosomal Peptide Synthetase
OEP- Outer membrane Efflux Protein or channel

OMR- Outer Membrane Receptors

PDB- Protein Data Bank

PFV- Protein Film Voltammetry

PutB- Ferric-siderophore reductase of *Shewanella oneidensis*

PCS- PseudoContact Shifts

PEP- Periplasmic Efflux or Accessory protein

PREs- Paramagnetic Relaxation Enhancements

RDCs- Residual Dipolar Couplings

RMSD- Root-Mean-Square Deviation

RND- Resistance, Nodulation, and Cell division

RR- Resonance Raman

SAXs- Small-Angle X-ray scattering

*Sb*FSR- Ferric-Siderophore Reductase from *Shewanella bicestrii*

SBPs- Siderophore-Binding Proteins

SbSIP- Siderophore-Interacting Protein from *Shewanella bicestrii*

SEC- Size Exclusion Column

SEM- Standard Error of the Mean

SfSIP- Siderophore-Interacting Protein from *Shewanella frigidimarina*

SHE- Standard Hydrogen Electrode

SIP- Siderophore Interacting Protein

TROSY- Transverse Relaxation Optimized SpectroscopY

WEFT- Water Eliminated Fourier Transform

SUPERWEFT- optimized version of WEFT

YqjH- Siderophore-Interacting Protein from *E. coli*

Resumo

Os metais são essenciais para a vida, e esta como a conhecemos não existiria sem eles. O ferro é o metal redox predominante em sistemas biológicos e a sua importância é patente nos registos geológicos mais antigos. As formações ferríferas acumuladas no fundo do mar durante mais de dois biliões de anos indicam que nos oceanos ferruginosos do período arqueano, o ferro serviu como dador de eletrões para o metabolismo fototrófico anoxigénico e como elemento estrutural e catalítico em macromoléculas biológicas. No entanto, após o Grande Evento de Oxidação (GOE) que se seguiu á evolução da fotossíntese oxigénica, o aumento dos níveis de oxigénio atmosférico levou à precipitação de Fe(II) solúvel em Fe(III) insolúvel causando uma diminuição dramática na biodisponibilidade deste elemento. Não obstante, o ferro manteve-se como um nutriente crucial para a vida.

Para evitar a escassez de ferro, os microrganismos utilizam diversas estratégias, incluindo a síntese de sideróforos, metabolitos secundários que possuem alta afinidade pelo ferro férrico, de forma a capturar este metal a partir do ambiente que os rodeia. No entanto, uma vez dentro da célula, a libertação de ferro desses complexos não ocorre espontaneamente. Este processo é mediado por proteínas específicas que podem ser agrupadas em duas famílias: a família de proteínas que interagem com sideróforos (SIP) que possui flavinas como cofatores e a família das redutases férricas (FSR) que contém centros de 2Fe-2S.

Nesta tese, para compreender as bases moleculares do processo de redução de complexos sideróforo-Fe(III), foram produzidas e caracterizadas proteínas SIP e FSR representativas de bactérias Gram-negativas. Foi determinada pela primeira vez a estrutura de uma proteína representante da família das FSR, FhuF de *E. coli*. A estrutura da FhuF revelou que esta é uma nova ferredoxina, uma vez que exibe um modo de coordenação do centro de 2Fe-2S

nunca reportado antes na literatura, fornecido pela sequência de ligação atípica C-C-x_{10}-C-x_2-C. Estes resultados, juntamente com as propriedades espectroscópicas atípicas da FhuF, posicionam-na junto com as ferroquelatases, curiosamente proteínas também envolvidas numa via de captação de ferro.

Esta tese também reporta a expressão de *Sb*FSR e *Sb*SIP de *Shewanella bicestrii*, mas dada a instabilidade da primeira, descreve apenas a caracterização funcional e estrutural de *Sb*SIP. A *Sb*SIP mostrou propriedades bioquímicas particulares, incluindo a capacidade de discriminar entre NADH e NADPH e, juntamente com sua estrutura, consolida a proposta para o centro ativo destas enzimas.

Globalmente, este trabalho preenche a lacuna de conhecimento relativo às propriedades estruturais das redutases de complexos sideróforo-Fe(III) e destaca características comuns entre elas. Essas características incluem centros ativos com carga eletrostática de superfície positiva que rodeiam os centros catalíticos FAD e 2Fe-2S, e o efeito Redox-Bohr. Estas características são provavelmente cruciais para ligar eficientemente complexos sideróforo-Fe(III) e facilitar a libertação de Fe(II) por transferência de eletrões acoplada a protões. Este conhecimento é crucial para o desenvolvimento de novas estratégias que visam este ponto de estrangulamento da via metabólica dos sideróforos para estimular ou inibir a proliferação microbiana em habitats diversos.

Do ponto de vista metodológico, durante esta tese foi desenvolvida uma nova estratégia para atribuição de sinais de Ressonância Magnética Nuclear (RMN) e determinação da estrutura de metaloproteínas, tendo-se realizado pela primeira vez a determinação da estrutura de uma proteína, PioC, usando apenas restrições paramagnéticas (PREs). Estes desenvolvimentos foram cruciais para confirmar o papel desta proteína, uma proteína de ferro-enxofre de alto potencial (HiPIP) de *R. palustris* TIE-1, na oxidação fotoferrotrófica do ferro e para entender melhor os detalhes moleculares desse processo. Este trabalho abre caminho para a exploração de alvos biológicos mais complexos como a FhuF e destaca o potencial da espectroscopia de RMN paramagnética para contribuir para a caracterização estrutural e funcional de metaloproteínas e/ou para a elucidação dos mecanismos de biossíntese de centros ferro-enxofre ou de hemos, vias metabólicas de extrema importância para todos os seres vivos.

Abstract

Metals are essential for life, and life as we know it, would not exist without them. Iron is the predominant redox active metal in biological systems and its importance can be recognized from the earliest geological evidence. Iron formations accumulated on the sea floor for over two billion years show that in the ferruginous Archaean oceans, iron likely served as an electron donor in anoxygenic phototrophic metabolism and structural and catalytic element in biological macromolecules. However, after the Great Oxidation Event (GOE) brought about by the evolution of oxygenic photosynthesis, the rise in atmospheric oxygen levels caused additional precipitation of soluble Fe(II) into insoluble Fe(III), leading to a dramatic decrease in the bioavailability of this element. Notwithstanding, iron was kept as a crucial nutrient for life.

To avoid iron shortage, microorganisms utilize diverse strategies including the synthesis of siderophores, secondary metabolites that have a high affinity for ferric iron, to scavenge this metal from their environment. However, once inside the cell, iron release from these complexes does not occur spontaneously. Instead, this process is mediated by specific proteins that can be grouped into two families: the siderophore-interacting protein (SIP) family that have a flavin cofactor and the ferric reductase family (FSR) that contain a 2Fe-2S cluster.

In this thesis, to understand the molecular bases for ferric-siderophore reduction we produce and characterize representative SIP and FSR proteins of Gram-negative bacteria. We determine for the first time the structure of a representative of the FSR family, FhuF from *E. coli*. The structure of FhuF revealed that it is a novel ferredoxin, which displays an unprecedented cluster coordination mode provided by the atypical binding motif C-C-x_{10}-C-x_2-C. These results together with the atypical spectroscopic properties of FhuF, cluster this

protein together with ferrochelatases, interestingly proteins that are also involved in an iron-uptake pathway.

In this work, we also report the expression of *Sb*FSR and *Sb*SIP from *Shewanella bicestrii,* and given the instability of the former, we only describe the functional and structural characterization of *Sb*SIP. *Sb*SIP showed distinct biochemical properties including the ability to discriminate between NADH and NADPH and together with its structure, this consolidates the proposal for the putative binding pocket of these enzymes.

Altogether, this work fills in the gap of knowledge regarding the structural and functional properties of Fe(III)-siderophore reductases and highlights common features amongst them. This includes pockets with positive electrostatic surface charges that surround both FAD and 2Fe-2S catalytic centers and, the Redox-Bohr effect. These features are likely crucial for efficiently binding Fe(III)-siderophores and facilitating Fe(II) release via proton-coupled electron transfer. This knowledge is fundamental for the development of novel strategies that target this funneling point of the siderophore pathway to stimulate or inhibit microbial proliferation in diverse environments.

On the methodological front, we developed a novel strategy for NMR signal assignment and structure determination of metalloproteins, having achieved for the first time the structure determination of a protein, PioC, using only paramagnetic constraints (PREs). These developments were crucial for confirming the role of this protein, a High Potential Iron-Sulfur Protein (HiPIP) from *R. palustris* TIE-1, in photoferrotrophic iron oxidation and for further understanding the molecular details regarding this process. This work paves the way for exploring more challenging biological targets such as FhuF and highlights the potential of paramagnetic NMR spectroscopy to contribute to the structural and functional characterization of metalloproteins and/or to the elucidation of iron-sulfur cluster or heme assembly mechanisms, biological pathways of the utmost importance for all living organisms.

Table of contents

Index of Figures

Index of Tables

“All we have to decide is what to do

with the time that is given to us.”

Gandalf.

I. Chapter I: General Introduction

This chapter incorporates sections of the following publications:

Trindade, I.B. & Louro, R. O., (2019). Chapter: 5: Introduction to biomolecular nuclear magnetic resonance and metals in Practical Approaches to Biological Inorganic Chemistry. Elsevier. (2nd edition) Crichton, R.R. & Louro, R.O;

Trindade I.B., Moe E, Louro RO (2020) Siderophore-Interacting Protein. Encycl Inorg Bioinorg Chem 1–12;

Trindade, I.B., Paquete, C.M. & Louro, R. O., (2021) Chapter 8: Extracellular Redox Chemistry in Metals, Microbes, and Minerals: The biogeochemical side of life. De gruyter.(ed) Sigel, A., Freisinger, E. & Sigel, R.K.O;

Trindade I.B., Coelho, A., Cantini, F., Piccioli, M. (2022) NMR of paramagnetic metalloproteins in solution: *Ubi venire, quo vadis*?. J. Inorg. Biochem 234: 1-15.

Metals for life

Metals are essential for life, and life as we know it would not exist without their contribution. This can be illustrated by the fact that 40 % of the proteome contains metals [1]. Unique nutrients, that cannot be synthesized or degraded by metabolic processes, their availability shaped the metabolism and structure of living organisms and acted as a selective pressure for more efficient capture and disposal mechanisms [2,3].

Of all the metals, iron is one of the most predominant redox-active metals in biological systems, where it is found in proteins occupying an unparalleled diversity of sites and cofactors including among others haem, iron-sulfur clusters, and diiron centers [1,4]. Its prevalence has likely originated from its high abundance and bioavailability before the Great Oxidation Event (GOE) in the early evolution of most forms of life, but also because iron's redox properties are versatile since they can be finely tuned by ligand hardness, geometry, and coordination [1,5,6].

Additionally, iron also plays a fundamental role as an energy source for various microorganisms with dissimilatory iron reduction and oxidation occupying their fair share in the iron biogeochemical cycle (Figure 1). Dissimilatory iron reduction has been very well characterized and reviewed elsewhere for Geobacteracaea and Shewanellacaea metal-reducing microorganisms [7–9]. Dissimilatory iron oxidation, on the other hand, has been less characterized. However, paleontology data together with the widespread kept ability of oxidizing Fe(II) points towards iron oxidation as an extant metabolism preserved since the Archean eon [5,10]. Within iron oxidation, photoferrotrophism, the use of light energy (photo-) and the reducing power of Fe(II) (-ferro-) to fix inorganic carbon (-autotrophic) is considered one of the earliest forms of photosynthesis that played an important role in the iron-rich Archean oceans. This process has been studied in *Rhodobacter ferroxidans* SW2 and in *Rhodopseudomonas palustris* which appear to use different molecular mechanisms [10–12]

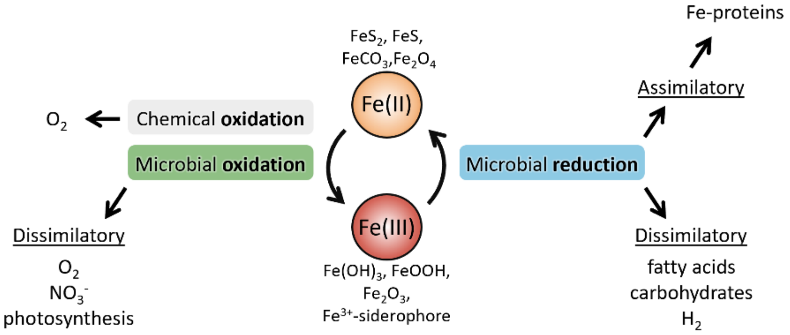

Figure I-**1** Iron biogeochemical cycle [5,13,14].

Currently, iron is still a highly abundant metal in the Earth's crust but despite its geological abundance, iron is often a growth-limiting factor for most forms of life [5]. This apparent paradox originates from the fact that in the presence of oxygen, iron precipitates into its ferric form, Fe(III), and thus, it's not readily available for utilization by living organisms [15].

Iron in biology is interconverted primarily between two oxidation states, ferrous, Fe(II), (+2), and ferric, Fe(III), (+3) forms. It is not found freely in nature, and thus, iron's reactivity depends highly on its surrounding conditions, including temperature, pH, and the nature of complexing ligands. Fe(II) is more abundant in anoxic environments and acidic environments, and less abundant in oxic and pH-neutral or basic environments, since it is readily oxidized into its Fe(III) form [5].

Siderophores to the rescue: Iron, not rare, just playing hard to get

To date, only some *Lactobacillus* spp. and *Borrelia burgdoferi* have been reported to not depend on iron for their survival. Most bacteria require micromolar to millimolar concentrations of intracellular iron and the average adult human body stores 1 to 3 g of iron [16–18].

Given that often the bioavailability of metals does not match the metabolic needs, (micro)organisms need to scavenge metals from their environment, whether this includes the tug-of-war for iron inside a host or fighting the odds of metal deprivation in the marine environment [19,20].

A commonly employed iron scavenging strategy is the use of siderophores (from the Greek “sidero”- meaning iron, and “phore”- meaning carrier). These are secondary metabolites (with a molecular mass typically of 500 to 1500 Da) that present a high affinity and selectivity for Fe(III). Siderophores are synthesized inside the cell and released outside the cell where they form Fe(III)-siderophore complexes which can then be incorporated back into the cell for iron release and further utilization in cellular metabolism [21,22].

Siderophores are produced by nearly all types of microorganisms in the tree of life, but they appear to be more prevalent and are better studied in bacteria [23]. Even within bacterial communities, not all bacteria are siderophore producers. Some are termed “cheaters”, meaning they do not produce their own siderophores but use siderophores produced by others, also known as xenosiderophores (from the Greek “xénos”-meaning alien or foreign) [24]. This means that siderophores can affect community dynamics leading to cooperative, exploitative, and/or competitive interactions between individuals. In turn, these interactions can lead to a co-evolutionary arms race between species and strains that lead to ecological dependencies that further contribute to the formation of stable communities [25]. This interaction between and within species was likely the evolutionary pressure that gave rise to the plethora of chemically diverse siderophores [25,26].

Siderophores can be classified into different types according to the chemical moieties that coordinate Fe(III): catecholates, phenolates, hydroxamates, carboxylates, amphiphilic, and mixed-type (Figure 2). Overall, different classes also mean that the affinities for Fe(III) vary substantially as well as the reduction potential for the Fe(III)/Fe(II) pair in complexed Fe-siderophores (Table 1), allowing fine tuning accordingly to cellular needs [22]. Siderophores change iron speciation, i.e. can form different Ligand-to-Metal (L:M) complexes depending on the different buffer conditions (salt and pH) and also depending on the ratio of available ligand to metal which in turn affects the reduction potential of these Fe(III)-complexes [27]. The most common coordination geometry is octahedral and the higher affinity for Fe(III) arises when negatively charged oxygens are the metal donor atoms (e.g. catecholate-type siderophores Figure 2, Table 1). These can also be substituted by nitrogen (e.g. hydroxamates, Figure 2, Table 1) or sulfur, however, these modifications reduce the affinity for Fe, and in turn, increase the affinity for other metals [22,28].

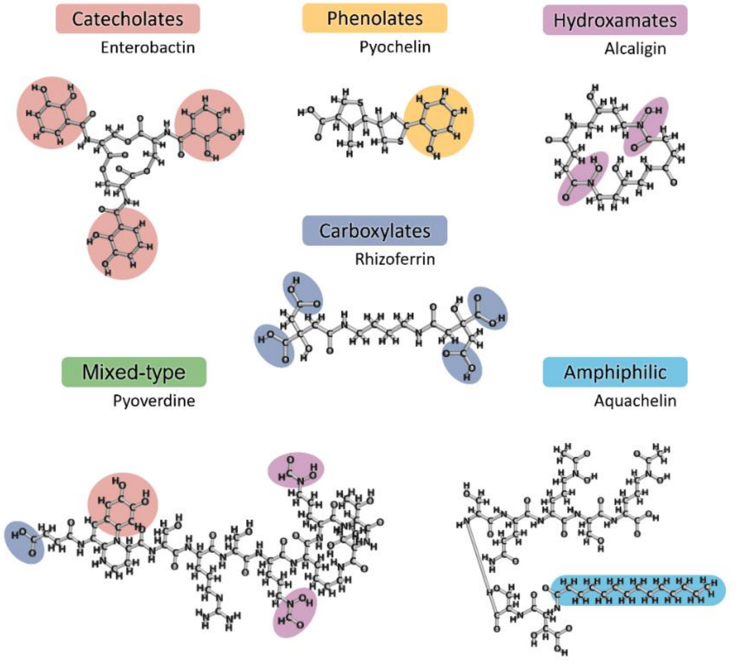

Figure I-**2** Examples of siderophores highlighting the different classes [29].

Table I-**1** Reduction potentials and thermodynamic stability constants for Fe of different siderophores at pH 7, *stability constant per Fe atom.

Siderophore	Reduction potential	Log KLFe(III) Log KLFe(II)	Class	Reference
Enterobactin	-750 mV	52.2 22.2	(tris)catecholate	[30]
Ferrichrome A	-448 mV	32.0 11.3	hydroxamate	[31]
Alcaligin (Fe_2L_3)	-443 mV	32.3* 12.3*	hydroxamate	[32]
Pyoverdine	-510 mV	30.8 9.0	Mixed-type (hydroxamate & catecholate)	[33]

Siderophore pathway: all ways lead to Fe(II)

Siderophore synthesis, release and Fe(III)-siderophore uptake

The siderophore pathway includes the synthesis inside the cytoplasm (1 in Figure 3), extracellular release into the environment (2 in Figure 3), iron complexation (3 in Figure 3), cell incorporation of Fe(III)-siderophores (4 and 5 in Figure 3), and finally, iron release for assimilatory uptake (6 in Figure 3). All these processes require tight regulation of the involved enzymes and transport systems [23]. Regulation commonly involves modulation of the transcriptional level of genes by the global iron regulator FUR (Ferric-Uptake Regulator). FUR proteins are commonly found in most prokaryotes and these act by dimerizing together with co-repressor Fe(II) to bind highly conserved palindromic A/T-rich sequences (Fur boxes) in the DNA, impairing gene expression of iron-responsive genes. This is key for guaranteeing iron homeostasis in response to various stresses. Under iron-limiting conditions, Fe-Fur complexes dissociate allowing the expression of genes such as the ones involved in siderophore biosynthesis [34,35].

The biosynthesis of siderophores occurs via two main pathways: the non-ribosomal peptide synthetase (NRPS) pathway and the NRPS-independent siderophore (NIS) synthetase pathway [36]. Examples of siderophores produced by the NRPS pathway include yersiniabactin, vibriobactin, mycobactin, and enterobactin [37–39]. This pathway relies on nonribosomal peptide synthetases (NRPSs), a family of large module-composed enzymes that function in a coordinated and sequential way to synthesize non-ribosomal peptides (NRPs) in which siderophores are included. All modules can exist in the same polypeptide chain (NRPSs, type I), or they exist individually in different interacting proteins (NRPSs, type II). The latter is the most common in bacteria whereas the former is more common in fungi. With the different modules, each NRPS selects, activates, and anchors each building block into the NRPS assembly line by peptide bond formation [40]. Each domain in the NRPS enzyme is highly substrate- and function-specific and therefore a genetic analysis predicts which substrates will bind and which siderophores will be produced. This predictability in the modular architecture of NRPSs gave rise to software such as antiSMASH and PRISM which can use sequence analysis to identify and predict the functionality of NRPS-encoding gene clusters [41,42]. The knowledge from these predictions is helping the discovery of novel peptides involved in iron uptake and the reprogramming of the biosynthetic machinery for the synthesis of novel peptides with improved and diversified bioactivities [40,43].

The NIS pathway relies on NIS synthetases and usually synthesizes polycarboxylate siderophores. However, other siderophore types (e.g., hydroxamates) are also produced by these enzymes, such as achromobactin, aerobactin, alcaligin, petrobactin, staphyloferrin A and B, legiobactin, schizokinen, and synechobactin. NIS synthetases are responsible for a single enzymatic reaction, typically activation of citric acid, via adenylation and nucleophilic capture of an amine or alcohol group which by releasing AMP produces a citryl intermediate. Multiple sequencing alignments of each type of NIS do not show significant sequence conservation but it has been proposed that this may be due to the limited number of validated NIS genes [44]. Often, more than one NIS enzyme is required to synthesize a siderophore, and usually, the biosynthetic pathway through NIS enzymes is discovered by homology searches using the aerobactin NIS synthetases encoded by the iuc operon in *Escherichia coli* K-12 [44,45].

Once the apo-siderophores are produced, the size and charge of these compounds prevent passive diffusion across the membrane, and thus, they must be exported via specialized secretion systems into the extracellular space for iron scavenging/complexation [46]. There is still much to unravel regarding the secretion mechanisms of apo-siderophores, however, from the identified secretion systems, the transporters can belong to three different structural families of bacterial multidrug resistance (MDR) translocases/transporters: the major facilitator superfamily (MFS), the resistance, nodulation, and cell division (RND) superfamily and the ABC superfamily [23]. MFS-transporters are found in all domains of life and move a variety of small compounds including nutrients, metabolites, signalling molecules, and even toxins and drugs across biological membranes. They can operate as uniporters, which transport a single substrate and require no energy input; symporters, that transport a substrate together with a coupling ion (typically protons); and antiporters, which transport a substrate and a co-substrate in opposite directions, with the binding of one dependent on the prior release of the other. Both the latter require external energy input, but unlike the former, they can transport substrates against their concentration gradient [47]. Some examples of MFS transporters that play a role in secreting siderophores include EntS for the secretion of enterobactin in *E. coli*, YhcA for the secretion of achromobactin in *Erwinia chrysanthemi*, LbtB for the secretion of legiobactin in *Legionella pneumophila* and others [23,48–51]. The RND family includes several members that are relevant to antibiotic resistance in Gram-negative bacteria and these function as proton antiporters. Some members of the RND family identified to play a role in the secretion of siderophores are: AcrB, AcrD that transport enterobactin in *E. coli*, ApeX that exports petrobactin in *Bacillus anthracis*, MmpL4, and MmpL5 that export mycobactins and carboxymycobactins from *Mycobacterium tuberculosis* [52–56].

From the ABC family involved in iron secretion, the following secretion systems have been identified: ExiT which exports exochelin from *Mycobacterium smegmatis* and IroC for the export of salmochelin. This later example, however, has been the subject of controversy since independent studies show that IroC is also responsible for the uptake of the Fe(III)-salmochelin. Given the current state-of-the-art regarding the mechanisms of siderophore uptake, it is possible that apo-siderophore release and Fe(III)-siderophore uptake operate through similar, if not, equal transport systems [21,54,57,58]. Overall, based on the almost exclusively characterized secretion system of enterobactin, it seems that siderophore secretion follows the three-component organization that is shared amongst most multidrug transporters [29,59]. This three-component organization consists of an inner membrane efflux protein or transporter/translocase (IEPs) (which can be any of the previously described families), an outer membrane efflux protein or channel (OEP), and a periplasmic efflux or accessory protein (PEP) that connects the two (Figure 3) [59,60]. The hypothesis is that enterobactin is exported to the periplasm by the inner membrane protein EntS and/or by RND transporters AcrB, AcrD, and MdtBC and then enterobactin goes through PEP member ArcA and/or MdtA into the OEP member TolC to be exported to the extracellular space [29,46,53]. Currently, only one other of the OEP and PEP members has been identified with a role in siderophore secretion: HgdD from *Anabaena sp.* PCC 7120 and MmpS4 & MmpS5 from *M. tuberculosis*, respectively [55,61]. Once in the extracellular space, apo-siderophores will bind available Fe(III) and then the Fe(III)-siderophore is incorporated back inside the cell. In Gram-negative bacteria, cell incorporation of Fe(III)-siderophores requires specific energy-dependent outer membrane receptors (OMR) since the majority of Fe(III)-siderophores are larger than 600 Da and thus porin-mediated transport is low. Typically, the affinity of these outer membrane transporters to the ferric siderophores is extremely high, in the range of 1–50 nM, allowing for the scavenging of these complexes from the environment. Once in the periplasm, they are bound to periplasmic siderophore-binding proteins, which are also designated as SBPs, for translocation into the cytoplasmic membrane via ABC-type transporters [22]. In Gram-positive bacteria, the import of Fe(III)-siderophores is similar except for the binding to the outer-membrane transporters [62]. In Gram-positive bacteria, Fe(III)-siderophores are transported directly via SBPs, permease(s), and an ATPase. SBPs are anchored in the membrane and specifically bind siderophores In both Fe(III) and apo-forms [63]. Two mechanisms have been proposed for the translocation of Fe(III)-siderophores into the cytoplasm: a displacement mechanism, whereby the initially bound apo-siderophore is replaced by the Fe(III)-siderophore, or by a siderophore-shuttle mechanism where Fe(III) is exchanged between the free Fe(III)-siderophore and the bound apo-siderophore and once exchanged, the Fe(III)-siderophore can be transported inside the cell for further iron release through specialized enzymes [21,62–65].

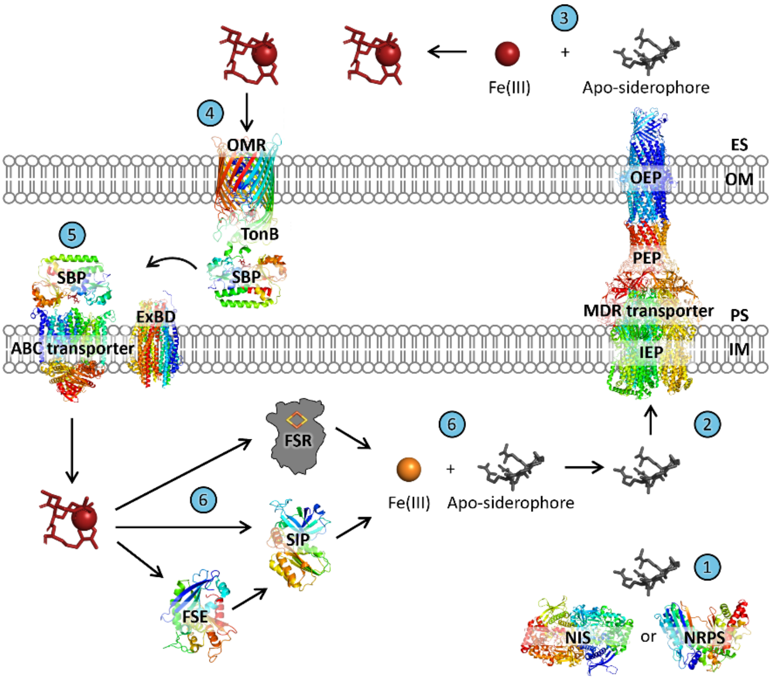

Figure I-**3** Overview of siderophore pathway in Gram-negative bacteria. Apo-siderophores are produced (1) via the NIS or the NRPS pathway and then secreted outside (2) via MDR transporters where they will incorporate Fe^{3+} forming Fe(III)-siderophores (3). These are then taken up to the periplasm (4) by energy-dependent (TonB ExBD) OMRs and delivered by SBP to ABC-transporters (5). Once in the cytoplasm, iron release from Fe(III)-siderophores occurs through different enzymes (6): Siderophore Interacting Protein (SIP), Ferric Siderophore Reductase (FSR), and Ferric Siderophore Esterase (FSE).

Iron release strategies from Fe(III)-siderophores

Once inside the cell, given the high affinities for Fe(III) and the very negative reduction potentials of Fe(III)-siderophores, iron release from these compounds does not occur spontaneously. Instead, iron release from Fe(III)-siderophore complexes can occur via a single mechanism or through a combination of different mechanisms: the hydrolysis of the Fe(III)-siderophore, redox-shift hypothesis, and/or reduction of the ferric iron within Fe(III)-siderophore complexes [27,66]. The hydrolysis of the Fe(III)-siderophore is mediated by esterases (FSE), Fe(III)-siderophore esterase (Figure 4), and it was observed for various siderophores including bacillibactin (by BesA esterase), enterobactin (by esterases Fes and PfeE), and fusarinine C (by esterase Sidj), salmochelin (by esterase IroD and IroE) [67]. Fes, the archetypical FSE from *E. coli* was purified in 1992, and the 43 kDa monomer was shown to efficiently catalyze the hydrolysis of Fe(III)-enterobactin, apo-enterobactin and Al(III)-enterobactin. From these compounds, a 4-fold greater activity was observed for the apo-enterobactin, suggesting that hydrolysis of ligand backbone is independent of bound metal [65]. This strategy is exclusive for siderophores that contain ester bonds and it requires a constant production of new siderophores for further iron acquisition [23].

The redox-shift hypothesis (Figure 4) contemplates the various ways by which the actual reduction potential of siderophores can be increased to ease iron release [66]. This includes proton-assisted dissociation of the siderophore complex, media lipophilicity, coupled Fe(II)-chelation, and ternary complex association. Proton-assisted dissociation of the siderophore complex requires a very low pH to guarantee complete dissociation, however competitive protonation (H^+) for siderophore ligand is a way to ease iron release from stable Fe(III)-siderophore complexes [66]. This proton competition can be illustrated by the fact that most siderophores have pH-dependent speciation (Figure 4) and often redox-Bohr effect, i.e., the reduction potential increases as the pH is lowered [31]. Another way by which the reduction potential of Fe(III)-siderophores can be increased is through media lipophilicity, for e.g. ferrioxamine E reduction potential in water is -468 mV vs SHE whereas in dichloromethane is -390 mV vs SHE [66]. Association with a strong Fe(II)-chelator is also a way to shift the equilibrium towards Fe(III)-reduction. Siderophores have a significantly lower affinity for Fe(II) than for Fe(III). However, in the presence of a strong Fe(II)-chelator, the effective reduction potential of Fe(III)-

siderophore complex shifts through coupled equilibria [66,68]. Ternary complex formation is effective for the reduction of ferrioxamine in conditions where the presence of BPDS (sulfonated bathophenanthroline) together with reducing agents ascorbate, glutathione, or NADH promotes the reduction of Fe(III) to Fe(II) enabling iron release [69].

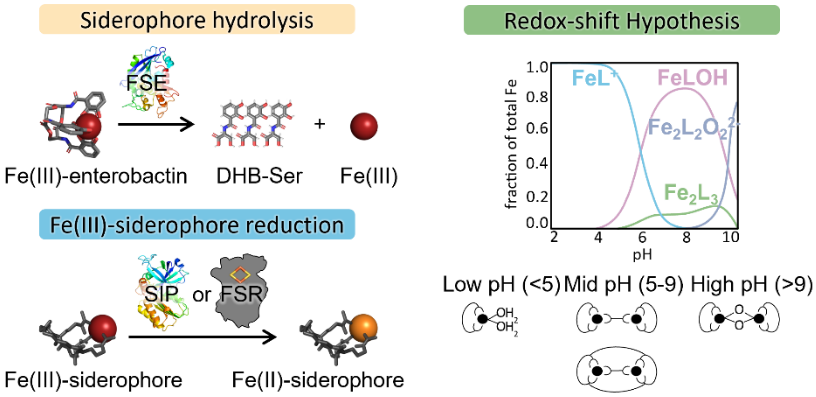

Figure I-**4** Main strategies of iron release reported for Gram-negative bacteria [32,65,70–72].

Ferric-Siderophore Reduction: One reaction to rule them all

At neutral pH and in the absence of ester bonds, the release of iron from Fe(III)-siderophores via reduction of the Fe(III) iron is the recurring mechanism. Upon reduction of Fe(III) to Fe(II), the stability of the complex is dramatically decreased given the lower affinity by approximately 20 log units of siderophore ligands to Fe(II) (Table 1). This has a positive impact on the kinetics of ligand exchange allowing time- and site-specific delivery of the metal. Reduction of the iron center is proposed to occur via small molecule reducing agents or by a superfamily of assimilatory Fe(III)-reductases [23,68]. Fe(III)-reductase activity has been a focus of study for more than 40 years [13]. However, only a few enzymes involved in this process have been isolated and characterized in detail. Great diversity exists in these enzymes, being found in different locations (cytoplasm, periplasm, and plasma membrane) [64,68,73,74]. In bacteria, Fe(III)-siderophore reduction occurs mostly in the cytoplasm, so far except for *Pseudomonas aeruginosa* where ferric-siderophore reduction can also occur in the periplasm [74]. In the cytosol, it involves a superfamily of proteins that are widely conserved across bacteria, and these are known as siderophore-interacting proteins (SIPs) [72]. These can belong to two distinct families: the SIP family and the FSR (Ferric-Siderophore Reductase) family [64,75]. For the SIP family, more members have been identified and characterized and thus these can be further distinguished into two broad groups: one that generates cytosolic reduced free flavins that subsequently reduce the Fe(III)-siderophores, and another that contain stably attached flavins and use NADH and/or NADPH as reducing agents [68,76]. SIPs, described throughout this thesis, are part of the latter group of enzymes. These are widely conserved among bacteria, most frequently in proteobacteria (64 %), but also in actinobacteria (33 %) and others (bacteroidetes, deinococcus–thermus, planctomycetes, gemmatimonadetes, fibrobacteres) [72]. The first example of SIP identified in the literature was ViuB from *Vibrio cholerae* [77]. ViuB was discovered as a product of the Fe(III)-vibriobactin utilization gene. The knockout of this protein showed that it is involved in the utilization of Fe(III)-vibriobactin in the cytoplasm and its activity could not be restored by Fes, the Fe(III)-enterobactin esterase produced by *E. coli.* This is an enzyme that promotes hydrolytic cleavage of the Fe(III)-siderophore complex, at the time, the only known mechanism for iron release from Fe(III)-siderophore complexes [65,77]. The terminology 'SIP' appeared later in 2006, when the first structure of a SIP from *Shewanella putrefaciens* (PDB code: 2GPJ) was determined by The Joint Center for Structural Genomics. Since then, other genes coding for SIPs have been found and characterized and these are usually clustered around the genes involved in siderophore biosynthesis and transport [64,72,75,78]. In 2011, Miethke and co-workers proposed two distinct subgroups of SIPs based on a comparative sequence analysis using ViuB as the founding sequence for SIPs. In this classification, the two subgroups can be distinguished based on the N-terminal and C-terminal sequences: subgroup I, represented by ViuB, contains a prominent C-terminal α-helical element, whereas subgroup II, represented by YqjH, misses this element, and contains insertions and extensions in the N-terminus [64]. It was also proposed that subgroup I utilize NADH as electron donor, whereas subgroup II utilizes NADPH [64]. However, it was recently shown that this classification is not a good proxy for understanding these enzymes. Indeed, *Shewanella frigidimarina* siderophore-interacting protein (*Sf*SIP) can utilize both NADH and NADPH and can also be reduced by ferredoxin despite being classified as part of subgroup I [79,80]. This observation suggests that the cofactor utilization should not be associated with the subgroup classification. Up to the present day, four structures of SIPs have been determined and all using X-ray crystallography being *Sf*SIP the highest resolution structure at 1.15 Å resolution [72,75,80]. The overall architecture is very similar, consisting of two domains (N-terminal or NAD(P)H-binding and C-terminal or FAD-binding) with the FAD buried in the interface in-between (Figure 5). The FAD is stabilized through aromatic stacking of the isoalloxazine ring by residues Tyr47, Tyr75, and Tyr245 in *Sf*SIP (Figure 5), which are conserved among the four structures [72]. YqjH from *E. coli*, FscN from *Thermobifida fusca*, and *Sf*SIP from *S. frigidimarina* are the most functionally characterized SIPs. YqjH is reduced by NADPH and it is able to reduce Fe(III)-enterobactin, the native siderophore produced by *E. coli* but is also able to reduce other Fe(III)-chelators including Fe(III)-dicitrate and Fe(III)-vibriobactin [64]. *Sf*SIP does not discriminate between NADH, and NADPH and it can be reduced by a small ferredoxin. It reduces three analogous siderophores produced by *Shewanella algae* (avaroferrin, bisucaberin, putrebactin) and ferrioxamine E [80,81]. On the other hand, FscN is specific for native siderophore

Fe(III)-fuscachelin and showed a preference for NADH. Overall the binding affinities for the Fe(III)-siderophores and NAD(P)H were reported in the micromolar range, and it has been postulated that Fe(III)-siderophore binding occurs in the proximity of the isoalloxazine ring of FAD through a triad of basic amino acid residues (Lys49, Lys257, and Lys259 *Sf*SIP, Figure 5) [64,75].

The function of SIPs is to make iron from Fe(III)-siderophores available in the cell for assimilation. This is achieved by removing iron from high-affinity Fe(III)-siderophore complexes. Iron removal is facilitated by reducing the Fe(III) to Fe(II), which decreases the stability of the complex promoting ligand exchange, thereby allowing time and site-specific delivery of iron [31,66]. Fe(III)-siderophore reduction also provides the advantage of recycling the siderophores for further rounds of iron uptake, saving the energy cost for their *de novo* biosynthesis [82].

The bioavailability of iron is a critical determinant in host-pathogen interactions, and thus it is not surprising that *sip* genes are often virulence-associated [83]. However, the role in iron acquisition and pathogenicity of SIPs was only studied in *Riemerella anatipestifer* CH3 with the construction of a *sip* gene deletion mutant (CH3Δ*sip*). This deletion attenuated the virulence of *R. anatipestifer* strain CH3 in ducklings and decreased the abilities of *R. anatipestifer* strain CH3 to adhere and invade Vero cells. Overall, this SIP was involved in iron acquisition, biofilm formation, and virulence; however, this gene is not required for iron acquisition in all *R. anatipestifer* strains, and no biochemical characterization exists regarding the mechanistic details of this SIP [84].

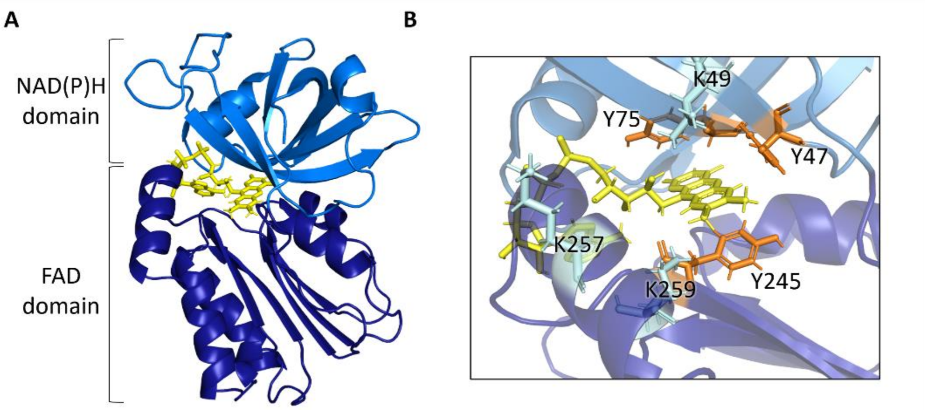

Figure I-**5 A)** Structure of SIP from *S. frigidimarina* (*Sf*SIP), PDB ID 6GEH. **B)** Close-up of FAD binding site with conserved stabilizing aromatic residues highlighted in orange and the structurally conserved basic triad of lysines highlighted in light blue.

The FSR family is represented by FhuF (Ferric hydroxamate uptake F) from *E. coli* and so far, this has been the only FSR ever isolated from Gram-negative bacteria. The *fhuF* (ferric hydroxamate uptake F) gene was first discovered for its high response sensitivity to iron concentration levels and *fhuF* deletion mutants showed a diminished ability to use ferrioxamine B as an iron source in agar plates [73,85]. FhuF protein was later purified and characterized. The protein was isolated both from cytoplasmic and membrane fractions and through mutant analysis, an atypical [2Fe-2S] binding motif coordinated by Cys-Cys-X_{10}-Cys-X_2-Cys (cysteine residues 244, 245, 256, and 259) was discovered [73]. The mid-point reduction potential of FhuF was determined as -310 mV vs SHE (pH 7.3). EPR and Mössbauer experiments of reduced FhuF showed unusual values for a 2Fe-2S protein and it is possible that the tetrahedral symmetry at the ferric ion site is distorted [71]. However, no structure or homologous structures have been determined for this family of proteins. Regardless, it was shown that FhuF is involved in iron utilization from hydroxamate-type siderophores (ferrichrome, ferrioxamine B and coprogen) possibly playing a role as a Fe(III)-siderophore reductase as shown through the oxidation of FhuF in the presence of ferrioxamine in EPR experiments [71].

As for FSRs in Gram-positive bacteria, a Fe(III)-siderophore reductase from *Bacillus halodurans*, FchR (Ferric citrate and hydroxamate reductase) displaying a similar 2Fe-2S cysteine binding motif CC-X_4-C-X_6-CX_2C but with only 19 % of sequence identity relative to FhuF (*E. coli*), was isolated and biochemically characterized. The *fchR* gene was found to cluster within the ferric-citrate/hydroxamate uptake system and the FchR protein is a Fe(III)-reductase for Fe(III)-dicitrate, Fe(III)-schizokinen, Fe(III)-aerobactin, and ferrichrome. It was also observed that Ga(III)-loaded siderophores can act as competitive inhibitors for FchR [86]. Very few studies exist regarding the physiological importance of FSRs. For *Shewanella oneidensis*, it was observed PutB had a negligible impact on iron physiology, suggesting the presence of alternative Fe(III)-siderophore reductases [87–89]. Unlike SIPs, no studies exist regarding the role of FSRs in the virulence of microorganisms. Interestingly, it was observed that, in some species, multiple Fe(III)-siderophore reductases exist, yet the relevance and the apparent redundancy of these proteins remains unexplored [75,80].

Once iron is released from Fe(III)-siderophores, apo-siderophores can be secreted outside for further rounds of iron uptake and iron can be incorporated in the labile iron pool or further used in the maturation of heme and non-heme Fe-containing proteins. Eventually, excess iron will be stored in proteins such as ferritin and bacterioferritin [90–92].

NMR for the study of metal-protein interactions

As previously observed in previous sections of this thesis, metals play a key role in life where the metal center(s) are essential for catalysis, electron transfer, and/or play a crucial role in ensuring stability and structural properties

[4]. Obtaining detailed information on the process of metal capture, transport, and ultimate delivery to assemble the biologically active cluster remains a challenge for which standardized methods do not exist [93]. Metal-containing compounds including metalloproteins not only have an inherent instability and frequently changing complex speciation but also often have unpaired electrons which defy most conventional methods.

NMR spectroscopy is a privileged technique for characterizing proteins and their role in key cellular processes since it probes structural and dynamic aspects at atomic resolution and spanning time scales from ns to days in conditions that mimic the physiological environment [94–98]. However, a significant part of key cellular processes and their enzymes rely on the participation of paramagnetic metals, i.e., metals that contain unpaired electrons. Near these metals, a “blind sphere” is created (Figure 6) where nuclear relaxation is enhanced, and signal detection becomes a challenge [99]. Often, the problem is circumvented by the substitution of the paramagnetic metal with a diamagnetic analog [100,101]. However, often this strategy fails because it leads to unfolded or misfolded proteins, or simply because the diamagnetic analog does not mimic the action exerted by the native paramagnetic metal. This challenge calls for novel methods that allow for reducing the “blind sphere” exerted by paramagnetic metals allowing structural biochemists the opportunity to explore key cellular processes such as bacterial iron acquisition and transport.

NMR of paramagnetic molecules: fundamentals

Like the NMR-active nuclei, electrons behave as magnetic dipoles when placed in a magnetic field. Consequently, the interaction between the unpaired electron and a nucleus (hyperfine interaction) can be mediated by chemical bonds (contact mechanism) or through space (dipolar mechanism). The distinguishing effect of the presence of unpaired electrons in a molecule derives from the fact that the magnetic moment of electrons is almost three orders of magnitude larger than that of protons. Therefore, the unpaired electron modifies the local magnetic field in its vicinity and causes pronounced effects in NMR spectra. The most visible are: unusual chemical shifts and temperature dependence of NMR signals affected by the unpaired electrons, line broadening and enhanced nuclear relaxation rates (Figure 6) (R_1 and R_2) [102,103]. Longitudinal relaxation (R_1) relates to the time necessary for the nuclear magnetization to return to equilibrium after excitation and is stimulated by fluctuations at frequencies near the Larmor frequency. Faster relaxation means that Nuclear Overhauser Enhancement (NOE) intensities (Figure 6), the typical constraints used for protein structure determination, are quenched, and shorter repetition times need to be used in experiments. Transverse relaxation (R_2) is stimulated by fluctuations of frequency near the Larmor frequency and lower. R_2 relates with the linewidth of NMR signals, therefore faster relaxation leads to broader signals (Figure 6) making their detection challenging [2].

The unpaired electron(s) enhance the relaxation of nuclear spins by three mechanisms, which are additive to “diamagnetic” nuclear relaxation: contact, dipolar, and Curie spin relaxation. The extent and the relative contribution of each of these mechanisms to R_1 and R_2 is modulated by three phenomena that may affect the correlation time: i) electron relaxation; ii) molecular tumbling in solution and iii) chemical or conformational exchange [104].

For nuclei belonging to atoms of residues directly bound to the paramagnetic metal ion, contact relaxation is often the dominating mechanism. In contact relaxation, the correlation time is determined by electron relaxation and by chemical exchange, when present. Therefore, R_1 and R_2 measurements, also known as Paramagnetic Relaxation Enhancements (PREs) provide a wealth of information on the extent of the interaction between the nuclei and the paramagnetic center and on the time dependence of this interaction. For nuclei belonging to atoms of residues not directly bound to the metal ion, the paramagnetic relaxation is dominated by the dipolar contribution. In this case, the relaxation rate becomes progressively slower with distance according to the inverse sixth power of the metal-nucleus separation since contact relaxation does not occur in these nuclei (Figure 6) [105].

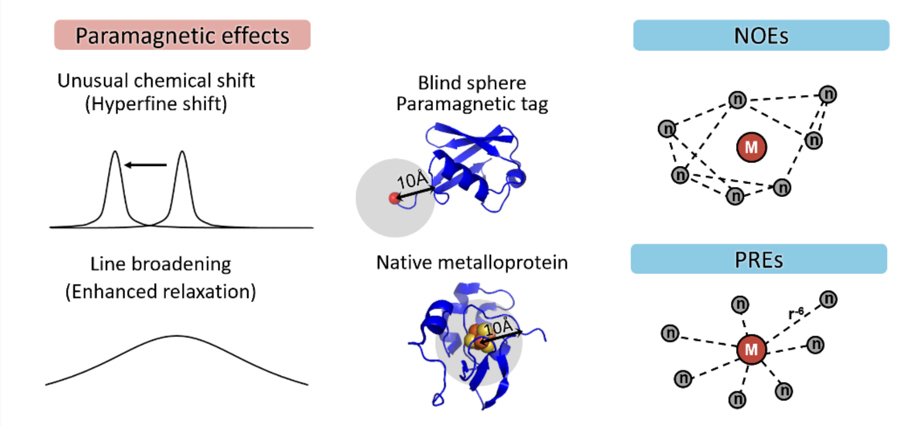

Figure I-**6** Representation of typical effects encountered in paramagnetic NMR spectra and a cartoon representation of Nuclear Overhauser Effect (NOE) vs Paramagnetic Relaxation Enhancement (PRE) measurements. M represents the metal center and n represents nuclei, typically referring to protons.

Electronic correlation times of metal centers span more than five orders of magnitude in the range from 10^{-13} to 10^{-8} s (Figure 7) [101]. Therefore, the nuclear relaxation properties of metal centers are diverse, and often require specialized strategies for spectral observation in each case [99,106,107].

Furthermore, the hyperfine interaction affects NMR chemical shifts and signal linewidths to different extents, which becomes a double-edged sword. On the one hand, paramagnetism can make the NMR investigation almost intractable, because signals can be broadened beyond detection or overwhelmed by sharp, diamagnetic signals. On the other hand, unique structural information can be obtained using tailored experimental approaches and by studying nuclei of low magnetogyric ratio such as ^{13}C and ^{15}N [107,108].

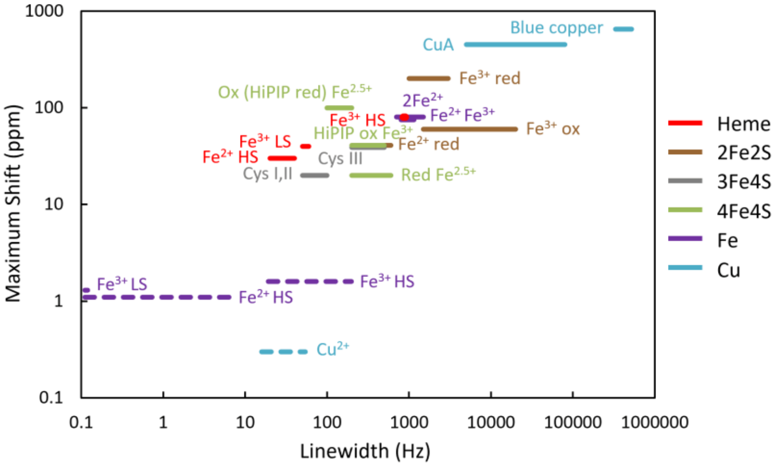

Figure I-**7** Maximum chemical shift and typical linewidths ranges observed in metalloproteins for βCH_2 protons of cysteines coordinating iron-sulfur (Fe-S) and copper (Cu) sites and for exchangeable NH protons for heme methyls.

Typically, the first step is the observation of NMR signals that are affected by the interaction with the paramagnetic center. The established strategy for their observation has two components: i) the acquisition of ^{1}H NMR spectra over large spectral windows using fast repetition rates for the suppression of slow relaxing protein signals and solvent; ii) the collection of a large number of scans for achieving sufficient S/N for very broad signals. WEFT (Water Eliminated Fourier Transform) and SUPERWEFT (optimized version of WEFT) pulse sequences, more recently revised to include gradients, broadband pre-saturation, and poly-chromatic pulses, are the most used sequences for ^{1}H NMR data collection, allowing both solvent suppression and the observation of broad paramagnetic signals [109–111].

Paramagnetic NMR: *ubi venire?*

The first spectrum of a metalloprotein in a paramagnetic state was collected for ferricytochrome *c* by Kowalsky in 1965 and soon it was extended to other proteins [112,113]. Subsequent work immediately revealed the power of paramagnetic NMR to characterize the structure of the paramagnetic cofactor with greater detail than that available by X-ray crystallography at the time [114]. The first measurements by NMR of the magnetic susceptibility of ferredoxin from *Clostridium pasteurianum* highlighted the importance of interpreting resonances outside the crowded diamagnetic region of proteins and this practice started to gain relevance [114,115]. In 1968, the temperature dependence of resonances of cyanometmyoglobin showed the possibility of distinguishing between shifts arising from hyperfine interactions and other mechanisms [114]. In 1970, the first spectra of an iron-sulfur protein and the temperature dependence of low field resonances were reported, giving rise to the first proposed model of cysteine-iron bonding in the ferredoxin from *C. pasteurianum* [116]. This type of spectroscopic studies in metalloproteins became popular in the following years when the development of the WEFT and SUPERWEFT pulse sequences contributed to overcoming the problems of dynamic range and allowed the utilization of water as a solvent without compromising the observation of the considerably broadened contact-shifted proton signals [109,117]. This boosted the elucidation of the electronic structure of the different paramagnetic centers in metalloproteins. Notwithstanding, the structure determination of paramagnetic proteins lingered for a few years because the fast nuclear R_1 and R_2 hampered the detection of dipolar and scalar connectivities, and adequate force field energy minimization parameters were difficult to select. Selective 1D NOEs and two-dimensional experiments were fundamental to overcome the loss of information around the metal center. In

1994, after assigning the missing connectivities in the vicinity of the paramagnetic center, the first solution structure of a paramagnetic protein was published: the High Potential Iron-Sulfur Protein (HiPIP) from *Ectothiorhodospira halophila* in its reduced $[Fe_4S_4]^{2+}$ form (PDB ID: 1PIH) [45–49]. Today, twenty-six years after the first structure of the nearly 12 000 NMR protein structures deposited in the PDB, about 12 % are metalloproteins and only about 1 % are paramagnetic metalloproteins (Table 2) [123]. This highlights both the enduring perception of the challenges of studying these systems by NMR spectroscopy and the vast untapped potential that this approach holds.

Table I-**2** Number of entries in the protein data bank for different search categories.

Total proteins PDB	162477
(metalloproteins)	81723
Total proteins by NMR	13526
(metalloproteins)	1560
Total paramagnetic proteins by NMR	115
(Co)	3
(Cu)	8
(Fe)	95
(Ni)	4
(Fe-Cu)	5

All the distance and geometric information that derives from the presence of a paramagnetic center has been crucial for obtaining the solution structure of metalloproteins and has allowed the investigation of the electronic structure of the active site of metalloproteins by NMR spectroscopy. This complements the experiments performed at cryogenic temperatures using other spectroscopies, such as Mössbauer and EPR but it also explores excited electronic states when they are thermally populated at physiological temperatures. This can be achieved by measuring the temperature dependence of the signals and fitting the data using the VanVleck formalism [101,124,125]. The analysis of the temperature dependence of NMR signals (Figure 8) has a pivotal role for the study of magnetically coupled systems as well as in the cases of spin admixture and chemical exchange. This work on the electronic structure and geometry of paramagnetic metallic cofactors in proteins evolved from the well-established investigation in inorganic chemistry [46–48]. Due to a combination of biological interest and more favorable electronic properties, hemes, iron-sulfur clusters, and copper centers have attracted more attention than other systems. Iron proteins have been the most extensively studied metalloproteins; not only because of their biological significance but also because iron centers can be characterized by several, and often complementary spectroscopies. With the exception of octahedral Fe(II) with strong field axial ligands such as histidines, methionines, and lysines, all iron centers in proteins have paramagnetic states at physiological temperatures. For iron proteins, the extent of paramagnetic effects varies greatly depending on the iron center and oxidation state [103].

NMR of Iron-Sulfur proteins

Iron-sulfur clusters are likely among the oldest metallic cofactors in biology [126,127]. Except for rubredoxins, which contain a single iron, all metal centers of iron-sulfur proteins are polymetallic, where each of the iron atoms is coordinated in approximate tetrahedral geometry to inorganic sulfide ions of the cluster and to the polypeptide by cysteine side chains, in most of the cases, or by cysteines/histidine(s) or cysteines/serine coordination (Figure 4) [128]. In this thesis, we focus on 2Fe-2S and 4Fe-4S clusters, other clusters can be found elsewhere [129].

In 2Fe-2S clusters, the two iron ions are linked by two bridging inorganic sulfide ions. In ferredoxins each iron is coordinated by two cysteines, whereas in mitoNEET-type and Rieske-type proteins one of the iron ions is coordinated by respectively, one or two histidines (Figure 8). The iron ions are antiferromagnetically coupled. In the oxidized state, this coupling between two, high-spin, Fe^{3+} ions lead to an S=0 ground state even though a significant paramagnetism may occur at room temperature due to the thermal population of excited paramagnetic states [130]. This gives rise to paramagnetically shifted signals which increase their shift with increasing temperature, the so-called anti-Curie behavior (Figure 8). This has been used in the study of iron-sulfur proteins containing 2Fe-2S and 4Fe-4S clusters, to identify the oxidation state of the cluster and its electronic structure. The two iron ions of the 2Fe–2S cluster are not equivalent due to differences in their primary (Rieske and mitoNEET proteins) or secondary (ferredoxins) coordination sphere and, upon reduction, the electron tends to be localized in one of them giving rise to a localized mixed valence [125]. However, the electronic state of reduced 2Fe-2S clusters is also affected by the ability of 2Fe-2S clusters to exchange one electron between the two iron ions due to the double exchange mechanism; the predominance of localized vs delocalized valence can be driven by subtle structural factors [131,132]. In Rieske-type ferredoxins, the iron coordinated to the histidines is the one that is redox-active [133]. The larger spin of the high-spin Fe^{3+} aligns with the magnetic field and the signals of the cysteines coordinating this iron display a large downfield shift and Curie-type temperature dependence. By contrast, the smaller spin of the high-spin Fe^{2+} is anti-parallel to the field and the signals of its coordinating cysteines (histidines in Rieske-type proteins) display anti-Curie temperature dependence (Figure 8) [130]. This offers a unique opportunity to identify the redox-active iron in the cluster.

For proteins containing 4Fe-4S clusters, valence delocalization is also observed [99]. In the case of ferredoxins, the cluster oxidizes from $[Fe_4S_4]^+$ to $[Fe_4S_4]^{2+}$ at low potential with the iron ions displaying the formal $2Fe^{2.5+}$- $2Fe^{2+}$

and $4Fe^{2.5+}$, respectively. In the case of HiPIPs, the reduced state $[Fe_4S_4]^{2+}$ again contains $4Fe^{2.5+}$ and oxidizes to $[Fe_4S_4]^{3+}$ with $2Fe^{2.5+}$ and $2Fe^{3+}$ [100]. In oxidized ferredoxins and reduced HiPIPs, the four irons are equivalent and antiferromagnetically coupled. The overall situation is therefore similar to $[Fe_2S_2]^{2+}$ ferredoxins where the electron spin has a ground state $S=0$ and paramagnetically shifted signals occur due to the thermal population of low-lying excited paramagnetic states. However, shorter electronic correlation times are observed for $[Fe_4S_4]^{2+}$ clusters, making the paramagnetically shifted ^1H signals of cysteine β-CH_2 much sharper than for $[Fe_2S_2]^{2+}$ clusters. For oxidized HiPIPs and reduced ferredoxins, the β-CH_2 protons of the cysteines coordinating the mixed valence irons are found at low field and with a Curie-type temperature dependence (Figure 8). The β-CH_2 protons of the cysteines coordinating Fe^{2+} in reduced ferredoxins and coordinating Fe^{3+} in oxidized HIPIPs are less shifted and display anti-Curie behavior. In the case of oxidized HiPIPs, where the magnetic coupling is expected to be slightly larger than in ferredoxins, the β-CH protons of the cysteines coordinating Fe^{3+} are also found at high fields (<0 ppm) [134–137].

Proteins containing iron-sulfur clusters were early targets of studies by NMR spectroscopy, providing insights into the structure of the clusters that were unresolved by X-ray at the time [116]. These early investigations revealed that contact shifts influence the spectral position of the signals of the cysteine beta protons and alpha carbons. For $[Fe_4S_4]^{2+}$ clusters, contact shifts provide information on the dihedral angle between Fe-S-Cβ-Hβ or Fe-S-Cβ-Cα. This influence is modulated according to contributions of unpaired spin density in Fe-S σ bonds and in pπ bonds of the sulfur, with the latter being the dominant term [138,139]. This provides an important geometrical constraint to define the structure of the protein in the vicinity of the cluster, which is often difficult by other NMR observables such as NOEs due to fast paramagnetic relaxation [99].

Often the redox activity of a polymetallic cluster is confined to a single iron atom. Assignment of the resonances of the ligands of the irons in the cluster allows pinpointing the relevant iron [124,129]. This is crucial mechanistic information because the rates of electron transfer decay exponentially with distance [140,141]. Furthermore, electrostatic interactions between partners depend on the presence and location of charges. These interactions contribute to the recognition and transient binding between redox partners and depend exponentially on distance [142,143]. Indeed, Fe-S clusters are also involved in other metabolic pathways not directly related to biological electron transfer [144–146]. This opens the possibility to use paramagnetic NMR for example to elucidate Iron-sulfur cluster assembly mechanisms within the mitochondrial matrix and to obtain insights into the catalytic mechanisms of R-SAM enzymes [134–137].

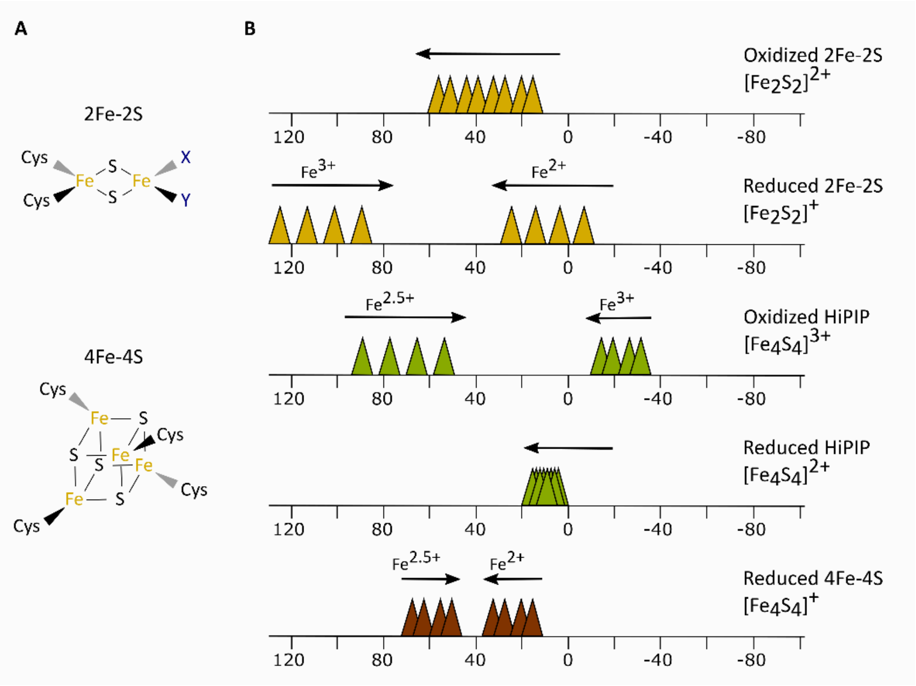

Figure I-**8** A) Clusters of iron-sulfur proteins where X and Y represent either cysteine and histidine (mitoNEET) or two histidines (Rieske-type). B) Typical position and temperature dependence of the signals of coordinating cysteines in various Fe-S clusters.

Paramagnetic NMR: *quo vadis*?

The previous sections showed the potential for paramagnetic NMR to contribute to the structural and functional characterization of metalloproteins and metalloenzymes. There are exciting perspectives on the theoretical, instrumentation, methodological and biological fronts for their future study by NMR. Protein structures and interactions can nowadays be monitored *in vitro* or *in cell*, thus opening unique opportunities to address biological functions [147,148].

On the methodological front, ingenious developments of NMR pulse programs are whittling away at the drawbacks of the paramagnetic effect on coherence transfer, and this can contribute to moving paramagnetic protein

NMR closer to the mainstream. Paramagnetic metalloproteins studied by NMR are woefully underrepresented in the PDB [149]. Given the undisputed relevance of metalloproteins and metalloenzymes for biological processes and for biotechnological applications, there is a vast untapped potential for the application of NMR to the study of the structure and function of paramagnetic metalloproteins.

References

[1] C. Andreini, I. Bertini, G. Cavallaro, G.L. Holliday, J.M. Thornton, Metal ions in biological catalysis: From enzyme databases to general principles, JBIC. 13 (2008) 1205–1218.

[2] R.R., Crichton, R.O. Louro, Practical Approaches to Biological Inorganic Chemistry, 2nd ed., Elsevier, 2019.

[3] J.J.R.F., Silva, R.J.P. Williams, The Biological Chemistry of the Elements, Oxford University Press, 2001.

[4] K.J. Waldron, J.C. Rutherford, D. Ford, N.J. Robinson, Metalloproteins and metal sensing, Nature. 460 (2009) 823–830.

[5] M. Ilbert, V. Bonnefoy, Insight into the evolution of the iron oxidation pathways, Biochim Biophys Acta. 1827 (2013) 161–175.

[6] H. Irving, R.J.P. Williams, Order of stability of metal complexes, Nature. 162 (1948) 746–745.

[7] R.O. Louro, N.L. Costa, A.P. Fernandes, A.V. Silva, I.B. Trindade, B.M. Fonseca, C.M. Paquete, Exploring the molecular mechanisms of extracellular electron transfer for harnessing reducing power in METs: Methodologies and approaches, in: Biomass, Biofuels, Biochemicals: Microbial Electrochemical Technology: Sustainable Platform for Fuels, Chemicals and Remediation, Elsevier, 2018: pp. 261–293.

[8] C.M. Paquete, G. Rusconi, A. v. Silva, R. Soares, R.O. Louro, A brief survey of the “cytochromome,” Adv. Microb. Physiol. 75 (2019) 69–135.

[9] B. Schink, Extracellular Redox Chemistry, in: Metals, Microbes, and Minerals - The Biogeochemical Side of Life, De Gruyter, 2021: pp. 33–58.

[10] A. Camacho, X.A. Walter, A. Picazo, J. Zopfi, Photoferrotrophy: Remains of an ancient photosynthesis in modern environments, Front. Microbiol. 8 (2017) 1–17.

[11] L.J. Bird, I.H. Saraiva, S. Park, E.O. Calcada, C.A. Salgueiro, W. Nitschke, R.O. Louro, D.K. Newman, Nonredundant Roles for Cytochrome c2 and Two High-Potential Iron-Sulfur Proteins in the Photoferrotroph *Rhodopseudomonas palustris* TIE-1, J. Bacteriol. 196 (2014) 850–858.

[12] L. Pereira, I.H. Saraiva, A.S.F. Oliveira, C.M. Soares, R.O. Louro, C. Frazão, Molecular structure of FoxE, the putative iron oxidase of *Rhodobacter ferrooxidans* SW2, Biochim Biophys Acta Bioenerg. 1858 (2017) 847–853.

[13] I. Schröder, E. Johnson, S. de Vries, Microbial ferric iron reductases, FEMS Microbiol Rev. 27 (2003) 427–447.

[14] A. Kappler, C. Bryce, M. Mansor, U. Lueder, J.M. Byrne, E.D. Swanner, An evolving view on biogeochemical cycling of iron, Nat Rev Microbiol. 19 (2021) 360–374.

[15] R.R. Crichton, J.-L. Pierre, Old Iron, Young Copper: from Mars to Venus, BioMetals. 14 (2001) 99–112.

[16] N. Abbaspour, R. Hurrell, R. Kelishadi, Review on iron and its importance for human health, J Res Med Sci. (2014) 164-174.

[17] E.D. Weinberg, The *Lactobacillus* Anomally: total iron abstinence, Perspect Biol Med. 40 (1997) 578–583.

[18] B. Troxell, H. Xu, X.F. Yang, *Borrelia burgdorferi*, a pathogen that lacks iron, encodes manganese-dependent superoxide dismutase essential for resistance to streptonigrin, J. Biol. Chem. 287 (2012) 19284–19293.

[19] M. Caza, J.W. Kronstad, Shared and distinct mechanisms of iron acquisition by bacterial and fungal pathogens of humans., Front Cell Infect. 3 (2013) 1–23.

[20] J.K. Moore, S.C. Doney, Iron availability limits the ocean nitrogen inventory stabilizing feedbacks between marine denitrification and nitrogen fixation, Global Biogeochem Cycles. 21 (2007) 1–12.

[21] K.N. Raymond, B.E. Allred, A.K. Sia, Coordination Chemistry of Microbial Iron Transport, Acc Chem Res. 48 (2015) 2496–2505.

[22] R.C. Hider, X. Kong, Chemistry and biology of siderophores, Nat Prod Rep. 27 (2010) 637–657.

[23] M. Miethke, M.A. Marahiel, Siderophore-Based Iron Acquisition and Pathogen Control, Microbiol Mol Biol Rev. 71 (2007) 413–451.

[24] S. O'Brien, A.M. Luján, S. Paterson, M.A. Cant, A. Buckling, Adaptation to public goods cheats in *Pseudomonas aeruginosa*, Proceedings of the Royal Society B: Biological Sciences. 284 (2017) 1-8.

[25] J. Kramer, Ö. Özkaya, R. Kümmerli, Bacterial siderophores in community and host interactions, Nat Rev Microbiol. 18 (2020) 152–163.

[26] D.L. McRose, M.R. Seyedsayamdost, F.M.M. Morel, Multiple siderophores: bug or feature?, J Biol Inorg Chem. 23 (2018) 983–993.

[27] A.L. Crumbliss, J.M. Harrington, Iron sequestration by small molecules: Thermodynamic and kinetic studies of natural siderophores and synthetic model compounds, Adv Inorg Chem. 61 (2009) 179–250.

[28] T.C. Johnstone, E.M. Nolan, Beyond iron: Non-classical biological functions of bacterial siderophores, Dalton Trans. 44 (2015) 6320–6339.

[29] B.R. Wilson, A.R. Bogdan, M. Miyazawa, K. Hashimoto, Y. Tsuji, Siderophores in Iron Metabolism: From Mechanism to Therapy Potential, Trends Mol. Med. 22 (2016) 1077–1090.

[30] W. Harris, K.N. Raymond, Ferric Ion Sequestering Agents: The Spectrophotometric and Potentiometric Evaluation of Two New Enterobactin Analogues: 1,5,9-N,N′,N′′-Tris(2,3-dihydroxybenzoyl)-cyclotriazatridecane and 1,3,5- N,N′,N′′-Tris(2,3-dihydroxybenzoyl) triaminomethylbenzene, J Am Chem Soc. 101 (1979) 6534–6541.

[31] H. Boukhalfa, A.L. Crumbliss, Chemical aspects of siderophore mediated iron transport, BioMetals. 15 (2002) 325–339.

[32] Z. Hou, K.N. Raymond, B. O'Sullivan, T.W. Esker, T. Nishio, A Preorganized Siderophore: Thermodynamic and Structural Characterization of Alcaligin and Bisucaberin, Microbial Macrocyclic Dihydroxamate Chelating Agents, Inorg Chem. 37 (1998) 6630–6637.

[33] A.-M. Albrecht-Gary, S. Blanc, N. Rachel, A.Z. Ocaktan, M.A. Abdallaht, Bacterial Iron Transport: Coordination Properties of Pyoverdin PaA, a Peptidic Siderophore of *Pseudomonas aeruginosa*, Inorg. Chem. 33 (1994) 6391–6402.

[34] B. Troxell, H.M. Hassan, Transcriptional regulation by Ferric Uptake Regulator (Fur) in pathogenic bacteria., Front Cell Infect. 3 (2013) 59.

[35] M.F. Fillat, The fur (ferric uptake regulator) superfamily: Diversity and versatility of key transcriptional regulators, Arch Biochem Biophys. 546 (2014) 41-52.

[36] C.S. Carroll, M.M. Moore, Ironing out siderophore biosynthesis: a review of non-ribosomal peptide synthetase (NRPS)-independent siderophore synthetases, Crit. Rev. Biochem. Mol. 53 (2018) 356–381.

[37] A.M. Gehring, K.A. Bradley, C.T. Walsh, Enterobactin Biosynthesis in *Escherichia coli*: Isochorismate Lyase (EntB) Is a Bifunctional Enzyme That Is Phosphopantetheinylated by EntD and Then Acylated by EntE Using ATP and 2,3-Dihydroxybenzoate, Biochemistry. 36 (1997) 8495–8503.

[38] L.E. Quadri, J. Sello, T.A. Keating, P.H. Weinreb, C.T. Walsh, Identification of a Mycobacterium tuberculosis gene cluster encoding the biosynthetic enzymes for assembly of the virulence-conferring siderophore mycobactin, Chem Biol. 5 (1998) 631–645.

[39] T.A. Keating, C.G. Marshall, C.T. Walsh, Reconstitution and characterization of the Vibrio cholerae vibriobactin synthetase from VibB, VibE, VibF, and VibH, Biochemistry. 39 (2000) 15522–15530.

[40] G.H. Hur, C.R. Vickery, M.D. Burkart, Explorations of catalytic domains in non-ribosomal peptide synthetase enzymology, Nat Prod Rep. 29 (2012) 1074–1098.

[41] M.A. Skinnider, C.A. Dejong, P.N. Rees, C.W. Johnston, H. Li, A.L.H. Webster, M.A. Wyatt, N.A. Magarvey, Genomes to natural products PRediction Informatics for Secondary Metabolomes (PRISM), Nucleic Acids Res. 43 (2015) 9645–9662.

[42] M.H. Medema, K. Blin, P. Cimermancic, V. de Jager, P. Zakrzewski, M.A. Fischbach, T. Weber, E. Takano, R. Breitling, AntiSMASH: Rapid identification, annotation and analysis of secondary metabolite biosynthesis gene clusters in bacterial and fungal genome sequences, Nucleic Acids Res. 39 (2011) 339-346.

[43] C.D. Hardy, A. Butler, β-Hydroxyaspartic acid in siderophores: biosynthesis and reactivity, J. Biol. Inorg. Chem. 23 (2018) 957–967.

[44] C.S. Carroll, M.M. Moore, Ironing out siderophore biosynthesis: a review of non-ribosomal peptide synthetase (NRPS)-independent siderophore synthetases, Crit Rev Biochem Mol Biol. 53 (2018) 356–381.

[45] V. de Lorenzo, A. Bindereif, B.H. Paw, J.B. Neilands, Aerobactin Biosynthesis and Transport Genes of Plasmid Co1V-K30 in *Escherichia coli* K-12, J Bacteriol. 165 (1986) 570–578.

[46] J. Furrer, D., Sanders, I.G., Hook-Barnard, M.A. McIntosh, Export of the siderophore enterobactin in *Escherichia coli*: involvement of a 43 kDa membrane exporter, Mol Microbiol. 44 (2002) 1225–1234.

[47] E.M. Quistgaard, C. Löw, F. Guettou, P. Nordlund, Understanding transport by the major facilitator superfamily (MFS): Structures pave the way, Nat Rev Mol Cell Biol. 17 (2016) 123–132.

[48] K. Nicolaisen, A. Hahn, M. Valdebenito, S. Moslavac, A. Samborski, I. Maldener, C. Wilken, A. Valladares, E. Flores, K. Hantke, E. Schleiff, The interplay between siderophore secretion and coupled iron and copper transport in the heterocyst-forming cyanobacterium *Anabaena* sp. PCC 7120, Biochim. Biophys. Acta - Biomembr. 1798 (2010) 2131–2140.

[49] M. Hannauer, E. Yeterian, L.W. Martin, I.L. Lamont, I.J. Schalk, An efflux pump is involved in secretion of newly synthesized siderophore by *Pseudomonas aeruginosa*, FEBS Lett. 584 (2010) 4751–4755.

[50] T. Tanabe, T. Funahashi, H. Nakao, S.I. Miyoshi, S. Shinoda, S. Yamamoto, Identification and Characterization of Genes Required for Biosynthesis and Transport of the Siderophore Vibrioferrin in *Vibrio parahaemolyticus*, J Bacteriol. 185 (2003) 6938–6949.

[51] C.H. Chatfield, B.J. Mulhern, V.K. Viswanathan, N.P. Cianciotto, The major facilitator superfamily-type protein LbtC promotes the utilization of the legiobactin siderophore by *Legionella pneumophila*, Microbiology (N Y). 158 (2012) 721–735.

[52] A.K. Hagan, A. Tripathi, D. Berger, D.H. Sherman, P.C. Hanna, Petrobactin is exported from *Bacillus anthracis* by the RND-type exporter apex, MBio. 8 (2017) 1-20.

[53] T. Horiyama, K. Nishino, AcrB, AcrD, and MdtABC multidrug efflux systems are involved in enterobactin export in *Escherichia coli*, PLoS One. 9 (2014) 1-7.

[54] G. Grass, Iron transport in *Escherichia coli*: All has not been said and done, BioMetals. 19 (2006) 159–172.

[55] R.M. Wells, C.M. Jones, Z. Xi, A. Speer, O. Danilchanka, K.S. Doornbos, P. Sun, F. Wu, C. Tian, M. Niederweis, Discovery of a Siderophore Export System Essential for Virulence of *Mycobacterium tuberculosis*, PLoS Pathog. 9 (2013) 1-14.

[56] C.M. Jones, R.M. Wells, A.V.R. Madduri, M.B. Renfrow, C. Ratledge, D.B. Moody, M. Niederweis, Self-poisoning of *Mycobacterium tuberculosis* by interrupting siderophore recycling, Proc Natl Acad Sci U S A. 111 (2014) 1945–1950.

[57] W. Zhu, J.E.L. Arceneaux, M.L. Beggs, B.R. Byers, K.D. Eisenach, M.D. Lundrigan, Exochelin genes in *Mycobacterium smegmatis*: identification of an ABC transporter and two non-ribosomal peptide synthetase genes, Mol Microbiol. 29 (1998) 629–639.

[58] M.L. v. Crouch, M. Castor, J.E. Karlinsey, T. Kalhorn, F.C. Fang, Biosynthesis and IroC-dependent export of the siderophore salmochelin are essential for virulence of *Salmonella enterica* serovar *Typhimurium*, Mol. Microbiol. 67 (2008) 971–983.

[59] H.I. Zgurskaya, H. Nikaido, MicroReview Multidrug resistance mechanisms: drug efflux across two membranes, Mol. Microbiol. 37 (2000) 219–225.

[60] C. Alvarez-Ortega, J. Olivares, J.L. Martínez, RND multidrug efflux pumps: What are they good for?, Front Microbiol. 4 (2013) 1–11.

[61] A. Hahn, M. Stevanovic, O. Mirus, E. Schleiff, The TolC-like protein HgdD of the cyanobacterium *Anabaena* sp. PCC 7120 is involved in secondary metabolite export and antibiotic resistance, J. Biol. Chem. 287 (2012) 41126–41138.

[62] T. Fukushima, B.E. Allred, A.K. Sia, R. Nichiporuk, U.N. Andersen, K.N. Raymond, Gram-positive siderophore-shuttle with iron-exchange from Fe-siderophore to apo-siderophore by *Bacillus cereus* YxeB, Proc Natl Acad Sci U S A. 110 (2013) 13821–13826.

[63] T. Fukushima, B.E. Allred, K.N. Raymond, Direct evidence of iron uptake by the Gram-positive siderophore-shuttle mechanism without iron reduction, ACS Chem Biol. 9 (2014) 2092–2100.

[64] M. Miethke, J. Hou, M.A. Marahiel, The siderophore-interacting protein YqjH acts as a ferric reductase in different iron assimilation pathways of *Escherichia coli*, Biochemistry. 50 (2011) 10951–10964.

[65] T.J. Brickman, M.A. McIntosh, Overexpression and purification of ferric enterobactin esterase from *Escherichia coli*. Demonstration of enzymatic hydrolysis of enterobactin and its iron complex, Journal of Biological Chemistry. 267 (1992) 12350–12355.

[66] S. Dhungana, A.L. Crumbliss, Coordination chemistry and redox processes in siderophore-mediated iron transport, Geomicrobiol J. 22 (2005) 87–98.

[67] R.J. Abergel, A.M. Zawadzka, T.M. Hoette, K.N. Raymond, Enzymatic hydrolysis of trilactone siderophores: Where chiral recognition occurs in enterobactin and bacillibactin iron transport, J Am Chem Soc. 131 (2009) 12682–12692.

[68] J.L. Pierre, M. Fontecave, & R.R. Crichton, Chemistry for an essential biological process: the reduction of ferric iron, BioMetals. 15 (2002) 341–346.

[69] K.A. Mies, J.I. Wirgau, A.L. Crumbliss, Ternary complex formation facilitates a redox mechanism for iron release from a siderophore, BioMetals. 19 (2006) 115–126.

[70] I. Spasojević, S.K. Armstrong, T.J. Brickman, A.L. Crumbliss, Electrochemical Behavior of the Fe(III) Complexes of the Cyclic Hydroxamate Siderophores Alcaligin and Desferrioxamine E, Inorg Chem. 38 (1999) 449–454.

[71] B.F. Matzanke, S. Anemüller, V. Schünemann, A.X. Trautwein, K. Hantke, FhuF, Part of a Siderophore-Reductase System, Biochemistry. 43 (2004) 1386–1392.

[72] I.B. Trindade, E. Moe, R.O. Louro, Siderophore-Interacting Protein, in: EIBC, Wiley, 2020: pp. 1–12.

[73] K. Müller, B.F. Matzanke, V. Schünemann, A.X. Trautwein, K. Hantke, FhuF, an iron-regulated protein of *Escherichia coli* with a new type of [2Fe-2S] center, Eur J Biochem. 258 (1998) 1001–1008.

[74] G. Ganne, K. Brillet, B. Basta, B. Roche, F. Hoegy, V. Gasser, I.J. Schalk, IIron release from the siderophore pyoverdine in *Pseudomonas aeruginosa* involves three new actors FpvC, FpvG and FpvH, ACS Chem. Biol. 12 (2017) 1056–1065.

[75] K. Li, W.H. Chen, S.D. Bruner, Structure and Mechanism of the Siderophore-Interacting Protein from the Fuscachelin Gene Cluster of *Thermobifida fusca*, Biochemistry. 54 (2015) 3989–4000.

[76] M. Fontecave, J. Covès, J.L. Pierre, Ferric reductases or flavin reductases?, Biometals. 7 (1994) 3–8.

[77] J.R. Butterton, S.B. Calderwood, Identification, cloning, and sequencing of a gene required for ferric vibriobactin utilization by *Vibrio cholerae*., J Bacteriol. 176 (1994) 5631–5638.

[78] S. Velankar, C. Best, B. Beuth, PDBe: protein data bank in Europe, Nucleic Acids Res. Spec. Publ. 38 (2010) 308–317.

[79] I.B. Trindade, B.M. Fonseca, P.M. Matias, R.O. Louro, E. Moe, A putative siderophore-interacting protein from the marine bacterium *Shewanella frigidimarina* NCIMB 400: cloning, expression, purification, crystallization and X-

ray diffraction analysis, Acta Crystallogr F Struct Biol Commun. 72 (2016) 667–671.

[80] I. Trindade, J.M. Silva, B.M. Fonseca, T. Catarino, M. Fujita, P.M. Matias, E. Moe, R.O. Louro, Structure and reactivity of a siderophore-interacting protein from the marine bacterium *Shewanella* reveals unanticipated functional versatility, J. Biol. Chem. 294 (2018) 157–167.

[81] S. Rütschlin, S. Gunesch, T. Böttcher, One Enzyme, Three Metabolites: *Shewanella algae* Controls Siderophore Production via the Cellular Substrate Pool, Cell Chem. Biol. 24 (2017) 598–604.

[82] F. Imperi, F. Tiburzi, P. Visca, E.P. Greenberg, Molecular basis of pyoverdine siderophore recycling in *Pseudomonas aeruginosa*, Proceedings of the National Academy of Sciences. 106 (2009) 20440–20445.

[83] A. Cruz, J. Xicohtencatl-Cortes, B. González-Pedrajo, M. Bobadilla, C. Eslava, I. Rosas, Virulence traits in cronobacter species isolated from different sources, Can J Microbiol. 57 (2011) 735–744.

[84] J. Tu, F. Lu, S. Miao, X. Ni, P. Jiang, H. Yu, L. Xing, S. Yu, C. Ding, Q. Hu, The siderophore-interacting protein is involved in iron acquisition and virulence of *Riemerella anatipestifer* strain CH3, Vet Microbiol. 168 (2014) 395–402.

[85] K. Hantke, V. Braun, Control of Bacterial Iron Transport by Regulatory Proteins, in: Metal Ions in Gene Regulation, 1998: pp. 11–44.

[86] M. Miethke, A.J. Pierik, F. Peuckert, A. Seubert, M.A. Marahiel, Identification and characterization of a novel-type ferric siderophore reductase from a gram-positive extremophile, J. Biol. Chem. 286 (2011) 2245–2260.

[87] C.M. Fennessey, M.E. Jones, M. Taillefert, T.J. Dichristina, Siderophores are not involved in Fe(III) solubilization during anaerobic Fe(III) respiration by *Shewanella oneidensis* MR-1, Appl Environ Microbiol. 76 (2010) 2425–2432.

[88] Z. Dong, S. Guo, H. Fu, H. Gao, Investigation of a spontaneous mutant reveals novel features of iron uptake in *Shewanella oneidensis*, Sci Rep. 7 (2017) 1-12.

[89] L. Liu, S. Li, S. Wang, Z. Dong, H. Gao, Complex iron uptake by the putrebactin mediated and Feo systems in *Shewanella oneidensis*, Appl Environ Microbiol. 84 (2018) 1-17.

[90] S.C. Andrews, A.K. Robinson, F. Rodríguez-Quiñones, Bacterial iron homeostasis, FEMS Microbiol Rev. 27 (2003) 215–237.

[91] L.D. Palmer, E.P. Skaar, Transition Metals and Virulence in Bacteria, Annu Rev Genet. 50 (2016) 67–91.

[92] R. Golonka, B.S. Yeoh, M. Vijay-Kumar, The Iron Tug-of-War between Bacterial Siderophores and Innate Immunity, J Innate Immun. 11 (2019) 249–262.

[93] E.O. by Jerome Nriagu, E.P. Skaar, Methods and Technologies for Analyzing Trace Metals in Biological Systems Diseases, in: Trace Metals and Infectious Diseases, 2015: pp. 311–400.

[94] A.R. Camacho-Zarco, V. Schnapka, S. Guseva, A. Abyzov, W. Adamski, S. Milles, M.R. Jensen, L. Zidek, N. Salvi, M. Blackledge, NMR Provides Unique Insight into the Functional Dynamics and Interactions of Intrinsically Disordered Proteins, Chem Rev. 122 (2022) 9331–9356.

[95] K. Wüthrich, NMR studies of structure and function of biological macromolecules (Nobel Lecture), Angew. Chem., Int. Ed. 42 (2003) 3340–3363.

[96] J.A. Purslow, B. Khatiwada, M.J. Bayro, V. Venditti, NMR Methods for Structural Characterization of Protein-Protein Complexes, Front. Mol. Biosci. 7 (2020) 1–8.

[97] Y. Hu, K. Cheng, L. He, X. Zhang, B. Jiang, L. Jiang, C. Li, G. Wang, Y. Yang, M. Liu, NMR-Based Methods for Protein Analysis, Anal Chem. 93 (2021) 1866–1879.

[98] P.J. Barrett, J. Chen, M.K. Cho, J.H. Kim, Z. Lu, S. Mathew, D. Peng, Y. Song, W.D. van Horn, T. Zhuang, F.D. Sönnichsen, C.R. Sanders, The quiet renaissance of protein nuclear magnetic resonance, Biochemistry. 52 (2013) 1303–1320.

[99] M. Invernici, I.B. Trindade, F. Cantini, R.O. Louro, M. Piccioli, Measuring transverse relaxation in highly paramagnetic systems, J Biomol NMR. 74 (2020) 431–442.

[100] G. Otting, Protein NMR using paramagnetic ions, Annu. Rev. Biophys. 39 (2010) 387–405.

[101] I. Bertini, C. Luchinat, G. Parigi, Solution NMR of Paramagnetic Molecules: Applications to Metallobiomolecules and Models, Elsevier, 2001.

[102] I. Bertini, P. Turano, A.J. Vila, Nuclear Magnetic Resonance of Paramagnetic Metalloproteins, Chem Rev. (1993) 2833–2932.

[103] M. Piccioli, P. Turano, Transient iron coordination sites in proteins: Exploiting the dual nature of paramagnetic NMR, Coord. Chem. Rev. 284 (2015) 313–328.

[104] I. Bertini, C. Luchinat, G. Parigi, R. Pierattelli, NMR spectroscopy of paramagnetic metalloproteins, ChemBioChem. 6 (2005) 1536–1549.

[105] M. Piccioli, Paramagnetic NMR spectroscopy is a tool to address reactivity, structure, and protein–protein interactions of metalloproteins: The case of iron–sulfur proteins, Magnetochemistry. 6 (2020) 1–21.

[106] I.B. Trindade, M. Invernici, F. Cantini, R.O. Louro, M. Piccioli, Sequence-specific assignments in NMR spectra of paramagnetic systems: A non-systematic approach, Inorganica Chim. Acta. 514 (2021) 1-8.

[107] S. Ciofi-Baffoni, A. Gallo, R. Muzzioli, M. Piccioli, The IR-^{15}N-HSQC-AP experiment: A new tool for NMR spectroscopy of paramagnetic molecules, J. Biomol. NMR. 58 (2014) 123–128.

[108] V. Ghini, S. Chevance, P. Turano, About the use of ^{13}C-^{13}C NOESY in bioinorganic chemistry, J. Inorg. Biochem. 192 (2019) 25–32.

[109] T. Inubushi, E.D. Becker, Efficient detection of paramagnetically shifted NMR resonances by optimizing the WEFT pulse sequence, J. Magn. Reson. 51 (1983) 128–133.

[110] A. Bondon, C. Mouro, PASE (PAramagnetic Signals Enhancement): A New Method for NMR Study of Paramagnetic Proteins, J. Magn. Reson. 134 (1998) 154–157.

[111] G. Helms, J.D. Satterlee, Keeping PASE with WEFT: SHWEFT-PASE pulse sequences for ^{1}H NMR spectra of highly paramagnetic molecules, Magn Reson Chem. 51 (2013) 222–229.

[112] A. Kowalsky, Nuclear Magnetic Resonance Studies of Cytochrome c. Possible Electron Delocalization, Biochemistry. 4 (1965) 2382–2388.

[113] W.D. Phillips, M. Poe, Contact Shifts and Magnetic Susceptibilities in Iron-Sulfur Proteins as determined from NMR spectra, Meth. Enzymol. 24 (1972) 304–317.

[114] K. Wüthrich, R.G. Shulman, J. Peisach, High-resolution proton magnetic resonance spectra of sperm whale cyanometmyoglobin., Proc. Natl. Acad. Sci. U.S.A. 60 (1968) 373–380.

[115] D.C. Blomstrom, E., Knight, W.D., Phillips, W, The nature of iron in ferredoxin, Proc. Natl. Acad. Sci. 51 (1964) 1085–1093.

[116] M. Poe, W.D. Phillips, C.C. Mcdonald, W. Lovenberg, Proton Magnetic Resonance Study of Ferredoxin from *Clostridium pasteurianum*, Proc. Natl. Acad. Sci. 65 (1970) 797–804.

[117] S.L. Patt, B.D. Sykes, Water eliminated fourier transform NMR spectroscopy, Chem. Phys. 56 (1972) 3182–3184.

[118] C.A. Salgueiro, D.L. Turner, H. Santos, J. Legall, A. v. Xavier, Assignment of the redox potentials to the four harms in *Desulfovibrio vulgaris* cytochrome c3 by 2D-NMR, FEBS J. 314 (1992) 155–158.

[119] S., Ramaprasad, R.D., Johnson, G.N. la Mar, Vinyl Mobility in Myoglobin as Studied by Time-Dependent Nuclear Overhauser Effect Measurements, J. Am. Chem. Soc. 106 (1984) 3632–3635.

[120] L. Banci, I. Bertini, L.D. Eltis, I.C. Felli, D.H.W. Kastrau, C. Luchinat, M. Piccioli, R. Pierattelli, M. Smith, The three-dimensional structure in solution of the paramagnetic high-potential iron-sulfur protein I from *Ectothiorhodospira halophila* through nuclear magnetic resonance, Eur J Biochem. 225 (1994) 715–725.

[121] I. Bertini, C. Luchinat, L.-J. Ming, M. Piccioli, M. Sola, J. Selverstone Valentine, Two-Dimensional ^{1}H NMR Studies of the Paramagnetic Metalloenzyme Copper-Nickel Superoxide Dismutase, Inorg Chem. 31 (1992) 4433–4435.

[122] D.S. Emerson, G.N. la Mar, Solution Structural Characterization of Cyanometmyoglobin: Resonance Assignment of Heme Cavity Residues by Two-Dimensional NMR, Biochemistry. 29 (1990) 1545–1556.

[123] H.M. Berman, J. Westbrook, Z. Feng, G. Gilliland, T.N. Bhat, H. Weissig, I.N. Shindyalov, P.E. Bourne, The Protein Data Bank, Nucleic Acids Res. Spec. Publ. 28 (2000) 1-8.

[124] I.B. Trindade, G. Hernandez, E. Lebègue, F. Barrière, T. Cordeiro, M. Piccioli, R.O. Louro, Conjuring up a ghost: structural and functional characterization of FhuF, a ferric siderophore reductase from *E. coli*, J. Biol. Inorg. Chem. 26 (2021) 313–326.

[125] R. Crichton, Biological Inorganic Chemistry: A New Introduction to Molecular Structure and Function, Third Edition, Elsevier, 2003.

[126] H. Raanan, D.H. Pike, E.K. Moore, P.G. Falkowski, V. Nanda, Modular origins of biological electron transfer chains, Proc. Natl. Acad. Sci. U.S.A. 115 (2018) 1280–1285.

[127] C. Bonfio, E. Godino, M. Corsini, F. Fabrizi de Biani, G. Guella, S.S. Mansy, Prebiotic iron–sulfur peptide catalysts generate a pH gradient across model membranes of late protocells, Nat Catal. 1 (2018) 616–623.

[128] H. Beinert, R.H. Holm, E. Mü, Iron-Sulfur Clusters: Nature's Modular, Multipurpose Structures, Science (1979). 277 (1997) 653–659.

[129] I. Bertini, S. Ciurli, C. Luchinat, The Electronic Structure of FeS Centers in Protein and Models. A Contribution to the Understanding of Their Electron, in: Iron-Sulfur Proteins Perovskites, Springer Berlin Heidelberg, 1995.

[130] L. Banci, I. Bertini, C. Luchinat, The ^{1}H NMR Parameters of Magnetically Coupled Dimers - The Fe_2S_2 Proteins as an Example, in: Structure and Bonding 72, 1990: pp. 114–136.

[131] L. Skjeldal, J.L. Markley, V.M. Coghlan, L.E. Vickery, 1H NMR Spectra of Vertebrate [2Fe-2S] Ferredoxins. Hyperfine Resonances Suggest Different Electron Delocalization Patterns from Plant Ferredoxins, Biochemistry. 30 (1991) 9078–9083.

[132] K. Cai, M. Tonelli, R.O. Frederick, J.L. Markley, Human Mitochondrial Ferredoxin 1 (FDX1) and Ferredoxin 2 (FDX2) Both Bind Cysteine Desulfurase and Donate Electrons for Iron-Sulfur Cluster Biosynthesis, Biochemistry. 56 (2017) 487–499.

[133] B. Xia, D. Jenk, D.M. LeMaster, W.M. Westler, J.L. Markley, Electron-nuclear interactions in two prototypical [2Fe-2S] proteins: Selective (chiral) deuteration and analysis of ^{1}H and ^{2}H NMR signals from the alpha and beta hydrogens of cysteinyl residues that ligate the iron in the active sites of human ferredoxin and Anabaena 7120 vegetative ferredoxin, Arch. Biochem. 373 (2000) 328–334.

[134] D. Suraci, G. Saudino, V. Nasta, S. Ciofi-Baffoni, L. Banci, ISCA1 Orchestrates ISCA2 and NFU1 in the Maturation of Human Mitochondrial [4Fe-4S] Proteins, J. Mol. Biol. 433 (2021) 1-17.

[135] D. Brancaccio, A. Gallo, M. Piccioli, E. Novellino, S. Ciofi-Baffoni, L. Banci, [4Fe-4S] cluster assembly in mitochondria and its impairment by copper, J Am Chem Soc. 139 (2017) 719–730.

[136] D. Brancaccio, A. Gallo, M. Mikolajczyk, K. Zovo, P. Palumaa, E. Novellino, M. Piccioli, S. Ciofi-Baffoni, L. Banci, Formation of [4Fe-4S] clusters in the mitochondrial iron-sulfur cluster assembly machinery, J. Am. Chem. Soc. 136 (2014) 16240–16250.

[137] F. Camponeschi, R. Muzzioli, S. Ciofi-Baffoni, M. Piccioli, L. Banci, Paramagnetic ^{1}H NMR Spectroscopy to Investigate the Catalytic Mechanism of Radical S-Adenosylmethionine Enzymes, J. Mol. Biol. 431 (2019) 4514–4522.

[138] I. Bertini, C. Luchinat, A. Rosato, NMR Spectra of Iron-Sulfur Proteins, Adv Inorg Chem. 47 (1999) 251–282.

[139] F. Capozzi, C. Luchinat, M. Piccioli, A.J. Vila, I. Bertini, The Fe4S4 Centers in Ferredoxins Studied through Proton and Carbon Hyperfine Coupling. Sequence-Specific Assignments of Cysteines in Ferredoxins from *Clostridium acidi urici* and *Clostridium pasteurianum*, J. Am. Chem. Soc. 116 (1994) 651–660.

[140] H.B. Gray, Chemical Bonds: An Introduction to Atomic and Molecular Structure, University Science Books, 1994.

[141] C.C. Page, C.C. Moser, X. Chen, P.L. Dutton, Natural engineering principles of electron tunnelling in biological oxidation ± reduction, Nature. 402 (1999) 47–52.

[142] B.M. Fonseca, C.M. Paquete, C.A. Salgueiro, R.O. Louro, The role of intramolecular interactions in the functional control of multiheme cytochromes c, FEBS Lett. 586 (2012) 504–509.

[143] M. Ubbink, The courtship of proteins: Understanding the encounter complex, FEBS Lett. 583 (2009) 1060–1066.

[144] I. Ferecatu, S. Gonçalves, M.P. Golinelli-Cohen, M. Clémancey, A. Martelli, S. Riquier, E. Guittet, J.M. Latour, H. Puccio, J.C. Drapier, E. Lescop, C. Bouton, The diabetes drug target MitoNEET governs a novel trafficking pathway to rebuild an Fe-S cluster into cytosolic aconitase/iron regulatory protein, J. Biol. Chem. 289 (2014) 28070–28086.

[145] R. Lill, S.-A. Freibert, Mechanisms of Mitochondrial Iron-Sulfur Protein Biogenesis, Annu. Rev. Biochem. 89 (2020) 471–499.

[146] N. Maio, B.A.P. Lafont, D. Sil, Y. Li, J.M. Bollinger, C. Krebs, T.C. Pierson, W.M. Linehan, T.A. Rouault, Fe-S cofactors in the SARS-CoV-2 RNA-dependent RNA polymerase are potential antiviral targets, Science (1979) 373 (2021) 236–241.

[147] D. Sakakibara, A. Sasaki, T. Ikeya, J. Hamatsu, T. Hanashima, M. Mishima, M. Yoshimasu, N. Hayashi, T. Mikawa, M. Wälchli, B.O. Smith, M. Shirakawa, P. Güntert, Y. Ito, Protein structure determination in living cells by *in-cell* NMR spectroscopy, Nature. 458 (2009) 102–105.

[148] B.B. Pan, F. Yang, Y. Ye, Q. Wu, C. Li, T. Huber, X.C. Su, 3D structure determination of a protein in living cells using paramagnetic NMR spectroscopy, Chem Comm. 52 (2016) 10237–10240.

[149] I.B. Trindade, A. Coelho, F. Cantini, M. Piccioli, R.O. Louro, NMR of paramagnetic metalloproteins in solution: *Ubi venire, quo vadis*?, J. Inorg. Biochem. 234 (2022).

“Structure without function is a corpse;
function without structure is a ghost”
Vogel and Wainwright

II. Chapter II: Conjuring up a ghost: Structural and functional characterization of FhuF, a ferric siderophore reductase from *E. coli*

This chapter was published as:

Trindade, I.B., Hernandez, G., Lebègue, E., Barrière, F., Cordeiro, T., Piccioli, M. & Louro, R.O. Conjuring up a ghost: Structural and functional characterization of FhuF, a ferric siderophore reductase from *E. coli*. J. Biol. Inorg. Chem. 26 (2021) 313–326

The author of this dissertation participated in all experiments described in this chapter, except in the SAXS experiments and in the Rosetta Model predictions.

Abstract

Iron is a fundamental element for virtually all forms of life. Despite its abundance, its bioavailability is limited, and thus, microbes developed siderophores, small molecules, which are synthesized inside the cell and then released outside for iron scavenging. Once inside the cell, iron removal does not occur spontaneously, instead this process is mediated by siderophore-interacting proteins (SIP) and/or by ferric-siderophore reductases (FSR). In the past two decades, representatives of the SIP subfamily have been structurally and biochemically characterized, however the same was not achieved for the FSR subfamily. Here, we initiate the structural and functional characterization of FhuF, the first and only FSR ever isolated. FhuF is a globular monomeric protein mainly composed by α-helices sheltering internal cavities in a fold resembling the “palm” domain found in siderophore biosynthetic enzymes. Paramagnetic NMR spectroscopy revealed that the core of the cluster has electronic properties in line with those of previously characterized 2Fe-2S ferredoxins and differences appear to be confined to the coordination of Fe(III) in the reduced protein. In particular, the two cysteines coordinating this iron appear to have substantially different bond strengths. In similarity with the proteins from the SIP subfamily, FhuF binds both the iron-loaded and the apo forms of ferrichrome in the micromolar range and cyclic voltammetry reveals the presence of redox-Bohr effect, which broadens the range of Fe(III)-siderophore substrates that can be thermodynamically accessible for reduction. This study suggests that despite the structural differences FSR and SIP proteins, mechanistic similarities exist between the two classes of proteins.

Introduction

"Structure without function is a corpse; function without structure is a ghost" (Vogel and Wainwright, 1969)

The Great Oxidation Event made the hitherto abundant iron a trace element as a consequence of precipitation of iron oxides [1]. Iron has, nonetheless, remained an essential element for nearly all organisms [2, 3]. To overcome iron limitation, almost all known bacterial species use siderophores, small molecules that scavenge iron from the extracellular environment, forming Fe(III)-complexes which are then taken up inside the cell [4, 5]. Different TonB-dependent receptors recognize different siderophores into the periplasm and their transport across the cytoplasmic membrane is dependent on ABC transporters. Once inside the cytoplasm, iron can be released via the action of esterases or via reduction by ferric-siderophore reductases [5]. The laboratory strain *Escherichia coli* K-12 can use diverse siderophores including hydroxamates (e.g. ferrichrome, ferrioxamine B, coprogen) and catecholates (e.g. enterobactin, yersiniabactin, salmochelin) and it contains at least five different uptake systems, including the ferrichrome operon (fhuACDB) and the enterobactin uptake system (*fepA*, *fepB*, *fes* and *fepCDG* genes) [6–10]. In the cytoplasm, two distinct ferric-siderophore reductases have been isolated. One is YqjH that belongs to the SIP (Siderophore-Interacting Protein) subfamily, which is able to catalyze the release of iron from Fe(III)-triscatecholates and Fe(III)-dicitrate. The other is FhuF, from the FSR (Ferric-Siderophore Reductase) subfamily that showed specificity for a group of hydroxamate-type siderophores, since iron removal from coprogen, ferrichrome, and ferrioxamine B is significantly reduced in FhuF-defective mutants [8, 11, 12]. Very little is known regarding the structure and function of the FSR subfamily of proteins, given the instability of the pure proteins [11]. FhuF is the only protein of the FSR subfamily ever isolated. Its transcription is derepressed by low iron levels via the iron regulator FUR, and repressed by OxyR, an oxidative response regulator [10]. This protein contains a 2Fe-2S cluster with unusual properties, including the unprecedented binding motif sequence C-C-x_{10}-C-x_2-C, unusual EPR g_z value for this kind of cluster (g_z=1.994), and unusual Mössbauer parameters with a low quadrupole splitting in the oxidized form ($\Delta E_{Q,4.2K}$= 0.474 mm s^{-1}) and unusually high quadrupole splitting for the Fe(III) component of the reduced form (ΔE_{Q190K}= 0.978 mm s^{-1}) [8, 11]. Furthermore, previous studies show that FhuF is truncated at the N-terminal end, and that it is loosely associated with the cytoplasmic membrane since it is possible to purify FhuF from both cytoplasmic and membrane fractions [11]. Here, we used a combination of Circular Dichroism (CD), SAXS, Rosetta modelling, electrochemistry, and paramagnetic NMR spectroscopy to advance the structural and functional characterization of FhuF from *E. coli* K-12.

Materials and Methods

Protein production and Purification

The plasmid pKF191, derived from pET-19b that codes for His-tagged FhuF protein was isolated and transformed into BL21 DE3 competent cells for expression [8, 11]. Freshly transformed cells were grown in Terrific Broth medium supplemented with 100 mg.L^{-1} ampicillin at 37 °C, 160 rpm until they reached an OD of 0.7, the temperature was then decreased to 30 °C and cells were collected after 4 hours. Cells were harvested by centrifugation for 10 min at 11 305 g and were then cooled to -20 °C. The cells were later defrosted and resuspended in 20 mM Potassium Phosphate buffer pH 7.6, 300 mM NaCl with a protease-inhibitor cocktail (Roche) and DNase I (Sigma) prior to a three-pass cell disruption at 6.9 MPa using a French press. The lysate was ultracentrifuged at 204 709 g for 90 min at 4 °C to remove cell membranes and debris. FhuF was purified from the supernatant using a His-trap affinity column (GE Healthcare) using a stepwise elution method. The fraction containing FhuF eluted at 20 mM Potassium Phosphate pH 7.6, 300 mM NaCl 250 mM imidazole. Eluted fractions were analyzed by SDS-PAGE with Blue-Safe staining (NZYTech) and UV-visible spectroscopy to select fractions containing pure FhuF. The imidazole was removed and FhuF was concentrated at 36°C using an Amicon® Ultra Centrifugal Filter with a cutoff of 10 kDa. For the SAXS data collection, FhuF fractions were further purified using a Superdex 75 10/300 GL from GE Healthcare at 1 mL.min^{-1}. Samples were kept at 30 °C with 0.5 mM of sodium azide and aliquots were sent for N-terminus sequencing to confirm the identity of the purified protein.

Circular dichroism

The Far-UV CD spectra of a 6.1 µM FhuF sample in 20 mM Potassium Phosphate pH 7.6 was recorded on a Jasco-815 spectrophotometer using a 1 mm quartz cell for high performance (QS) (Hellma Analytics). All CD measurements are an average of 4 accumulations collected in the 190 nm to 260 nm wavelength range using a 0.1 nm data pitch, and 2 nm bandwidth at 50 nm/min. The CD spectra were input into the BeStSel webserver to predict secondary elements content [13]. The thermal denaturation of FhuF was followed by monitoring changes in spectral features as a function of temperature ranging from 4 to 81 °C with 7 °C steps. The values for the unfolded fraction f_U were obtained by linear extrapolation of the folded θ_F and unfolded θ_U baselines into the transition zone using the following equation:

1) $$f_U = \frac{\theta - \theta_F}{\theta_U - \theta_F}$$

where θ is the mean residue ellipticity. By fitting to a sigmoidal equation, we extracted the melting temperature (T_m) of FhuF (i.e., the temperature when f_U=0.5).

Small-Angle X-ray Scattering

Synchrotron SEC-SAXS data on FhuF was collected on the B21 (ESRF, Grenoble, France) beamline exploiting its in-line HPLC system (Agilent 1200 HPLC). To this end, we injected 50 µL samples with 8.9 $mg.mL^{-1}$ of SEC purified protein in a 4.6 mL Shodex KW402.5-4F size exclusion column at a flow rate of 0.16 $mL.min^{-1}$. Two-second frames were acquired using a Pilatus 2 M pixel detector. Data collection conditions are described in Table S1, and no measurable radiation damage or significant signs of interparticle interference or aggregation were detected. The SEC mobile phase consisted of 20 mM Potassium Phosphate buffer pH 7.6, 150 mM NaCl. The scattering intensities from the respective monomeric elution single-peak region were integrated and buffer subtracted to produce the SAXS-profile of FhuF using the ScÅtter software [14]. Further processing was performed using the ATSAS software suite [15]. The P(r) distribution function was obtained by indirect Fourier Transform. The Rg value was estimated by applying the Guinier approximation in the range $s < 1.3/Rg$. The SEC-SAXS profile raw data were deposited in the repository for small-angle scattering data SASBDB under the project "SAXS of FhuF - A ferric-siderophore reductase" with the accession code SASDJ28 [16]. From SEC-SAXS data, a low-resolution ab initio molecular envelope was generated for FhuF, with the program DAMMIF using the ATSAS package using the pair-wise distance distribution (P(r)) calculated from range $0.012<s< 0.37$ $Å^{-1}$ [15]. Twenty independent models were generated, and then superimposed and averaged to define the most populated volume and test the robustness of the models.

FhuF Modeling

The model for FhuF was built by homology modeling using as templates the known crystal structures of proteins bearing the FhuF domain, including enzymes involved in iron siderophore biosynthesis in pathogenic bacteria [17].

There are 36 instances of this domain found in the PDB database. The multi-template modeling was performed with RosettaCM using evolutionary coupling-derived distance restraints [18, 19]. With RosettaCM, the most homologous portions from the multiple templates are hybridized into a single model while modeling the missing residues de novo. We sampled the diversity of conformational space by building a total of 4000 models, denoted pool. We scored each model by its Rosetta energy score (*Ei*) and relative agreement to the SEC–SAXS data (reduced χ_i^2)) using the following hybrid-scoring function:

2)
$$Z_i = Z_{SAXS}^i + Z_{Rosetta}^i = w_{saxs} \cdot \left(\frac{\chi_i^2 - \langle\chi^2\rangle}{\sigma_{SAXS}}\right) + (1 - w_{saxs}) \cdot \left(\frac{E_i - \langle E\rangle}{\sigma_{Rosetta}}\right)$$

where χ_i^2 and $E_i$were standardized to $Z_{SAXS}^i$and $Z_{Rosetta}^i$, respectively, using the mean values ($\langle\chi^2\rangle$) and $\langle E\rangle$and standard deviations (σ_{SAXS} and $\sigma_{Rosetta}$) of the pool, with w_{saxs} defining the weight of each term. The reduced χ_i^2 was given by CRYSOL 3.0 [15].

NMR spectroscopy

^{1}H temperature dependence experiments

A sample of approximately 500 µM of oxidized FhuF in 20 mM Potassium Phosphate buffer pH 7.6 with 300 mM NaCl was lyophilized and solubilized in D_2O (99.9 atom %) for ^{1}H temperature dependence experiments. Reduced FhuF was obtained using the same sample by degassing it and by adding an excess of sodium borohydride in an anaerobic chamber. ^{1}H NMR experiments were performed on a Bruker Avance II 500MHz NMR spectrometer equipped with a 5mm BBI probe. A total of 61440 transients were acquired using the super-WEFT pulse sequence (180-τ-90-AQ) with 103 ms of recycle time and τ values of 45 ms, to dampen the diamagnetic signals and suppress the solvent.

For each temperature, in degrees Celsius, the chemical shift of each proton signal [$(\Delta\upsilon/\upsilon_o)^{con}{}_j$] was referenced to TMS at 0 ppm using the H_2O signal as a secondary reference (5.11 - 0.012 x T ppm). The temperature dependence of the contact shift of the cysteine protons was determined according to the VanVleck formalism:

$$3)\qquad \left(\frac{\Delta v}{v_0}\right)_j^{con} = \frac{2\pi g\mu_B}{3\gamma_I kT}\cdot\frac{A_j}{h}\cdot\sum_i \frac{C_{ji}S'_i(S'_i+1).(2S'_i+1)exp\left(\frac{-E_i}{kT}\right)}{(2S'_i+1)exp\left(\frac{-E_i}{kT}\right)}$$

where g is the Free-spin electron g factor, μ_B is the Bohr magneton, γ_I is the free-electron magnetogyric ratio for the ^{1}H, k is the Boltzmann constant, T is the absolute temperature, A_j is the electron-nuclear coupling constant, h is the Planck constant, C_{ji} reflect the contribution of each spin (S_1 and S_2) to the total spin (S') for each i level [20–23]. The E_i are the energy values of the eigenstates S' ranging from $|S_1-S_2|$ to $|S_1+S_2|$ described by the perturbative Heisenberg Hamiltonian as a function of the magnetic exchange coupling constant J according to equation 4:

$$4)\qquad E_i = \frac{1}{2}JS'_i(S'_i+1).$$

Equation 3 was fit to the experimental data using the solver routine in MSExcel using standard parameters. Standard errors were determined from the diagonal elements of the covariance matrix considering 1 ppm experimental uncertainty in the chemical shift measurements [24].

^{15}N ^{13}C FhuF: Binding experiments

Experiments were performed at 305 K using a Bruker AVANCE III spectrometer operating at 800 MHz equipped with a TCI cryoprobe. The reference ^{1}H^{15}N TROSY-HSQC experiment was acquired with 64 transients using the pulse sequence trosyetf3gpsi from the BRUKER catalogue with 250 µM of

$^{15}N^{13}C$ labeled FhuF in 20 mM Potassium Phosphate buffer pH 7.0 with 300 mM NaCl. The TROSY version of the HSQC was chosen because it provided sharper signals that facilitated the analysis. Binding experiments were performed using samples of 200 µM of $^{15}N^{13}C$ labeled FhuF against increasing amounts of ligand (L): ferrichrome, apo-ferrichrome. All are oxidized to prevent electron transfer upon binding. Following each addition, a 16 transients $^{1}H^{15}N$ TROSY-HSQC experiment was recorded. Chemical shift perturbations (Δ_{bind}) of the NMR signals from FhuF (Protein, P) were plotted against the molar ratio (R) of [L]/[P]. The data were fitted using least-squares minimization to a 1:1 binding model using equations [25].

$$5) \qquad \Delta\delta_{bind} = \frac{1}{2}\Delta\delta_{bind}^{\infty}\left(A - \sqrt{(A^2 - 4R)}\right);$$

$$6) \qquad A = 1 + R + \frac{Kd([P]_0 R + [L]_0)}{[P]_0[L]_0};$$

where $\Delta\delta_{bind}^{\infty}$ is the maximal chemical shift perturbation of the NMR signals resulting from the complex formation between the protein and the ligand, and $[P]_0$ is the initial protein concentration and $[L]_0$ is the stock concentration of ligand. Only chemical shift perturbations ($\Delta\delta_{bind}$) equal to or larger than 0.025 ppm were considered significant. The standard deviation of the fitted value of K_d was calculated using all data.

Electrochemical experiments

Cyclic voltammetry was performed in a three-electrode cell with an edge plane pyrolytic graphite disk electrode (PGE, 3 mm diameter) obtained from IJ Cambria Scientific Ltd. as the working electrode. All cyclic voltammetry measurements were recorded using an Ag/AgCl, KCl 3 M as reference electrode and a graphite rod as counter electrode. Electrochemical experiments were performed at room temperature with a SP-300 potentiostat driven by EC-Lab V10.40 software from Bio-Logic (Bio-Logic Science Instruments, France). PGE was immersed in diluted protein solution (100 µM) for 3 days before electrochemical measurements in protein-free aqueous electrolyte (20 mM Potassium Phosphate buffer) at different pH values between pH 5 and pH 9. All solutions were degassed by bubbling argon for 10 min before each measurement. In order to facilitate the reading, the potentials discussed in the manuscript are reported in V vs SHE (E/V vs SHE = E/V vs Ag/AgCl + 0.210 V).

Results and Discussion

FhuF is a globular helix-bundle protein

Expression and purification of FhuF gave rise to a folded and soluble functional domain encompassing residues 18–262. The protein eluted from the SEC column at a volume corresponding to an apparent molar mass of ca 26.9 kDa, demonstrating that FhuF (28 kDa) is monomeric, migrating through the column as a folded protein. NMR data in solution revealed that FhuF is indeed well-folded at 32 °C (Figure 1A) as seen from the broad resonance dispersion of the $^{1}H^{15}N$ fingerprint, reflecting the presence of secondary and tertiary structure elements, thus compatible with well-folded protein. The CD profile of FhuF also indicates the presence of stable structural elements within the overall protein structure (Figure 1B), displaying positive values below 200 nm and two negative bands at 208 and 222 nm, commonly associated with ⍰-helical conformations. BeStSel predicts an α-helical content of 55 % and 40 % of unordered/turn elements with a small contribution of antiparallel β-sheet [13]. The thermal denaturation curve of FhuF followed by the changes in the CD signals at 211 and 222 nm show a cooperative folding-unfolding transition with a Tm of 58-60 °C, indicating that the protein has a defined tertiary structure (Figure 1B inset) that unfolds by increasing temperature.

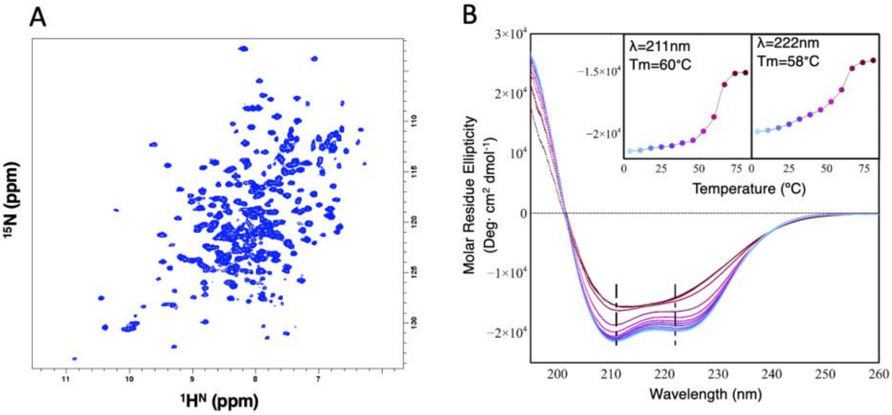

Figure II-**1** **A)** 2D 1H15N TROSY-HSQC spectrum of ^{15}N/^{13}C-labeled FhuF portraying the typical fingerprint of a folded protein. **B)** CD spectra of FhuF at different temperatures (4 to 81°C). (Inset) Thermal denaturation measured by changes in the signal at 211 and 222.

We have employed SAXS to probe further the overall structure of FhuF. Our synchrotron SEC−SAXS data confirmed that FhuF is also a monomeric globular particle in solution, with a radius of gyration of 21.5±0.10 Å and a maximum distance of 88.0±5 Å (Table I) (Figure 2A).

.

Table II-**1** SEC-SAXS data analysis.

	FhuF
Overall parameters	
R_g (Å) [from *P(r)*]	21.49± 0.10
R_g (Å) [from Guinier]	21.51± 0.10
D_{max} (Å)	88.0± 5.0
Porod volume estimate, *Vp* (Å^3)	37902.8
Molecular weight estimate (kDa)[a]	25.8 (7.8%)
Oligomeric state	Monomer
Software	
SEC-SAXS data integration	ScÅtter
P(r)	GNOM 5.0
Ab initio Modelling / <NSD> (Å)[b]	DAMMIF[c] / 0.727±0.049 Å
Simulated SAXS	CRYSOL
SASBDB accession code	SASDJ28

[a] Calculated with SAXSMoW 2.1[26]. The discrepancy to the sequence weight of FhuFΔ1-17 is given inside parentheses.

[b] Mean ± STD.

[c] Refinement with DAMMIF [15].

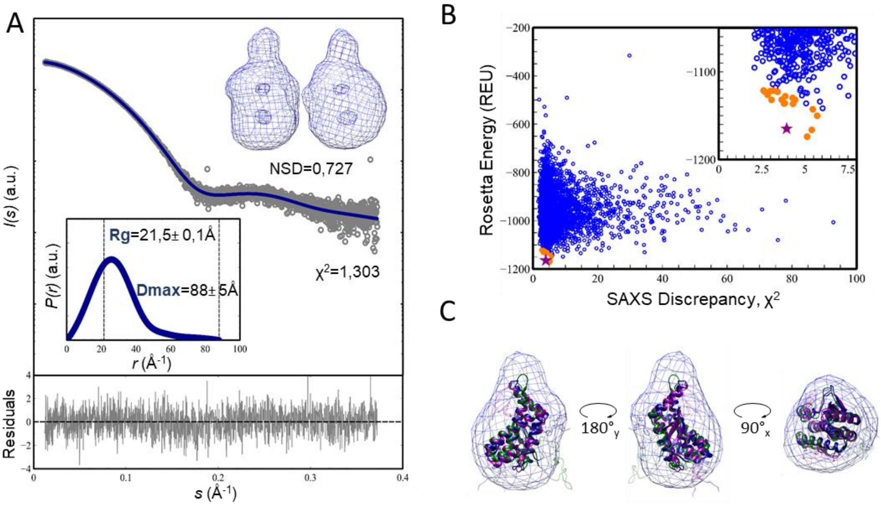

Figure II-**2** Structural model of FhuF. **A)** SAXS intensity, I(s), of FhuF (gray circles) and Scattering profile of the ab initio model (blue line). **B)** Rosetta energy vs. SAXS discrepancy χ2 scatter plot. **C)** SAXS *ab initio* reconstruction of FhuF (blue envelope).

The Kratky representation of the protein SAXS data (Figure S1) is bell-shaped, as expected for highly spherical/globular proteins, contrary to disordered proteins that do not display a clear maximum [27]. Nevertheless, the smooth asymmetrical tailing in its pairwise distance distribution (*P(r)*) suggests the presence of moderate flexibility or a slight deviation from a compact sphere (Figure 2A). Accordingly, the SAXS-derived low-resolution structure is oblong with a spatially separated lobe and two regions inside the envelope with lower density probability resembling small cavities. To gain more structural insight into FhuF, we used Rosetta to predict its potential structure, using multiple templates sharing sequence similarity with FhuF, and incorporating evolutionary coupling constraints into the homology modeling protocol [18, 19]. Interestingly, all identified templates were enzymes involved in the iron siderophore biosynthesis process with a FhuF-like domain within their overall structure. Examples are the AcsD from the plant pathogen *Pectobacterium chrysanthemi* and IucA from the human pathotype *Klebsiella pneumonia* [17, 28]. Both have three domains that resemble a cupped hand and these are designated thumb domain 1, palm domain 2, and fingers domain 3. The palm domain is FhuF-like, and in the context of AcsD/IucA, contributes with the active site residues. We only used the palm-domain regions as templates. To improve the modeling and eliminate false-positives, we used SAXS to score, discriminate, and validate all FhuF models. SAXS-based approaches were successfully applied in loop modeling, distinguishing protein-protein interfaces as well as improving structure prediction accuracy from unbiased MD simulations [29–32]. Herein, we used SAXS information combined with Rosetta energy to identify those models with the lowest possible scoring energy, and which best fit the SAXS data [29]. Figure 2B shows the energies of all models with respect to their SAXS discrepancy scores (reduced χ^2). The best-scored models display a similar well-folded central core, faithfully matching the *ab initio* envelope's high-density region (Figure 2C). The C-terminal part containing the four conserved cysteine residues from the 2Fe-2S cluster is less defined in the models, mostly due to the high uncertainty in the iron-cluster geometry and lack of structural constraints driving the modeling. FhuF contains a 2Fe-2S cluster with unprecedented binding motif sequence Cys-Cys-x_{10}-Cys-x_2-Cys. Without a template for the iron-cluster, predicting this region *de novo* remains a challenging task in structural biology, even with the incorporation of evolutionary coupling constraints [19]. Nevertheless, in most models, the cysteines are spatially clustered, at a distance adequate to accommodate a 2Fe-2S cluster (Figure 3A). The well-defined core of the model is primarily α-helical, in agreement with the CD data, comprising a four-helix bundle (α1:88-114; α2:153-177; α3:180-202; α4:205-216) sandwiched between a three-stranded antiparallel β-sheet (β1:53-56; β2:125-129; β3:135-140) and a two-stranded antiparallel β-sheet. The overall fold is analogous to the palm domain within AcsD/IcuA-like proteins (Figure 3B).

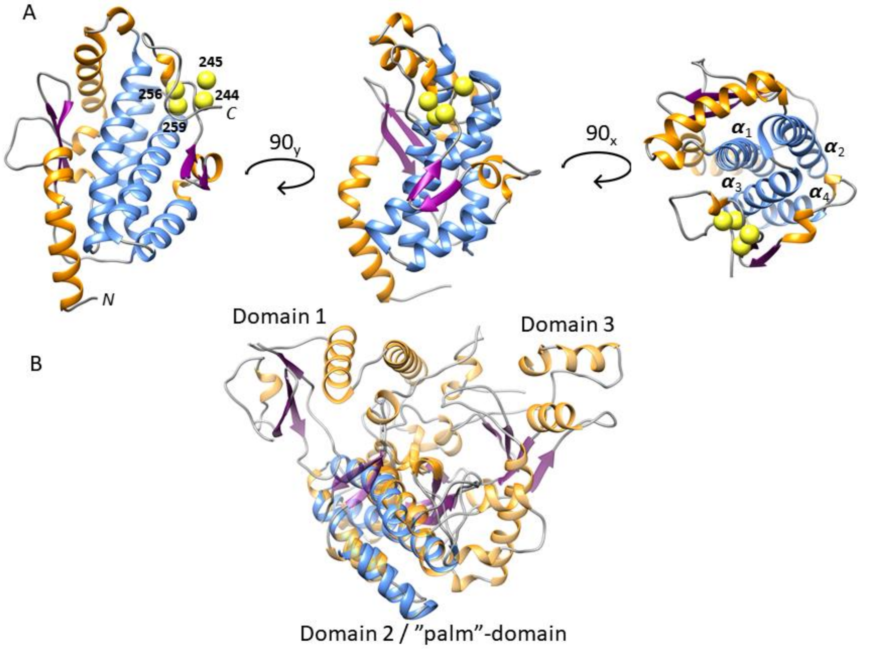

Figure II-**3** FhuF model vs closest homologues. **A)** FhuF model, core four-helix bundle in blue, other helices in orange, and β-sheets in purple. The Sγ atoms of the 2Fe-2S coordinating cysteines as yellow spheres. **B)** Overlay of FhuF and AcsD structure (PDB:2W02).

Paramagnetic NMR suggests that the core of the 2Fe2S cluster structure is similar to that of other ferredoxins

The unprecedented binding motif of the 2Fe2S cluster, involving cysteines 244, 245, 256 and 259 together with the unusual g_z value reported for the reduced form and the unusual Mössbauer parameters for the ferric iron of the reduced form of the cluster suggested the presence of a novel 2Fe-2S cluster structure [8, 11]. This is expected to affect the electronic structure parameters of the cluster that can be explored by NMR spectroscopy probing the paramagnetic effect on the protons of the cysteines coordinating the cluster. Indeed, there are paramagnetically shifted signals both in the oxidized and reduced forms of FhuF. In the reduced form these shifts arise from the presence of an unpaired electron in the 2Fe-2S cluster. In the oxidized form these arise from the presence of thermally populated paramagnetic excited states at room temperature even though the ground state of the cluster is diamagnetic. Figures 4 and 5 show that FhuF is amenable to detailed characterization of the electronic properties of the 2Fe2S cluster by paramagnetic NMR spectroscopy because it displays resolved features in both oxidation states. FhuF is unusual in this respect because vertebrate 2Fe2S ferredoxins typically display unsuitable spectra in the reduced state whereas the opposite is observed for 2Fe2S plant ferredoxins [33]. Figure 4A shows the downfield region of 1D ^{1}H NMR spectra of oxidized FhuF. The spectrum of FhuF has a similar pattern of signals to that observed in *Hu*Fd (Human ferredoxin) where a total of five broad peaks (a-e) are observed, one at 11 ppm (e), and four between 32 and 57 ppm (a-d) [33]. All five signals exhibit anti-Curie temperature dependence (Figure 4B), i.e. signals shift further downfield as the temperature is increased, consistent with an antiferromagnetically coupled Fe(III)-Fe(III) pair, as reported by EPR and Mössbauer spectroscopy [11]. A 2Fe-2S cluster containing two antiferromagnetically coupled Fe(III) has an S = 0 ground-state which is diamagnetic, thus the paramagnetic effect observed arises from thermal population of excited spin-states in the orbital manifold. The temperature dependence of these signals is well reproduced by the VanVleck formalism using the E_i values obtained with J = 300 cm^{-1} and A_j/h ranging between 0.63 and 3.07 MHz. This J value is in the high range compared with those reported for spinach and algal ferredoxins (J = 290 cm^{-1} and 185 cm^{-1}) based on measurements of the temperature dependence of paramagnetic shifts of cysteine ligands to the clusters, the temperature dependence of magnetic susceptibility and on ENDOR, Mössbauer and EPR data [34–36]. The A_j/h values for β-CH_2 cysteine protons fall in the expected range of 1 to 3 MHz obtained from proton ENDOR data on a

$[Fe_4S_4]^{3+}$ and rubredoxin models [21, 37]. The lower value of 0.63 MHz, calculated for peak e, therefore, also argues for assigning this signal to an α-CH proton of a cysteine bound to the cluster [21]. Therefore, by analogy with *Hu*Fd, the peak at 11 ppm most likely accounts for an α-hydrogen of one of the four ligated cysteines, and the peaks between 57-32 ppm arise from the cysteinyl β-hydrogens [33].

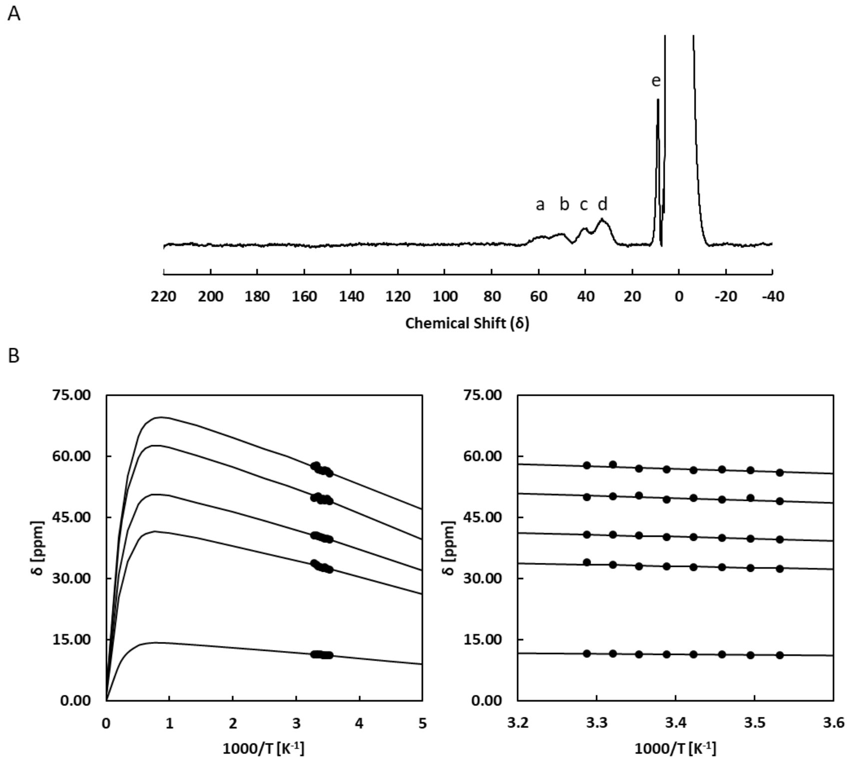

Figure II-**4** **A)** 1D ^1H NMR spectrum of oxidized FhuF **B)** Respective temperature dependence of hyperfine shift of β-CH_2 and α-CH protons. Lines represent the fitting of equation 3, Aj/h between 3.07MHz and 0.63MHz, J value of 300 cm^{-1} ± 2.5cm^{-1}.

The 1D ^1H NMR spectrum of reduced FhuF (Figure 5A) revealed nine peaks, five (A(III)-E(III)) between 199-104 ppm and four between 42-11 ppm (F(III)-I(II)). Unlike the oxidized spectrum, the reduced spectrum of FhuF does not resemble the spectra of reduced *Hu*Fd. Instead, it resembles the reduced spectrum of *Anabaena* 7120 vegetative ferredoxin (Vfd) [38]. Despite the similar pattern, the signals of the *Anabaena* ferredoxin do not reach beyond 140 ppm whereas in FhuF the most downfield signals reach to nearly 200 ppm. This suggests that one of the iron coordinating cysteines has an unusually strong bond. Of the nine peaks, the two less downfield-shifted signals exhibit anti-Curie temperature dependence (H(II)-I(II)) while the remaining seven, more far-shifted, exhibit Curie temperature dependence (A(III)-G(III)) (Figure 5B). Signals with anti-Curie temperature dependence are assigned to protons of cysteines that are ligated to Fe(II), whereas signals with Curie temperature dependence are assigned to protons of cysteines that are ligated to Fe(III) [21, 33]. The observation of seven peaks with Curie temperature dependence and the differences in intensities of some peaks, for example, peak F appears to be of lower intensity, argue for the presence of heterogeneity in the cluster environment in the reduced FhuF. Indeed, the observation of one clear extra peak from the 6 expected for a pair of βCH_2 and one αCH for each cysteine suggest that in the reduced state there are at least two coordination modes for the Fe (III). Nonetheless, Figure 5B shows that the experimental data are well reproduced using $J = 115\ cm^{-1}$ and A_j/h values between 0.31 and 2.13 MHz. Only peak C shows an apparent temperature dependence that would require distinct and unrealistically high values for A_j/h and J. Nonetheless, the common J for all other signals together with a value of A_j/h within the expected range of 1-3 MHz also places the prediction of peak C in the correct chemical shift range. This argues for the apparent steeper temperature dependence of this signal to be of different origin, such as a temperature dependent conformational change [39].

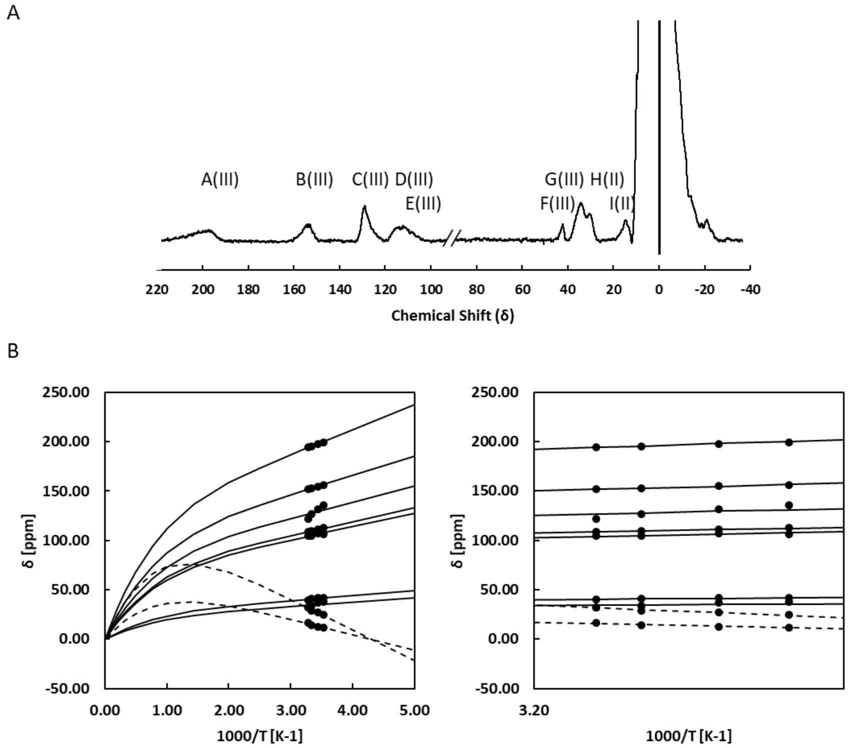

Figure II-**5** **A)** 1D ^{1}H NMR spectra of reduced FhuF. **B)** Temperature dependence of hyperfine shift of β-CH$_2$ and α-CH protons. Lines represent the fitting of equation 3 with A_j/h between 2.30 MHz and 0.31 MHz and a J of 115 cm^{-1} ± 2.5 cm^{-1}.

A *J* value of 115 cm^{-1} is also comparable with that reported for spinach and algal ferredoxins (100 cm^{-1} and 115 cm^{-1}) [35, 36]. The decrease in *J* value from oxidized to reduced state has been proposed to be the result of the larger ionic radius of Fe(II), which leads to a less efficient Heisenberg exchange mechanism between the two iron atoms [21]. Given that the *J* values for the oxidized and reduced states of FhuF fall within typical values for 2Fe-2S ferredoxins, and these values report on the coupling between the iron atoms via the inorganic sulfurs, these results strongly suggest that the core of the cluster is maintained in FhuF [40]. Mössbauer data show that only the parameters for the Fe(III) of the reduced cluster are unusual, whereas the parameters for the Fe(II) are typical for tetrahedral coordination. This agrees with paramagnetic ^{1}H NMR experiments. This observation and the fact that the differences in the cluster binding motif sequence of FhuF vs the typical binding sequence for other ferredoxins is restricted to the separation of the first two cysteines in the sequence (C-C-x_{10}-C-x_2-C in FhuF vs the typical C-x_2-C-$x_{8\text{-}15}$-C-x_2-C), we tentatively propose that the Fe(III) in the reduced state is bound to cysteines 244 and 245. Binding of vicinal cysteines to iron has precedent in the literature and was reported to lead to a cysS-Fe-Scys angle that is systematically wider than the ideal tetrahedral geometry, in agreement with the Mössbauer data for FhuF [11, 41]. In the present case it appears to lead also to different bonding strength by the two cysteines binding the Fe(III) in the cluster.

FhuF binds ferrichrome and apo-ferrichrome

When oxidized, 2Fe-2S proteins are S’ = 0, however some paramagnetism arises from the population of the excited states at room temperature. In FhuF, the effects of the 2Fe-2S paramagnetism are clearly reflected in the ^{1}H^{15}N TROSY-HSQC of FhuF where only 215 backbone peaks out of 235 expected are observed (Figure 1A and Figure 6A). At least 20 peaks are undetected, and these most likely correspond to the residues that fall in the “blind sphere”, the region that surrounds the paramagnetic 2Fe-2S cluster [42]. Even with the use of paramagnetic-tailored experiments it was not possible to detect all the expected resonances [43, 44]. Nonetheless, upon the addition of ferrichrome to FhuF, spectral changes were observed (Figure 6A), including the disappearance of peaks. These results are consistent with the binding of the Fe(III)-containing siderophore, which being also paramagnetic, leads to fast relaxation and peak broadening beyond detection in its vicinity [45]. Additionally, other spectral changes are observed, of which, peak shifts in the fast-exchange regime allow the determination of a dissociation constant of 53 ± 26 µM (Figure 6B). Similarly, upon the addition of apo-ferrichrome, spectral changes also occur, suggesting the binding of apo-ferrichrome to FhuF. Surprisingly, as previously found with ferrichrome but to a lesser extent, some peaks are also bleached suggesting that not only the presence of the paramagnetic center (Fe(III) of ferrichrome) is contributing to this phenomenon (Figure S2A). Given the expected presence of cavities in the structure (Figure 2A), it is likely that the binding of both apo- and holo-ferrichrome lead to conformational changes that bring further regions of the protein into the reach of the "blind sphere" generated by the 2Fe2S cluster.

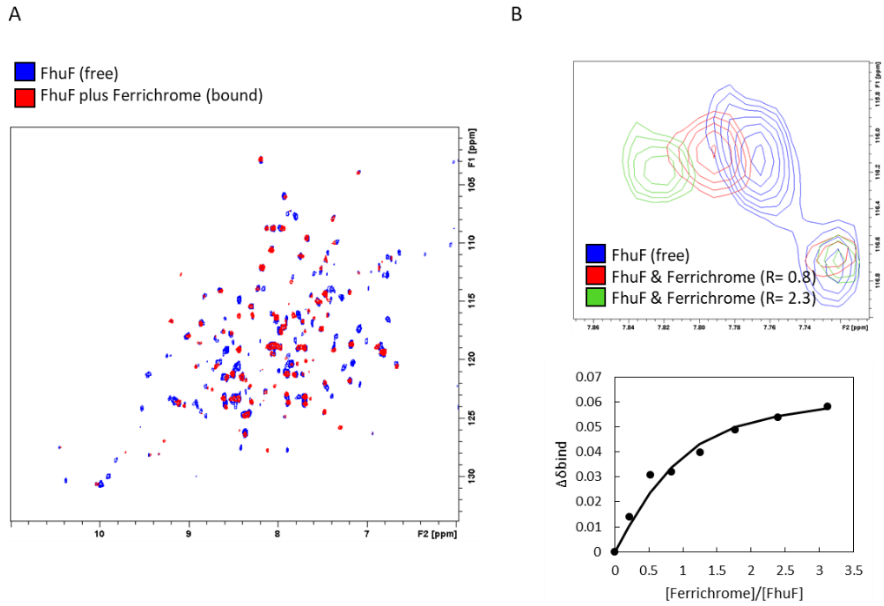

Figure II-**6** FhuF binds ferrichrome. **A)** 2D $^{1}H^{15}N$ TROSY-HSQC spectra of $^{15}N^{13}C$-FhuF portraying spectral changes observed upon the addition of ferrichrome. **B)** Representative peak in fast-exchange regime, respective binding, and fitting curve. R = [ligand]/[protein].

The reduction potential of FhuF is pH dependent broadening its catalytic capability

FhuF does not display favorable electrochemical characteristics requiring extensive stabilization to observe a redox signal from the adsorbed protein onto PGE (Figure 7A and Figure S3). This likely causes degradation of some of the protein at the surface of the electrode giving rise to the broad signal observed at higher potential in Figure 7B, which is not reproducible in terms of potential or linewidth across different runs. By contrast, the signals at lower potential are reproducible and display a half-height width of the anodic and cathodic signals close to the theoretical value of 90 mV for a single electron transfer step (Figure 7B) [46, 47]. The midpoint potential of – 370 mV vs SHE at pH 7.4 is consistent with earlier studies which report a reduction formal potential of -310 +/- 25 mV vs NHE at pH 7.3 for FhuF at cryogenic temperatures [8]. Cyclic voltammetry experiments performed at different pH values (Table II) show that FhuF presents a redox-Bohr effect as also observed for a ferric-siderophore reductase from the SIP subfamily from *Shewanella frigidimarina* [12].

Table II-**2** Reduction potentials of FhuF as a function of pH determined from cyclic voltammetry measurements.

pH	Formal potential (V vs SHE)
5.4	-0.24 ± 0.07
6.4	-0.30 ± 0.08
7.4	-0.36 ± 0.09
8.2	-0.42 ± 0.09
9.1	-0.48 ± 0.09

The formal reduction potential changes by 60 mV for every pH unit in good agreement with the expectation for a Nernstian equilibrium for a coupled one proton and one electron transfer (2.3RT/nF). Fitting of the pH dependence of the potentials shows that the pka_{ox} value must be lower than 5 and the pka_{red} must be higher than 9 [48]. This is especially significant since the normal range of *E. coli* growth can span pH 5 to 9 with some *E. coli* strains even surviving in lower acidic environments [49]. Therefore, the cyclic voltammetry data show that within this pH range the FhuF formal reduction potential shifts from -250 mV to -490 mV vs SHE. The lower value is particularly significant since it broadens the diversity of siderophores that can be reduced by FhuF and provides a rational for the unexpected observation of Ferrioxamine B reduction reported in the literature [8].

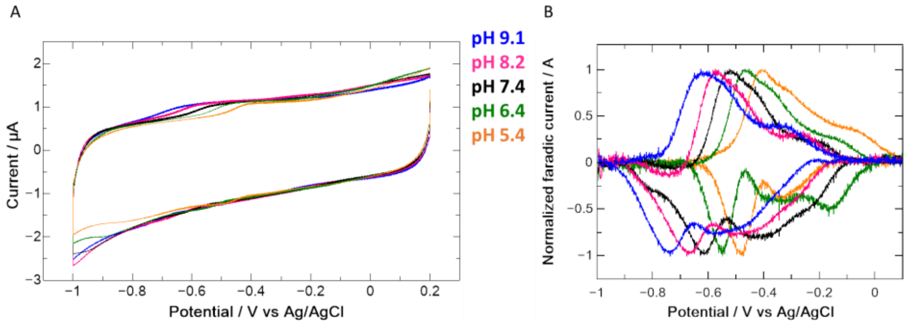

Figure II-**7** FhuF displays pH-dependent redox properties. **A)** Raw voltammograms of FhuF at 100 mV/s. **B)** and Faradaic signal of FhuF obtained by subtracting the capacitive current from the raw voltammograms using QSoas.

Conclusion

The FSR subclass of siderophore interacting proteins has thus far resisted characterization. In this work we obtained a structural and functional characterization of this important class of enzymes for iron uptake. FhuF binds both ferrichrome and apo-ferrichrome, advocating for its role as a bona-fide ferric siderophore reductase. The combination of SAXS data with the Rosetta derived model revealed that FhuF shares the “palm domain” with the siderophore biosynthetic enzymes, suggesting a common evolutionary origin that is distinct from that of SIP subfamily. SIPs, despite performing the same function, display significant structural homology with the diverse family of

FAD/NAD(P)H oxidoreductases [50]. Paramagnetic NMR spectroscopy established that the perturbation of the cluster vs typical 2Fe-2S ferredoxins appears to be confined to the periphery involving only the cysteine ligands, in particular those coordinating Fe(III) in the reduced state showing the hallmarks of very different bond strengths for the two cysteines coordinating this iron. This asymmetric bonding of one cysteine to Fe(III) may be at the origin of the two conformations that appear to exist in the reduced state. Nonetheless, the information that the 2Fe-2S rhomboid core is not disturbed combined with the Mössbauer data and crystallographic knowledge of the geometrical consequences of vicinal cysteine binding to iron allowed us to tentatively assign the ligands of the two irons of the cluster. Knowing which of the two irons is redox active in the cluster is essential to understand the molecular mechanism of siderophore reduction by this protein once a more detailed structure is available. Interestingly, the presence of a redox-Bohr effect in FhuF shows that this aspect of molecular mechanism is common in siderophore-interacting proteins in both SIP and the FSR subfamilies. For the proteins in the SIP subfamily, that use a flavin co-factor, this is not surprising given the direct thermodynamic coupling of electron and proton transfer in the isoalloxazine ring. By contrast for proteins in the FSR subfamily it means that an acid-base residue that titrates in the physiological pH range needs to be placed near the 2Fe-2S cluster, eventually engaged in H-bonding interaction, to allow proton-electron coupling [51]. This strongly suggests that the pH dependence of the reduction potential in siderophore interacting proteins is a consequence of a common selective pressure on these proteins to enhance their physiological activity. Indeed, the broader redox range afforded by the pH dependence of the potential increases the diversity of siderophores that are accessible for iron extraction by this protein and provides a rational for the observation of reaction of FhuF with the low potential siderophore ferrioxamine B [8]. The present work sets the stage for a detailed investigation regarding the mechanism of ferric-siderophore reduction together with a detailed molecular characterization of the enzymes responsible for this process.

Acknowledgments

The authors are grateful to Prof Alfred Trautwein, who established the first contact with Prof Bethold Matzanke who graciously made the FhuF expression system available that allowed this work to be performed. ROL recalls vividly the ICBIC 5 organized in Lübeck by Alfred and which marked the start of his scientific career. The authors are also grateful the Dr. João Vicente for helpful discussions and technical assistance with respect to the CD data.

This article is based upon work from COST Action CA15133, supported by COST (European Cooperation in Science and Technology). We acknowledge the France-Portugal PHC PESSOA program for support, project 40814ZE. Financial support was provided by European EC Horizon2020 TIMB3 (Project 810856). This work was funded by national funds through FCT– Fundação para a Ciência e a Tecnologia, I.P. (FCT), Project MOSTMICRO-ITQB with refs UIDB/04612/2020 and UIDP/04612/2020. N-terminal sequencing service was provided by the ITQB Research facilities. We acknowledge the use of Bio-SAXS beamline B21 (DLS-Dicot). The NMR data were acquired at CERMAX, ITQB-NOVA, Oeiras, Portugal with equipment funded by FCT, project AAC 01/SAICT/2016. IBT and GH are financially supported by national funds through the FCT PT-NMR PhD Program via PD/BD/135187/2017 and PD/00065/2013, respectively. TNC is recipient of the grant CEECIND/01443/1017.

The authors declare no conflict of interests.

References

[1] Holland HD (2006) The oxygenation of the atmosphere and oceans. Philos Trans R Soc B Biol Sci 361:903–915

[2] Weinberg ED (1997) The *lactobacillus* anomaly: Total iron abstinence. Perspect Biol Med 40:578–583

[3] Elli M, Zink R, Rytz A, et al (2000) Iron requirement of Lactobacillus spp. in completely chemically defined growth media. J Appl Microbiol 88:695–703

[4] Williams RJP (2012) Iron in evolution. FEBS Lett 586:479–484

[5] Miethke M, Marahiel MA (2007) Siderophore-Based Iron Acquisition and Pathogen Control. Microbiol Mol Biol Rev 71:413–451

[6] Braun V, Braun M (2002) Iron transport and signaling in *Escherichia coli*. FEBS Lett 529:78–85

[7] Hantke K, Nicholson G, Rabsch W, Winkelmann G (2003) Salmochelins, siderophores of *Salmonella enterica* and uropathogenic *Escherichia coli* strains, are recognized by the outer membrane receptor IroN. Proc Natl Acad Sci 100:3677–3682

[8] Matzanke BF, Anemüller S, Schünemann V, et al (2004) FhuF, Part of a Siderophore-Reductase System. Biochemistry 43:1386–1392

[9] Watts RE, Totsika M, Challinor VL, et al (2011) Contribution of siderophore systems to growth and urinary tract colonization of asymptomatic bacteriuria *Escherichia coli*. Infect Immun 80:333–344

[10] Stojiljkovic I, Bäumler AJ, Hantke K (1994) Fur Regulon in Gram-negative Bacteria. J. Mol. Biol. 236:531–545

[11] Müller K, Matzanke BF, Schünemann V, et al (1998) FhuF, an iron-regulated protein of *Escherichia coli* with a new type of [2Fe-2S] center. Eur J Biochem 258:1001–1008

[12] Trindade IB, Silva JM, Fonseca BM, et al (2019) Structure and reactivity of a siderophore-interacting protein from the marine bacterium *Shewanella* reveals unanticipated functional versatility. J Biol Chem 294:157–167

[13] Micsonai A, Wien F, Bulyáki É, et al (2018) BeStSel: A web server for accurate protein secondary structure prediction and fold recognition from the circular dichroism spectra. Nucleic Acids Res 46:W315–W322

[14] Robert Rambo (2017) ScÅtter. www.bioisis.net/tutorials/9

[15] Franke D, Petoukhov M V., Konarev P V., et al (2017) ATSAS 2.8: A comprehensive data analysis suite for small-angle scattering from macromolecular solutions. J Appl Crystallogr 50:1212–1225

[16] Valentini E, Kikhney AG, Previtali G, et al (2015) SASBDB, a repository for biological small-angle scattering data. Nucleic Acids Res 43:D357–D363

[17] Schmelz S, Kadi N, McMahon SA, et al (2009) AcsD catalyzes enantioselective citrate desymmetrization in siderophore biosynthesis. Nat Chem Biol 5:174–182

[18] Song Y, DiMaio F, Wang RYR, et al (2013) High resolution comparative modeling with RosettaCM. Structure 21:1735–1742

[19] Kamisetty H, Ovchinnikov S, Baker D (2013) Assessing the utility of coevolution-based residue-residue contact predictions in a sequence- and structure-rich era. Proc Natl Acad Sci 110:15674–15679

[20] Pierattelli R, Banci L, Turner DL (1996) Indirect determination of magnetic susceptibility tensors in peroxidases: A novel approach to structure elucidation by NMR. J Biol Inorg Chem 1:320–329

[21] Bertini I, Ciurli S, Luchinat C (1995) The Electronic Structure of FeS Centers in Proteins and Models A Contribution to the Understanding of Their

Electron Transfer Properties. In: Structure and Bonding. Springer Berlin Heidelberg, pp 1–57

[22] Bertini I, Luchinat C, Parigi G (2001) Solution NMR of Paramagnetic Molecules. Elsevier

[23] Banci L, Bertini I, Luchinat C (1990) The ^{1}H NMR Parameters of Magnetically Coupled Dimers The. In: Structure and Bonding 72. Springer-Verlag Berlin Heidelberg, pp 114–135

[24] Vetterling WT, Flannery BP, Teukolsky S (1989) Numerical recipes in Pascal: the art of scientific computing. Cambridge University Press

[25] Fonseca BM, Paquete CM, Neto SE, et al (2013) Mind the gap: Cytochrome interactions reveal electron pathways across the periplasm of *Shewanella oneidensis* MR-1. Biochem J 449:101–108

[26] Piiadov V, Ares de Araújo E, Oliveira Neto M, et al (2019) SAXSMoW 2.0: Online calculator of the molecular weight of proteins in dilute solution from experimental SAXS data measured on a relative scale. Protein Sci 28:454–463

[27] Cordeiro TN, Sibille N, Germain P, et al (2019) Interplay of Protein Disorder in Retinoic Acid Receptor Heterodimer and Its Corepressor Regulates Gene Expression. Structure 27:1270-1285

[28] Bailey DC, Drake EJ, Grant TD, Gulick AM (2016) Structural and functional characterization of aerobactin synthetase IucA from a hypervirulent pathotype of *Klebsiella pneumoniae*. Biochemistry 55:3559–3570

[29] Borges PT, Brissos V, Hernandez G, et al (2020) Methionine-Rich Loop of Multicopper Oxidase McoA Follows Open-to-Close Transitions with a Role in Enzyme Catalysis. ACS Catal 10:7162–7176

[30] Rossi P, Shi L, Liu G, et al (2015) A hybrid NMR/SAXS-based approach for discriminating oligomeric protein interfaces using Rosetta. Proteins 83:309–317

[31] Zhao C, Shukla D (2018) SAXS-guided Enhanced Unbiased Sampling for Structure Determination of Proteins and Complexes. Sci Rep 8:1–13

[32] Jiménez-García B, Pons C, Svergun DI, et al (2015) PyDockSAXS: Protein-protein complex structure by SAXS and computational docking. Nucleic Acids Res 43:W356–W361

[33] Xia B, Jenk D, LeMaster DM, et al (2000) Electron-nuclear interactions in two prototypical [2Fe-2S] proteins: Selective (chiral) deuteration and analysis of ^{1}H and ^{2}H NMR signals from the alpha and beta hydrogens of cysteinyl residues that ligate the iron in the active sites of human ferredoxin. Arch Biochem Biophys 373:328–334

[34] Benini S, Ciurli S, Luchinat C (1995) Oxidized and Reduced [Fe_2Q_2] (Q = S, Se) Cores of Spinach Ferredoxin: A Comparative Study Using ^{1}H NMR Spectroscopy. Inorg Chem 34:417–420

[35] Palmer G, Dunham WR, Fee JA, et al (1971) The magnetic susceptibility of spinach ferredoxin from 77-250°K: A measurement of the antiferromagnetic coupling between the two iron atoms. BBA - Bioenerg 245:201–207

[36] Anderson RE, Dunham WR, Sands RH, et al (1975) On the nature of the iron sulfur cluster in a deuterated algal ferredoxin. Biochim Biophys Acta 408:306–318

[37] Werth MT, Kurtz DM, Howes BD, Huynh BH (1989) Observation of S = 2 EPR Signals From Ferrous Iron—Thiolate Complexes: Relevance To Rubredoxin-Type Sites in Proteins. Inorg Chem 28:1357–1361

[38] Cheng H, Westler WM, Xia B, et al (1995) Protein expression, selective isotopic labeling, and analysis of hyperfine-shifted NMR signals of *Anabaena* 7120 vegetative [2Fe-2S] ferredoxin. Arch. Biochem. Biophys. 316:619–634

[39] Banci L, Bertini I, Piccioli M, et al (1993) The Electronic Structure of $[Fe_4S_4]^{3+}$ Clusters in Proteins. An Investigation of the Oxidized High-Potential Iron-Sulfur Protein II from *Ectothiorhodospira vacuolata*. Biochemistry 32:9387–9397

[40] Bertrand P, Gayda JP, Fee JA, et al (1987) Comparison of the spin-lattice relaxation properties of the two classes of [2Fe-2S] clusters in proteins. Biochim Biophys Acta (BBA)/Protein Struct Mol 916:24–28

[41] Archer M, Huber R, Tavares P, et al (1995) Crystal structure of desulforedoxin from *Desulfovibrio gigas* determined at 1.8 Å resolution: A novel non-heme iron protein structure. J Mol Biol 251:690–702

[42] Trindade IB, Invernici M, Cantini F, et al (2020) PRE-driven Protein NMR Structures: an Alternative Approach in Highly Paramagnetic Systems. FEBS J. 288: 3010–3023

[43] Ciofi-Baffoni S, Gallo A, Muzzioli R, Piccioli M (2014) The IR-^{15}N-HSQC-AP experiment: A new tool for NMR spectroscopy of paramagnetic molecules. J Biomol NMR 58:123–128

[44] Invernici M, Trindade IB, Cantini F, et al (2020) Measuring transverse relaxation in highly paramagnetic systems. J Biomol NMR 74:431–442

[45] Banci L, Camponeschi F, Ciofi-Baffoni S, Piccioli M (2018) The NMR contribution to protein–protein networking in Fe–S protein maturation. J Biol Inorg Chem 23:665–685

[46] Léger C, Bertrand P (2008) Direct electrochemistry of redox enzymes as a tool for mechanistic studies. Chem Rev 108:2379–2438

[47] Fourmond V (2016) QSoas: A Versatile Software for Data Analysis. Anal Chem 88:5050–5052

[48] Louro RO, Catarino T, Salgueiro CA, et al (1996) Redox-Bohr effect in the tetrahaem cytochrome c_3 from *Desulfovibrio vulgaris*: A model for energy transduction mechanisms. J Biol Inorg Chem 1:34–38

[49] Small P, Blankenhorn D, Welty D, et al (1994) Acid and base resistance in *Escherichia coli* and *Shigella flexneri*: Role of rpoS and growth pH. J Bacteriol 176:1729–1737

[50] Trindade IB, Moe E, Louro RO (2020) Siderophore-Interacting Protein. Encycl Inorg Bioinorg Chem 1–12

[51] Fonseca BM, Paquete CM, Salgueiro CA, Louro RO (2012) The role of intramolecular interactions in the functional control of multiheme cytochromes *c*. FEBS Lett 586:504–509

“How long should you try? Until.”

Jim Rohn

III. Chapter III: The structure of a novel ferredoxin – FhuF, a ferric-siderophore reductase from *E. coli* K-12 with a novel 2Fe-2S cluster coordination

This chapter will be submitted as:

Trindade I.B., Rollo, F., Todorovic, S., Catarino, T., Moe, E., Matias, P.M., Piccioli, M., Louro, R.O. The structure of a novel ferredoxin – FhuF, a ferric-siderophore reductase from *E.coli* K-12 with a novel 2Fe-2S cluster coordination. JACS

The author of this dissertation participated in all experiments described in this chapter, except for the structural calculations and refinement of FhuF and in the Resonance Raman experiments.

Abstract

Iron is a vital element for life. However, after the Great Oxidation Event (GOE), the bioavailability of this element became limited. To overcome iron shortage and to scavenge this essential nutrient, microorganisms use siderophores, secondary metabolites that have some of the highest affinities for ferric iron. The crucial step of iron release from these compounds to be integrated into cellular components is mediated by specific proteins that can be either Siderophore-Interacting Proteins (SIPs) or Ferric-siderophore reductases (FSRs).

In this work, we report for the first time the structure of an FSR. FhuF from laboratory strain *Escherichia coli* K-12 is the archetypical FSR, known for its atypical 2Fe-2S cluster with the binding motif C-C-X_{10}-C-X_2-C. The 1.9Å resolution crystallographic structure of FhuF shows the only 2Fe-2S protein known to have two consecutive cysteines binding different Fe atoms. This novel coordination found in FhuF, finally explains the unusual spectroscopic properties found in this protein. The function of FhuF was also confirmed, showing an impressive ability to reduce hydroxamate-type siderophores at very high rates when compared to flavin-based siderophore-interacting proteins.

Overall, this work closes the knowledge gap regarding the structural properties of ferric-siderophore reductases and simultaneously, opens the door for further understanding of the diverse mechanistic abilities of these proteins in the siderophore recycling pathway.

Introduction

The high abundance of reduced sulfur and ferrous iron in the early ocean enabled the assembly of these two elements into clusters by the emergent Life and their use as redox centers [1,2]. Today, more oxidizing conditions following the Great Oxygenation Event (GOE) have led to the precipitation of iron as ferric minerals, dramatically lowering its bioavailability [3]. Regardless, proteins containing these clusters are found ubiquitously throughout all domains of life, playing roles in essential metabolic processes such as photosynthesis and respiration. Iron-sulfur proteins comprise a family of proteins with remarkable diversity in both cofactor configuration and reduction potential extending over a 1 V range [2]. Even among proteins containing the same cluster type, reduction potentials can be modulated by protein interactions, which can even lead to discrimination within the individual components of the cluster, i.e., in each Fe of a 2Fe-2S cluster, the reduction potentials can be differentiated to yield localized valence in odd electron states [4]. This remarkable wide range of reduction potentials and diverse structural motifs allows iron-sulfur proteins to act as electron carriers in a variety of biological processes. Ironically, this includes their function in iron acquisition pathways as the catalytic center of Ferric-Siderophore Reductases (FSRs) [5–8]. Siderophores are secondary metabolites specialized for iron scavenging [9]. However, once inside the cell, iron release from these compounds does not occur spontaneously, instead, it is mediated by diverse enzymes [10,11]. These can contain either flavins as redox cofactors and are named Siderophore-Interacting Proteins (SIPs), or 2Fe-2S clusters and are designated Ferric siderophore reductases (FSRs) [11–13]. Generally, these are proteins that promote iron release from Ferric-siderophores through the reduction of ferric iron, Fe(III), to its ferrous form, Fe(II), promoting the dissociation of the Fe(III)-siderophore complex. Specifically, the FSR family is characterized by the atypical cysteine binding motif C-C-X_{10}-C-X_2-C that coordinates a 2Fe-2S cluster, as found in FhuF from *Escherichia coli* K-12, the archetypical FSR [5]. This protein displays a range of unusual spectroscopic properties: an EPR spectrum in the reduced state with a g_z value of 1.994, which is smaller than that typically found in 2Fe-2S clusters of diverse proteins; Mössbauer spectra with a quadrupole splitting for the oxidized protein of ΔE_q = 0.474 mm/s which is lower than that typically found in 2Fe-2S clusters, whereas for the reduced cluster the Mössbauer parameters for the ferric iron change considerably, with the quadrupole splitting increasing to 3.3 mm/s; NMR spectra with unusual chemical shifts, especially in the reduced state where paramagnetic signals are found significantly downfield from those previously reported for other proteins containing 2Fe-2S clusters [5,7,8]. To understand how the unusual structural and spectroscopic features of FhuF come together to achieve its physiological function, here we report, for the first time, the three-dimensional structure of this protein, being the first structure of a member of the Ferric-Siderophore Reductase family of proteins. FhuF reveals a different cluster coordination mode provided by the atypical cysteine-binding motif. We further complete the spectroscopic characterization of this protein by performing Resonance Raman spectroscopy and we confirm the function of FhuF as a ferric-siderophore reductase of hydroxamate-type siderophores.

Methods

Protein Expression and Purification

FhuF WT was expressed and purified as previously reported [5,7]. The mutated FhuF (FhuF-C143S) was expressed and purified as previously reported with minor modifications. Briefly, the plasmid pKF143S that codes for His-tagged FhuF (FhuF-C143S) mutant protein was transformed into BL21 DE3 competent cells for expression. Transformed cells were grown in Luria Bertani medium supplemented with 100 mg/L ampicillin at 37 °C, 160 rpm until they reached an OD of 0.7; the temperature was then decreased to 30 °C, and cells were harvested by centrifugation after 18 hours and stored at -80 °C. The cells were later defrosted and resuspended in 20 mM Potassium Phosphate buffer pH 7.6, 300 mM NaCl with a protease-inhibitor cocktail (Roche) and DNase I (Sigma) prior to a three-pass cell disruption at 6.9 MPa using a French press. The lysate was ultracentrifuged at 204709 *g* for 90 min at 4 °C to remove cell membranes and debris. FhuF was then purified from the supernatant using a His-trap affinity column (GE Healthcare) where the fraction containing FhuF was eluted at 20 mM Potassium Phosphate pH 7.6, 300 mM NaCl with 250 mM imidazole. Eluted fractions were analyzed by SDS-PAGE with Blue-Safe staining (NZYTech) and UV-visible spectroscopy to select fractions containing pure FhuF. The imidazole was removed and FhuF was concentrated at 36 °C using an Amicon® Ultra Centrifugal Filter with a cut-off of 30 kDa. Several aliquots were frozen using liquid nitrogen and kept at -80 °C while others were kept at 30 °C for a week, to promote autolysis, before a second His-trap purification step was performed. The final purified FhuF (His-tag free) was then concentrated from the flowthrough of a second passage through the His-trap column using an Amicon Ultra Centrifugal Filter (Millipore) with a 30 kDa cut-off. Sample aliquots were sent for N-terminus sequencing to confirm the identity and the first amino-acid residues of the purified protein samples. For storage, aliquots were flash-frozen in liquid nitrogen or kept under anaerobic conditions for further use.

Structure determination

N-terminally truncated and mutated FhuF (FhuF–C143S) at a concentration of 50 mg/ml was crystallized in 0.2 M Magnesium chloride hexahydrate 0.1 M Tris-HCl pH 8.2 30% PEG w/v 4000 using the hanging drop vapor diffusion technique (2 μl protein:2 μl reservoir) [5,7]. Crystals were harvested and soaked in a 2 μl drop of cryoprotectant solution (0.2 M magnesium chloride hexahydrate 0.1 M Tris-HCl pH 8.2 30 % PEG w/v 4000 with 5 % glycerol) prior to flash-freezing in liquid nitrogen. Diffraction data was collected at 100 K to 1.9 Å resolution at ALBA Synchrotron Beamline XALOC. The images were processed with autoPROC, which makes use of XDS and the CCP4 suite for integration and conversion of integrated intensities to structure factors, and an anisotropic resolution cut-off was applied with STARANISO [14–18]. The data collection and processing statistics are listed in Table 1. The structure was solved by molecular replacement (MR) using PHASER in the CCP4 suite [16]. The phasing model was obtained with AlphaFold2 (through Google Colab) using the sequence of the mature FhuF protein from which the first 16 residues (Met-1 until Thr-16) were deleted [19]. The structure was rebuilt with BUCCANEER, corrected and completed with COOT and an initial refinement was undertaken using REFMAC5 in the CCP4 suite [20–22]. Structure refinement was performed using PHENIX [23]. Throughout the refinement, the model was periodically checked and corrected with COOT against σ_A-weighted $2|F_o|-|F_c|$ and $|F_o|-|F_c|$ electron-density maps. Solvent molecules were added manually by inspection of electron-density maps in COOT. Hydrogen atoms were included in calculated positions with the PHENIX READYSET tool and isotropic displacement parameters (ADPs) were refined for all non-hydrogen atoms. In the final refinement cycles, the relative X-ray/stereochemistry and X-ray/ADP weights were optimized to reduce the gap between R-cryst and R-free. The final values of R-cryst and R-free were 21.1 % and 24.5 % respectively, with a maximum likelihood estimate of the overall coordinate error of 0.26 Å [23]. The refinement statistics are presented in Table 2. The model stereochemical quality was analyzed with MOLPROBITY and there are no outliers in the Ramachandran (Ramachandran, 1968) φ,ϕ plot [24]. The coordinates and experimental structure factors have been submitted to the Protein Data Bank with accession code 7QP5. Pictures were produced using PyMOL [25,26].

Table III-**1** Data collection and processing statistics.

Data Collection	**FhuF**
Beamline	ALBA XALOC
Detector	PILATUS
Wavelength (Å)	0.97934 Å
Space Group	*C* 2
Unit cell parameters:	
a, b, c (Å)	116.91, 73.57, 71.88
β (°)	113.4
Data Processing	AutoPROC / STARANISO
Resolution limits of ellipsoid fitted to resolution cut-off surface (Å)	1.99, 1.90, 2.90
Resolution, spherical limits (Å)	65.9 – 1.92 (2.11 – 1.92)
Nr. Observations	74725 (2314)
Unique reflections	22524 (1127)
Multiplicity	3.3 (2.1)
Completeness, spherical (%)	52.7 (10.7)
Completeness, ellipsoidal (%)	81.6 (51.8)
R-merge (%) [b]	7.8 (56.7)
R-p.i.m. (%) [c]	5.0 (49.2)
$<I/\sigma(I)>$	9.3 (1.4)
$CC_{1/2}$	0.997 (0.560)
ISa [d]	15.2
Wilson B (Å^2)	37.2
Z [e]	2
Estimated V_M [f]	2.54
Estimated Solvent Content (%) [f]	51.5
Raw data DOI	-

[a] Values in parentheses refer to the highest resolution shell; [b] R-merge = merging R-factor, $(\Sigma_{hkl} \Sigma_i |I_i(hkl) - <I(hkl)>|) / (\Sigma_{hkl} \Sigma_i I(hkl)) \times 100$ %; [c] R-p.i.m. = precision-independent R-factor, $\Sigma_{hkl} [1/(N-1)]^{1/2} \Sigma_i |I_i(hkl) - <I(hkl)>| / (\Sigma_{hkl} \Sigma_i I_i(hkl)) \times 100$ % [27]. For each unique Bragg reflection with indices (hkl), I_i is the i-th observation of its intensity and N its multiplicity; [d] according to; [e] Nr. molecules in the asymmetric unit; [f] According to [28,29].

Resonance Raman experiments

For resonance Raman (RR) spectroscopic experiments, 2 µL of the sample (350 µM FhuF WT in 20 mM Potassium Phosphate buffer pH 8 with 300 mM NaCl) were introduced, under strictly anaerobic conditions, into a liquid-nitrogen-cooled cryostat (Linkam), mounted on a microscope stage and cooled down to 77 K. Spectra from the frozen sample were collected in backscattering geometry using a confocal microscope coupled to a Raman spectrometer (Jobin-Yvon LabRam 800 HR, HORIBA) equipped with 1200 mm^{-1} grating and a liquid-nitrogen-cooled CCD detector. The 458 nm line from an Argon ion laser (Coherent Innova) was used as the excitation source. Typically, 8 spectra accumulated for 60 s each using a laser power of 5.3 mW at the sample, were co-added to improve the signal-to-noise ratio (S/N). The background scattering was removed by subtraction of a polynomial function and the spectra were deconvoluted using LabSpec 5.4 software.

Stopped-flow experiments

The kinetic experiments were performed with HI-TECH Scientific Stopped-flow equipment (SF-61DX2) installed inside an anaerobic glove box (Mbraun MB150-GI). The temperature of the drive syringes and mixing chamber was maintained at 20 °C using a water bath. Sample solutions were prepared with 20 mM Potassium Phosphate buffer pH 8 with 300 mM NaCl and in the presence of the O_2 scavenging system (30 mM glucose, 375 nM glucose oxidase, and 750 nM catalase). The time course of the reactions was monitored using a photodiode array. Solutions were prepared inside the anaerobic chamber with degassed water and all experiments were performed in duplicate. Data were analyzed using Kinetics Studio version 2.32 (TgK Scientific).

Ferric-siderophore reduction experiments were performed at 20 °C in the stopped-flow apparatus, using 15 µM $FhuF_{red}$ against either 50 µM of bisucaberin or 15 µM of ferrichrome (after mixing). $FhuF_{red}$ was prepared using sodium dithionite and then its excess was removed through buffer exchange in a HiTrap® Desalting Column (GE Healthcare). The different concentrations were used to avoid and deal with the spectra overlap between FhuF and the Fe(III)-siderophores. The reduction rate constants were obtained by fitting the kinetic traces at 452 nm.

Results and Discussion

FhuF, an entirely novel structure

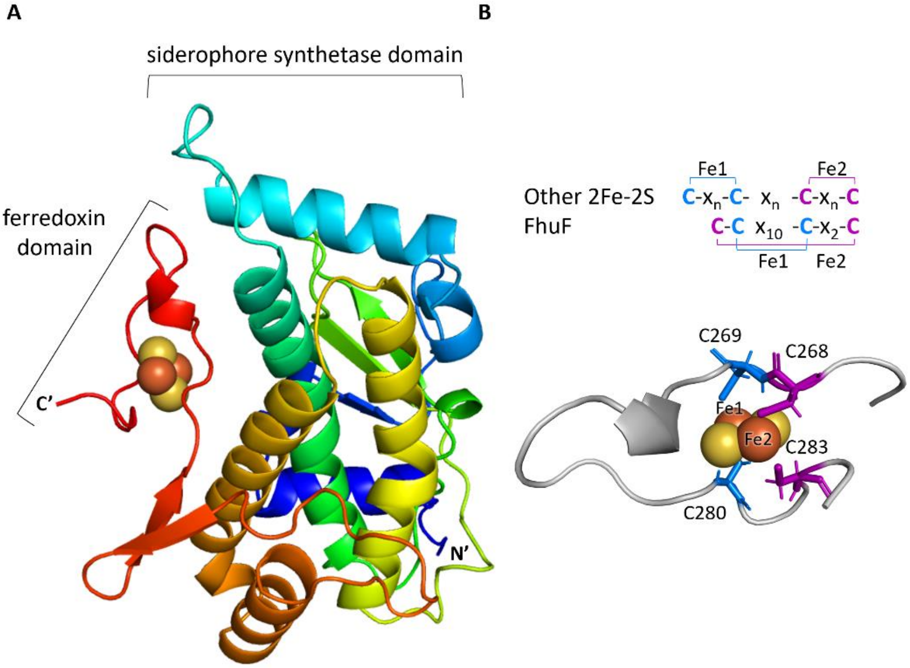

Figure III-**1** **A)** X-ray structure of FhuF. **B)** Highlight of “ferredoxin” domain and schematic representation of the 2Fe-2S coordination mode in FhuF in comparison with other 2Fe-2S proteins where n equals 2 or higher amino acid residues between cysteines.

FhuF was isolated for the first time in 1998, however only dilute samples were stable for a few days at 4 °C, and thus the instability of FhuF and its homologs has hindered the structure determination of representatives of the FSR protein family [5,13]. The instability of FhuF was mainly translated into two main observables: first, non-reversible protein aggregation upon concentration higher than 10 mg/mL; and second, protein autolysis losing the first 17 amino-acid residues in the N-terminus together with the histidine tag. This means that 43 residues from the initial starting expression sequence (Supplementary Table

S1) are gradually lost during the process of protein sample preparation. To increase sample concentration and sample homogeneity for crystallization experiments while simultaneously preventing protein denaturation, samples of FhuF were kept at high concentrations at 30 °C for a week to promote faster autolysis, and then samples were run a second time through the His-trap column. These two steps in sample preparation increased sample homogeneity, and together with the use of the FhuF-C143S mutant instead of WT FhuF, promoted less protein aggregation through the prevention of intermolecular disulfide bond formation, thus improving crystal quality and diffraction limits. The crystal structure of FhuF was determined to 1.9 Å resolution and deposited in the Protein Data Bank with accession number 7QP5 (Figure 1 and Table 2).

The sequence of the structure deposited in the PDB is derived from the expressed gene that also codes for an N-terminal His-tag (Supplementary Table S1), and the numbering used in this manuscript is based on that, thus, with extra 24 amino-acid residues than the gene-derived protein sequence.

The structure (Figure 1 A) of FhuF can be described as containing two domains, a 2Fe-2S cluster binding domain (“ferredoxin” domain) and a domain which reveals a high similarity with the palm domain in siderophore synthetases (“siderophore-synthetase domain”). This structure revealed various unprecedented features. One is the “siderophore synthetase” domain which is unexpected since the other family of ferric-siderophore reductases, SIPs, from the Siderophore-Interacting Proteins family, resemble oxidoreductases instead [30]. Yet, this agrees with the previously obtained Rosetta-derived structural model [7]. This domain is composed of a three-stranded antiparallel β-sheet that is sandwiched between four and two α-helix bundles.

Table III-**2** Refinement statistics of FhuF.

Dataset	**FhuF**
Resolution limits (Å)[a]	65.9 – 1.92 (2.00 – 1.92)
% R_{work} [b]	21.1 (30.0)
% R_{free} [c]	24.5 (37.0)
ML coordinate error estimate (Å) [d]	0.26
Model composition and completeness	
Regions omitted [e]	17A-18A, 17B-18B
Non-hydrogen protein atoms [f]	3906
2Fe-2S clusters	2
Solvent molecules	173
Mean B values (Å^2) [g]	
Protein	34.3
2Fe-2S clusters	29.7
Solvent	35.2
Model r.m.s. deviations from ideality	
Bond lengths (Å)	0.005
Bond angles (°)	0.642
Chiral centers (Å^3)	0.039
Planar groups (Å)	0.006
Model validation [h]	
% Ramachandran outliers	0
% Ramachandran favored	97.9
% Rotamer outliers	0.23
% C$^\beta$ outliers	0
Clash score	6.0
PDB Accession code	7QP5

[a] Values in parentheses refer to the highest resolution shell; [b] $R_{\text{work}} = (\Sigma_{hkl} ||F_{obs}(hkl)| - |F_{calc}(hkl)||) / (\Sigma_{hkl} |F_{obs}(hkl)|) \times 100$ %; [c] R_{free} is calculated as above from a random sample containing 5% of the total number of independent reflections measured; [d] Maximum-likelihood estimate by PHENIX; [e] Chains A and B correspond to the two independent molecules in the asymmetric unit; [f] Including atoms in the alternate conformations of disordered groups of residues; [g] Calculated from isotropic or equivalent isotropic B-values; [h] Calculated with MolProbity.

Second, the "ferredoxin" domain reveals a novel fold, where all coordinating cysteines are within the same loop, a fold that differs from those reported in previously characterized proteins containing 2Fe-2S clusters. Additionally, FhuF displays a novel cysteine coordination mode. The typical coordination mode for proteins containing 2Fe-2S clusters displays two consecutive cysteines that bind the same Fe atom. Instead, in FhuF, two consecutive cysteines, that atypically happen to be sequential neighbors, C268 and C269, bind different Fe atoms (Figure 1 B) pairing in an unprecedented way. Thus, C269 and C280 pair together and bind Fe1 (Figure 1 B) and C268 and C283 pair together to bind Fe2. Hydrogen bonds to the cluster coordinating cysteines (Figure 2 A) were also found between Cys-269 (backbone O) and Ser-117 (Sidechain Hγ) and Asn-210 (Sidechain Hδ1), Cys-269 (Sidechain Sγ) with Arg-271 (backbone Nη), and Cys-268 (backbone O and N-H) with a water molecule, and then between Cys-280 (backbone O) with Cys-283 (backbone N-H). Furthermore, from the structure, we can further explain that among these, the hydrogen bond between the backbone N-H of Arg-271 and Sγ of Cys-269 is likely responsible for the extra paramagnetically-shifted resonance found with Curie-type temperature dependence in NMR experiments (Figure 5 Chapter II, signal C(III)) [7]. The value of chemical shift observed for this signal (C(III), Figure 5 Chapter II) is similar to the value calculated by the hybrid density function based on the distances measured in the crystal structure [31]. This proposal provides a rationale for the steep slope observed for the temperature dependence of this signal that reflects the gradual disruption of the bond at higher temperatures.

The geometry of the 2Fe-2S cluster positions FhuF into the ferrochelatase class

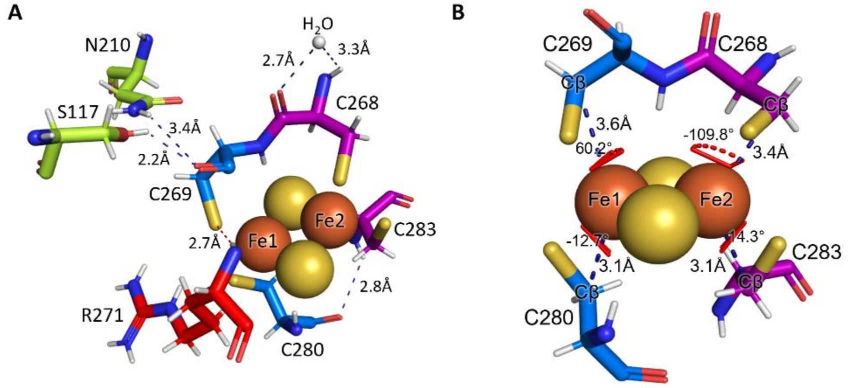

Figure III-**2 A)** Map of hydrogen bonds of cluster-coordinating cysteine residues. **B)** Distance and geometry of Fe-coordinating cysteines.

The concept of rack-induced bonding of metal clusters in proteins to tune their reactivity was proposed by Lumry and Eyring nearly 70 years ago and used by Bo Malmström in the mid-nineteen-sixties to interpret the properties of blue copper proteins [32]. It was found that the distorted coordination imposed by the rigid organization of the protein ligands was at the origin of the unusual spectroscopic properties of the metal center. The different coordination mode of the 2Fe-2S cluster in FhuF, which lowers its symmetry vs. typical 2Fe-2S clusters, may be the basis for the unusual spectroscopic properties displayed by this protein [8]. This is in line with Resonance Raman (RR) spectrum of FhuF (Figure 3).

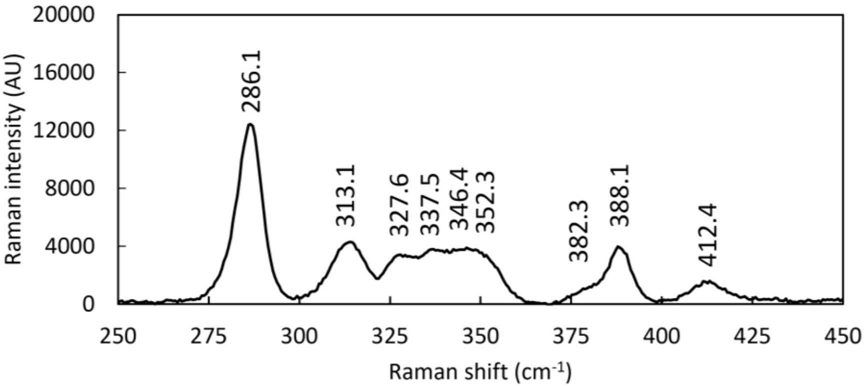

Figure III-**3** Resonance Raman spectrum of FhuF measured with 458 nm excitation, 60 s accumulation time and 5.3 mW laser power, at -190 °C.

RR spectra of Fe–S cluster containing proteins are obtained with a laser whose wavelength matches the energy of the S → Fe CT transition to selectively enhance modes involving the metal–ligand stretching coordinates transition. Different types of clusters have distinct RR fingerprints, and furthermore, for each cluster type, vibrational modes involving predominantly bridging (Fe–S)b and terminal (Fe–S)t vibrations (involving inorganic sulfur and cysteinyl sulfur ligands, respectively) can be distinguished in the spectra. RR spectra of different proteins that carry the same type of cluster may show some variations. These variations can be directly correlated with protein-specific (but typically minor) differences in Fe–S bond strengths and Fe–St–C–C dihedral angles, which govern the extent of mixing between cysteinyl St–C–C bending and (Fe–S)t stretching modes and the complexity of the spectra [33,34].

The presence of $\tilde{\nu} \leq 300$ cm^{-1} (B_{3u}^{t}) mode in RR spectra of oxidized FhuF is an unambiguous indicator of a $[2Fe\text{-}2S]^{2+}$ cluster. For the clusters with complete cysteinyl coordination, B_{3u}^{t} and A_{g}^{t} modes are found in the 281-291 cm^{-1} and 326-340 cm^{-1} ranges, respectively [33]. In clusters where one Cys has been mutated to e.g., Ser, B_{3u}^{t} and A_{g}^{t} are upshifted to the 289-302 and 332-351 cm^{-1} ranges, respectively. Therefore, the observed RR spectra are consistent with the 2Fe-2S cluster in FhuF being all-Cys coordinated but more distorted than previously characterized clusters, i.e., with lower symmetry, due to the number of identified RR bands (Figure 3).

Protein	FhuF (PDB 7QP5)
Fe-Fe-S-Cβ (º)	Fe1 62.455
	Fe1 -11.335
	Fe2 108.58*
	Fe2 -13.375*

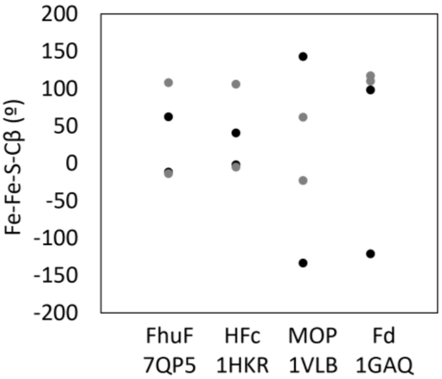

Figure III-**4** Dihedral angles Fe-Fe-S-Cβ for FhuF and representative members of each class of 2Fe-2S proteins according to their geometry. Class C is represented by human ferrochelatase (*H*Fc, PDB 1HKR), class B is represented by aldehyde oxidoreductase (MOP, PDB 1VLB) and class A is represented by maize leaf ferredoxin (Fd, PDB 1GAQ). Measurements were made with PyMOL. Black circles represent angles measured with respect to Fe1 and gray circles represent angles measured with respect to Fe2.

Additionally, the electronic structure of 2Fe2S clusters was found to be correlated with the orientation of the ligands, which is characterized by the dihedral angle Fe-Fe-S-Cβ of the coordinating cysteines [35]. Based on this dihedral angle, proteins containing 2Fe-2S clusters for which the structure is known, fall into three classes: class A congregating *bona fide* ferredoxins, including the thioredoxin-like ferredoxin; class B represented by xanthine oxidases; and a third class (C) for which the sole known structure to date is that of ferrochelatase [36]. Measurement of the dihedral angles Fe-Fe-S-Cβ in FhuF places it together with human ferrochelatase (PDB 1HRK) (Figure 4), considering that from an electronic point of view the sign for the dihedral angle can be exchanged (Figure 4) [36]. This structural similarity between FhuF and ferrochelatase is also in agreement with their similar values for quadrupole splitting of the ferric iron in the Mössbauer spectra and highlights the good correlation between coordination geometry and the Mössbauer properties [8].

Reduced FhuF localizes the additional electron in iron 2

The structure of FhuF reported here allows us to make the connection between the valence trapping observed spectroscopically and the actual location of the additional electron in the 2Fe-2S cluster upon reduction. The EPR spectrum of reduced FhuF is distinctly rhombic even though the value of g_z is lower than 2, a situation unprecedented for 2Fe-2S clusters. However, coupling between a ferric and a ferrous iron can bring the value of g_z well below 2, in agreement with the observation of an electronic exchange coupling of 300 cm^{-1} [7,35]. This value was determined from the temperature dependence of the paramagnetically shifted NMR signals of the cysteines coordinating the cluster and is larger than the values previously reported for plant and algal 2Fe-2S ferredoxins, approaching that of Rieske proteins [37,38].

The NMR spectra of 2Fe-2S ferredoxins fall into two broad categories: one includes those obtained from plants and photosynthetic bacteria such as *Anabaena*, whereas the other includes those obtained from vertebrates and bacteria such as *E. coli*. The differences were assigned to differences in the g-tensor anisotropy of the two categories, which is rhombic for the photosynthetic ferredoxins and axial for the others [39]. As seen in the previous section, FhuF is assigned to a geometric class that is different from ferredoxins and for which there are no reported NMR spectra. The NMR spectra of FhuF do not conform to the classification of NMR spectra from ferredoxins since the oxidized spectrum shows downshifted signals similarly to vertebrate ferredoxins, but the reduced spectrum is unique and displays signals paramagnetically shifted downfield up to 200 ppm [7]. This indicates that a strong hyperfine coupling exists between the unpaired electron in the cluster and the β-CH_2 protons of one of the coordinating cysteines.

Observation of the iron to β-CH_2 distances for coordinating cysteines in 2Fe-2S clusters of the diverse classes of proteins shows that FhuF is the one with the greatest bond length asymmetry, with distances of 3.6 and 3.1 Å for cysteines 269 and 280, respectively. This suggests that the iron atom bound by these cysteines is the one that remains oxidized. Thus, upon reduction, it is most likely that the extra electron localizes in the Fe2 that is coordinated by Cys-268 and Cys-283 (Figure 2 B). In agreement with this proposal, the hydrogen bond between the backbone NH of Arg-271 and the Sγ of Cys-269 (Figure 2 A) that is likely responsible for the extra paramagnetically-shifted resonance found with Curie-type temperature dependence shows that Fe1 coordinated by Cys-269 is the ferric iron in the reduced FhuF [7]. The Fe2 coordinated by the cysteine pair Cys-268 and Cys-283 is also the Fe atom that is more solvent-exposed (Figure 6 C), further supporting the hypothesis that this is where electron localization takes place assuming that no significant conformational changes occur upon partner interaction [4,40].

FhuF reduces Fe(III)-hydroxamate siderophores

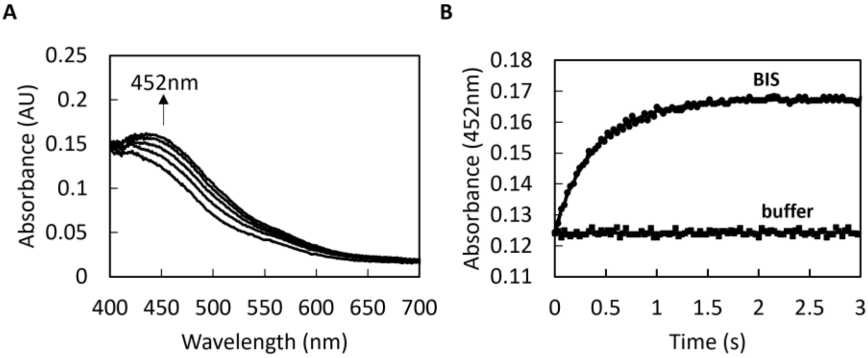

Figure III-**5** Reduction of Fe(III)-siderophores by FhuF_{red}. **A)** Representative UV-visible spectral changes upon mixing reduced FhuF with Fe(III)-bisucaberin. **B)** Kinetic trace of FhuF oxidation (452 nm) upon Fe(III)-siderophore addition (BIS-bisucaberin). Data were collected at 20 °C.

It was previously hypothesized that FhuF is involved in the siderophore pathway, possibly playing a role as a ferric-siderophore reductase. This was based on the observed reduced growth from *E.coli* FhuF deletion mutants on plates with ferrioxamine B as sole iron source and also from the removal of iron from coprogen, ferrichrome and ferrioxamine B which was significantly lower [5]. EPR experiments using reduced FhuF also showed a direct reduction of ferrioxamine E. Additionally, it was later observed that FhuF can bind both apo- and Fe(III)-rich ferrichrome [7]. Here we show that FhuF also reduces other hydroxamate siderophores, including ferrichrome and bisucaberin (Figure 5 and Figure S1).

All experiments were performed anaerobically with the presence of an oxygen-scavenging system since FhuF is very sensitive to the presence of vestigial oxygen concentrations. Despite our efforts, the reduction of FhuF was only observed with sodium dithionite (Figure S1 A) and sodium borohydride. No reduction was observed with NADH, NADPH or ferredoxin (spinach, 2Fe-2S) (data not shown), common electron donors of SIPs, the other family of ferric-siderophore reductases.

Upon mixing reduced FhuF (FhuF_{red}) with Fe(III)-siderophores (bisucaberin or ferrichrome), immediate spectral changes characterized by an increase in absorption at 452 nm were observed (Figure 5 A and Figure S1 B). These are consistent with the oxidation of FhuF and reduction of Fe(III)-siderophore. Experiments were performed at 20 °C to decrease the reaction rate so that it could be measurable with the available equipment. The rate constants of Fe(III)-siderophore reduction were determined ($2.74\pm0.08\ s^{-1}$ for bisucaberin and $110\pm7.3\ s^{-1}$ for ferrichrome) using the kinetic trace at 452 nm, which is the wavelength of maximum absorbance for a protein containing 2Fe-2S cluster. Even though the concentrations used in this work are slightly different from those used in the work of SIP from *S. frigidimarina*, the orders of magnitude difference encountered shows that FhuF reduces Fe(III)-siderophores faster. This is likely because the reduction potential of FhuF is significantly lower than *Sf*SIP (FhuF -420 mV, *Sf*SIP -320 mV at pH≈8) thus providing a more favorable driving force for the reaction [7,30].

The electrostatics of FhuF reveals common pockets among ferric-siderophore reductases

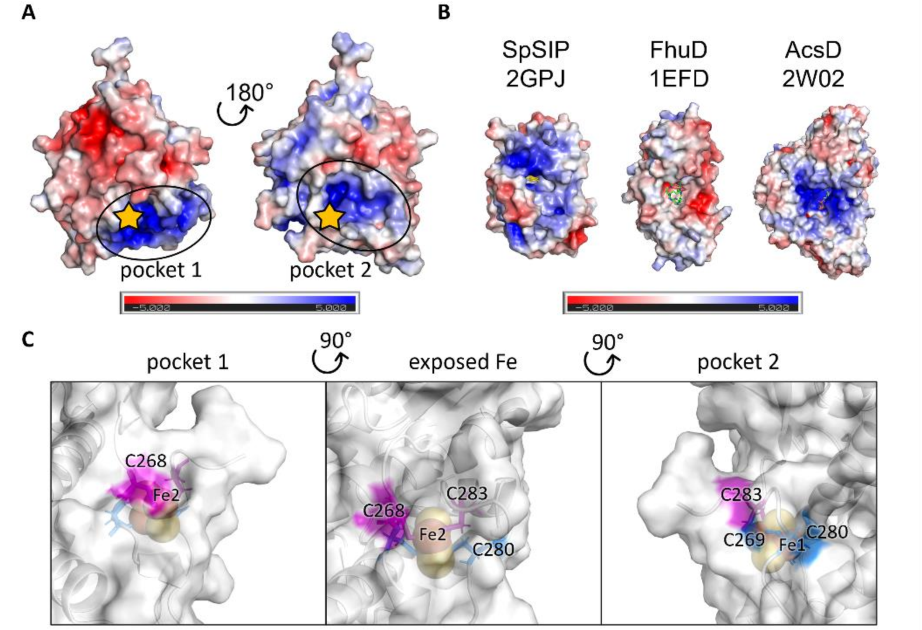

Figure III-**6** Electrostatics of FhuF and putative binding pockets. **A)** Electrostatic surface potential (−5 to +5 kT/e) of FhuF reveals putative binding pockets, where the star indicates the location of the 2Fe-2S cluster. **B)** Electrostatic surface potential (−5 to +5 kT/e) of other proteins that interact with siderophores. **C)** Close-up between pocket 1 and 2 showing that the 2Fe-2S cluster of FhuF sits on a ridge between these two positively charged pockets, exposing one of the Fe atoms (Fe2) to the solvent.

The electrostatic surface of FhuF revealed three main charged regions. These include two positively charged regions that surround the 2Fe-2S cluster located in a neutral region between the two (pocket 1 and 2, Figure 6). Pocket 2 matches one of the regions of lower density probability found in the SAXS-derived low-resolution structure and using SwissDock this is the predicted region for ferrichrome binding. Furthermore, it is also interesting to compare the electrostatic surface of FhuF with the representatives of the SIP family (Figure

6B), ferric-siderophore reductases that contain a FAD cofactor [7,41,42]. It is apparent that in both cases a positively charged pocket surrounds the catalytic center. In the SIP family, siderophores are predicted to bind in a region composed of a triad of lysines, and despite the electrostatic similarities of the pocket, this lysine triad is not found in FhuF [12,30]. It is likely that these positively charged cavities create a favorable environment for transiently accommodating Fe(III)-siderophores and driving their reduction. It has been previously observed that the redox-Bohr effect is a common feature of these enzymes. Positively charged pockets provide an environment compatible with redox-Bohr effect. Upon electron transfer from the protein to the siderophore the positively charged pocket favors the coupled release of a proton to maintain charge neutrality. The proton-coupled electron transfer has the mechanistic advantage of increasing the very low reduction potential of siderophores, easing their reduction, and also enhancing ferrous iron solubility.

Interestingly, when we compare the electrostatics of FhuF with other proteins which interact with siderophores, pocket 2 of FhuF resembles the pocket found in siderophore synthetases (AcsD in Figure 6 B). Given this similarity, we used NMR spectroscopy to test the ability of FhuF to bind ATP, but no binding was observed (Data not shown) [43]. Additionally, the electrostatics of FhuF differ dramatically from those of proteins that transport siderophores, such as FhuD (Figure 6 B), which instead contain very negatively charged pockets. For proteins whose task is to carry siderophores but not reduce them, the negatively charged pocket guarantees that the reduction potential of the bound Fe(III)-siderophores is kept very low, making sure that the iron is not adventitiously reduced and released and it is, instead, delivered to the appropriate destination.

Conclusions

The first structure of an FSR reported in this work, the enzyme FhuF from *E. coli* K-12, opens new perspectives in the study of this class of proteins. The electrostatics of FhuF revealed a common feature for Fe(III)-siderophore reductases. A positively charged (proton-rich) pocket that surrounds the catalytic center guarantees the propitious environment for redox-Bohr effect, which is itself a common functional feature for both families of these enzymes. The coupled release of a proton upon electron transfer causes a drop in the local pH enhancing ferrous iron solubility upon reduction. Additionally, the 2Fe-2S cluster in FhuF sits on a ridge between two positively charged areas, suggesting that different binding sites exist for the different interacting partners, in a way that minimizes the release of "free" ferrous iron, which is highly reactive and leads to the generation of deleterious radicals [44].

The structure of FhuF shows that this is a novel 2Fe-2S protein, given the unprecedented fold and coordination found for the binding of the 2Fe-2S cluster. This explains the atypical spectroscopic features of this protein, in particular with respect to the paramagnetic NMR spectra. However, despite having a novel coordination mode, the cluster of FhuF shares common geometrical properties with ferrochelatases, which interestingly, are proteins that are also involved in the handling of iron in the anabolic metabolism. However, there are no reports of paramagnetic NMR studies of ferrochelatases that can serve as a comparison despite the abundant literature regarding this enzyme owing to its role in debilitating human diseases [45]. Furthermore, in human ferrochelatase, the role of the 2Fe-2S cluster remains unclear. Although it is essential for the activity and stability of the protein, it is not directly involved in catalysis, i.e., the insertion of ferrous iron into protoporphyrin to form heme [46].

Additionally, the similarity of FhuF with siderophore synthetases also draws attention to a previously reported ferrichrome modification upon cellular uptake [47]. We have not tested the ability of FhuF to perform this reaction, but it is an interesting hypothesis that, if confirmed, would reveal an additional layer of the impact of the activity of FhuF in microbe-microbe interactions and how these proteins have shaped the evolution of iron uptake pathways. It is also interesting to note that FhuF showed very high rates of reduction of hydroxamate siderophores, a type of siderophores not known to be produced by *E. coli* strains. This catalytic activity of FhuF reflects an opportunistic lifestyle that enhances ecological fitness, and which has been retained even in this laboratory strain. Additionally, *E. coli* strains express flavin-based ferric-siderophore reductases (SIP family) including YqjH, which is apparently specific for the reduction of ferric triscatecholates including hydrolyzed ferric-enterobactin complex [12]. Altogether, the specificity of these enzymes reflects the cost/benefit interplay of having a protein that on one hand requires iron for its maturation but on the other hand can ease iron release very efficiently into the cellular metabolism.

The metabolic positioning of FhuF remains open for discussion. It was previously observed from pull-down assays that FhuF interacts with OppD which is annotated as an Oligopeptide transport ATP-binding protein and with YdbK annotated as a probable pyruvate-flavodoxin oxidoreductase [48]. The former (OppD) may be a siderophore transporter of unknown substrate preference. The latter (YbdK) is a putative electron donor for FhuF. Given the low reduction potential of FhuF, it is likely that its electron donor is a very low reduction potential donor. The pyruvate oxidation activity of YbdK was tested *in vitro* using Methyl Viologen as electron acceptor, which has a reduction potential in the appropriate range to make the reaction thermodynamically feasible. Furthermore, both FhuF and YdbK are upregulated under oxidative stress signaling. These conditions exacerbate the need for iron, and the reduction of FhuF by YdbK allows it to reduce ferric-siderophores, making iron available for anabolic metabolism. In this respect, it is interesting to note that the expression of FhuF is also linked to the abundance of downstream intracellular iron sinks as can be deduced by the observed up-regulation of FhuF in *E. coli* overexpressing ferritin [49].

With this work, we finally have detailed structural knowledge for the representatives of both families of cytoplasmic ferric-siderophore reductases. This makes accessible a further understanding of the role and mechanistic potential of these enzymes, information of crucial relevance when considering therapeutic intervention via targeting of iron uptake, which is essential for nearly all known organisms [50,51]. Indeed, within the siderophore pathway, SIPs and FSRs provide a narrow choke point between a wide diversity of cell surface siderophore receptors and intracellular iron-containing or storage proteins [52]. Inhibitors for this crucial step on the siderophore pathway can potentially reduce access to iron for anabolic metabolism and stop the recycling of apo-siderophores for subsequent rounds of iron uptake.

Acknowledgements

The authors are grateful to Prof Alfred Trautwein, who established the first contact with Prof Berthold Matzanke, who graciously made the FhuF expression system available that allowed this work to be performed. To Kelly Frade, for the early help in finding the most stabilizing buffer for FhuF. To Paula Chicau and the N-terminal sequencing facility at ITQB for providing the measurements used in this work.

The X-ray diffraction data collections were performed at XALOC beamline at ALBA Synchrotron with the collaboration of ALBA staff. This work benefited from access to CERMAX, ITQB-NOVA, Oeiras, Portugal with equipment funded by FCT, project AAC 01/SAICT/2016. Financial support was provided by European EC Horizon2020 TIMB3 (Project 810856). Financial support was also provided by Project MOSTMICROITQB with refs UIDB/04612/2020 and UIDP/04612/2020. Fundação para a Ciência e a Tecnologia (FCT) Portugal is also acknowledged for funding through project PTDC/BIA-BQM/30176/2017, and through FCT PT-NMR PhD Program via PD/BD/135187/2017 to IBT.

References

[1] W. Martin, M.J. Russell, On the origins of cells: A hypothesis for the evolutionary transitions from abiotic geochemistry to chemoautotrophic prokaryotes, and from prokaryotes to nucleated cells, Phil. Trans. R. Soc. Lond. B. 358 (2003) 59–85.

[2] J. Liu, S. Chakraborty, P. Hosseinzadeh, Y. Yu, S. Tian, I. Petrik, A. Bhagi, Y. Lu, Metalloproteins containing cytochrome, iron-sulfur, or copper redox centers, Chem. Rev. 114 (2014) 4366–4369.

[3] R.J.P. Williams, The Bakerian Lecture, 1981 Natural Selection of the Chemical elements, Proc. R. Soc. Lond. 213 (1981) 361–397.

[4] L.B. Dugad, G.N. la Mar, L. Banci, I. Bertini, Identification of Localized Redox States in Plant-Type Two-Iron Ferredoxins Using the Nuclear Overhauser Effect, Biochemistry. 29 (1990) 2263–2271.

[5] K. Müller, B.F. Matzanke, V. Schünemann, A.X. Trautwein, K. Hantke, FhuF, an iron-regulated protein of *Escherichia coli* with a new type of [2Fe-2S] center, Eur J Biochem. 258 (1998) 1001–1008.

[6] M. Miethke, A.J. Pierik, F. Peuckert, A. Seubert, M.A. Marahiel, Identification and characterization of a novel-type ferric siderophore reductase from a gram-positive extremophile, J. Biol. Chem. 286 (2011) 2245–2260.

[7] I.B. Trindade, G. Hernandez, E. Lebègue, F. Barrière, T. Cordeiro, M. Piccioli, R.O. Louro, Conjuring up a ghost: structural and functional

characterization of FhuF, a ferric siderophore reductase from *E. coli*, J. Biol. Inorg. Chem. 26 (2021) 313–326.

[8] B.F. Matzanke, S. Anemüller, V. Schünemann, A.X. Trautwein, K. Hantke, FhuF, Part of a Siderophore-Reductase System, Biochemistry. 43 (2004) 1386–1392.

[9] S.D. Springer, A. Butler, Microbial ligand coordination: Consideration of biological significance, Coord. Chem. Rev. 306 (2016) 628–635.

[10] I. Schröder, E. Johnson, S. de Vries, Microbial ferric iron reductases, FEMS Microbiol Rev. 27 (2003) 427–447.

[11] M. Miethke, M.A. Marahiel, Siderophore-Based Iron Acquisition and Pathogen Control, Microbiol Mol Biol Rev. 71 (2007) 413–451.

[12] M. Miethke, J. Hou, M.A. Marahiel, The siderophore-interacting protein YqjH acts as a ferric reductase in different iron assimilation pathways of *Escherichia coli*, Biochemistry. 50 (2011) 10951–10964.

[13] K. Li, W.H. Chen, S.D. Bruner, Structure and Mechanism of the Siderophore-Interacting Protein from the Fuscachelin Gene Cluster of *Thermobifida fusca*, Biochemistry. 54 (2015) 3989–4000.

[14] C. Vonrhein, C. Flensburg, P. Keller, A. Sharff, O. Smart, W. Paciorek, T. Womack, G. Bricogne, Data processing and analysis with the autoPROC toolbox, Acta Crystallogr. D Biol. Crystallogr. 67 (2011) 293–302.

[15] W. Kabsch, XDS, Acta Crystallogr. D Biol. Crystallogr. 66 (2010) 125–132.

[16] A.J. McCoy, R.W. Grosse-Kunstleve, P.D. Adams, M.D. Winn, L.C. Storoni, R.J. Read, Phaser crystallographic software, J Appl Crystallogr. 40 (2007) 658–674.

[17] P. Evans, Scaling and assessment of data quality, Acta Crystallogr. D Biol. Crystallogr. 62 (2006) 72–82.

[18] P.R. Evans, G.N. Murshudov, How good are my data and what is the resolution?, Acta Crystallogr. D Biol. Crystallogr. 69 (2013) 1204–1214.

[19] J. Jumper, R. Evans, A. Pritzel, T. Green, M. Figurnov, O. Ronneberger, K. Tunyasuvunakool, R. Bates, A. Žídek, A. Potapenko, A. Bridgland, C. Meyer, S.A.A. Kohl, A.J. Ballard, A. Cowie, B. Romera-Paredes, S. Nikolov, R. Jain, J. Adler, T. Back, S. Petersen, D. Reiman, E. Clancy, M. Zielinski, M. Steinegger, M. Pacholska, T. Berghammer, S. Bodenstein, D. Silver, O. Vinyals, A.W. Senior, K. Kavukcuoglu, P. Kohli, D. Hassabis, Highly accurate protein structure prediction with AlphaFold, Nature. 596 (2021) 583–589.

[20] K. Cowtan, The Buccaneer software for automated model building. 1. Tracing protein chains, Acta Crystallogr. D Biol. Crystallogr. 62 (2006) 1002–1011.

[21] P. Emsley, B. Lohkamp, W.G. Scott, K. Cowtan, Features and development of Coot, Acta Crystallogr. D Biol. Crystallogr. 66 (2010) 486–501.

[22] G.N. Murshudov, P. Skubák, A.A. Lebedev, N.S. Pannu, R.A. Steiner, R.A. Nicholls, M.D. Winn, F. Long, A.A. Vagin, REFMAC5 for the refinement of macromolecular crystal structures, Acta Crystallogr. D Biol. Crystallogr. 67 (2011) 355–367.

[23] A. Brünger, Free R value: a novel statistical quantity for assessing the accuracy of crystal structures, Nature. 355 (1992) 472–475.

[24] V.B. Chen, W.B. Arendall, J.J. Headd, D.A. Keedy, R.M. Immormino, G.J. Kapral, L.W. Murray, J.S. Richardson, D.C. Richardson, MolProbity: All-atom structure validation for macromolecular crystallography, Acta Crystallogr. D Biol. Crystallogr. 66 (2010) 12–21.

[25] S. Velankar, C. Best, B. Beuth, PDBe: protein data bank in Europe, Nucleic Acids Res. Spec. Publ. 38 (2010) 308–317.

[26] W.L. DeLano, The PyMOL Molecular Graphics System, Version 2.3. New York, NY: Schrödinger LLC., (2020).

[27] K. Diederichs, P.A. Karplus, Improved R-factors for diffraction data analysis in macromolecular crystallography, Nature. 4 (1997) 269–276.

[28] K. Diederichs, Quantifying instrument errors in macromolecular X - Ray data sets, Acta Crystallogr. D: Struct. Biol. 66 (2010) 733–740.

[29] B.W. Matthews, Solvent Content of Protein Crystals, J. Mol. Biol. 33 (1968) 491–497.

[30] I. Trindade, J.M. Silva, B.M. Fonseca, T. Catarino, M. Fujita, P.M. Matias, E. Moe, R.O. Louro, Structure and reactivity of a siderophore-interacting protein from the marine bacterium *Shewanella* reveals unanticipated functional versatility, J. Biol. Chem. 294 (2018) 157–167.

[31] S.J. Wilkens, B. Xia, F. Weinhold, J.L. Markley, W.M. Westler, NMR Investigations of *Clostridium pasteurianum* Rubredoxin. Origin of Hyperfine ^{1}H, ^{2}H, ^{13}C, and ^{15}N NMR Chemical Shifts in Iron-Sulfur Proteins As Determined by Comparison of Experimental Data with Hybrid Density Functional Calculations, J. Am. Chem. Soc. 120 (1998) 4806–4814.

[32] B.G. Malmstrom, Rack-induced bonding in blue-copper proteins, Eur. J. Biochem. 223 (1994) 711–718.

[33] S. Todorovic, M. Teixeira, Resonance Raman spectroscopy of Fe–S proteins and their redox properties, J. Biol. Inorg. Chem. 23 (2018) 647–661.

[34] G. Caserta, L. Zuccarello, C. Barbosa, C.M. Silveira, E. Moe, S. Katz, P. Hildebrandt, I. Zebger, S. Todorovic, Unusual structures and unknown roles of FeS clusters in metalloenzymes seen from a resonance Raman spectroscopic perspective, Coord. Chem. Rev. 452 (2022) 1–13.

[35] M. Orio, J.M. Mouesca, Variation of average g values and effective exchange coupling constants among [2Fe-2S] clusters: A density functional theory study of the impact of localization (trapping forces) versus

delocalization (double-exchange) as competing factors, Inorg, Chem. 47 (2008) 5394–5416.

[36] S. Gambarelli, J.M. Mouesca, Correlation between the Magnetic g Tensors and the Local Cysteine Geometries for a Series of Reduced [2Fe-2S*] Protein Clusters. A Quantum Chemical Density Functional Theory and Structural Analysis, Inorg.Chem. 43 (2004) 1441–1451.

[37] L. Skjeldal, J.L. Markley, V.M. Coghlan, L.E. Vickery, ^{1}H NMR Spectra of Vertebrate [2Fe-2S] Ferredoxins. Hyperfine Resonances Suggest Different Electron Delocalization Patterns from Plant Ferredoxins, Biochemistry. 30 (1991) 9078–9083.

[38] B. Xia, D. Jenk, D.M. LeMaster, W.M. Westler, J.L. Markley, Electron-nuclear interactions in two prototypical [2Fe-2S] proteins: Selective (chiral) deuteration and analysis of ^{1}H and ^{2}H NMR signals from the alpha and beta hydrogens of cysteinyl residues that ligate the iron in the active sites of human ferredoxin and *Anabaena* 7120 vegetative ferredoxin, Arch. Biochem. 373 (2000) 328–334.

[39] H.M. Holden, B.L. Jacobson, J.K. Hurley, G. Tollin, B.-H. Oh, L. Skjeldal, Y.K. Chae, H. Cheng, B. Xia, J.L. Markley, Structure-Function Studies of [2Fe-2S] Ferredoxins, J. Bioenerg. Biomembr. 26 (1994) 67-88.

[40] L. Banci, I. Bertini, C. Luchinat, R. Pierattelli, N. v Shokhirev, F.A. Walker, Analysis of the Temperature Dependence of the 1 H and 13 C Isotropic Shifts of Horse Heart Ferricytochrome c: Explanation of Curie and Anti-Curie Temperature Dependence and Nonlinear Pseudocontact Shifts in a Common Two-Level Framework, J Am Chem Soc. 120 (1998) 8472–8479.

[41] A. Grosdidier, V. Zoete, O. Michielin, SwissDock, a protein-small molecule docking web service based on EADock DSS, Nucleic Acids Res. Spec. Publ. 39 (2011) 1–8.

[42] A. Grosdidier, V. Zoete, O. Michielin, Fast docking using the CHARMM force field with EADock DSS, J. Comput. Chem. 32 (2011) 2149–2159.

[43] S. Schmelz, N. Kadi, S.A. McMahon, L. Song, D. Oves-Costales, M. Oke, H. Liu, K.A. Johnson, L.G. Carter, C.H. Botting, M.F. White, G.L. Challis, J.H. Naismith, AcsD catalyzes enantioselective citrate desymmetrization in siderophore biosynthesis, Nat. Chem. Biol. 5 (2009) 174–182.

[44] D. Touati, Iron and Oxidative Stress in Bacteria, Arch. Biochem. Biophys. 373 (2000) 1–6.

[45] H.D. Basavarajappa, R.S. Sulaiman, X. Qi, T. Shetty, S. Sheik Pran Babu, K.L. Sishtla, B. Lee, J. Quigley, S. Alkhairy, C.M. Briggs, K. Gupta, B. Tang, M. Shadmand, M.B. Grant, M.E. Boulton, S. Seo, T.W. Corson, Ferrochelatase is a therapeutic target for ocular neovascularization, EMBO Mol. Med. 9 (2017) 786–801.

[46] D. Pain, A. Dancis, Roles of Fe-S proteins: From cofactor synthesis to iron homeostasis to protein synthesis, Curr Opin Genet Dev. 38 (2016) 45–51.

[47] A. Hartmannt, V. Braun, Iron Transport in *Escherichia coli*: Uptake and Modification of Ferrichrome, J. Bacteriol. 143 (1980) 1–10.

[48] M. Arifuzzaman, M. Maeda, A. Itoh, K. Nishikata, C. Takita, R. Saito, T. Ara, K. Nakahigashi, H.C. Huang, A. Hirai, K. Tsuzuki, S. Nakamura, M. Altaf-Ul-Amin, T. Oshima, T. Baba, N. Yamamoto, T. Kawamura, T. Ioka-Nakamichi, M. Kitagawa, M. Tomita, S. Kanaya, C. Wada, H. Mori, Large-scale identification of protein-protein interaction of *Escherichia coli* K-12, Genome Res. 16 (2006) 686–691.

[49] H. Abdul-tehrani, A.J. Hudson, Y. Chang, A.R. Timms, C. Hawkins, J.M. Williams, P.M. Harrison, J.R. Guest, S.C. Andrews, Ferritin Mutants of *Escherichia coli* Are Iron Deficient and Growth Impaired, and fur Mutants are Iron Deficient, J. Bacteriol. 181 (1999) 1415–1428.

[50] S.C. Andrews, A.K. Robinson, F. Rodríguez-Quiñones, Bacterial iron homeostasis, FEMS Microbiol Rev. 27 (2003) 215–237.

[51] R.C. Hider, X. Kong, Chemistry and biology of siderophores, Nat Prod Rep. 27 (2010) 637–657.

[52] K. Honarmand Ebrahimi, P.L. Hagedoorn, W.R. Hagen, Unity in the biochemistry of the iron-storage proteins ferritin and bacterioferritin, Chem. Rev. 115 (2015) 295–326.

“Science, my lad, is made up of mistakes, but mistakes which are useful
to make, because they lead little by little to the truth”
Adapted from Jules Verne

IV. Chapter IV: Ferric-siderophore reduction in *Shewanella bicestrii*: Structural and functional characterization of *Sb*SIP reveals an overlooked specificity of siderophore-interacting proteins

This chapter will be submitted as:

Trindade, I.B., Fonseca, B.M., Catarino, T., Matias, P.M., Moe, E., Louro, R.O. Ferric-siderophore reduction in *Shewanella bicestrii*: Structural and functional characterization of *Sb*SIP reveals an overlooked specificity of siderophore-interacting proteins. Biochemistry

The author of this dissertation participated in all experiments described in this chapter except for the refinement of *Sb*SIP structure.

Abstract

Shewanella sp. is a bacterial genus widespread in marine and brackish water environments, and an emergent opportunistic pathogen. The environmental versatility of these bacteria is highly dependent on their ability to produce an abundance of iron-rich proteins, mainly multiheme *c*-type cytochromes. Although iron plays a vital role in the ability of *Shewanella* to survive in many different environments, very few studies exist regarding the strategies by which these bacteria scavenge iron from the environment. Small molecule siderophore-mediated iron transport is a strategy commonly employed for iron acquisition, and it was identified amongst *Shewanella* spp. over two decades ago. *Shewanella* species produce hydroxamate-type siderophores and it was also observed that iron removal from these compounds can occur in the cytoplasm via Fe(III)-siderophore reduction mediated by flavin-containing siderophore-interacting proteins (SIPs). The genome of *Shewanella bicestrii* isolated from an infected child contains representatives of the two different cytosolic families of Fe(III)-siderophore reductases: the flavin-containing siderophore interacting protein family (SIP) and the iron−sulfur ferric siderophore reductases family (FSR).

We report the expression and purification of the flavin-containing (*Sb*SIP) and iron-sulfur cluster-containing (*Sb*FSR) siderophore-interacting proteins of *S. bicestrii*. The structural and functional characterization of *Sb*SIP shows distinct features from the highly homologous SIP from *Shewanella frigidimarina* (*Sf*SIP). This includes significant structural differences, different binding affinities for NADH and NADPH and lower rates of Fe(III)-siderophore reduction results which consolidate the putative binding pocket for these proteins.

Overall, our work highlights the unnoticed specificity of the SIP family and further explores the methodological aspects of studying this family of enzymes.

Introduction

Iron is one of the most abundant elements in the Earth's crust, and in its biogeochemical cycling mainly interconverts between its reduced, Fe(II), and its oxidized form, Fe(III). It is a key element for life, mediating fundamental redox reactions and participating in various biological processes by being an essential component of numerous proteins [1–3]. Despite its abundance, in an oxygen-rich atmosphere like the present one, iron precipitates in its oxidized form, and thus, it is not readily bioavailable [4,5]. To overcome iron shortage microorganisms release siderophores, i.e., secondary metabolites with a high affinity for ferric iron which solubilize and scavenge iron for intracellular uptake [6–8]. The main steps of the siderophore pathway include its intracellular synthesis, extracellular release into the environment, iron complexation, cellular uptake, and cellular iron release through specialized enzymes [9,10]. These can belong to the Siderophore-Interacting Protein (SIP) family or to the Ferric-Siderophore Reductase family (FSR). So far, few studies exist regarding the function of FSRs and thus, the function of these two families of enzymes is apparently redundant: to reduce ferric iron inside the Fe(III)-siderophore complex into its ferrous form, lowering the affinity of the complex and thus, promoting iron release [11].

The *Shewanella* genus is well known for its respiratory versatility, an ability that is facilitated by an extensive repertoire of iron-containing proteins, specifically, multiheme cytochromes [12,13]. Because of this, *shewanellaceae* have higher iron requirements than many well-known bacteria, *e.g.,* approximately four-fold more than *Escherichia coli* [14]. Despite its importance, there is still much to be learned regarding the iron acquisition pathways of this genus. Two decades ago, the iron-sequestering abilities of 51 strains of *Shewanella putrefaciens* isolated from different sources (fish, water, and warm-blooded animals) were assessed, where more than half of the strains produced hydroxamate-type siderophores [15]. It is now becoming increasingly recognized that to thrive in a wide diversity of iron-deficient habitats ranging from the ocean bed to the eukaryotic host, *Shewanella* species adapt metabolically, including through the production of different siderophores and subsequent different proteins for their utilization [16,17]. Some examples include the production of cyclic dihydroxamate putrebactin by *S. putrefaciens*, and the production of asymmetrical avaroferrin by *Shewanella algae*. Also, different *Shewanella* species have different Fe(III)-siderophore reductases [18]. For instance, *S. frigidimarina* produces only a representative of the SIP family (*Sf*SIP), whereas some species such as *S. bicestrii* produces representatives of both SIP and FSR families [11,19–22].

In our work, we investigated siderophore-iron release from *S. bicestrii* also known as *S. putrefaciens* (DSM 9451) and *Shewanella* sp. JAB-1. *S. bicestrii* was first identified as part of three Extended Spectrum β-lactamase (ESBL)-producing bacteria in a bile sample of a 10-year-old child suffering from cholangitis [23].

Here we report the production of both Siderophore-Interacting Protein (*Sb*SIP) and Ferric-Siderophore Reductase (*Sb*FSR) proteins from *S. biscestrii.* Given the instability of the latter, we only report the structure and biochemical characterization of *Sb*SIP. *Sb*SIP showed distinct binding preferences for NADH and NADPH, and slower Fe(III)-siderophore reduction ability than previously characterized *Sf*SIP [20,24]. Furthermore, the structure of *Sb*SIP revealed unprecedented folding which limits the access to the FAD cofactor. Altogether, these results point towards an unexpected specificity for this family of enzymes.

Methods

Production of *Sb*SIP and *Sb*FSR

*Sb*FSR and *Sb*SIP expression vectors were designed based on the SLIC (Sequence and Ligation Independent Cloning) method developed by Scholz and co-workers [25]. Primers were designed as described to include an HRV 3C protease cleavage site and ccdB counter-selection (3C-LP1 and ccdB-LP2). *sbsip* and *sbfsr* gene fragments were amplified using KAPA2G Robust PCR kit from a colony of commercially available *S. putrefaciens* DSM 9451 (DSMZ) grown on an Luria Bertani (LB) agar plate. PCR fragments were then ligated into pCoofy38, a vector containing an N-terminal Thioredoxin-His$_{10}$ tag using a Gibson Assembly® Cloning Kit (New England BioLabs). Plasmids were extracted and transformed into competent *E. coli* BL21(DE3) cells for expression. Proteins were expressed by growing expression strains in LB Broth Media (*Sb*SIP) or Terrific Broth Media (*Sb*FSR) supplemented with 50 mg/L kanamycin at 37 °C, 150 rpm, and at an OD$_{600}$ of 0.5-0.7, expression was induced with 1 mM IPTG. After approximately 30 hours, cells were harvested by centrifugation and frozen at -80 °C. Cells were later defrosted and resuspended in 20 mM Potassium Phosphate buffer pH 7.6 with 300 mM NaCl and a protease inhibitor cocktail (Roche) together with DNase I (Sigma) prior to a three-pass cell disruption at 6.9 MPa using a French press. The lysate was ultracentrifuged at 204 709 g for 75 min at 4 °C to remove cell membranes and debris. Proteins were purified from the supernatant using a His-trap affinity column (GE Healthcare) with a stepwise elution method. The fraction containing *Sb*FSR was eluted at 20 mM Potassium Phosphate pH 7.6, 300 mM NaCl with 250 mM imidazole whereas *Sb*SIP was eluted with 150 mM imidazole. Eluted fractions were analyzed by SDS-PAGE using Blue-Safe staining (NZYTech) and UV–visible spectroscopy to select fractions containing *Sb*FSR and *Sb*SIP. The fractions of each protein were pooled, and the imidazole was removed through dialysis overnight and proteins were concentrated using an

Amicon ® Ultra Centrifugal Filter with a cutoff of 30 kDa. The *Sb*FSR quantity was very small, and fractions precipitated after concentration and thus, Trx-His$_{10}$ tag cleavage was only performed for *Sb*SIP. *Sb*SIP fractions were incubated with HRV 3C Protease overnight at 4 °C with agitation, and the final purified *Sb*SIP was concentrated from the flowthrough of a second passage through the His-trap column using an Amicon Ultra Centrifugal Filter (Millipore) with a 30 kDa cutoff. The purity of *Sb*SIP was confirmed by SDS-PAGE using Blue Safe staining (NzyTech), N-terminal sequencing analysis, and UV-Visible spectroscopy. An extinction coefficient of free FAD ε_{450nm}= 11 300 M^{-1} cm^{-1} was used for quantification purposes [26].

Crystallization and structure determination of SbSIP

Purified *Sb*SIP (Trx-His10 tag free) at a concentration of 10 mg/ml crystallized in a solution containing 1.8 M Ammonium sulfate with 0.01M Cobalt(II) chloride hexahydrate and 0.1 M MES pH 6.5 using the hanging drop vapor diffusion technique (1 µl protein:1 µl reservoir). Crystals were harvested and soaked in a 2 µl drop of cryo solution (1.8 M Ammonium sulfate 0.1 MES pH 6.5 with 30 % glycerol) prior to flash-freezing in liquid nitrogen. Diffraction data was collected at 100 K to a resolution of 1.86 Å at the ALBA beamline XALOC (Barcelona, Spain) The images were processed with AutoProc and STARANISO, which make use of XDS and the CCP4 suite for integration and conversion of integrated intensities to structure factors [27–32]. The data processing statistics are listed in Table 1. The structure was solved by molecular replacement using PHASER in the CCP4 suite and a previously determined SIP crystal structure from *S. putrefaciens* (PDB 2GPJ, Joint Center for Structural Genomics) as phasing model. Two *Sb*SIP protein chains (A and B), each one bound to a FAD moiety were located in the asymmetric unit of the crystal structure, and the model was automatically corrected with BUCCANEER/REFMAC in the CCP4 suite [33,34].

After an initial refinement using REFMAC5 in the CCP4 suite, structure refinement was continued using PHENIX [35]. Hydrogen atoms were included in calculated positions with the PHENIX READYSET tool, and isotropic atomic displacement parameters (ADPs) were refined for all non-hydrogen atoms. Throughout the refinement, the model was periodically checked and corrected with COOT against σA-weighted 2|Fo|-|Fc| and |Fo|-|Fc| electron-density maps. Solvent molecules were added automatically by the ArpWarp solvent protocol via the CCP4 suite and validated by inspection of electron-density maps in COOT [36]. In the final refinement cycles, a TLS rigid body refinement of the ADPs was carried out, considering 7 and 6 rigid body groups for SbSIP chains A and B, respectively, determined with the PHENIX FIND_TLS_GROUPS tool from a previous refinement with isotropic ADPs. The final values of R and R-free were 0.168 and 0.200 respectively, with a maximum likelihood estimate of the overall coordinate error of 0.17 Å [37]. The refinement statistics are presented in Table 2. The model stereochemical quality was analyzed with MOLPROBITY and there are no outliers in the Ramachandran φ,ϕ plot [38]. The coordinates and structure factors have been submitted to the Worldwide Protein Data Bank (wwPDB consortium, 2018) with accession codes 1xxx and r1xxxsf. Pictures were produced using PyMOL [39].

Table IV-**1** Data collection and processing statistics.

Beamline	ALBA XALOC
Detector	PILATUS 6M
Wavelength (Å)	0.97918
Data Processing	AutoProc/STARANISO
Space Group	$P\ 4_3\ 2_1\ 2$
Unit cell parameters (Å)	a=82.44, c=250.85
Resolution limits of ellipsoid fitted to resolution cut-off surface (Å)	2.29, 2.29, 1.71
Resolution, spherical limits (Å)	78.32 – 1.86 (2.03 – 1.86)
Nr. Observations	317355 (13920)
Unique reflections	49068 (2453)
Multiplicity	6.5 (5.7)
Completeness, spherical (%)	66.9 (15.0)
Completeness, ellipsoidal (%)	93.7 (68.2)
R-merge (%) [a]	5.1 (74.6)
R-meas (%) [b]	5.6 (82.0)
CC $^{1/2}$	1 (0.819)
<I/σ(I)>	19.3 (2.2)
ISa	36.6
Wilson Plot B (Å^2)	44.2
Z [c]	2
V_m	3.72
Estimated Solvent Content (%)	67.0

[a] R-merge = merging R-factor, $(\Sigma_{hkl}\ \Sigma_i\ |I_i(hkl) - <I(hkl)>|)\ /\ (\Sigma_{hkl}\ \Sigma_i\ I(hkl)) \times 100\%$.

[b] R-meas = redundancy independent R-factor, $\Sigma_h\ [N_{hkl}/(N_{hkl}-1)]^{1/2}\ \Sigma_i\ |I_i(hkl) - <I(hkl)>|\ /\ \Sigma_{hkl}\ \Sigma_i\ I_i(hkl) \times 100\%$, where *I* is the observed intensity, <*I*> is the average intensity of multiple observations from symmetry-related reflections, and N_{hkl} is their multiplicity [40].

[c] Nr. monomers in the asymmetric unit according to Matthews coefficient [41].

Protein Film Voltammetry (PFV) of *Sb*SIP

PFV experiments of *Sb*SIP were performed at 25ºC using a three-electrode electrochemical cell configuration with PGE (pyrolytic graphite edge) electrode, graphite rod (counter electrode) and an Ag/AgCl 3 M KCl (reference electrode) inside a Coy anaerobic glovebox chamber using a CHI electrochemical analyzer (CHI instruments). The electrode was cleaned and freshly polished before every experiment. The polishing routine consisted of a 10 min nitric acid incubation at room temperature followed by 10 min of hand-polishing with a 1.0

µM alumina aqueous slurry. The electrode was thoroughly rinsed with water and left to dry and then *Sb*SIP was immobilized by pipetting 7 µL of a 250 µM solution of *Sb*SIP in 20 mM Potassium Phosphate buffer at pH 7.6 with 100 mM KCl. Once fully dried, the electrode was rinsed to remove protein excess and immersed in Potassium Phosphate buffer at different pH values. Experiments were performed at different scan rates and then the buffer was collected, and the pH measured for confirmation. QSoas was used to subtract the capacitive current and extract the reduction potentials. Potentials are reported in mV versus the Standard Hydrogen Electrode (SHE) by the addition of 210 mV to those measured [42].

^{31}P NMR: NAD(P)H binding experiments

NAD(P)H and *Sb*SIP were prepared in 20 mM Tris-HCl buffer at pH 8 with 100 mM KCl containing 10 % of $^{2}H_2O$ (99.9 atom %). Using the standard Bruker pulse program "zgdc," one-dimensional proton-decoupled ^{31}P spectra were acquired with 2048 scans, d1 of 1.3 s at 25 °C on a Bruker Avance II 500 MHz equipped with a SEX probe for ^{31}P detection. Samples of 100 µM or 57 µM of NADH and NADPH, respectively, were titrated against increasing concentrations of *Sb*SIP. Collected spectra were visualized and analyzed using TopSpin 3.6 (Bruker). For NADH binding, the concentration of free and bound species was determined from the relative intensity of each peak and the dissociation constant (Kd) was calculated using the equation previously described [20]. For NADPH binding, the chemical shift perturbations (Δδ) of the NMR signals from NADPH that resulted from the complex formation with *Sb*SIP in fast exchange regime were plotted against the molar ratio (R) of [*Sb*SIP]/[NADPH]. Results were fitted and the dissociation constant (Kd) was determined as described by Fonseca and co-workers [43].

Kinetic Experiments

The kinetic experiments were performed with HI-TECH Scientific Stopped-flow equipment (SF-61DX2) installed inside an anaerobic glove box (Mbraun MB150-GI). The temperature of the drive syringes and mixing chamber was maintained at 25 °C using a water bath. Sample solutions were prepared with 20 mM Potassium Phosphate buffer pH 7 with 100 mM KCl and in the presence of the O_2 scavenging system (10 mM glucose, 375 nM glucose oxidase, and 750 nM catalase) [44]. The time course of the reactions was monitored using a photodiode array. Solutions were prepared inside the anaerobic chamber with degassed water and all experiments were performed in triplicate. Data were analyzed with Kinetics Studio version 2.32 (TgK Scientific).

Reduction of both *Sb*SIP and *Sf*SIP with NADH and NADPH was performed by mixing 1 mM of these compounds with 20 µM of *Sb*SIP or *Sf*SIP. The reduction with sodium dithionite was performed by mixing 3 mM of this compound with 20 µM *Sb*SIP.

Fe(III)-siderophores putrebactin and bisucaberin were kindly provided by Prof. Masaki Fujita. Reduction of these by reduced *Sb*SIP (*Sb*SIP$_{semi}$) was performed after reducing *Sb*SIP with sodium dithionite. The latter was achieved by using excess sodium dithionite which was then removed through buffer exchange in a HiTrap® Desalting Column (GE Healthcare). Ferric-siderophore reduction experiments were then performed using 20µM *Sb*SIP$_{semi}$ against 100µM of ferric-siderophore in the stopped-flow apparatus. The reduction rate constants were obtained from the fitting of the kinetic traces at 600 nm. Catalytic experiments with NAD(P)H and ferric-siderophores were attempted, however spectra overlap prevented an unambiguous interpretation of the results, and thus, these data were excluded from this manuscript. Ferrozine assays were also attempted. However, in the presence of the oxygen-scavenging system, absorption changes were observed in the absence of *Sb*SIP (control).

Ferrozine is a very strong ferrous iron chelator and in the absence of oxygen the shift in chemical equilibrium is sufficient for Fe(III)-siderophore reduction to take place at detectable rates without enzymatic mediation.

Results and Discussion

Production of Fe(III)-siderophore reductases SbSIP and SbFSR

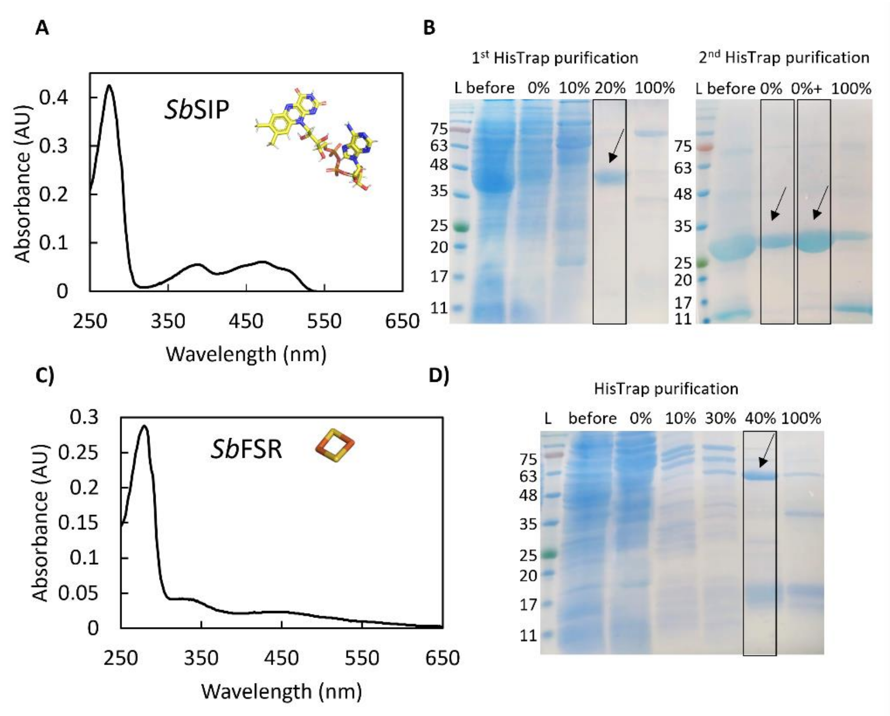

Figure IV-**1** Production of *Sb*SIP and *Sb*FSR. **A)** UV-visible profile of pure SbSIP. **B)** SDS-PAGE gels of purification steps of *Sb*SIP before (1st HisTrap purification) and after HRV 3C incubation step (2nd HisTrap purification). **C)** UV-visible profile of fraction containing SbFSR. **D)** SDS-PAGE gel of *Sb*FSR purification. Boxes represent fractions used for further experiments and arrows show gel band of proteins of interest. Percentages represent the amount of imidazole used out of a 500mM stock solution.

*Sb*SIP was purified to apparent purity (>95%) and migrated as a single band at approximately 30 kDa (42 kDa before HRV 3C protease incubation) on a

15% SDS–PAGE gel, as expected from theoretical calculations (Fig. 1B). The purified protein appeared yellow and the UV–visible spectrum showed the typical spectral features of an oxidized flavoprotein in the UV–visible region (Figure 1A), with absorption peaks at 387nm and 471nm and distinct shoulders located at 445nm and 502nm. *Sb*FSR was not purified to complete purity (Figure 1D) given that the sample was very unstable and precipitated shortly after the first purification step. Regardless, a single band of protein with the expected molecular weight, approximately 50kDa (*Sb*FSR plus thioredoxin-his_{10} tag) migrated on a 15% SDS–PAGE gel, as expected from theoretical calculations (Fig. 1D). The fractions containing *Sb*FSR were reddish brown, and the UV–visible spectra showed the typical spectral features of an oxidized 2Fe-2S protein in the UV–visible region, with maximum absorption peaks at 340nm and 451nm (Fig. 1C). The sequence of SbFSR shows identities of 35% to FhuF (*Escherichia coli* K-12) and 22% to FchR (*Alkalihalophilus pseudofirmus*). It has an identical cluster binding motif sequence ($\text{C-C-x}_{10}\text{-C-x}_2\text{-C}$) and a structure prediction using AlphaFold2, shows overall folding conservation when compared to FhuF [45]. However, *Sb*FSR contains three extra α-helices and a longer N-terminal loop (Supplementary Information, Figure S1) which may contribute to the observed protein instability.

The structure of SbSIP reveals a distinct electrostatic surface potential

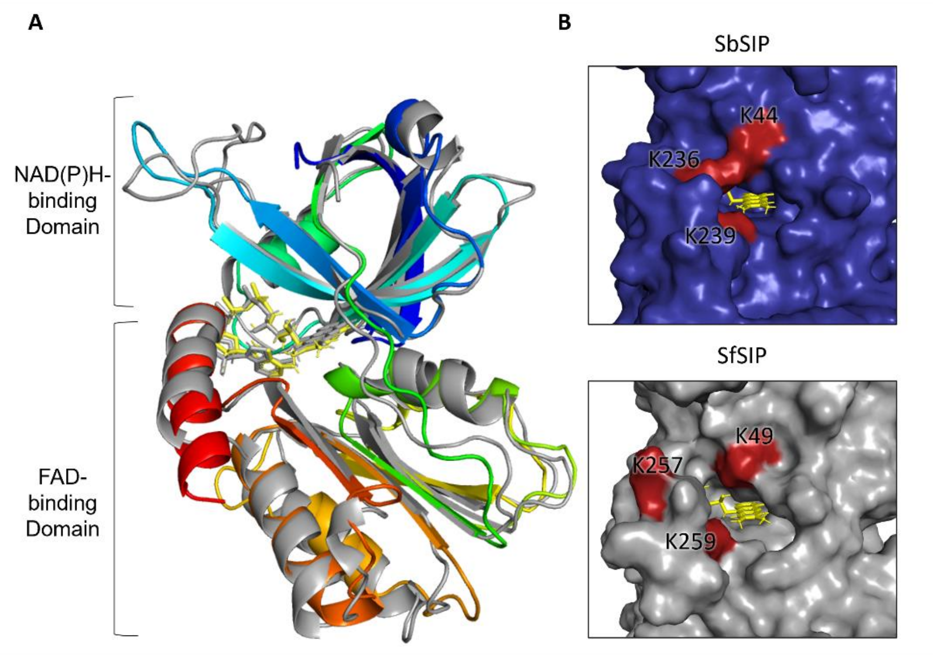

Figure IV-**2** Structural characterization of *Sb*SIP.**A)** Structure of *Sb*SIP (blue to red from the N′ to the C′ terminal) versus *Sf*SIP (gray, PDB 6GEH) aligned with PyMOL **B)** Molecular surfaces of *Sb*SIP and *Sf*SIP highlighting the lysine triad [46].

The structure of *Sb*SIP was determined at 1.9 Å resolution (Figure 2, Table 2). As previously described for other SIPs, the structure revealed two domains: N-terminal or NAD(P)H-binding and C-terminal or FAD-binding domain. The NAD(P)H-binding domain consists of the typical β1– α1– β2 Rossman fold architecture composed of a manifold of β-antiparallel-strands (β1– β6) and two short α-helices (α1 and η1). The FAD-binding domain is composed of five antiparallel β -strands (β7– β11) with two short α-helices (α2 and α3) connecting the long loops.

Table IV-**2** Final refinement statistics of *Sb*SIP.

Resolution limits (Å)	62.71 – 1.86 (1.90 – 1.86)
R-factor (%) [a]	16.9 (20.0)
nr.reflections	46650
Free R-factor (%) [b]	17.4 (27.6)
nr. reflections	2412
Overall coordinate error estimate (Å) [c]	0.17
Model composition	
Non-hydrogen protein atoms	3826
Solvent molecules	323
FAD ligand	106
Model r.m.s. deviations from ideality	
Bond lengths (Å)	0.012
Bond angles (º)	1.15
Chiral centers (Å^3)	0.063
Planar groups (Å)	0.012
Model completeness and validation	
Regions omitted	1-3 and 247-251 in chain A
	1-5 and 249-251 in chain B
Mean B values (Å^2) [d]	
protein	39.0
solvent molecules	39.4
FAD ligand	28.6
Ramachandran plot statistics.	
Residues in:	
most favored regions (%)	96.3
allowed regions (%)	3.7
disallowed regions (%)	0.0
Rotamer outliers (%)	1.2
C^{β} outliers	0.0
Clash Score	2.05
Molprobity Score	1.29

[a] R-factor = $\Sigma_{hkl} ||F_o|-|F_c|| / \Sigma_{hkl} |F_o|$, where $|F_o|$ and $|F_c|$ are the observed and calculated structure factor amplitudes, respectively; [b] Free R-factor is the cross-validation R-factor computed from a randomly chosen subset of 5% of the total number of reflections, which were not used during the refinement.; [c] Maximum-likelihood estimate with PHENIX; [d] Calculated from the equivalent isotropic B values.

The FAD shows a planar conformation, and it is stabilized through aromatic stacking interactions of the isoalloxazine ring with Tyr-60, and Tyr-225 and hydrogen bonds with residues Thr-61 (backbone O and N), Tyr-59 (side chain OH), Val-75 (backbone N), and Asp-73 (backbone O). The negatively charged phosphate groups from the FAD group are also stabilized through hydrogen bonds with Thr-60 (backbone N), Glu-232 (backbone N), His-77 (side chain N$\varepsilon 2$), Gly-81 (backbone N), Ser-84 (Side chain Oγ), Ala-83 (backbone N). The triad of basic amino-acid residues (Lys-45, Lys-236, and Lys-239 in SIP from *S. putrefaciens*) that has been proposed to form the Fe(III)-siderophore binding pocket is well-conserved (Lys-44, Lys-236 and Lys-239 in *Sb*SIP). As previously observed for *Sp*SIP, Lys-44 forms a ridge with Lys-236, making the access to the FAD cofactor smaller when compared to *Sf*SIP. Despite our best efforts, which included co-crystallization and protein NMR assignment experiments, the binding site for both ferric-siderophores and electron donors in SIPs remains open for discussion. Sequence alignment with previously characterized SIPs shows 82% identity with *Sp*SIP (PDB code 2GPJ), 31% with FscN (PDB code 4YHB), 30% with *Sf*SIP (PDB code 6GEH), and 28% with YqjH (no structure available). Indeed, when superimposing the structure of *Sb*SIP and *Sf*SIP, very few differences are observed. Surprisingly, the visualization of the electrostatic surface potential of these two proteins argues for remarkable differences (Figure 3). Both *Sb*SIP and *Sf*SIP contain very positively charged pockets that provide access to the FAD cofactor through the isoalloxazine ring. However, the pocket of *Sb*SIP is substantially smaller when compared to *Sf*SIP. Also, in *Sf*SIP it seems that the FAD cofactor is accessible through the negatively charged phosphate groups and the pocket surface that surrounds it is still positively charged allowing NAD(P)H the possibility of binding through both sides. In *Sb*SIP, the access through the negatively charged phosphate groups seems more limited, and the electrostatic surface is negatively charged. It is likely that these differences in access to the FAD cofactor are the key selection factors to discriminate redox partners, including Fe(III)-siderophores and electron donors.

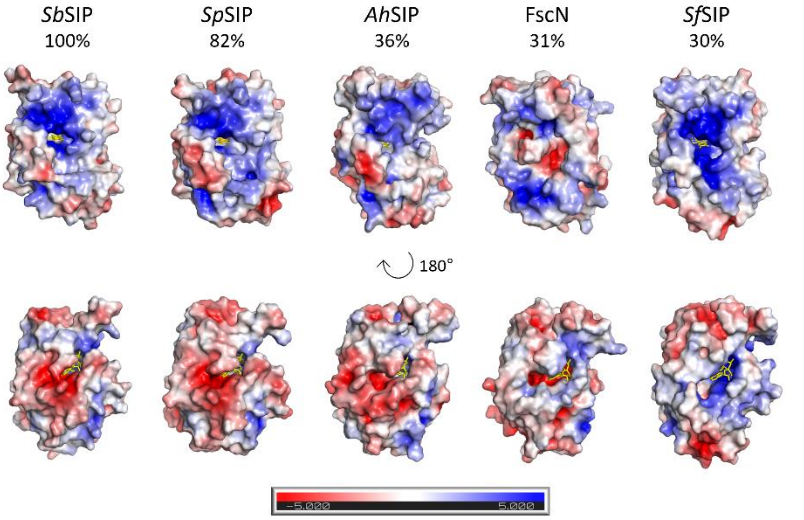

Figure IV-**3** Electrostatic surface potential (−5 to +5 kT/e) of various SIPs, from *S. bicestrii* (PDB XXXX), *S. putrefaciens* (*Sp*SIP, PDB 2GPJ), *Aeromonas hydrophila* (*Ah*SIP PDB 6K2L), *S. frigidimarina* (*Sf*SIP PDB 6GEH), and *T. fusca* (FscN 4YHB).The surfaces are shown from most similar to least similar (left to right) in the same orientation. The top row highlights the access through the isoalloxazine ring and the bottom all surfaces after a 180º rotation to the left. Surfaces were calculated using the APBS plugin in PyMOL [47].

*Sb*SIP performs proton-coupled electron transfer

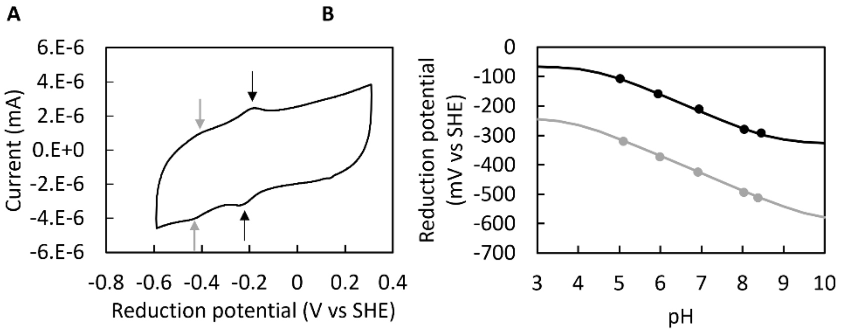

Figure IV-**4** *Sb*SIP voltammetry experiments: A) representative voltammogram of *Sb*SIP, pH 7, at 100mV.s^{-1}. B) pH dependence of reduction potentials of *Sb*SIP with solid line representing the respective simulations

.

Flavin are redox centers that can couple one and two electron transfer with proton transfer and this ability can be studied using protein film voltammetry (PFV). *Sb*SIP presents two well-defined voltammetric signals (Figure 4 A) and the midpoint potentials of these signals are reported in Table 1. This voltammetric response shows significant differences from previously characterized *Sf*SIP where only one voltammetric signal was reported [20]. Overall, from the reduction potentials obtained it is likely that one of the signals corresponds to the transition between the oxidized and semiquinone state, and the other signal corresponds to the transition from the semiquinone to the hydroquinone state. The appearance of this later signal once again highlights the differences found in the surface of *Sb*SIP vs *Sf*SIP which can dictate interactions with the electrode surface and its access to the FAD cofactor. However, the remaining data shows comparable results to *Sf*SIP: one of the reduction potentials obtained is very similar (-210 mv vs SHE at pH 7 for *Sb*SIP and -228mV vs SHE at pH 7, for *Sf*SIP, Table 3); *Sb*SIP also a presents redox-Bohr effect extending throughout all the physiological pH range, with predicted pK_{ox} lower than 4.5 and pK_{red} higher than 8.5 (Figure 4B).

Table IV-**3** pH dependence of the mid-point reduction potentials of *Sb*SIP. Values are averages of two experiments and respective standard error of the mean (SEM).

pH	E1(1/2)(V vs SHE)	E2 (1/2)(V vs SHE)
5.02	-0.106 ± 1.2	-0.315 ± 4.5
5.94	-0.163 ± 3.7	-0.368 ± 5.2
6.94	-0.214 ± 4.0	-0.422 ± 2.5
8.04	-0.280 ± 0.5	-0.492 ± 1.5
8.46	-0.294 ± 2.2	-0.510 ± 2.5

*Sb*SIP discriminates NADH from NADPH

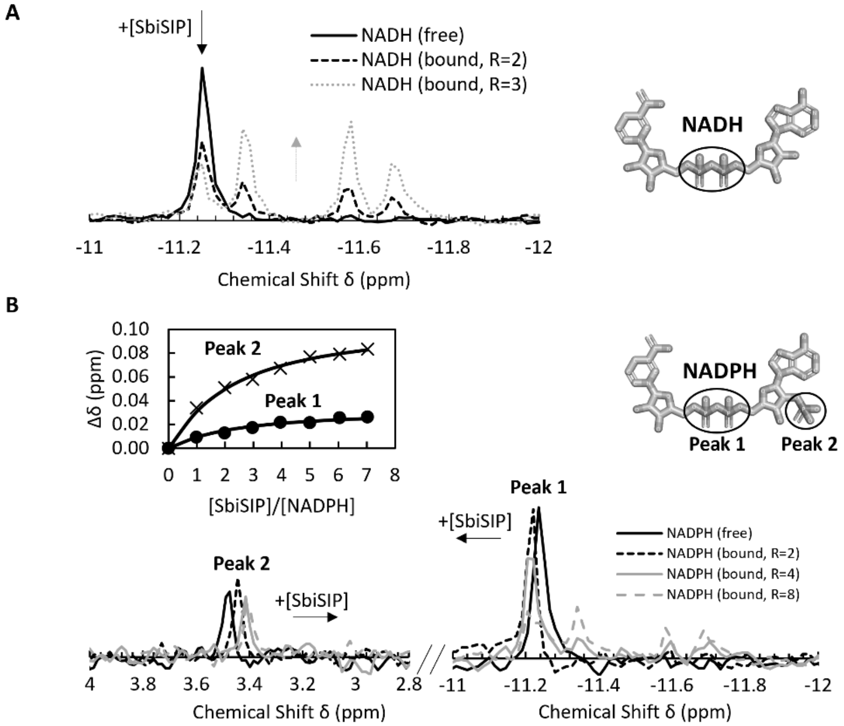

Figure IV-**5** ^{31}P NMR binding experiments of NAD(P)H versus *Sb*SIP. **A)** Proton-decoupled spectra corresponding to 100µM of NADH and changes with increasing amounts of *Sb*SIP. **B)** 57 µM of NADPH and changes with increasing amounts of *Sb*SIP. Insert shows binding curve monitoring the chemical shift perturbation.

Upon mixing *Sb*SIP with NADH and NADPH significant chemical shift changes (Figure 5 A and B) were observed in the ^{31}P spectra of these compounds. *Sb*SIP interacts with NAD(P)H, in agreement with previously characterized SIPs. In the NMR timescale, binding of NADH to *Sb*SIP occurs in the slow-exchange regime since resonances for the free and bound states coexist, while for NADPH this occurs in the fast-exchange regime. This is coherent with the one-order-of-magnitude difference between the dissociation constants found for NADH and NADPH, of 17µM and 107µM, respectively. Both dissociation constants are consistent with transient interactions, although there is a clear preference of *Sb*SIP for NADH. This shows that the electrons used to reduce this enzyme come predominantly from the bacterial catabolic metabolism This is in contrast with the previously characterized SIP from *S. frigidimarina* (*Sf*SIP) which does not discriminate between NADH and NADPH with affinities of approximately 20 µM for both. Another contrasting feature is the fact that for *Sb*SIP the 2' phosphate signal is perturbed upon binding whereas this did not happen for *Sf*SIP. The comparison between the FAD access pockets of *Sb*SIP and *Sf*SIP shows that the access to the FAD pocket in *Sb*SIP is smaller. Considering that binding likely occurs near the isoalloxazine ring to facilitate electron transfer, this explains the lower affinity for NADPH and the perturbation of the 2' phosphate signal of NADPH likely through steric clashing.

***Sb*SIP can be reduced by both NADH and NADPH**

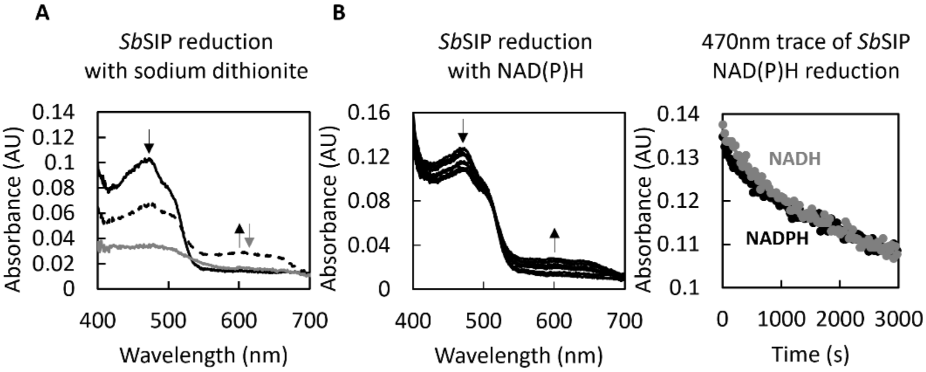

Figure IV-**6** Reduction of *Sb*SIP with various electron donors. **A)** Spectral changes observed after mixing *Sb*SIP with sodium dithionite. Arrows indicate the decrease at 470nm and increase at 600nm (semiquinone state, dashed line) and decrease at both 470nm and 600nm (hydroquinone state, in gray). **B)** Spectral changes observed after mixing *Sb*SIP with NAD(P)H and respective kinetic traces at 470nm, NADH in gray and NADPH in black.

Given the differences found for the binding of *Sb*SIP with NADPH we then explored the reactivity of this enzyme. Upon mixing excess amounts of sodium dithionite with *Sb*SIP, absorption spectral changes were characterized by a decrease at 470nm and an increase at 600nm, followed by a decrease at both 470nm and 600nm. These changes are consistent with the full reduction of *Sb*SIP in two steps, first, the formation of the semiquinone state followed by the formation of the hydroquinone state (Figure 6A).

In the presence of the oxygen scavenging system, it was also possible to observe the reduction of *Sb*SIP with NAD(P)H. Upon mixing excess amounts of NAD(P)H with *Sb*SIP, absorption spectral changes were characterized by a decrease at 470nm and an increase at 600nm. These changes are consistent with the transition of *Sb*SIP from the oxidized to the semiquinone state. Full reduction into the hydroquinone state was not observed, in agreement with the more positive potential of NAD(P)H vs the more negative voltammetric signal of *Sb*SIP (Figure 4). Despite the differences found in the ^{31}P NMR binding experiments, no significant differences were found in the reduction rate of *Sb*SIP with NAD(P)H. This likely occurs due to the use of excess reductant that allows to establish saturating conditions and therefore binding is not the rate-limiting step. The observation of reduction of *Sb*SIP by NAD(P)H in the presence of the oxygen scavenging system led us to revisit the reactivity of the previously characterized *Sf*SIP which also showed the same behavior (Supplementary data Figure S2). Interestingly, these results suggest that oxygen is an efficient inhibitor of SIPs. This provides a mechanism to avoid the deleterious effect of free ferrous iron in the cell, i.e., the production of reactive oxygen species through the Fenton reaction, by preventing the formation of ferrous iron at the source.

*Sb*SIP reduces bisucaberin and putrebactin slower than *Sf*SIP

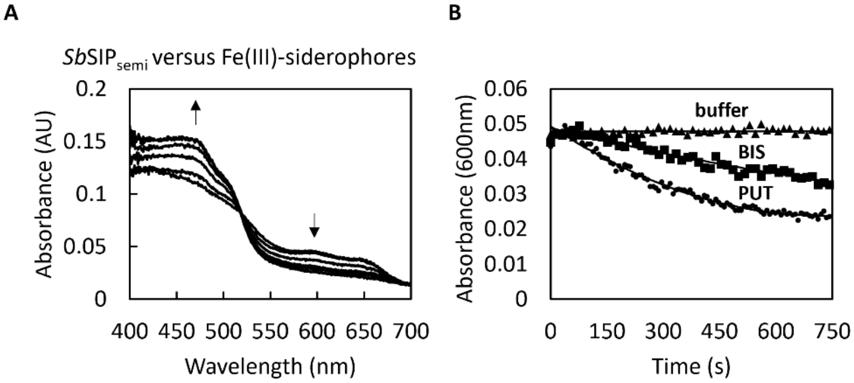

Figure IV-**7** Fe(III)-siderophore reduction by *Sb*SIP. **A)** Absorption spectra changes after mixing *Sb*SIP$_{semi}$ with Fe(III)-siderophore bisucaberin. Up arrow indicates the increase in absorbance at 470nm and the down arrow indicates the decrease in the absorbance at 600 nm. **B)** Respective kinetic traces of *Sb*SIP at 600 nm, showing the reduction of bisucaberin (BIS) and putrebactin (PUT).

The results of protein film voltammetry show that *Sb*SIP has the adequate thermodynamic properties to reduce ferric-siderophores. Therefore, its capability to perform the reaction was tested by stopped-flow kinetic assays. *Sb*SIP in the semiquinone state (*Sb*SIP$_{semi}$) was prepared using sodium dithionite. Upon mixing of *Sb*SIP$_{semi}$ with ferric siderophores (bisucaberin (BIS) and putrebactin (PUT) absorption spectra changes showed an increase at 470nm and a decrease at 600nm (Figure 2A). This is consistent with the transfer of one electron from the semiquinone flavin to the Fe(III)-siderophore yielding fully oxidized *Sf*SIP and Fe^{2+}. Fe(III)-siderophore reduction was observed and the rate constant of reduction was determined (0.0014 ± 0.0002 s^{-1} for BIS and $0.0031 \pm 5.0\text{x}10^{-5}$ s^{-1} for PUT) from the kinetic trace at 600 nm to avoid spectral interference from the Fe(III)-siderophores. The reduction rates for both Fe(III)-siderophores presented rate constants of similar magnitude however these rate constants are almost one order of magnitude lower than those found for *Sf*SIP [20]. These results were surprising given that *Sb*SIP and *Sf*SIP display very similar reduction potentials. However, they may simply reflect the structural differences found. Despite its high structural similarity to *Sf*SIP, the surface access to the FAD cofactor is substantially diminished. Given that electron transfer decays exponentially, an order of magnitude difference in electron transfer rates, as observed here, can arise from a small increase in distance, smaller than 3Å, for the productive complex as described by the Dutton-Moser rule. It is also likely that these differences highlight the tailoring of these proteins for different siderophore substrates [48,49].

Conclusion

Here we present the characterization and structure determination of a novel SIP from *S. bicestrii* (*Sb*SIP). The comparison with the previously characterized *Sf*SIP suggests that the presence of the redox-Bohr effect is a common feature of this protein class. The coupled transfer of electrons and protons in the physiological pH range is clearly advantageous for the activity of this enzyme. The redox-Bohr effect implies that the driving force for Fe(III)-siderophore reduction is enhanced at high pH, where the solubility of Fe^{3+} is low. Moreover, it ensures that iron reduction is accompanied by the release of a proton resulting in local pH reduction and enhanced Fe^{2+} solubility. With regards to the structure, *Sb*SIP revealed unexpected structural differences versus previously characterized SIPs. A smaller FAD pocket, likely reflecting the specificity for NADH and possibly a direct link to catabolism and/or preferential use of specific siderophores. Furthermore, the similar affinity for NADH to that found for *Sf*SIP reveals that it is through this positively charged pocket that binding takes place.

However, open issues remain to unravel. For example, very few studies exist regarding the exact siderophores, and corresponding Fe(III)-siderophore structures produced by the different species of *Shewanella*, or even which microorganisms form symbiotic relationships with the different *Shewanella* species. Thus, the other scenario may be that SIPs are "tailored" to specifically target xenosiderophores as observed in the case of *E. coli*'s native siderophore enterobactin. Most microorganisms do not synthesize this siderophore but nonetheless express the ferric enterobactin esterase (Fes). This is also true for some *Shewanella* species, and it could provide a means to release iron when it is complexed with enterobactin, the strongest siderophore described to date [50]. Furthermore, it is also important to reflect upon the environmental context of different *Shewanella* species including where they were isolated from and their different iron requirements. *S. frigidimarina* was isolated from the Antarctic soil bed at very cold temperatures whereas *S. bicestrii* was isolated from the warmth of the human body [23,51]. The lower access to the FAD in *Sb*SIP may have been an evolutionary adaptation to slow down the rates of siderophore reduction at the higher temperature of the *S.bicestrii* habitat. This provides a kinetic control on the production of Fe(II) that may be essential to enable the metabolism to handle this essential but potentially toxic element, while maintaining similar thermodynamic driving force. Additionally, the lower reduction rates can also be a consequence for the fact that the genome of *S. bicestrii* codes for two ferric-siderophore reductases, *Sb*SIP and *Sb*FSR, whereas the genome of *S. frigidimarina* only codes for *Sf*SIP. Again, kinetic control of the relative activities of the two enzymes may be important in the metabolic regulation of the handling of iron, which operates on a much faster response time scale than transcriptional regulation. Nonetheless, it is also possible that the binding of siderophores is affected by temperature, either with respect to their affinity to *Sb*SIP or due to the temperature dependence of speciation equilibria which changes iron availability.

Overall, this study reveals a previously unseen specificity for siderophore-interacting proteins. It also highlights how the physicochemical context of iron availability together with the ecological community that surrounds it constitute key factors shaping the function of these enzymes. These factors are now ripe for exploration and will likely be the make-it-or-break-it in the context of using these enzymes as targets to combat bacterial infections and antimicrobial resistance.

Acknowledgements

The authors are grateful to Anaísa Coelho for teaching the SLIC methodology and to Maria Firmino for providing us with the sequences for *sip* and *fsr* genes of *S. bicestrii*, to Filipe Rollo for the assistance with the crystallization robot, to Masaki Fujita for kindly providing the Fe(III)-siderophores putrebactin and bisucaberin, and to Filipe Folgosa for sharing the oxygen-scavenging recipe with us. The X-ray diffraction data collections were performed at XALOC beamline at ALBA Synchrotron with the collaboration of ALBA staff. This work benefited from access to CERMAX, ITQB-NOVA, Oeiras, Portugal with equipment funded by FCT, project AAC 01/SAICT/2016. Financial support was provided by European EC Horizon2020 TIMB3 (Project 810856). Financial support was also provided by Project MOSTMICRO-ITQB with refs UIDB/04612/2020 and UIDP/04612/2020. Fundação para a Ciência e a Tecnologia (FCT) Portugal is also acknowledged for funding through project PTDC/BIA-BQM/30176/2017, and through FCT PT-NMR PhD Program via PD/BD/135187/2017 to IBT.

References

[1] C. Andreini, I. Bertini, G. Cavallaro, G.L. Holliday, J.M. Thornton, Metal ions in biological catalysis: From enzyme databases to general principles, JBIC. 13 (2008) 1205–1218.

[2] K.J. Waldron, J.C. Rutherford, D. Ford, N.J. Robinson, Metalloproteins and metal sensing, Nature. 460 (2009) 823–830.

[3] M. Ilbert, V. Bonnefoy, Insight into the evolution of the iron oxidation pathways, Biochim Biophys Acta. 1827 (2013) 161–175.

[4] J.J.R.F., Silva, R.J.P. Williams, The Biological Chemistry of the Elements, Oxford University Press, 2001.

[5] A. Kappler, C. Bryce, M. Mansor, U. Lueder, J.M. Byrne, E.D. Swanner, An evolving view on biogeochemical cycling of iron, Nat Rev Microbiol. 19 (2021) 360–374.

[6] R.C. Hider, X. Kong, Chemistry and biology of siderophores, Nat Prod Rep. 27 (2010) 637–657.

[7] S.D. Springer, A. Butler, Microbial ligand coordination: Consideration of biological significance, Coord. Chem. Rev. 306 (2016) 628–635.

[8] B.R. Wilson, A.R. Bogdan, M. Miyazawa, K. Hashimoto, Y. Tsuji, Siderophores in Iron Metabolism: From Mechanism to Therapy Potential, Trends Mol. Med. 22 (2016) 1077–1090.

[9] M. Miethke, M.A. Marahiel, Siderophore-Based Iron Acquisition and Pathogen Control, Microbiol Mol Biol Rev. 71 (2007) 413–451.

[10] B. Schink, Extracellular Redox Chemistry, in: Metals, Microbes, and Minerals - The Biogeochemical Side of Life, De Gruyter, 2021: pp. 33–58.

[11] I.B. Trindade, E. Moe, R.O. Louro, Siderophore-Interacting Protein, in: EIBC, Wiley, 2020: pp. 1–12.

[12] C.M. Paquete, G. Rusconi, A. v. Silva, R. Soares, R.O. Louro, A brief survey of the “cytochromome,” Adv. Microb. Physiol. 75 (2019) 69–135.

[13] R.O. Louro, N.L. Costa, A.P. Fernandes, A.V. Silva, I.B. Trindade, B.M. Fonseca, C.M. Paquete, Exploring the molecular mechanisms of extracellular electron transfer for harnessing reducing power in METs: Methodologies and approaches, in: Biomass, Biofuels, Biochemicals: Microbial Electrochemical Technology: Sustainable Platform for Fuels, Chemicals and Remediation, Elsevier, 2018: pp. 261–293.

[14] D. Ghosal, M. v. Omelchenko, E.K. Gaidamakova, V.Y. Matrosova, A. Vasilenko, A. Venkateswaran, M. Zhai, H.M. Kostandarithes, H. Brim, K.S. Makarova, L.P. Wackett, J.K. Fredrickson, M.J. Daly, How radiation kills cells: Survival of *Deinococcus radiodurans* and *Shewanella oneidensis* under oxidative stress, FEMS Microbiol. Rev. 29 (2005) 361–375.

[15] L. Gram, Siderophore-mediated iron sequestering by *Shewanella putrefaciens*, Appl Environ Microbiol. 60 (1994) 2132–2136.

[16] K. Chakraborty, V.K. Kizhakkekalam, M. Joy, Macrocyclic polyketides with siderophore mode of action from marine heterotrophic *Shewanella algae*: Prospective anti-infective leads attenuate drug-resistant pathogens, J. Appl. Microbiol. 130 (2021) 1552–1570.

[17] L. Liu, W. Wang, S. Wu, H. Gao, Recent Advances in the Siderophore Biology of *Shewanella*, Front. Microbiol. 13 (2022).

[18] S. Rütschlin, S. Gunesch, T. Böttcher, One Enzyme, Three Metabolites: *Shewanella algae* Controls Siderophore Production via the Cellular Substrate Pool, Cell Chem. Biol. 24 (2017) 598–604.

[19] K. Li, W.H. Chen, S.D. Bruner, Structure and Mechanism of the Siderophore-Interacting Protein from the Fuscachelin Gene Cluster of *Thermobifida fusca*, Biochemistry. 54 (2015) 3989–4000.

[20] I. Trindade, J.M. Silva, B.M. Fonseca, T. Catarino, M. Fujita, P.M. Matias, E. Moe, R.O. Louro, Structure and reactivity of a siderophore-interacting

protein from the marine bacterium *Shewanella* reveals unanticipated functional versatility, J. Biol. Chem. 294 (2018) 157–167.

[21] J.M. Janda, S.L. Abbott, The genus *Shewanella*: From the Briny Depths Below To Human Pathogen, Crit. Rev. Microbiol. 7828 (2012) 1–21.

[22] K.M. Ledyard, A. Butler, Structure of putrebactin, a new dihydroxamate siderophore produced by *Shewanella putrefaciens*, J. Biol. Inorg. Chem. 2 (1997) 93–97.

[23] A. Jousset, L. Dabos, R. Bonnin, D. Girlich, A. Potron, N. Cabanel, L. Dortet, P. Glaser, T. Naas, CTX-M-15-Producing *Shewanella* sp Clinical Isolate Expressing OXA-535, a Chromosome-Encoded OXA-48 Variant, Putative Progenitor of the Plasmid-Encoded OXA-436, Antimicrob. Agents Chemother. 62 (2018) 1879–1896.

[24] I.B. Trindade, B.M. Fonseca, P.M. Matias, R.O. Louro, E. Moe, A putative siderophore-interacting protein from the marine bacterium *Shewanella frigidimarina* NCIMB 400: cloning, expression, purification, crystallization and X-ray diffraction analysis, Acta Crystallogr F Struct Biol Commun. 72 (2016) 667–671.

[25] J. Scholz, H. Besir, C. Strasser, S. Suppmann, A new method to customize protein expression vectors for fast, efficient and background free parallel cloning, BMC Biotechnol. 13 (2013) 1–11.

[26] P. Macheroux, UV-visible spectroscopy as a tool to study flavoproteins, in: Methods in Molecular Biology, 1999: pp. 1–7.

[27] C. Vonrhein, C. Flensburg, P. Keller, A. Sharff, O. Smart, W. Paciorek, T. Womack, G. Bricogne, Data processing and analysis with the autoPROC toolbox, Acta Crystallogr. D Biol. Crystallogr. 67 (2011) 293–302.

[28] W. Kabsch, XDS, Acta Crystallogr. D Biol. Crystallogr. 66 (2010) 125–132.

[29] P. Evans, Scaling and assessment of data quality, Acta Crystallogr. D Biol. Crystallogr. 62 (2006) 72–82.

[30] P.R. Evans, G.N. Murshudov, How good are my data and what is the resolution?, Acta Crystallogr. D Biol. Crystallogr. 69 (2013) 1204–1214.

[31] M.D. Winn, C.C. Ballard, K.D. Cowtan, E.J. Dodson, P. Emsley, P.R. Evans, R.M. Keegan, E.B. Krissinel, A.G.W. Leslie, A. McCoy, S.J. McNicholas, G.N. Murshudov, N.S. Pannu, E.A. Potterton, H.R. Powell, R.J. Read, A. Vagin, K.S. Wilson, Overview of the CCP4 suite and current developments, Acta Crystallogr. D Biol. Crystallogr. 67 (2011) 235–242.

[32] E. Potterton, P. Briggs, M. Turkenburg, E. Dodson, A graphical user interface to the CCP4 program suite, Acta Crystallogr. D Biol. Crystallogr. D59 (2003) 1131–1137.

[33] K. Cowtan, The Buccaneer software for automated model building. 1. Tracing protein chains, Acta Crystallogr. D Biol. Crystallogr. 62 (2006) 1002–1011.

[34] G.N. Murshudov, P. Skubák, A.A. Lebedev, N.S. Pannu, R.A. Steiner, R.A. Nicholls, M.D. Winn, F. Long, A.A. Vagin, REFMAC5 for the refinement of macromolecular crystal structures, Acta Crystallogr. D Biol. Crystallogr. 67 (2011) 355–367.

[35] P.V. Afonine, R.W. Grosse-Kunstleve, N. Echols, J.J. Headd, N.W. Moriarty, M. Mustyakimov, T.C. Terwilliger, A. Urzhumtsev, P.H. Zwart, P.D. Adams, Towards automated crystallographic structure refinement with phenix.refine, Acta Crystallogr. D Biol. Crystallogr. 68 (2012) 352–367.

[36] P. Emsley, B. Lohkamp, W.G. Scott, K. Cowtan, Features and development of Coot, Acta Crystallogr. D Biol. Crystallogr. 66 (2010) 486–501.

[37] A. Brünger, Free R value: a novel statistical quantity for assessing the accuracy of crystal structures, Nature. 355 (1992) 472–475.

[38] V.B. Chen, W.B. Arendall, J.J. Headd, D.A. Keedy, R.M. Immormino, G.J. Kapral, L.W. Murray, J.S. Richardson, D.C. Richardson, MolProbity: All-atom structure validation for macromolecular crystallography, Acta Crystallogr. D Biol. Crystallogr. 66 (2010) 12–21.

[39] S. Velankar, C. Best, B. Beuth, PDBe: protein data bank in Europe, Nucleic Acids Res. Spec. Publ. 38 (2010) 308–317.

[40] K. Diederichs, P.A. Karplus, Improved R-factors for diffraction data analysis in macromolecular crystallography, Nature. 4 (1997) 269–276.

[41] B.W. Matthews, Solvent Content of Protein Crystals, J. Mol. Biol. 33 (1968) 491–497.

[42] E.P. Friis, J.E.T. Andersen, L.L. Madsen, N. Bonander, P. Moller, J. Ulstrup, Dynamics of *Pseudomonas aeruginosa* azurin and its Cys3Ser mutant at single-crystal gold surfaces investigated by cyclic voltammetry and atomic force microscopy, Electrochim. Acta. 43 (1998) 1114–1122.

[43] B.M. Fonseca, C.M. Paquete, S.E. Neto, I. Pacheco, C.M. Soares, R.O. Louro, Mind the gap: cytochrome interactions reveal electron pathways across the periplasm of *Shewanella oneidensis* MR-1, Biochem. 449 (2013) 101–108.

[44] F. Folgosa, M.C. Martins, M. Teixeira, The multidomain flavodiiron protein from *Clostridium difficile* 630 is an NADH:oxygen oxidoreductase, Sci. Rep. 8 (2018) 1–13.

[45] J. Jumper, R. Evans, A. Pritzel, T. Green, M. Figurnov, O. Ronneberger, K. Tunyasuvunakool, R. Bates, A. Žídek, A. Potapenko, A. Bridgland, C. Meyer, S.A.A. Kohl, A.J. Ballard, A. Cowie, B. Romera-Paredes, S. Nikolov, R. Jain, J. Adler, T. Back, S. Petersen, D. Reiman, E. Clancy, M. Zielinski, M. Steinegger, M. Pacholska, T. Berghammer, S. Bodenstein, D. Silver, O. Vinyals, A.W. Senior, K. Kavukcuoglu, P. Kohli, D. Hassabis, Highly accurate protein structure prediction with AlphaFold, Nature. 596 (2021) 583–589.

[46] W.L. DeLano, The PyMOL Molecular Graphics System, Version 2.3. New York, NY: Schrödinger LLC., (2020).

[47] N.A. Baker, D. Sept, S. Joseph, M.J. Holst, J. Andrew McCammon, Electrostatics of nanosystems: Application to microtubules and the ribosome, Proc. Natl. Acad. Sci. U.S.A. 98 (2001) 10037-10041.

[48] C.C. Moser, P.L. Dutton, Engineering protein structure for electron transfer function in photosynthetic reaction centers, Biochim Biophys Acta Bioenerg. 1101 (1992) 171–176.

[49] M. Ubbink, The courtship of proteins: Understanding the encounter complex, FEBS Lett. 583 (2009) 1060–1066.

[50] V. Gasser, L. Kuhn, T. Hubert, L. Aussel, P. Hammann, I.J. Schalk, The Esterase PfeE, the Achilles’ Heel in the Battle for Iron between *Pseudomonas aeruginosa* and *Escherichia coli*, Int. J. Mol. Sci. 22 (2021) 1–17.

[51] N. Bozal, M.J. Montes, E. Tudela, F. Jiménez, J. Guinea, *Shewanella frigidimarina* and *Shewanella livingstonensis* sp. nov. isolated from Antarctic coastal areas, Int. J. Syst. Evol. Microbiol. 52 (2002) 195–205.

“Shu-ha-ri –

shu (to obey the form),

ha (to break the form),

and ri (to transcend the form).”

Budo concept

V. Chapter V: PRE-driven Protein NMR Structures - an alternative paradigm in Highly Paramagnetic Systems

This chapter was published as and incorporates the following publications:

Trindade, I.B., Invernici, M., Cantini, F., Louro, R.O. & Piccioli, M. (2021) PRE-driven Protein NMR Structures: an Alternative Approach in Highly Paramagnetic Systems. FEBS Journal. 288: 3010–3023.3.

Trindade, I.B., Invernici, M., Cantini, F., Louro, R.O. & Piccioli, M. (2020) NOE-less protein structures-an alternative paradigm in Highly Paramagnetic Systems. arXiv 13–16.

Trindade, I.B., Invernici, M, Cantini, F., Louro, R.O. & Piccioli, M. (2020) ^{1}H, ^{13}C and ^{15}N assignment of the paramagnetic high potential iron–sulfur protein (HiPIP) PioC from *Rhodopseudomonas palustris* TIE-1. Biomol NMR Assign 14:211–215.

Trindade, I.B., Invernici, M., Cantini, F., Louro, R.O. & Piccioli, M (2021) Sequence-specific assignments in NMR spectra of paramagnetic systems: A non-systematic approach. Inorganica Chim. Acta 514:1-8.

The author of this dissertation participated in all experiments described in this chapter except ^{13}C-direct experiments.

Abstract

Metalloproteins play key roles across biology, and knowledge of their structure is essential to understand their physiological role. For those metalloproteins containing paramagnetic states, the enhanced relaxation caused by the unpaired electrons often makes signal detection unfeasible near the metal center, precluding adequate structural characterization right where it is more biochemically relevant. Here, we report a protein structure determination by NMR where two different sets of restraints, one containing Nuclear Overhauser Enhancements (NOEs) and another containing Paramagnetic Relaxation Enhancements (PREs), are used separately and eventually together. The protein PioC from *Rhodopseudomonas palustris* TIE-1 is a High Potential Iron-Sulfur Protein (HiPIP) where the [4Fe-4S] cluster is paramagnetic in both oxidation states at room temperature providing the source of PREs used as alternative distance restraints. Comparison of the family of structures obtained using NOEs only, PREs only, and the combination of both reveals that the pairwise root-mean-square deviation (RMSD) between them is similar and comparable with the precision within each family. This demonstrates that, under favorable conditions in terms of protein size and paramagnetic effects, PREs can efficiently complement and eventually replace NOEs for the structural characterization of small paramagnetic metalloproteins and de novo-designed metalloproteins by NMR.

Introduction

Metalloproteins represent 40 to 47% of all known enzymes [1,2] and, for all of them, the metal center(s) are essential for catalysis, electron transfer, and metal storage/transport, or they play a crucial role in determining stability and structural properties [3–12].

Structural biologists are mainly interested in obtaining detailed information in the proximity of the metal center(s), where the biochemically relevant events occur.

NMR is a privileged approach for characterizing metalloproteins since it can provide the structure in solution at atomic resolution, information about the amplitudes and time-scales of internal dynamics [13–15], as well as hints on the electronic structure and oxidation states of the metal center [16] in conditions that mimic the physiological context. A significant part of the metalloproteome contains paramagnetic metal ions. Their presence perturbs the chemical shift and relaxation of NMR signals in ways that can be converted into structural and dynamic information [17,18]. Early attempts to convert paramagnetic nuclear relaxation rates in NMR restraints and include them into solution structure protocols achieved the first solution structures of paramagnetic proteins [19]. The introduction of residual dipolar couplings (RDCs) arising from self-oriented paramagnetic proteins [20] combined with pseudocontact shifts (PCS) and crosscorrelation rates (CCR) succeeded, in the case of cytochrome c', to obtain the first backbone structure of a protein in the absence of NOE measurements [21] and, at the same time, opened the possibility to use orientational restrains also in diamagnetic proteins. Nitroxide radicals used as site-directed spin labels allowed the conversion of Paramagnetic Broadening Effects into distance restraints for large molecular weight proteins [22]. This work led to the introduction of the 'concept' of Paramagnetic Relaxation as long-range restraints for non-native metalloproteins and the acronym PRE (Paramagnetic Relaxation Enhancements) was coined [23]. Since they are long-range constraints, PREs are a good alternative/complement to RDCs to obtain solution structures when NOES and scalar couplings are unable/insufficient to define the structure. Extrinsic paramagnetic centers can be attached via conjugation to specific, solvent-exposed sites [24] and, indeed, the use of PRE soon flourished.

Macromolecular structures using PRE data have been characterized not only for soluble proteins [23,25], but also for protein–protein [26–28] and protein–nucleic acid complexes [29–31], membrane proteins [32], unfolded, or partially unfolded states [33–36], proteins in living cells [37,38]. Also in solid state protein NMR spectroscopy, PREs coupled with PCS [39,40] provided accurate solid-state structures in the absence of conventional distance or dihedral angle restraints [41,42] as well as information on the oligomerization interface of large membrane proteins [43]. Actually, applications of PREs go beyond their use as structural constraints for obtaining 'static' NMR structures: They may unravel structural information on transient, invisible, intermediates [44] and provide information on encounter complexes [45–47], interdomain motions [48], transient protein associations [49–51], nonspecific protein–DNA interactions [52] and also in drug discovery [53–56]. However, several aspects, such as the accuracy of PRE data [57] and the weak correlation observed between distance derived PREs and those found in crystallographic structures [58,59] deserve further investigations. For example, it has been shown for lanthanide ions that magnetic anisotropy provides a substantial angular dependence of nuclear relaxation rates [60,61]. Nonspecific intermolecular PREs and crosscorrelations between Curie Spin Relaxation and dipolar spin–spin couplings [62,63] might be responsible for the deviation of paramagnetic relaxation rates from the r^{-6} dependency (r being the metal-to-nucleus distance)[58]. These factors limit the accuracy of PREs especially at longer metal-to-proton distances; on the other hand, at shorter metal-to-proton distances, the paramagnetism-induced line broadening prevents the detection of NMR signals limiting the information available at the close proximity of the paramagnetic center. For the above reasons, small-sized metalloproteins are interesting cases to study the behavior of paramagnetic relaxation when the paramagnetic center is not affected by local mobility and represents the crucial part of the protein. Moreover, tailored experiments increased the availability of PRE values also at shorter metal-to-nucleus distances [64]. In these conditions, PREs are usable not only as long-range restraints but also as medium and short-range restraints. A $[Fe_4S_4]^{2+}$ cluster possesses a negligible magnetic anisotropy, and it is buried within the protein. These rules out the many effects that give rise to relaxation anisotropy. Therefore, PioC, a small (54 aa residues) HiPIP (High Potential Iron Protein) from *R. palustris* TIE-1 represents a peculiar and interesting system to assess nuclear relaxation properties, analyze the relative contribution of NOE and PREs and discuss the use of PREs as alternative to NOE for the portion of the protein where the presence of paramagnetic metal ions poses a challenge for the detection of classical structural restraints and even for signal detection [21]. The interplay between NOEs and paramagnetism-based restraints has been addressed by many groups, and there are many evidences of the fact that the replacement of NOEs with other restraints is feasible, when the alternative restraints considered, arise from different complementary sources [65–68]. Sparse NOE and chemical shifts can be used together with sophisticated modeling methods to obtain well-defined solution structures [69,70]. Protein structures have also been determined without NOEs using orientational restraints from at least two full sets of RDC [21,71–73]. Tagging a protein with lanthanide ions at four different sites succeeded to obtain a backbone structure without NOEs [74], whereas the use of different lanthanide ions on a single metal center required a minimal number of NOEs to obtain a structure [75]. A backbone structure was obtained using a combination of PRE, RDC, PCS, CCR, and backbone NOEs, which were used to properly define α helices [76]. Paramagnetic Relaxation Enhancements (PRE) are dipole–dipole restraints, like NOEs. Therefore, if a sufficient number of PRE restraints are available throughout the entire protein, they should restrain the conformational space with efficiency comparable to NOEs, even when, like in a metalloprotein, the distance restraints all involve a single point, that is, the native paramagnetic center of the system. To explore these issues, the NMR solution structure of the small iron–sulfur protein PioC from *R. palustris* TIE-1 [77] was pursued as a paradigmatic challenge. PioC mediates the electron transfer between the reaction center and the iron-oxidase in the photoferrotrophic metabolism of *R. palustris* TIE-1. It contains a [4Fe-4S] cluster with a very high reduction potential (E0 = +450 mV vs SHE), being stable in the $[Fe_4S_4]^{2+}$ oxidation state. With 54 amino acids, it is the smallest HiPIP ever isolated. Its 3D structure is unknown, but homology modeling with other HiPIPs suggests that the protein has a compact globular structure, characterized by the absence of topologically relevant secondary structure elements; it is instead predicted to be composed essentially by a series of loops and turns wrapped around the [4Fe-4S] cluster [78,79]. The electronic properties of $[Fe_4S_4]^{2+}$ in HiPIPs have been studied in detail over the past 40 years [3,80-88]. The magnetic coupling within the [4Fe-4S] cluster makes the electronic correlation times of the individual iron ions much shorter than isolated high spin Fe^{3+} or Fe^{2+} ion; nevertheless, paramagnetic contributions to nuclear relaxation are significant for nuclei within a 10Å sphere from the cluster [89,90]. Therefore, PioC is a suitable system to address an important issue for inorganic biochemistry: Is it possible to improve methods for measuring relaxation rates in paramagnetic systems to the point that PREs can be used as the sole source of restraints to define the structure of a metalloprotein?

Material and Methods

Protein expression and purification

E. coli BL21 DE3 cells were transformed with pET32h, a plasmid containing the construct thioredoxin–6xHis–thrombin cleavage site–PioC, and with pDB1281, a plasmid that carries the machinery for the assembly of iron-sulfur clusters. Cells were grown in Luria-Bertani (LB) supplemented with

100mg.dm^{-3} ampicillin and 35mg.dm^{-3} chloramphenicol until the OD$_{600nm}$ of 0.6 where they were induced with 1.0mM arabinose and 20μM FeCl$_3$ and 200μM cysteine were added. Cells were again incubated until the OD$_{600nm}$ of 1 and then harvested and washed in M9 minimal media salts before resuspension in M9 minimal media. Once re-suspended, cells were incubated for one hour before induction with 0.5mM IPTG. After 4hr cells were harvested by centrifugation and disrupted using a French Press at 1000psi. The lysate was ultra-centrifuged at 204 709g for 90 min at 4ºC to remove cell membranes and debris and the supernatant was dialyzed overnight against 50 mM Potassium Phosphate buffer pH 5.8 with 300mM NaCl before injection in a His-trap affinity column (GE Healthcare). The fraction containing Histag-PioC eluted with 250mM imidazole and was incubated overnight with Thrombin (GE Healthcare) for digestion. The final purified PioC (His-tag free) was then concentrated from the flow through of a 2nd passage through the His-trap column using an Amicon Ultra Centrifugal Filter (Millipore) with a 3kDa cutoff. The purity of PioC was confirmed by SDS-PAGE with Blue Safe staining (NzyTech) and by UV-Visible spectroscopy. Three samples of PioC were produced (unlabeled, single ^{15}N-labeled, double ^{13}C &^{15}N-labeled) and the expression and purification protocol was identical throughout except in the addition of ammonium sulfate ($^{15}N_2$, 99%) and [U-$^{13}C_6$] D-glucose in the M9 minimal media when labeling was required.

NMR experiments

All experiments were recorded using Bruker AVANCE-NEO spectrometers, equipped with cryogenically cooled triple resonance inverse detection probeheads (CP-TXI), except ^{13}C-detected experiments, which were acquired at 176.05 MHz using a cryogenically cooled probehead optimized for ^{13}C direct detection (CP-TXO), and ^{1}H experiments which were recorded at 400 MHz using a room temperature, selective 5mm ^{1}H probe without pulsed field gradients. All spectra were processed using the Bruker software TopSpin. Standard radio frequency pulses and carrier frequencies for triple resonance experiments were used. The set of NMR experiments used for sequence specific assignment, NOE collection and ^{15}N relaxation analysis is summarized in Table S1. To identify signals affected by the hyperfine interaction, tailored experiments were performed [64, 115, 118]. Experimental parameters are summarized in Table S2. Data analysis and resonances assignment were performed using CARA 1.9 [131]. The complete assignment has been submitted in BRMB entry 34487 [132].

Structure Calculations

Structure calculations were performed with the program CYANA 2.1 [133, 134]. NOEs were analyzed and converted into upper distance limits and used for manual structure calculation in CYANA 2.1. Backbone dihedral angle constraints were derived from ^{15}N, ^{13}C', ^{13}Cα,^{13}Cβ, and Hα chemical shifts, using TALOS+ and added as restraints. All structure ensembles presented here were refined with molecular dynamics using AMBER-16 [135] and force field parameters for the 4Fe4S cluster as previously described [136, 137] and validated using PDBstat and PSVS programs [138, 139]. Detailed description of the methodology used for structure calculation and refinement is reported in supplementary material.

Results and Discussion

NMR experiments currently available for measuring ^{1}H R_1 and R_2 rates [23,57] fail to provide PRE data in the proximity of the paramagnetic center, where many signals are broadened beyond detection. This limits the use of PREs in metalloproteins, in which the paramagnetic center is also the core of the protein. Recently, we developed experiments [64,91] that provided accurate ^{1}H R_1 and R_2 values in the range 50–500 s^{-1} and substantially improved the amount of PRE restraints in the close proximity of the paramagnetic center. Accurate measurements of both R_1 and R_2 rates are important to obtain reliable information on the metal-to-proton distances and to use PREs also as short-range restraints. A standard ^{15}N HSQC experiment on a PioC sample shows only 39 amide resonances out of expected 49 non-proline residues. However, a ^{15}N IR-HSQC-AP experiment, specifically designed to observe fast relaxing resonances, shows additional 10 resonances, demonstrating that all HN signals of PioC can be detected (Figure 1A).

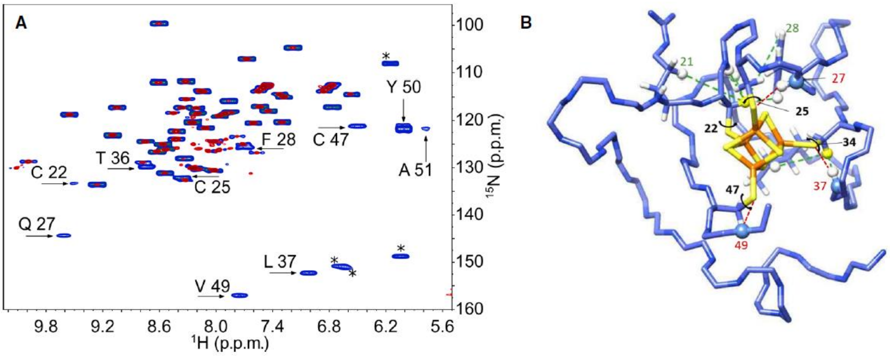

Figure V-**1 A)** 500 MHz 298K, ^{15}N-HSQC spectrum on PioC collected using the HSQC-AP experiment (blue), overlaid with a standard ^{15}N HSQC spectrum (red). Labelled signals are observable only in the HSQC-AP spectrum. Signals marked with asterisks are folded peaks arising from side chains. **B)** Cluster-derived NMR restraints: dihedral angles χ^2 of cluster-bound Cysteines (black), hydrogen bonds between HN residues and Sγ of Cysteines (red), ^{1}H NOEs between well-resolved ^{1}H βCH_2 Cys resonances and surrounding protons (green). Molecular graphics performed with UCSF Chimera.

The complete resonance assignment of the protein was obtained combining the conventional approach based on triple resonance experiments (Table S1) with a non-systematic procedure using a combination of 1D NOEs, ^{13}C direct detection, double and triple resonance experiments recorded with parameters optimized à-la-carte (Table S2) [92]. These experiments provided the complete NMR assignment of PioC (BRMB entry 34487) [93]. We assigned (excluding the N-ter Val 1) 100% of backbone ^{1}HN, ^{13}C, and ^{15}N resonances, 98% of Hα, 86% and 91% of ^{1}H and ^{13}C side chains atoms, respectively. However, even though the ^{1}H resonance were almost completely assigned, ^{15}N and ^{13}C HSQC-NOESY experiments at high magnetic field gave only 344 meaningful NOEs, that without any additional information on the [4Fe-4S] cluster binding mode, were insufficient to obtain a converged structure. Three factors quench these NOE intensities: (i) the small rotational correlation time (3.4×10^{-9} s, from ^{15}N relaxation); (ii) paramagnetic relaxation affecting at least 50% of the protein; and (iii) the absence of secondary structure elements, typical of HiPIPs. We introduced the cluster into structure calculations: bond distances and angles defining the geometry of the cubane cluster, that are not accessible via NMR, are given by introducing a special residue into the CYANA library [94], as described in Supporting Information. The introduction of the cluster gave structures with backbone and heavy atoms RMSD of 1.27 ± 0.20 Å and 1.95±0.20 Å. Indeed, the cluster is the essential structural element to drive the fold of the polypeptide chain. Paramagnetic NMR experiments provided structural constraints for cluster-binding residues (through coordinative or hydrogen bonds) crucial to define their orientation: Cys βCH_2 hyperfine shifts were converted into four χ^2 dihedral angle constraints defining the cluster binding topology according to a procedure already described [95], seven crucial 1D NOEs provided distances between Cys βCH_2 and neighboring residues (Figure S1), large ^{15}N contact shifts, observed for Gln27, Val37, and Leu49 [93] were taken as an evidence of three hydrogen bonds, respectively, linking HN to the Sγ atoms of the preceding (i-2 or i-3) cluster-bound cysteine residues [96]. Only fourteen constraints of this type are available, but they are extremely important to frame the cluster within the protein and to provide restraints where other experimental approaches fail to provide information. These cluster-derived restraints are shown in Figure 1B. When these constraints were also included into structure calculation, a well-converged structure was obtained (Figure 2A), with backbone and heavy atoms RMSD of 1.04±0.30Å and 1.81±0.30 Å (residues 5–50).

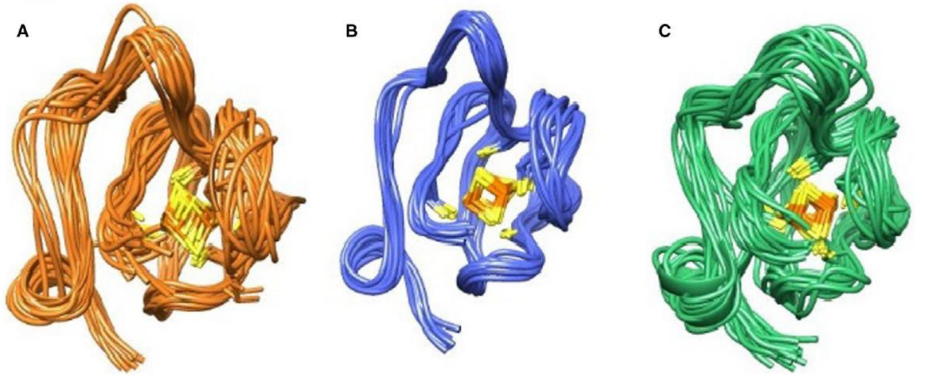

Figure V-**2** Solution structure of PioC obtained using NOEs only (orange, A), the full set of NMR restraints (blue, B), PREs only (green, C). In all cases, the families of 20 conformers were obtained from Torsion Angle Dynamics (CYANA2.1) and refinement using molecular dynamics (AMBER-16 package). Residues 5–49 are shown. Molecular graphics performed with UCSF Chimera.

We next considered the impact of PREs: To this end, we collected R_1 and R_2 values of all amide protons using the ^{15}N-IR-HSQC-AP (48 ^{1}H R_1 values) and the R2-weighted ^{15}N-HSQC-AP experiments (50 ^{1}H R_2 values) [64]. For non-exchangeable protons, a ^{13}C-IR-HSQC-AP provided R_1 values of 200 ^{1}H protons of backbone ^{1}Hα and side chains. Finally, ^{1}H and ^{13}C resonances of cluster-bound Cys residues, identified and assigned using rapid recycling experiments, provided thirteen R_1 and R_2 values from inversion recovery and linewidth analysis of one dimensional ^{1}H and ^{13}C experiments. Overall, 306 ^{1}H (amide protons plus backbone ^{1}Hα and aliphatic side chains) and 5 ^{13}C relaxation rates, amounting to ca. six rates per residue, were measured (Table S3). The behavior of HN, Hα, and Hβ rates is shown in Figure 3 and points out that about 60 % of signals are affected by the paramagnetic center. The $R_{1,2para}$ contributions are calculated according to:

1) $R_{1,2obs} = R_{1,2dia} + R_{1,2para}$

For backbone atoms, $R_{1,2dia}$ (red lines in Figure 3) were estimated from averaged values of residues 4–7, that do not belong to the flexible N-term loop (Figure S2) and are not affected by paramagnetism. For side chains protons, the R_{1dia} values were taken by considering for each type of proton, the average value obtained by considering only values within the standard deviation. Then, R1,2 para (blue histograms in Figure 3) are converted into distances (r_{MH}) according to the Solomon–Bloembergen equations [97].

2)
$$R_1 = \frac{2}{15}\left(\frac{\mu_0}{4\pi}\right)^2 \frac{\gamma_I^2 \mu_B^2 g_e^2 S(S+1)}{r_{MH}^6}\left(\frac{\tau_c}{1+(\omega_I-\omega_S)^2\tau_c^2}+\frac{3\tau_c}{1+\omega_I^2\tau_c^2}+\frac{6\tau_c}{1+(\omega_I+\omega_S)^2\tau_c^2}\right)$$

3)
$$R_2 = \frac{1}{15}\left(\frac{\mu_0}{4\pi}\right)^2 \frac{\gamma_I^2 \mu_B^2 g_e^2 S(S+1)}{r_{MH}^6}\left(4\tau_C+\frac{\tau_c}{1+(\omega_I-\omega_S)^2\tau_c^2}+\frac{3\tau_c}{1+\omega_I^2\tau_c^2}+\frac{6\tau_c}{1+(\omega_I+\omega_S)^2\tau_c^2}+\frac{6\tau_c}{1+\omega_S^2\tau_c^2}\right)$$
$$+\frac{1}{5}\left(\frac{\mu_0}{4\pi}\right)^2 \frac{\omega_I^2 \mu_B^4 g_e^4 S^2(S+1)^2}{(3kT)^2 r_{MH}^6}\left(4\tau_r+\frac{3\tau_r}{1+\omega_I^2\tau_r^2}\right)$$

In the equations, we considered $\tau_c = 6 \times 10^{-12}$s, arising from an estimated value of τ_e for each iron ion, $\tau_r = 3 \times 10^{-9}$s obtained from ^{15}N relaxation, and S = 1, arising from the lowest excited state of the electron spin ladder of the $[Fe_4S_4]^{2+}$ cluster. Distances obtained from eqs (2 and 3) were then converted into upper limit distances (upl). For non-exchangeable protons, we obtained overall 122 upl. For amide HN resonances, when R_1 and R_2 provided different upper distance limits for the same ^{1}HN proton, the upper limit value was taken by considering the less restrictive value among the two. In these cases, the upper limit value was given a weighting factor 2. For the 49 non-proline residues, 30 upper distance limits were used.

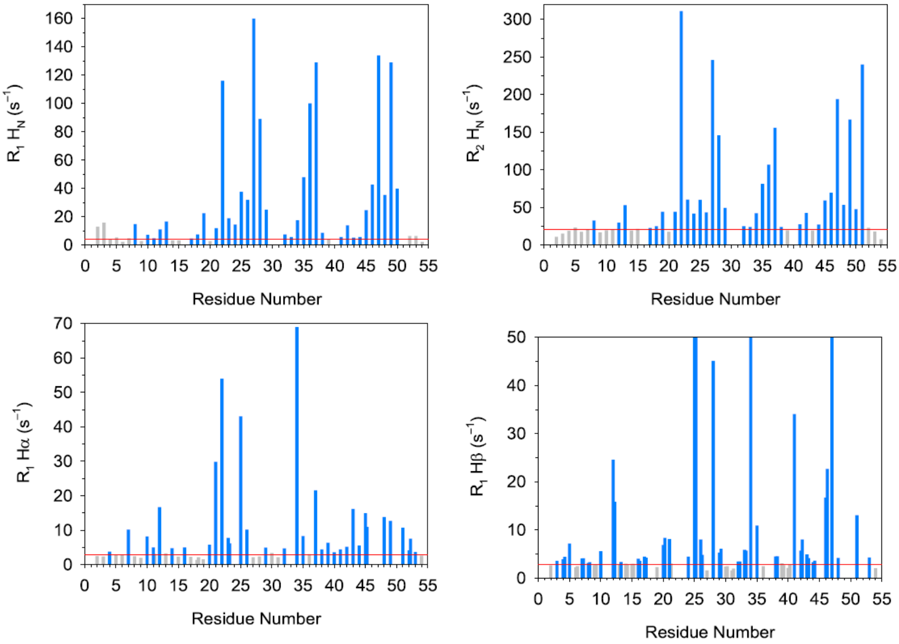

Figure V-**3** Longitudinal and transverse relaxation rates of amide and aliphatic protons. Horizontal red lines show the average diamagnetic values. Blue histograms are rates converted into PRE values. Values of Hβ are out of scale (see Table S3).

Since we do not have *à priori* the information on which iron of the cluster is causing the dipole coupling with each nucleus, in a first structure calculation all PRE-based upper limit distance restraints were assigned to the mass center of the cluster, rather than to a specific iron ion of the cluster. This was obtained by adding at the end of the protein sequence a special linker made of 100 pseudo-residues called LL2. The 'atoms' of LL2 pseudo-residues have zero mass and zero van der Waals radii, thus the linker can freely pass through the structure during simulated annealing. The last residue of the linker is an ION residue (CYANA library) which has been subsequently linked at fixed distances with the four iron ions and with the four sulfur ions of the cluster, with van der Waals contact taken to zero in order to avoid distortions or additional contribution to the overall energy. In this construct, the ION residue represents therefore the mass center of the cubane. Additional 1.4 Å (where 1.4 Å is the distance between each iron and the mass center of the cubane in the typical [4Fe-4S] structure) was added to all upl values obtained from PREs and all restraints were given to the center of mass of the cubane. To perform the final refinement via AMBER, for each PRE restraint the center of mass of the cubane has been replaced with the closest iron ion of the cluster as resulting from the structure obtained with CYANA (or with the two closest iron ions when ambiguous metal-to-proton distances occur) and the upper limit distance taken from equations (2 and 3). Paramagnetic relaxation enhancements that are violated in a significant number of structures were critically analyzed, taking also into account the NOES. It was found that, while no violations have been observed for PREs obtained from non-exchangeable protons, some of the PRE values of exchangeable HN gave rise to consistent violations. Some of them are due to local internal dynamics (^{15}N relaxation shown in Figure S2). However, some of the R_1 and R_2 HN values belonging to the residues 5–20 (i.e., the N-terminal part preceding the cluster-binding region) and to residues 42–44 (part of the long loop between Cys 34 and Cys 47) showed consistent violations that are not accounted by ^{15}N relaxation. All these residues have calculated iron-to-proton distances in the range 7–11 Å, while no violations were observed for HN distances in the range 4–7 Å. This effect is observed only for exchangeable amide protons; indeed, aliphatic protons values were in very good agreement with the structure also at distances > 10 Å. This suggests that magnetic susceptibility anisotropy is not the only factor responsible for the deviation from equations 2 and 3 [58,61], as also previously observed in Cu(II) proteins [59]. Intermolecular effects and/or solute–solvent interactions could be possible factors affecting the quantitative analysis of HN relaxation rates. PREs giving rise to consistent violations were excluded from structure calculation. Overall, 175 PRE restraints were retained from relaxation-rate data (Table S4), and the total number of distance restraints (NOE and PRE) was increased to 533. A summary of these restraints is reported in Table S5.

The addition of relaxation-based NMR restraints gave a more tightly converged NMR structure, with backbone and side chain RMSD values of 0.62±0.11Å and 1.14±0.13Å, respectively (Fig. 2B). PRE data improved the quality of the structure not only in the proximity of the cluster, but throughout the entire protein. The combination of both types of restraints led to statistical parameters that are indicative of a highly precise structure of a well-folded protein of small/medium size (Table S6). Finally, we addressed the question of whether an NMR structure obtained without NOEs is able to achieve good accuracy and precision. Figure 2C shows the family of structures obtained without the 344 NOEs from ^{13}C and ^{15}N-NOESY-HSQC experiments. The structure has backbone and heavy atoms RMSD of 1.31±0.27Å and 2.00±0.32Å, respectively. The overall precision is obviously lower than that obtained with the full set of restraints and it is also lower than that obtained with NOE-only, because of the lower number of restraints, but still lies within an acceptable structure quality range. The per-residue comparison of backbone RMSD (Figure 4A) shows that the family obtained with the full set of restraints has always the lowest RMSD (except Thr24), indicating that the combination of NOEs and PREs improves the precision in all the protein regions. PREs provide information exactly where NOEs are missing, thus complementing NOE data. In several protein regions, the NOE-only family has an RMSD similar to the family obtained with the full set of restraints, indicating that NOEs drive the structure toward a minimum.

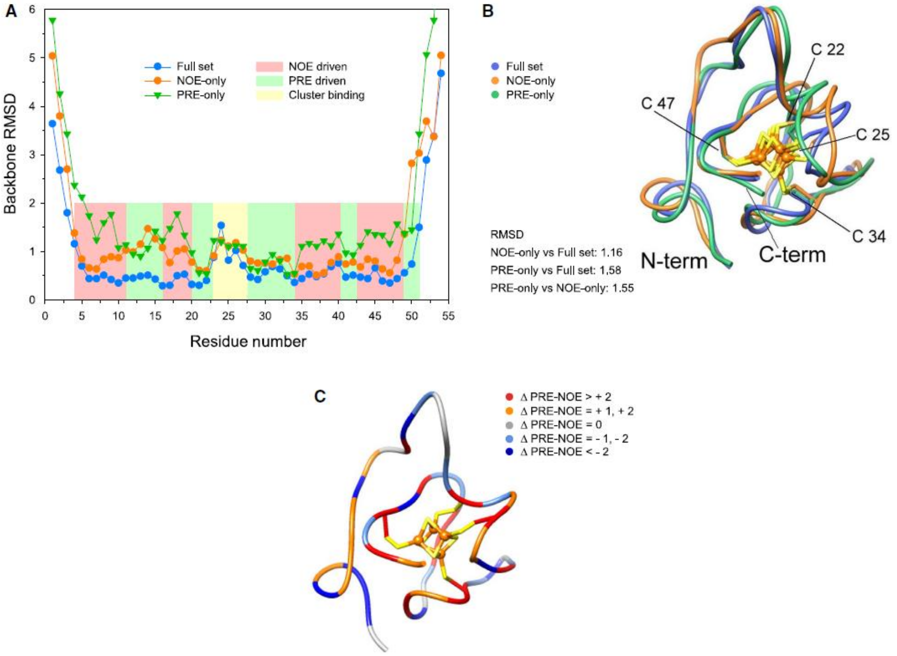

Figure V-**4** **A)** per-residue RMSD values of the three different families. The relative contribution of the different set of constraints on a per residue basis is shown with the color code indicated in the Figure. **B)** Superimposing of the most representative structures of each ensemble obtained with different sets of constraints. Figure reports also pairwise backbone RMSD values. **C)** Regions where the number of PRE restraints exceeds that of long-range NOE restraints are shown in red and orange; regions where the opposite occurs are shown in blue and light blue. Molecular graphics performed with UCSF Chimera.

Conversely, in other protein regions, the precision is improved by the use of PREs; in these regions, the structure quality is PRE driven. The loop surrounding the cluster and containing Cys 22 and Cys 25 of the CXXC binding motif in HiPIPs has a different trend. Here, the RMSD values of the three families are similar and higher than average values. This is the situation in which, not only NOEs but also PREs are missing due to the close proximity to the paramagnetic center. Essentially, for this fragment the structure is given by the cluster-binding topology, by the dihedral angles of Cys bound residues, and by the hydrogen bonds identified by ^{15}N contact shift. We can obtain clues on the accuracy of the structures by comparing the most representative structures of the three families: the PREonly, the NOE-only, and the full-set structures. As shown in Figure 4B, the pairwise RMSD between them are all similar and comparable with the precision within each family. The representative conformer selected from the ensemble obtained with the full set of restraints is, for most of the protein, in an average position among the representative conformers of the PRE-only and NOE-only ensemble. The PRE-only structure ensemble is essentially the same, although with a larger RMSD, as the one obtained with the full set of restraints. Finally, Figure 4C points out the relative impact of PREs vs long-range NOEs. As expected, residues surrounding the cluster have a dominance of PREs; however, also regions from a larger sphere, such as stretch 10–13, experiences the contribution of PREs. Noteworthy, an opposite behavior is observed for the aromatic residue surrounding the cluster Trp46, which experiences both NOEs and PREs. This large hydrophobic residue has the role of maintaining the hydrophobicity of the cluster and protecting it from solvent accessibility. Therefore, it gives rise to many long-range NOEs, extending from the close proximity of the paramagnetic center to the diamagnetic region.

Conclusions

Notwithstanding the exciting perspectives opened by computational biologists [98–101], the quest for novel experimental restraints remains of primary importance for structural modeling. Up to date, a dense network of NOEs has always been considered essential for NMR structures, because restraints between residues that are far apart in the primary sequence define the relative orientation of different structural motifs [102]. Factors such as protein size, electronic correlation times of metal ion(s) and internal mobility modulate the interplay between paramagnetism-based and conventional NMR restraints and their relative contribution to the final structure. The NMR structure of PioC is a proof of concept that PREs may drive a solution structure and eventually act as the sole source of NMR restraints. When a protein is small enough to be affected by paramagnetism in a large percentage, then NOEs are not essential anymore, if relaxation rates are measured virtually for all ^{1}H spins. In PioC, the $[Fe_4S_4]^{2+}$ cluster provides upper distance limits for PREs up to 13 Å, while the average protein radius is about 15 Å, thus being an ideal case for obtaining an accurate and well-converged PRE-driven NMR structure. In this case, an extended network where all the ^{1}H spins are linked to a single point (the metal center) via long-range dipolar couplings can completely replace a network of short-range dipole–dipole ^{1}H-^{1}H couplings. The availability of PREs from aliphatic protons circumvents the lack of accuracy for long metal-to-proton distances of exchangeable protons. This represents an opportunity for the characterization and structural study of metallopeptides and *de novo*-designed and bio-inspired metalloenzymes [103–105]. These results argue for the systematic use of PREs in structure calculations of metalloproteins where metal substitution is not possible since they provide distance restraints in protein regions where NOEs are sparse due to paramagnetism, and where most biochemically relevant events occur.

Acknowledgements

We are grateful to Prof. Gaetano Montelione for the enlightening discussions during his stay at CERM as invited Professor. This work benefited from access to CERM/CIRMMP, the Instruct-ERIC Italy centre. Fi-nancial support was provided by European EC Horizon2020 TIMB3 (Project 810856) Instruct-ERIC (PID 4509). This article is based upon work from COST Action CA15133, supported by COST (European Co-operation in Science and Technology). Fondazione Ente Cassa di Risparmio di Firenze (CRF 2016 0985) is acknowledged for providing fellowship to MI. This work was funded by national funds through

FCT– Fundação para a Ciência e a Tecnologia, I.P., Project UIDB/04612/2020 and UIDP/04612/2020, Fundação para a Ciência e a Tecnologia (FCT) Portugal Grant PD/BD/135187/2017 to IBT.

References

1. Andreini, C., Bertini, I., Cavallaro, G., Holliday, G. L. & Thornton, J. M. (2008) Metal ions in biological catalysis: from enzyme databases to general principles, J Biol Inorg Chem. 13, 1205-1218.
2. Waldron, K. J., Rutherford, J. C., Ford, D. & Robinson, N. J. (2009) Metalloproteins and metal sensing, Nature. 460, 823-830.
3. Beinert, H. (2000) Iron-sulfur proteins: ancient structures, still full of surprises, J Biol Inorg Chem. 5, 2-15.
4. Cai, K., Liu, G., Frederick, R. O., Xiao, R., Montelione, G. T. & Markley, J. L. (2016) Structural/Functional Properties of Human NFU1, an Intermediate [4Fe-4S] Carrier in Human Mitochondrial Iron-Sulfur Cluster Biogenesis, Structure. 24, 2080-2091.
5. Mulliez, E., Duarte, V., Arragain, S., Fontecave, M. & Atta, M. (2017) On the Role of Additional [4Fe-4S] Clusters with a Free Coordination Site in Radical-SAM Enzymes, Frontiers in chemistry. 5, 17.
6. Ciofi-Baffoni, S., Nasta, V. & Banci, L. (2018) Protein networks in the maturation of human iron-sulfur proteins, Metallomics. 10, 49-72.
7. Perard, J. & Ollagnier de Choudens, S. (2018) Iron-sulfur clusters biogenesis by the SUF machinery: close to the molecular mechanism understanding, J Biol Inorg Chem. 23, 581-596.
8. Freibert, S. A., Weiler, B. D., Bill, E., Pierik, A. J., Muhlenhoff, U. & Lill, R. (2018) Biochemical Reconstitution and Spectroscopic Analysis of Iron-Sulfur Proteins, Methods Enzymol. 599, 197-226.

9. Rouault, T. A. (2019) The indispensable role of mammalian iron sulfur proteins in function and regulation of multiple diverse metabolic pathways, Biometals. 32, 343-353.

10. Jia, M., Sen, S., Wachnowsky, C., Fidai, I., Cowan, J. A. & Wysocki, V. (2020) Characterization of [2Fe-2S]-Cluster-Bridged Protein Complexes and Reaction Intermediates by use of Robust Native Mass Spectrometric Methods, Angew Chem Int Ed Engl. 6724–6728.

11. Adinolfi, S., Puglisi, R., Crack, J. C., Iannuzzi, C., Dal Piaz, F., Konarev, P. V., Svergun, D. I., Martin, S., Le Brun, N. E. & Pastore, A. (2017) The Molecular Bases of the Dual Regulation of Bacterial Iron Sulfur Cluster Biogenesis by CyaY and IscX, Front. Mol. Biosci. 4, 97, 2-12.

12. Wachnowsky, C., Hendricks, A. L., Wesley, N. A., Ferguson, C., Fidai, I. & Cowan, J. A. (2019) Understanding the Mechanism of [4Fe-4S] Cluster Assembly on Eukaryotic Mitochondrial and Cytosolic Aconitase, Inorg Chem. 58, 13686-13695.

13. Arthanari, H., Takeuchi, K., Dubey, A. & Wagner, G. (2019) Emerging solution NMR methods to illuminate the structural and dynamic properties of proteins, Curr Opin Struct Biol. 58, 294-304.

14. Bax, A. & Clore, G. M. (2019) Protein NMR: Boundless opportunities, J Magn Reson. 306, 187-191.

15. Cai, K. & Markley, J. L. (2018) NMR as a Tool to Investigate the Processes of Mitochondrial and Cytosolic Iron-Sulfur Cluster Biosynthesis, Molecules. 23, 2213, 1-34.

16. Piccioli, M. & Turano, P. (2015) Transient iron coordination sites in proteins: exploiting the dual nature of paramagnetic NMR, Coord Chem Rev. 284, 313-328.

17. Barry, C. D., North, A. C. T., Glasel, J. A., Williams, R. J. P. & Xavier, A. V. (1971) Quantitative Determination of Mononucleotide Conformations in

Solution using Lanthanide Ion Shift and Broading NMR Probes, Nature. 232, 236-245.

18. Brassington, J. G., Williams, R. J. P. & Wright, P. E. (1975) Assignment of the n.m.r. spectrum of iron(III) protoporphyrin IX dicyanide using paramagnetic shift and broadening probes, Journal of the Chemical Society, Chemical Communications, 9, 338-340.

19. Bertini, I., Couture, M. M. J., Donaire, A., Eltis, L. D., Felli, I. C., Luchinat, C., Piccioli, M. & Rosato, A. (1996) The solution structure refinement of the paramagnetic reduced HiPIP I from *Ectothiorhodospira halophila* by using stable isotope labeling and nuclear relaxation, Eur J Biochem. 241, 440-452.

20. Tolman, J. R., Flanagan, J. M., Kennedy, M. A. & Prestegard, J. H. (1995) Nuclear magnetic dipole interactions in field-oriented proteins: information for structure determination in solution, Proc Natl Acad Sci USA. 92, 9279-9283.

21. Hus, J. C., Marion, D. & Blackledge, M. (2000) De novo determination of protein structure by NMR using orientational and long-range order restraints, J Mol Biol. 298, 927-936.

22. Battiste, J. L. & Wagner, G. (2000) Utilization of site-directed spin labelling and high-resolution heteronuclear nuclear magnetic resonance for global fold determination of large proteins with limited Nuclear Overhauser Effect data, Biochemistry. 39, 5355-5365.

23. Donaldson, L. W., Skrynnikov, N. R., Choy, W.-Y., Muhandiram, D. R., Sarkar, B., Forman-Kay, J. D. & Kay, L. E. (2001) Structural Characterization of Proteins with an Attached ATCUN Motif by Paramagnetic Relaxation Enhancement NMR Spectroscopy, J Am Chem Soc. 123, 9843-9847.

24. Kosen, P. A. (1989) Spin Labeling of Proteins, Methods Enzymol. 177, 86-121.

25. Gaponenko, V., Howarth, J. W., Columbus, L., Gasmi-Seabrook, G., Yuan, J., Hubbell, W. L. & Rosevear, P. R. (2000) Protein global fold determination using site-directed spin and isotope labeling, Protein Sci. 9, 302-309.

26. Gross, J. D., Moerke, N. J., von der Haar, T., Lugovskoy, A. A., Sachs, A. B., McCarthy, J. E. G. & Wagner, G. (2003) Ribosome Loading onto the mRNA Cap Is Driven by Conformational Coupling between eIF4G and eIF4E, Cell. 115, 739-750.

27. Mal, T. K., Skrynnikov, N. R., Yap, K. L., Kay, L. E. & Ikura, M. (2002) Detecting Protein Kinase Recognition Modes of Calmodulin by Residual Dipolar Couplings in Solution NMR, Biochemistry. 41, 12899-12906.

28. Rumpel, S., Becker, S. & Zweckstetter, M. (2008) High-resolution structure determination of the CylR2 homodimer using paramagnetic relaxation enhancement and structure-based prediction of molecular alignment, J Biomol NMR. 40, 1-13.

29. Varani, L., Gunderson, S. I., Mattaj, I. W., Kay, L. E., Neuhaus, D. & Varani, G. (2000) The NMR structure of the 38 kDa U1A protein – PIE RNA complex reveals the basis of cooperativity in regulation of polyadenylation by human U1A protein, Nature Struct Biol. 7, 329-335.

30. Iwahara, J., Anderson, D. E., Murphy, E. C. & Clore, G. M. (2003) EDTA-derivatized deoxythymidine as a tool for rapid determination of protein binding polarity to DNA by intermolecular paramagnetic relaxation enhancement, J Am Chem Soc. 125, 6634-6635.

31. Ueda, T., Kato, A., Ogawa, Y., Torizawa, T., Kuramitsu, S., Iwai, S., Terasawa, H. & Shimada, I. (2004) NMR study of repair mechanism of DNA photolyase by FAD-induced paramagnetic relaxation enhancement, J Biol Chem. 279, 52574-9.

32. Roosild, T. P., Greenwald, J., Vega, M., Castronovo, S., Riek, R. & Choe, S. (2005) NMR Structure of Mistic, a Membrane-Integrating Protein for Membrane Protein Expression, Science. 307, 1317-1321.

33. Bertoncini, C. W., Jung, Y.-S., Fernández, C. O., Hoyer, W., Griesinger, C., Jovin, T. M. & Zweckstetter, M. (2005) Release of long-range tertiary interactions potentiates aggregation of natively unstructured a-synuclein, Proc Natl Acad Sci USA. 102, 1430-1435.

34. Dedmon, M. M., Lindorff-Larsen, K., Christodoulou, J., Vendruscolo, M. & Dobson, C. M. (2005) Mapping long-range interactions in alpha-synuclein using spin-label NMR and ensemble molecular dynamics simulations, J Am Chem Soc. 127, 476-477.

35. Felitsky, D. J., Lietzow, M. A., Dyson, H. J. & Wright, P. E. (2008) Modeling transient collapsed states of an unfolded protein to provide insights into early folding events, Procs Nat Acad Sci U.S.A. 105, 6278-83.

36. Song, J., Guo, L. W., Muradov, H., Artemyev, N. O., Ruoho, A. E. & Markley, J. L. (2008) Intrinsically disordered gamma-subunit of cGMP phosphodiesterase encodes functionally relevant transient secondary and tertiary structure, Proc Natl Acad Sci U S A. 105, 1505-10.

37. Pan, B. B., Yang, F., Ye, Y., Wu, Q., Li, C., Huber, T. & Su, X. C. (2016) 3D structure determination of a protein in living cells using paramagnetic NMR spectroscopy, Chem Commun (Camb). 52, 10237-10240.

38. Muntener, T., Haussinger, D., Selenko, P. & Theillet, F. X. (2016) In-Cell Protein Structures from 2D NMR Experiments, J Phys Chem Lett. 7, 2821-2825.

39. Balayssac, S., Bertini, I., Bhaumik, A., Lelli, M. & Luchinat, C. (2008) Paramagnetic shifts in solid-state NMR of proteins to elicit structural information., Proc Natl Acad Sci USA. 105, 17284-17289.

40. Luchinat, C., Parigi, G., Ravera, E. & Rinaldelli, M. (2012) Solid state NMR crystallography through paramagnetic restraints, J Am Chem Soc. 134, 5006-5009.

41. Sengupta, I., Nadaud, P. S., Helmus, J. J., Schwieters, C. D. & Jaroniec, C. P. (2012) Protein fold determined by paramagnetic magic-angle spinning solid-state NMR spectroscopy, Nature Chem. 4, 410-417.

42. Nadaud, P. S., Helmus, J. J., Kall, S. L. & Jaroniec, C. P. (2009) Paramagnetic Ions Enable Tuning of Nuclear Relaxation Rates and Provide Long-Range Structural Restraints in Solid-State NMR of Proteins, J Am Chem Soc. 131, 8108-8120.

43. Wang, S., Munro, R. A., Kim, S. Y., Jung, K.-H., Brown, L. S. & Ladizhansky, V. (2012) Paramagnetic Relaxation Enhancement Reveals Oligomerization Interface of a Membrane Protein, J Am Chem Soc. 134, 16995-16998.

44. Iwahara, J. & Clore, G. M. (2006) Detecting transient intermediates in macromolecular binding by paramagnetic NMR, Nature. 440, 1227-1230.

45. Volkov, A. N., Worrall, J. A. R., Holtzmann, E. & Ubbink, M. (2006) Solution structure and dynamics of the complex between cytochrome c and cytochrome c peroxidase determined by paramagnetic NMR, Proc Natl Acad Sci USA. 103, 18945-18950.

46. Xu, X., Reinle, W., Hannemann, F., Konarev, P. V., Svergun, D. I., Bernhardt, R. & Ubbink, M. (2008) Dynamics in a Pure Encounter Complex of Two Proteins Studied by Solution Scattering and Paramagnetic NMR Spectroscopy, J Am Chem Soc. 130, 6395-6403.

47. Tang, C., Iwahara, J. & Clore, G. M. (2006) Visualization of transient encounter complexes in protein-protein association, Nature. 444, 383-386.

48. Tang, C., Schwieters, C. D. & Clore, G. M. (2007) Open-to-close transition in apo maltose-binding protein observed by paramagnetic NMR, Nature. 449, 1078-1082.

49. Hansen, D. F., Westler, W. M., Kunze, M. B. A., Markley, J. L., Weinhold, F. & Led, J. J. (2012) Accurate Structure and Dynamics of the Metal-Site of Paramagnetic Metalloproteins from NMR Parameters Using Natural Bond Orbitals, J Am Chem Soc. 134, 4670-4682.

50. Tang, C., Ghirlando, R. & Clore, G. M. (2008) Visualization of Transient Ultra-Weak Protein Self-Association in Solution Using Paramagnetic Relaxation Enhancement, J Am Chem Soc. 130, 4048-4056.

51. Tang, C., Louis, J. M., Aniana, A., Suh, J. Y. & Clore, G. M. (2008) Visualizing transient events in amino-terminal autoprocessing of HIV-1 protease, Nature. 455, 693-6.

52. Baker, K. A., Hilty, C., Peti, W., Prince, A., Pfaffinger, P. J., Wider, G., Wüthrich, K. & Choe, S. (2006) NMR-derived dynamic aspects of N-type inactivation of a Kv channel suggest a transient interaction with the T1 domain, Biochemistry. 45, 1663-72.

53. John, M., Pintacuda, G., Park, A. Y., Dixon, N. E. & Otting, G. (2006) Structure Determination of Protein-Ligand Complexes by Transferred Paramagnetic Shifts, J Am Chem Soc. 128, 12910-12916.

54. Jahnke, W., Perez, L. B., Paris, C. G., Strauss, A., Fendrich, G. & Nalin, C. M. (2000) Second-site NMR screening with a spin-labeled first ligand, J Am Chem Soc. 122, 7394-7395.

55. Bertini, I., Fragai, M., Lee, Y.-M., Luchinat, C. & Terni, B. (2004) Paramagnetic metal ions in ligand screening: the CoII matrix metalloproteinase 12, Angew Chem Int Ed. 43, 2254-2256.

56. Softley, C. A., Bostock, M. J., Popowicz, G. M. & Sattler, M. (2020) Paramagnetic NMR in drug discovery, J. Biomol. NMR. 74, 287-309

57. Iwahara, J., Tang, C. & Clore, G. M. (2007) Practical aspects of ^{1}H transverse paramagnetic relaxation enhancement measurements on macromolecules, J Magn Reson. 184, 185-195.

58. Orton, H. W. & Otting, G. (2018) Accurate Electron–Nucleus Distances from Paramagnetic Relaxation Enhancements, J. Am. Chem. Soc. 140, 7688-7697.

59. Ma, L., Jørgensen, A. M. M., Sorensen, G. O., Ulstrup, J. & Led, J. J. (2000) Elucidation of the Paramagnetic R1 Relaxation of Heteronuclei and Protons in Cu(II) Plastocyanin from *Anabaena variabilis*, J Am Chem Soc. 122, 9473-9485.

60. Suturina, E. A., Mason, K., Geraldes, C., Chilton, N. F., Parker, D. & Kuprov, I. (2018) Lanthanide-induced relaxation anisotropy, Phys Chem Chem Phys. 20, 17676-17686.

61. Parker, D., Suturina, E. A., Kuprov, I. & Chilton, N. F. (2020) How the Ligand Field in Lanthanide Coordination Complexes Determines Magnetic Susceptibility Anisotropy, Paramagnetic NMR Shift, and Relaxation Behavior, Acc Chem Res. 53, 1520–1534

62. Pintacuda, G., Kaikkonen, A. & Otting, G. (2004) Modulation of the distance dependence of paramagnetic relaxation enhancements by CSA x DSA cross-correlation, J Magn Reson. 171, 233-243.

63. John, M., Park, A. Y., Pintacuda, G., Dixon, N. E. & Otting, G. (2005) Weak alignment of paramagnetic proteins warrants correction for residual CSA effects in measurements of pseudocontact shifts, J Am Chem Soc. 127, 17190-17191.

64. Invernici, M., Trindade, I. B., Cantini, F., Louro, R. O. & Piccioli, M. (2020) Measuring transverse relaxation in highly paramagnetic systems, J Biomol NMR. 74, pages 431–442

65. Williamson, M. P., Havel, T. F. & Wüthrich, K. (1985) Solution Conformation of Proteinase Inhibitor IIA from Bull Seminal Plasma by 1H Nuclear Magnetic Resonance and Distance Geometry, J Mol Biol. 182, 295-315.

66. Morris, A. T. & Dwek, R. A. (1977) Some recent applications of the use of paramagnetic centres to probe biological systems using nuclear magnetic resonance, Q Rev Biophys. 10, 421-84.

67. Parigi, G., Ravera, E. & Luchinat, C. (2019) Magnetic susceptibility and paramagnetism-based NMR, Prog Nucl Magn Reson Spectrosc. 114-115, 211-236.

68. Billeter, M., Wagner, G. & Wüthrich, K. (2008) Solution NMR structure determination of proteins revisited, J Biomol NMR. 42, 155-158.

69. Arnesano, F., Banci, L. & Piccioli, M. (2006) NMR structures of paramagnetic metalloproteins, Q Rev Biophys. 38, 167-219.

70. Koehler, J. & Meiler, J. (2011) Expanding the utility of NMR restraints with paramagnetic compounds: background and practical aspects, Prog Nucl Magn Reson Spectrosc. 59, 360-389.

71. Hass, M. A. S. & Ubbink, M. (2014) Structure determination of protein-protein complexes with long-range anisotropic paramagnetic NMR restraints, Curr Op Struct Biol. 24, 45-53.

72. Sala, D., Huang, Y. J., Cole, C. A., Snyder, D. A., Liu, G., Ishida, Y., Swapna, G. V. T., Brock, K. P., Sander, C., Fidelis, K., Kryshtafovych, A., Inouye, M., Tejero, R., Valafar, H., Rosato, A. & Montelione, G. T. (2019) Protein structure prediction assisted with sparse NMR data in CASP13, Proteins. 87, 1315-1332.

73. Banci, L., Bertini, I., Eltis, L. D., Felli, I. C., Kastrau, D. H. W., Luchinat, C., Piccioli, M., Pierattelli, R. & Smith, M. (1994) The three dimensional structure in solution of the paramagnetic protein high-potential iron-sulfur protein I from *Ectothiorhodospira halophila* through nuclear magnetic resonance, Eur J Biochem. 225, 715-725.

74. Bertini, I., Donaire, A., Feinberg, B. A., Luchinat, C., Piccioli, M. & Yuan, H. (1995) Solution structure of the oxidized 2[Fe4S4] ferredoxin from *Clostridium pasteurianum*, Eur J Biochem. 232, 192-205.

75. Louro, R. O., Pacheco, I., Turner, D. L., LeGall, J. & Xavier, A. V. (1996) Structural and functional characterization of cytochrome c3 from *D. desulfuricans* ATCC 27774 by *1*H-NMR, FEBS Lett. 390, 59-62.

76. Turner, D. L., Brennan, L., Chamberlin, S. G., Louro, R. O. & Xavier, A. V. (1998) Determination of solution structures of paramagnetic proteins by NMR, Eur Biophys J. 27, 367-375.

77. Kudhair, B. K., Hounslow, A. M., Rolfe, M. D., Crack, J. C., Hunt, D. M., Buxton, R. S., Smith, L. J., Le Brun, N. E., Williamson, M. P. & Green, J. (2017) Structure of a Wbl protein and implications for NO sensing by *M. tuberculosis*, Nature commun. 8, 2280.

78. Iwahara, J., Schwieters, C. D. & Clore, G. M. (2004) Ensemble approach for NMR structure refinement against H-1 paramagnetic relaxation enhancement data arising from a flexible paramagnetic group attached to a macromolecule, J Am Chem Soc. 126, 5879-5896.

79. Miao, Q., Liu, W. M., Kock, T., Blok, A., Timmer, M., Overhand, M. & Ubbink, M. (2019) A Double-Armed, Hydrophilic Transition Metal Complex as a Paramagnetic NMR Probe, Angew Chem Int Ed Engl. 58, 13093-13100.

80. Liu, W.-M., Overhand, M. & Ubbink, M. (2014) The application of paramagnetic lanthanoid ions in NMR spectroscopy on proteins, Coord Chem Rev. 273-274, 2-12.

81. Nitsche, C. & Otting, G. (2017) Pseudocontact shifts in biomolecular NMR using paramagnetic metal tags, Prog Nucl Magn Reson Spectrosc. 98-99, 20-49.

82. Cetiner, E. C., Jonker, H. R. A., Helmling, C., Gophane, D. B., Grunewald, C., Sigurdsson, S. T. & Schwalbe, H. (2019) Paramagnetic-iterative

relaxation matrix approach: extracting PRE-restraints from NOESY spectra for 3D structure elucidation of biomolecules, J Biomol NMR. 73, 699-712.

83. Matei, E. & Gronenborn, A. M. (2016) (19)F Paramagnetic Relaxation Enhancement: A Valuable Tool for Distance Measurements in Proteins, Angew Chem Int Ed Engl. 55, 150-4.

84. Joss, D. & Haussinger, D. (2019) Design and applications of lanthanide chelating tags for pseudocontact shift NMR spectroscopy with biomacromolecules, Prog Nucl Magn Reson Spectrosc. 114-115, 284-312.

85. Ramelot, T. A., Cort, J. R., Goldsmith-Fischman, S., Kornhaber, G. J., Xiao, R., Shastry, R., Acton, T. B., Honig, B., Montelione, G. T. & Kennedy, M. A. (2004) Solution NMR structure of the iron-sulfur cluster assembly protein U (IscU) with zinc bound at the active site, J Mol Biol. 344, 567-83.

86. Lamosa, P., Brennan, L., Vis, H., Turner, D. L. & Santos, H. (2001) NMR structure of *Desulfovibrio gigas* rubredoxin: a model for studying protein stabilization by compatible solutes, Extremophiles. 5, 303-11.

87. Bertini, I., Cavallaro, G., Cosenza, M., Kümmerle, R., Luchinat, C., Piccioli, M. & Poggi, L. (2002) Cross Correlation Rates Between Curie Spin and Dipole-Dipole relaxation in Paramagnetic Proteins: the Case of Cerium Substituted Calbindin D9k, J Biomol NMR. 23, 115-125.

88. Kateb, F. & Piccioli, M. (2003) New routes to the detection of relaxation allowed coherence transfer in paramagnetic molecules, J Am Chem Soc. 125, 14978-14979.

89. Otting, G. (2010) Protein NMR using paramagnetic ions, Annu Rev Biophys. 39, 387-405.

90. Pintacuda, G., Park, A. Y., Keniry, M. A., Dixonj, N. E. & Otting, G. (2006) Lanthanide labeling offers fast NMR approach to 3D structure determinations of protein-protein complexes, J Am Chem Soc. 128, 3696-3702.

91. Clore, G. M. (2015) Practical Aspects of Paramagnetic Relaxation Enhancement in Biological Macromolecules, Methods enzymol. 564, 485-497.

92. Madl, T., Bermel, W. & Zangger, K. (2009) Use of Relaxation Enhancements in a Paramagnetic Environment for the Structure Determination of Proteins Using NMR Spectroscopy, Angew Chem Int Ed. 48, 8259-8262.

93. Tang, Y., Huang, Y. J., Hopf, T. A., Sander, C., Marks, D. S. & Montelione, G. T. (2015) Protein structure determination by combining sparse NMR data with evolutionary couplings, Nat Methods. 12, 751-754.

94. Raman, S., Lange, O. F., Rossi, P., Tyka, M., Wang, X., Aramini, J., Liu, G., Ramelot, T. A., Eletsky, A., Szyperski, T., Kennedy, M. A., Prestegard, J., Montelione, G. T. & Baker, D. (2010) NMR structure determination for larger proteins using backbone-only data, Science. 327, 1014-1018.

95. Al-Hashimi, H. M., Valafar, H., Terrell, M., Zartler, E. R., Eidsness, M. K. & Prestegard, J. H. (2000) Variation of molecular alignment as a means of resolving orientational ambiguities in protein structures from dipolar couplings, J Magn Reson. 143, 402-406.

96. Kontaxis, G., Delaglio, F. & Bax, A. (2005) Molecular fragment replacement approach to protein structure determination by chemical shift and dipolar homology database mining, Methods Enzymol. 394, 42-78.

97. Tian, F., Valafar, H. & Prestegard, J. H. (2001) A dipolar coupling based strategy for simultaneous resonance assignment and structure determination of protein backbones, J Am Chem Soc. 123, 11791-11796.

98. Yagi, H., Pilla, K. B., Maleckis, A., Graham, B., Huber, T. & Otting, G. (2013) Three-Dimensional Protein Fold Determination from Backbone Amide Pseudocontact Shifts Generated by Lanthanide Tags at Multiple Sites, Structure. 21, 883-890.

99. Bertini, I., Donaire, A., Jiménez, B., Luchinat, C., Parigi, G., Piccioli, M. & Poggi, L. (2001) Paramagnetism-based Versus Classical Constraints: An

Analysis of the Solution Structure of Ca Ln Calbindin D9k., J Biomol NMR. 21, 85-98.

100. Barbieri, R., Luchinat, C. & Parigi, G. (2004) Backbone-only protein solution structures with a combination of classical and paramagnetism-based constraints: a method that can be scaled to large molecules., ChemPhysChem. 21, 797-806.

101. Bird, L. J., Saraiva, I. H., Park, S., Calcada, E. O., Salgueiro, C. A., Nitschke, W., Louro, R. O. & Newman, D. K. (2014) Nonredundant roles for cytochrome c2 and two high-potential iron-sulfur proteins in the photoferrotroph *Rhodopseudomonas palustris* TIE-1, J Bacteriol. 196, 850-8.

102. Rayment, I., Wesenberg, G., Meyer, T. E., Cusanovich, M. A. & Holden, H. M. (1992) Three-dimensional structure of the high-potential iron-sulfur protein isolated from the purple phototrophic bacterium Rhodocyclus tenuis determined and refined at 1.5 A resolution, J Mol Biol. 228, 672-86.

103. Stelter, M., Melo, A. M., Hreggvidsson, S., Saraiva, L. M., Teixeira, M. & Archer, M. (2010) Structure at 1.0 A resolution of a high-potential iron-sulfur protein involved in the aerobic respiratory chain of *Rhodothermus marinus*, J Biol Inorg Chem. 15, 303-13.

104. Dickson, D. P. E., Johnson, C. E., Middleton, P., Rush, J. D., Cammack, R., Hall, D. O., Mullinger, R. N. & Rao, K. K. (1976) Mossbauer Spectroscopic Studies of iron-Sulphur Proteins with four-iron active centres., J Physique Colloq. 37, C6-171-C6-175.

105. Emptage, M. H., Kent, T. A., Huynh, B. H., Rawlings, J., Orme-Johnson, W. H. & Münck, E. (1980) Nature of the Iron-Sulfur Centers in a Ferredoxin from *Azotobacter vinelandii* - Mossbauer Studies and Cluster Displacement Experiments, J Biol Chem. 255, 1793-1796.

106. Blondin, G. & Girerd, J.-J. (1990) Interplay of electron exchange and electron transfer in metal polynuclear complexes in proteins or chemical models, Chem Rev. 90, 1359-1376.

107. Garcia-Serres, R., Clemancey, M., Latour, J. M. & Blondin, G. (2018) Contribution of Mossbauer spectroscopy to the investigation of Fe/S biogenesis, J Biol Inorg Chem. 23, 635-644.

108. Mouesca, J.-M. & Lamotte, B. (1998) Iron-Sulfur clusters and their electronic and magnetic properties, Coord Chem Revs. 178-180, 1573-1614.

109. Noodleman, L., Case, D. A., Mouesca, J.-M. & Lamotte, B. (1996) Valence electron delocalization in polynuclear iron-sulfur clusters, JBIC. 1, 177-182.

110. Bertini, I., Capozzi, F., Eltis, L. D., Felli, I. C., Luchinat, C. & Piccioli, M. (1995) Sequence specific assignment of ligand cysteine protons of oxidized, recombinant HiPIP I from *Ectothiorhodospira halophila*, Inorg Chem. 34, 2516-2523.

111. Hagen, W. R. (2008) Biomolecular EPR spectroscopy.

112. Bertini, I., Cowan, J. A., Luchinat, C., Natarajan, K. & Piccioli, M. (1997) Characterization of a partially unfolded high potential iron protein relevant to the folding pathway and cluster stability, Biochemistry. 36, 9332-9339.

113. Banci, L., Camponeschi, F., Ciofi-Baffoni, S. & Piccioli, M. (2018) The NMR contribution to protein-protein networking in Fe-S protein maturation, JBIC. 23, 687-687.

114. Machonkin, T. E., Westler, W. M. & Markley, J. L. (2002) 13C-13C 2D NMR: a novel strategy for the study of paramagnetic proteins with slow electronic relaxation times, J Am Chem Soc. 124, 3204-3205.

115. Ciofi-Baffoni, S., Gallo, A., Muzzioli, R. & Piccioli, M. (2014) The IR-N-15-HSQC-AP experiment: a new tool for NMR spectroscopy of paramagnetic molecules, J Biomol NMR. 58, 123-128.

116. Ciofi-Baffoni, S., Gallo, A., Muzzioli, R. & Piccioli, M. (2014) The IR-15N-HSQC-AP experiment: a new tool for NMR spectroscopy of paramagnetic molecules, J Biomol NMR. 58, 123-128.

117. Bermel, W., Bertini, I., Felli, I. C., Piccioli, M. & Pierattelli, R. (2006) 13C-detected protonless NMR spectroscopy of proteins in solution, Progr NMR Spectrosc. 48, 25-45.

118. Trindade I B. , I. M., Cantini F, Louro R O , Piccioli M (2020) Sequence-specific Assignments in NMR Spectra of paramagnetic systems: A non-systematic approach, Inorg Chim Acta. 514, 119984.

119. Trindade, I. B., Invernici, M., Cantini, F., Louro, R. O. & Piccioli, M. (2020) ^{1}H, ^{13}C and ^{15}N assignment of the paramagnetic high potential iron-sulfur protein (HiPIP) PioC from *Rhodopseudomonas palustris* TIE-1, Biomol Nmr Assign. 14, 211–215.

120. Bertini, I., Capozzi, F., Luchinat, C., Piccioli, M. & Vila, A. J. (1994) The Fe4S4 centers in ferredoxins studied through proton and carbon hyperfine coupling. Sequence specific assignments of cysteines in ferredoxins from *Clostridium acidi urici* and *Clostridium pasteurianum*, J Am Chem Soc. 116, 651-660.

121. Lin, I. J., Gebel, E. B., Machonkin, T. E., Westler, W. M. & Markley, J. L. (2005) Changes in hydrogen-bond strenght explain reduction potentials in 10 rubredoxin variants, Proc Natl Acad Sci USA. 102, 14581-14586.

122. Bertini, I., Luchinat, C., Parigi, G. & Ravera, E. (2016) NMR of Paramagnetic Molecules, Elsevier.

123. Yang, J., Anishchenko, I., Park, H., Peng, Z., Ovchinnikov, S. & Baker, D. (2020) Improved protein structure prediction using predicted interresidue orientations, Proc Natl Acad Sci U S A. 117, 1496-1503.

124. Cong, Q., Anishchenko, I., Ovchinnikov, S. & Baker, D. (2019) Protein interaction networks revealed by proteome coevolution, Science. 365, 185-189.

125. Senior, A. W., Evans, R., Jumper, J., Kirkpatrick, J., Sifre, L., Green, T., Qin, C., Zidek, A., Nelson, A. W. R., Bridgland, A., Penedones, H., Petersen, S., Simonyan, K., Crossan, S., Kohli, P., Jones, D. T., Silver, D., Kavukcuoglu, K. & Hassabis, D. (2020) Improved protein structure prediction using potentials from deep learning, Nature. 577, 706-710.

126. Grime, G. W., Zeldin, O. B., Snell, M. E., Lowe, E. D., Hunt, J. F., Montelione, G. T., Tong, L., Snell, E. H. & Garman, E. F. (2020) High-Throughput PIXE as an Essential Quantitative Assay for Accurate Metalloprotein Structural Analysis: Development and Application, J Am Chem Soc. 142, 185-197.

127. Lopez-Mendez, B. & Guntert, P. (2006) Automated protein structure determination from NMR spectra, J Am Chem Soc. 128, 13112-13122.

128. Kim, J. D., Pike, D. H., Tyryshkin, A. M., Swapna, G. V. T., Raanan, H., Montelione, G. T., Nanda, V. & Falkowski, P. G. (2018) Minimal Heterochiral de Novo Designed 4Fe-4S Binding Peptide Capable of Robust Electron Transfer, J Am Chem Soc. 140, 11210-11213.

129. Lombardi, A., Pirro, F., Maglio, O., Chino, M. & DeGrado, W. F. (2019) De Novo Design of Four-Helix Bundle Metalloproteins: One Scaffold, Diverse Reactivities, Acc Chem Res. 52, 1148-1159.

130. Nanda, V., Senn, S., Pike, D. H., Rodriguez-Granillo, A., Hansen, W. A., Khare, S. D. & Noy, D. (2016) Structural principles for computational and de novo design of 4Fe-4S metalloproteins, Biochim Biophys Acta. 1857, 531-538.

131. Keller, R. & Wüthrich, K. (2002) A New Software for the Analysis of Protein NMR Spectra in

132. Trindade, I.B., Invernici, I., Cantini, F., Louro, R.O., Piccioli, M. (2020) ^{1}H, ^{13}C and ^{15}N Assignment of the Paramagnetic High Potential Iron-Sulfur Protein (HiPIP) PioC from *Rhodopseudomonas palustris* TIE-1, Biomol NMR Assign.

133. Güntert, P. (2004) Automated NMR structure calculation with CYANA, Methods Mol Biol. 278, 353-378.

134. Guntert, P. & Buchner, L. (2015) Combined automated NOE assignment and structure calculation with CYANA, J Biomol NMR. 62, 453-71.

135. D.A. Case, I. Y. B.-S., S.R. Brozell, D.S. Cerutti, T.E. Cheatham, III, V.W.D. Cruzeiro, T.A. Darden, R.E. Duke, D. Ghoreishi, M.K. Gilson, H. Gohlke, A.W. Goetz, D. Greene, R Harris, N. Homeyer, S. Izadi, A. Kovalenko, T. Kurtzman, T.S. Lee, S. LeGrand, P. Li, C. Lin, J. Liu, T. Luchko, R. Luo, D.J. Mermelstein, K.M. Merz, Y. Miao, G. Monard, C. Nguyen, H. Nguyen, I. Omelyan, A. Onufriev, F. Pan, R. Qi, D.R. Roe, A. Roitberg, C. Sagui, S. Schott-Verdugo, J. Shen, C.L. Simmerling, J. Smith, R. Salomon-Ferrer, J. Swails, R.C. Walker, J. Wang, H. Wei, R.M. Wolf, X. Wu, L. Xiao, D.M. York and P.A. Kollman (2018) AMBER 2018.

136. Carvalho, A. T. & Swart, M. (2014) Electronic structure investigation and parametrization of biologically relevant iron-sulfur clusters, Journal of chemical information and modeling. 54, 613-20.

137. Karmi, O., Marjault, H. B., Pesce, L., Carloni, P., Onuchic, J. N., Jennings, P. A., Mittler, R. & Nechushtai, R. (2018) The unique fold and lability of the [2Fe-2S] clusters of NEET proteins mediate their key functions in health and disease, J Biol Inorg Chem. 23, 599-612.

138. Tejero, R., Snyder, D., Mao, B., Aramini, J. M. & Montelione, G. T. (2013) PDBStat: a universal restraint converter and restraint analysis software package for protein NMR, J Biomol NMR. 56, 337-51.

139. Bhattacharya, A., Tejero, R. & Montelione, G. T. (2007) Evaluating protein structures determined by structural genomics consortia, Proteins: Structure, Function, and Bioinformatics. 66, 778-795.

“If I have seen further than others,

it is by standing upon the shoulders of giants.”

Isaac Newton

VI. Chapter IV: Protein interactions in *Rhodopseudomonas palustris* TIE-1 reveal the molecular basis for resilient photoferrotrophic iron oxidation

This chapter will be submitted as:

Trindade, I.B., Firmino, M. O., Noordam, S., Alves, M.A., Fonseca, B.M., Piccioli, M., Paquete, C.M., Louro, R.O. (2022) Protein interactions in *Rhodopseudomonas palustris* TIE-1 reveal the molecular basis for resilient photoferrotrophic iron oxidation. Molecules

The author of this dissertation participated in all experiments described in this chapter, except for the expression and purification of PioA.

Abstract

Rhodopseudomonas palustris is an alphaproteobacterium with an impressive metabolic versatility, including the ability to utilize ferrous iron as an electron donor to fix carbon dioxide using light energy. This process, named photoferrotrophic iron oxidation, is one of the most ancient metabolisms still existing on Earth and it is sustained by the *pio* operon coding for three proteins (PioA, PioB and PioC). PioB and PioA form a porin-cytochrome complex on the outer membrane which through iron oxidation transfers the electrons to the periplasmic High Potential Iron-sulfur Protein (HiPIP) PioC, which in turn transfers to the Light-Harvesting Reaction Center (LH-RC). Previous studies have shown that deletion of PioA alone was the most detrimental deletion for Fe(II) oxidation activity. By contrast, deletion of PioC resulted in an only partial loss, pointing towards Rpal_4085, another periplasmic HiPIP as a possible substitute. Additionally, Rpal_4085 is homologous to PioC and its expression is strongly upregulated in photoferrotrophic conditions.

In this work, using NMR spectroscopy, we map the interactions of PioC with PioA and the LH-RC identifying key involved amino-acid residues. We also observe that PioA directly reduces the LH-RC, and this is the most likely substitute upon PioC deletion. Whereas Rpal_4085 shows significant electronic and structural differences highlighting its independent functional role. We further explore the differences between Rpal_4085 and PioC which prevent Rpal_4085 from reducing the LH-RC. Overall, this work confirms the predicted *pio* operon pathway, where the HiPIP PioC mediates electron transfer between PioA and LH-RC and further highlights the use of paramagnetic NMR for understanding key biological processes.

Introduction

Photoferrotrophism is proposed to be one of the most ancient types of photosynthesis that predate oxygenic photosynthesis and is likely to have contributed to the deposition of Pre-Cambrian banded iron formations [1,2]. In the ferruginous Archean Ocean, photoferrotrophism enabled microorganisms to grow by using sunlight to drive the coupling of the biogeochemical cycles of iron and carbon [3]. Extant photoferrotrophs are phylogenetically diverse and use both soluble ferrous iron compounds and insoluble iron minerals as electron donors [4]. Whereas soluble ferrous iron can permeate the outer envelope of bacterial cells and be oxidized by proteins in contact with the energized cytoplasmic membrane, the oxidation of insoluble iron minerals requires the uptake of electrons from outside of the cell in a process called extracellular electron transfer (EET) [5–7]. The study of the molecular bases for EET identified cytochromes *c* as major players in the process. In Gram-negative bacteria, protein complexes containing a cytochrome inserted in the cavity of a porin that permeates the outer membrane were identified, whereas in Gram-positive bacteria, these are substituted by molecular wires formed by cytochromes that extend the full thickness of the cell wall [8–12].

Rhodopseudomonas palustris (*R. palustris*) is one of the most metabolically versatile organisms known, and the strain TIE-1 engages in photoferrotrophism [13,14]. This metabolism is sustained by the *pio* operon coding for three proteins. PioA and PioB, form the archetypal cytochrome and porin complex on the outer membrane that engages in EET [15]. PioC is a High Potential Iron-sulfur Protein (HiPIP) predicted to be mobile in the specialized periplasmic invaginations containing the LH-RC with the role of transferring electrons from PioA to the LH-RC in non-cyclic photosynthesis [14]. In addition to non-cyclic photosynthesis, TIE-1 also engages in cyclic photosynthesis involving the bc1 complex embedded in the cytoplasmic membrane and mediated by the soluble redox shuttle cytochrome c_2 also present in the periplasm [14]. The photoferrotrophic metabolism is of great interest for studies on how life and Earth co-evolved through the coupling of biogeochemical cycles sustained by sunlight, and because it can be co-opted for biotechnological processes of low carbon footprint [1,3]. In this last aspect, *R. palustris* has been abundantly studied and numerous demonstrations of the biotechnological potential of its metabolism have been reported [3,16]. In this context, it is important to clarify the final aspects of the electron-transfer pathway connecting extracellular iron minerals or conducting electrodes with the LH-RC. It was found that deletion mutation of PioC impairs photoferrotrophic activity but does not abolish it [13,17]. The search for an alternative to PioC led to the identification of the gene *rpal_4085* which encodes an additional HiPIP protein that is upregulated fourfold in planktonic illuminated cells [14,18]. Although Rpal_4085 was postulated to be able to replace PioC based on its common nature and similar reduction potential, it is unable to donate electrons to the Illuminated LH-RC, appearing instead, to be involved in the response to the presence of divalent metals [14].

In this work to close the gap of knowledge regarding the photoferrotrophic metabolism of *R. palustris* TIE-1 we explore the interactions and electron transfer processes between PioA, PioC and Rpal_4085 to the LH-RC. We show that PioA can directly transfer electrons to the LH-RC and therefore, sustains photoferrotrophism in the absence of PioC. Rpal_4085, despite being a HiPIP with a similar reduction potential at high pH, presents distinct structural and electronic features that likely explain its inability to substitute PioC.

Materials and Methods

Expression and purification of ^{15}N-PioC

PioC was expressed and purified as previously reported [14,19]. Briefly, *E. coli* BL21 DE3 cells were double transformed with pET32h, a plasmid containing the construct thioredoxin-6xHis-thrombin cleavage site-PioC and with pDB1281, a plasmid that carries the machinery for the assembly of iron-sulfur clusters. Cells were grown at 37°C in Luria–Bertani (LB) supplemented with 100 µg/mL ampicillin and 35 µg/mL chloramphenicol until the OD_{600nm} of 0.6. Then they were induced with 1.0mM arabinose and 20µM $FeCl_3$. Cells were again incubated until the OD_{600nm} of 1 and then harvested and washed in M9 minimal media salts before resuspension in M9 minimal media with the addition of ammonium sulfate (^{15}N, 99%). Once resuspended, cells were incubated for 1h before induction with 0.5mM IPTG. After 4h cells were harvested by centrifugation and stored at -80ºC. Cells were then thawed and resuspended in 50mM Potassium Phosphate buffer pH 5.8 with 300mM NaCl before a three-passage disruption using a French Press at 1000 psi. The lysate was ultra-centrifuged at 204,709 × g for 90 min at 4°C to remove cell membranes and debris and the supernatant was dialyzed overnight against 50 mM Potassium Phosphate buffer pH 5.8 with 300mM NaCl before loading in a His-trap affinity column (GE Healthcare). The fraction containing Histag-PioC eluted with 250 mM imidazole and was incubated overnight with Thrombin (GE Healthcare) for digestion. The final purified PioC (His-tag free) was then concentrated from the flowthrough of a second passage through the His-trap column, using an Amicon Ultra Centrifugal Filter (Millipore) with a 3 kDa cut-off. The purity of PioC was confirmed by SDS-PAGE with Blue Safe staining (NZYTech) and by UV–Visible spectroscopy. For protein film voltammetry and NMR binding experiments, different aliquot samples of PioC were dialyzed overnight in the respective appropriate buffers. An extinction coefficient at 390nm (ε_{390nm}= 16 000 $M^{-1}cm^{-1}$) for the 4Fe-4S cluster was used for quantification purposes [20].

Expression and purification of LH-RC

R. palustris was grown anaerobically on YP medium at 30°C under a 36-W white fluorescent lamp for 5 days before cells were harvested by centrifugation and stored at -80ºC. Cells we thawed and resuspended in 20mM Tris-HCl pH 8 before a three-passage disruption using a French Press at 1000 psi. The lysate was then ultracentrifuged at 204,709 × g for 90 min, at 4°C and membrane pellets were solubilized using 20 mM Tris-HCl pH 8 with 1% SB-12 and left stirring for 1h at room temperature before the second ultracentrifugation at 204,709 × g, at 4°C. The supernatant was loaded into a DEAE Sepharose and the fraction containing LH-RC was eluted with 300mM NaCl. The purity of LH-RC was confirmed by SDS-PAGE with Blue Safe staining (NZYTech) and by UV–Visible spectroscopy. The extinction coefficient at 803nm (ε_{800nm}= 2 570 000 $M^{-1}cm^{-1}$) for the bacteriochlorophyll a pigments was used for quantification purposes [21].

Expression and purification of PioA

PioA was expressed as previously reported [22]. Briefly, *Shewanella oneidensis* MR-1_Δmtr cells which are the deletion mutant of the mtr operon were electroporated with pBAD202/D-TOPO expression vector containing a C-terminal Strep II tag together with *pioA* gene [22]. Cells were grown at 30°C in LB supplemented 50µg/mL of kanamycin until the OD_{600nm} of 0.4-0.6 before induction with 1.0mM arabinose. After 6h, cells were harvested by centrifugation at 10 000 × g for 10min at 4°C. Cells were then resuspended in 50mM Sodium Phosphate buffer pH 8.0 with 300mM NaCl together with a protease inhibitor cocktail (Roche), DNase I (Sigma-Aldrich), and 1mM dithiothreitol before a three-passage disruption using a French Press at 1000 psi. The lysate was centrifuged at 5 500 × g for 30min at 4°C and then ultracentrifuged at 185 000 × g for 60min. PioA was purified from the supernatant using a Strep-Tactin XT Superflow Column (IBA-Lifesciences) followed by a Superdex 75 10/300 GL size exclusion column (GE Healthcare). Eluted fractions were analyzed by SDS-PAGE with heme and Blue-Safe staining (NZYTech) and UV-Visible spectroscopy to select fractions containing pure PioA [23]. The identity of the protein was confirmed by Mass spectrometry and N-terminal sequencing. An extinction coefficient at 409nm (ε_{409nm} = 125 000 $M^{-1}cm^{-1}$) per heme was used for quantification purposes [24].

Expression and purification of Rpal_4085

Rpal_4085 was expressed as previously reported with slight modifications in the purification protocol [14]. Briefly, *E. coli* BL21 DE3 cells were double transformed with pET32h, a plasmid containing the construct thioredoxin-6xHis-thrombin cleavage site-Rpal_4085 and with pDB1281, a plasmid that carries the machinery for the assembly of iron-sulfur clusters. Cells were grown at 37°C in LB supplemented with 100 µg/mL ampicillin and 35 µg/mL chloramphenicol until the OD_{600nm} of 0.6. Then the pDB182 plasmid was induced with 1.0mM arabinose, 20µM $FeCl_3$ and 200µM cysteine. Once the OD_{600nm} reached 1-1.2, protein expression was induced with 0.5mM IPTG. After 3h cells were harvested by centrifugation and stored at -80ºC. Cells were then thawed and resuspended in 50mM Potassium Phosphate buffer pH 8.0 with 300mM NaCl before a three-passage disruption using a French Press at 1 000psi. The lysate was ultra-centrifuged at 204,709 × g for 90min at 4 °C to remove cell membranes and debris and the supernatant was dialyzed overnight against 50mM Potassium Phosphate buffer pH 8.0 with 300mM NaCl before loading in a His-trap affinity column (GE Healthcare). The fraction containing Histag-Rpal_4085 was eluted with 250mM imidazole and incubated overnight with Thrombin (GE Healthcare) for digestion. After removing the imidazole, a second passage through the His-trap column was performed to remove the His-tagged protein. The final purified Rpal_4085 (His-tag free) was then concentrated from the flowthrough of a second passage through the His-trap column, using an Amicon Ultra Centrifugal Filter (Millipore) with a 3kDa cut-off. The purity of Rpal_4085 was confirmed by SDS-PAGE with Blue Safe staining (NZYTech).and by UV–Visible spectroscopy. For protein film voltammetry and NMR binding experiments, different aliquot samples of Rpal_4085 were dialyzed overnight in the respective appropriate buffers. An extinction coefficient at 390nm (ε_{390nm}= 16 000$M^{-1}cm^{-1}$) for the 4Fe-4S cluster was used for quantification purposes [20].

Protein film voltammetry of PioC and Rpal_4085

Cyclic voltammetry experiments were conducted at 25ºC inside a Coy anaerobic chamber with a CHI electrochemical analyzer (CHI instruments) using a three-electrode electrochemical cell configuration with PGE (working electrode), graphite rod (counter electrode), and an Ag/AgCl 3M KCl (reference electrode). The PGE working electrode was cleaned with nitric acid, water, and freshly polished before every experiment using 1.0µm and 0.3µm alumina slurry. After washing with bidistilled water, the electrode was left to dry before depositing 10µL of a protein sample at a concentration of approximately ~250µM on the working electrode. The sample was allowed to dry on the surface of the electrode before carrying out the experiments at different scan rates in 50mM Potassium Phosphate with different pH values. The pH of the buffer was confirmed after each experiment.

Data were analyzed with Excel followed by QSoas [25]. All the reduction potentials are reported in mV versus the standard hydrogen electrode (SHE) by the addition of 210 mV to the measured values [26].

^{1}H NMR Temperature dependence experiments:

A sample of approximately 300µM of reduced (as purified) PioC and Rpal_4085 in 50mM Potassium Phosphate buffer pH 7.6 with 300 mM KCl with 10% D_2O was used for ^{1}H temperature dependence experiments.^{1}H NMR experiments were performed on a Bruker Avance II 500 MHz NMR spectrometer equipped with a 5mm PAQXI probe. A total of 3584 transients were acquired using the super-WEFT pulse sequence (180-τ-90-AQ) with 122ms of recycle time and τ values of 119ms, to dampen the diamagnetic signals and suppress the solvent.

^{15}N PioC: NMR binding experiments:

Experiments were performed at 298K using a Bruker AVANCE II+ spectrometer operating at 500MHz equipped with a 5mm TCI C/N Prodigy cryoprobe. The reference standard ^{1}H-^{15}N HSQC experiment was acquired with 72 transients using the pulse sequence hsqcf3gpph1913C from the BRUKER catalogue and the reference paramagnetic 1H-15N HSQC experiment was acquired as previously described with 256 transients [27]. The duration of each experiment was either 1h (100µM PioC) or 3h (25µM PioC). Both experiments were performed with ^{15}N-labeled PioC in 50mM Potassium Phosphate pH 7.0 with 300mM NaCl (plus 0.01%DDM for binding with LH-RC) with 10%D_2O. Binding experiments were performed using samples of 100 µM (PioC vs LH-RC) or 25µM (PioC vs PioA) of ^{15}N-labeled PioC with increasing amounts of ligand (L): LH-RC or PioA. At each titration point, the spectra were acquired (dark spectra) and then samples were incubated for 30 min ≈10 cm under a 36-W white fluorescent lamp (light spectra). Spectra (standard and paramagnetic) were acquired before and after the illumination step.

Reduction of LH-RC by PioA

Electron transfer experiments of PioA between the LH-RC were carried out inside a Coy anaerobic chamber. The redox state of PioA was followed spectrophotometrically from 250nm to 700nm using a Shimadzu 1800 spectrophotometer. PioA at approximately 0.25µM in 50 mM Sodium Phosphate buffer pH 8 with 300mM NaCl was reduced using stepwise additions of Sodium Dithionite, and the excess of the reducing agent was prevented by monitoring the absorption band of unreacted Sodium Dithionite at 315nm [28]. An excess of $NADP^+$ (200x) was added to PioA to serve as an electron sink for the reaction, while catalytic amounts of LH-RC were added to start the reaction. Spectral changes were recorded after every addition, and before and after a 60 min illumination step (36-W white fluorescent lamp).

Results and Discussion

Probing photoferrotrophic iron oxidation interactions using NMR spectroscopy

Using deletion mutants, it has been previously observed that PioABC proteins are required for photoferrotrophic Fe(II) oxidation and growth on Fe(II). These led to the hypothesis that PioA which sits in the membrane in a complex with porin PioB, oxidizes Fe(II) and transfers this electron to periplasmic protein PioC which in turn transfers to the LH-RC. To confirm the proposed pathway, using NMR spectroscopy, we mapped the interactions between PioA, PioC and the LH-RC [13,14].

NMR is a highly sensitive method to probe protein-protein interactions. The binding of an NMR-silent protein to an NMR-visible protein can induce chemical shift changes and/or alter resonances’ linewidth [29,30]. Once resonances have been assigned, these spectral changes provide residue-specific information regarding the interface between two proteins. We recently assigned 99.5% of backbone chemical shifts of PioC NMR spectra using a combination of standard and paramagnetically-tailored experiments [19,31]. Upon mixing unlabelled PioA into ^{15}N-labeled PioC, spectral changes were observed confirming the proposed interaction between these two proteins. Two kinds of spectral changes were observed: chemical shift changes for residues C34, N44, K53, T36 and linewidth broadening for residues R21, K4 and R26 (Figure 1 A). When we map these residues into the three-dimensional structure of PioC together with its electrostatic surface, four of these residues are at the forefront of a positive pocket that constitutes the most accessible surface to the 4Fe-4S cluster (Figure 1 B and C).

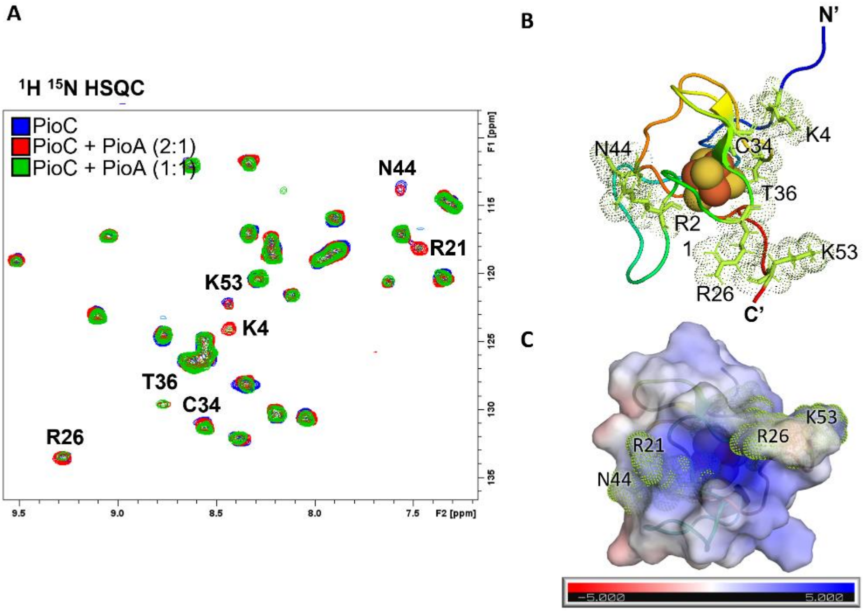

Figure VI-**1** Mapping the interactions between PioC and PioA. **A)** ^{1}H^{15}N-HSQC spectra of ^{15}N PioC with increasing amounts of PioA. Both chemical shift changes and line broadening effects can be observed on HN resonances **B)** Protein mapping of changing resonances in 3D structure of PioC. **C)** Electrostatic surface potential (−5 to +5 kT/e) of PioC (PDB ID 6XYV) highlighting residues that interact with PioA, electrostatic surface potentials were calculated using the APBS plugin in PyMOL [32].

Using EPR spectroscopy, it was previously observed that PioC was able to transfer electrons to the LH-RC upon sample illumination. To understand what residues were important for interaction between these proteins we titrated LH-RC into PioC. Upon mixing LH-RC against PioC, chemical shift changes in residues N17, A19, R48, K20, T36 and line-broadening effects in residues C22 and T36 (Figure 2 A) were observed. The residues involved in this interaction are different from the ones that interact with PioA, however, they still agglomerate at the surface closer to access the 4Fe-4S cluster (Figure 2 B and C).

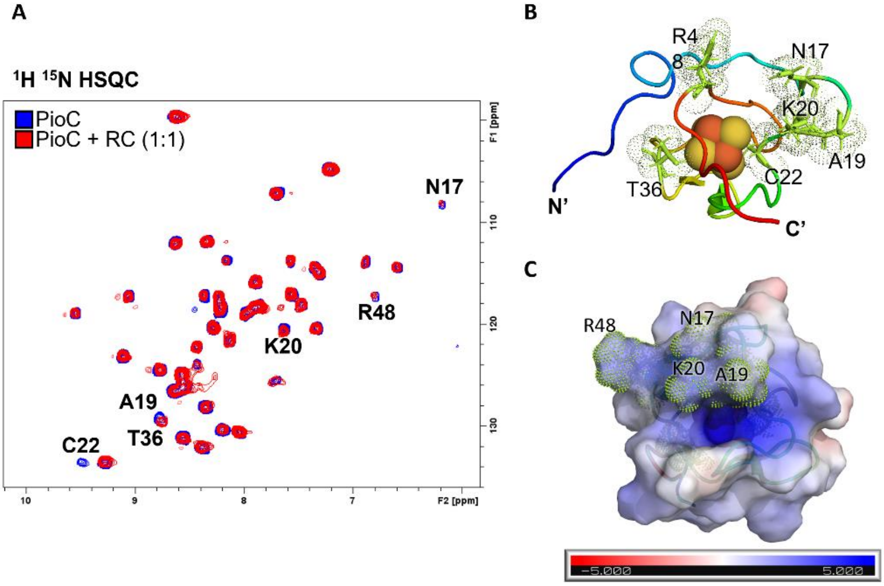

Figure VI-**2** Mapping the interactions between PioC and LH-RC. **A)** ^{1}H^{15}N-HSQC spectra of ^{15}N PioC with and without LH-RC. Both chemical shift changes and line broadening effects can be observed on HN resonances **B)** Protein mapping of changing resonances in 3D structure of PioC. **C)** Electrostatic surface potential (−5 to +5 kT/e) of PioC (PDB ID 6XYV) highlighting residues that interact with LH-RC, electrostatic surface potentials were calculated using the APBS plugin in PyMOL [32].

Overall, the spectral changes observed between PioC and PioA and the LH-RC confirm the proposed *pio* operon pathway.

Rpal_ 4085 – why can't it substitute PioC?

Once the *pio* operon pathway was confirmed, we then aimed for understanding why Rpal_4085, despite being an HiPIP, cannot transfer electrons to the LH-RC [14].

The 4Fe-4S cluster in the reduced form of HiPIPs is diamagnetic but at room temperature, excited electronic states that are paramagnetic are thermally populated due to the small energy gap to the ground state. Therefore, the electronic structure of the 4Fe-4S cluster impacts the temperature dependence of hyperfine-shifted signals outside of the protein envelope arising from α-CH and β-CH_2 protons of the cluster coordinating cysteines. All signals exhibited anti-Curie temperature dependence (i.e., signals shift further downfield as the temperature is increased) indicating an increased population of paramagnetic excited states. The similar slope of the temperature dependence of the signals (Figure 3) and the similar range of their values indicates that the electronic structure of the 4Fe-4S cluster in the two proteins is similar, but the difference in chemical shift indicates that the coordination geometry of the cysteines is different [33]. Furthermore, Rpal_4085 appears to be in a slow exchange between two conformations at room temperature leading to duplication of signals. In our hands, from the different conditions tested (pH from 5.6 to 7.6) the two conformations were always present. This can reflect physiologically relevant states or simply an artifact of protein production.

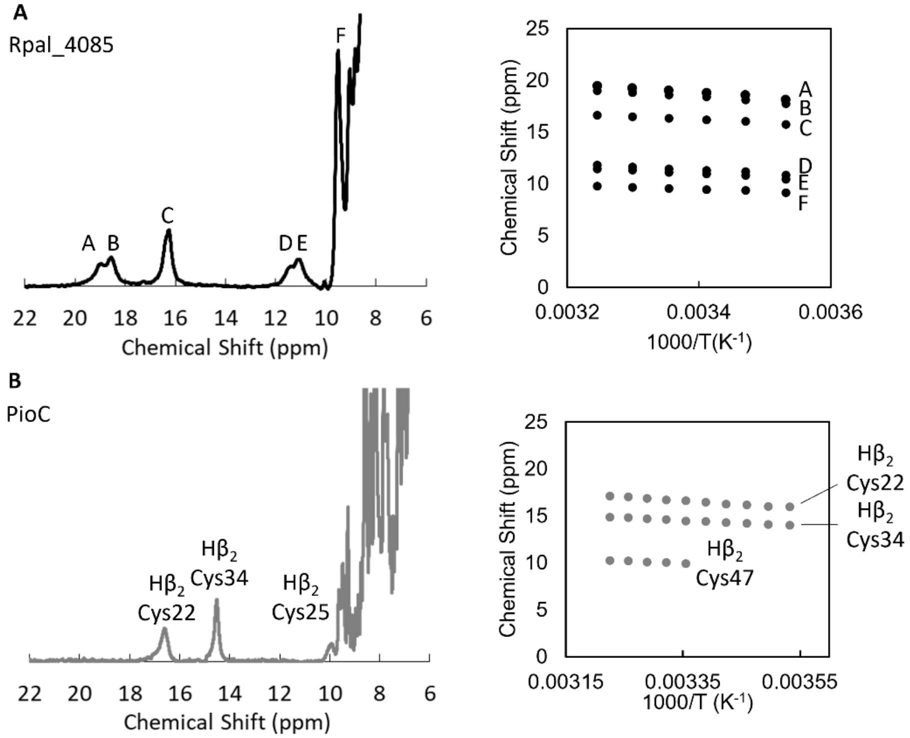

Figure VI-**3** Paramagnetic NMR spectroscopy of PioC and Rpal_4085. **A)** 1D ^{1}H NMR spectra of reduced Rpal_4085 and temperature dependence of hyperfine shift of β-CH2 and α-CH protons outside the diamagnetic envelope. **B)** 1D ^{1}H NMR spectra of reduced PioC and temperature dependence of hyperfine shift of β-CH2 and α-CH protons outside the diamagnetic envelope.

We further investigated if the differences in cluster geometry were sufficient to reflect differences in the reactivity of these proteins. Thus, the reduction potentials of PioC and Rpal_4085 were measured in the range of 6 to 8.1 (Figure 4). Rpal_4085 displayed a more positive reduction potential when compared with PioC, as previously reported at pH 9 [14]. However, Rpal_4085 has a much more pronounced redox-Bohr effect (Figure 4), with a larger pH dependence of the reduction potential than PioC. This arises from the coupling of electron transfer with protonation of nearby residues leading to well-separated pK_a^{ox} and pK_a^{red} [34]. The consequence is that the reduction potential of these proteins is significantly different in the physiological pH range with the potential of Rpal_4085 becoming increasingly positive at lower pH values. The potential of Rpal_4085 surpasses that of the Reaction Centre of anoxygenic phototrophs (~430mV) in the physiological pH range making electron transfer theromdynamically unfavourable. This may be a design feature arising from the fact that Rpal_4085 is overexpressed in the presence of divalent metal cations including Mn(II), Fe(II), Co(II), and Ni(II) [14]. Redox-active heavy metal toxicity is mediated by enhanced Fenton reaction promoted by their reduced states [35]. The higher potential of Rpal_4085 may help in keeping these metals oxidized, and therefore in a less reactive state. Furthermore, the increased potential at lower pH enhances the capacity of Rpal_4085 in oxidizing these metals in the conditions in which they tend to be more soluble.

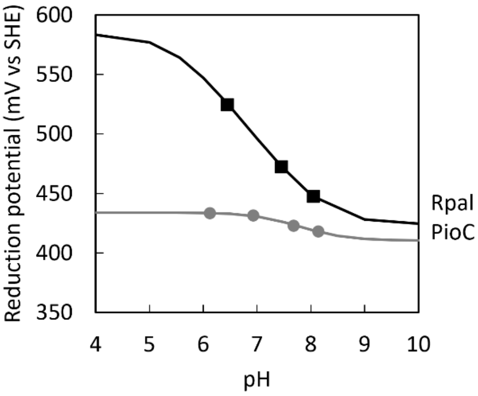

Figure VI-**4** pH dependence of the reduction potentials of PioC and Rpal_4085. The lines were calculated for the coupled transfer of one proton with one electron considering Pka_{ox}= 7.6 and $pKa_{red=}$8.0 for PioC and pKa_{ox}=5.5 and pKa_{red}=8.2 for Rpal_4085 [34].

We then further investigated the differences between these two HiPIPs by looking at the 3D structure and respective electrostatic surface of these proteins. The structure of PioC has been recently determined and it is accessible through PDB accession code: 6WYV, whereas Rpal_4085 structure was modeled through the online version of AlphaFold [36,37]. Even though the identity of these proteins is 33 %, clear differences can be observed. In PioC's structure, there is an evident positive pocket that provides access to the 4Fe-4S cluster, whereas in Rpal_4085 this pocket is absent. Furthermore, Rpal_4085 predicted model structure shows two arms that are completely absent in PioC's structure (Figure 5).

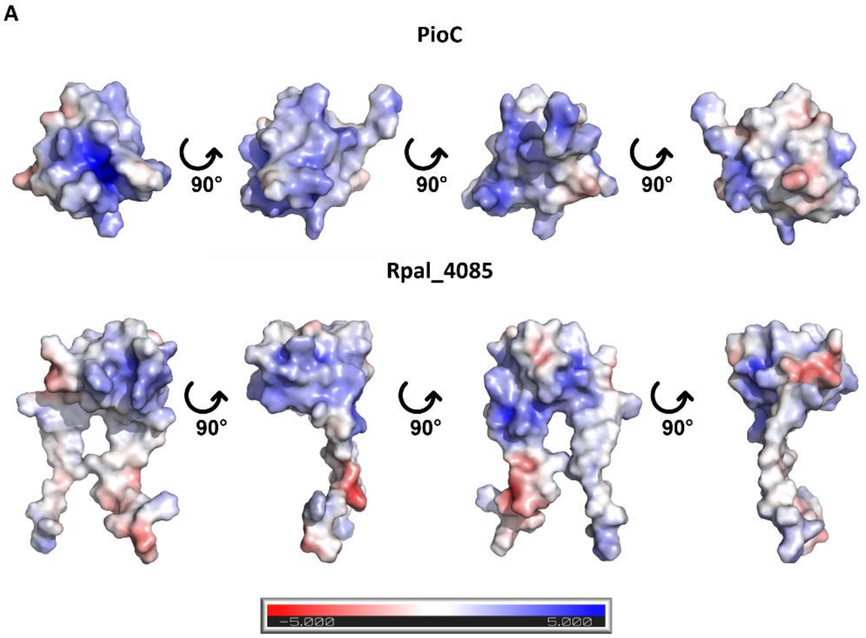

Figure VI-**5** Electrostatic surface potential (−5 to +5 kT/e) of PioC (PDB ID 6XYV) and Rpal_4085 (AlphaFold model), electrostatic surface potentials were calculated using the APBS plugin in PyMOL [32,37].

We then aligned both proteins using PyMOL. Even though the core of the 3D structures seem similar (Figure 6 B), from the electrostatic surface (Figure 6 A) and overlay of both structures with the interacting residues determined by NMR it becomes evident why Rpal_4085 cannot interact with PioA nor with the

LH-RC. Neither the electrostatic surface nor the access to the 4Fe-4S center are conserved.

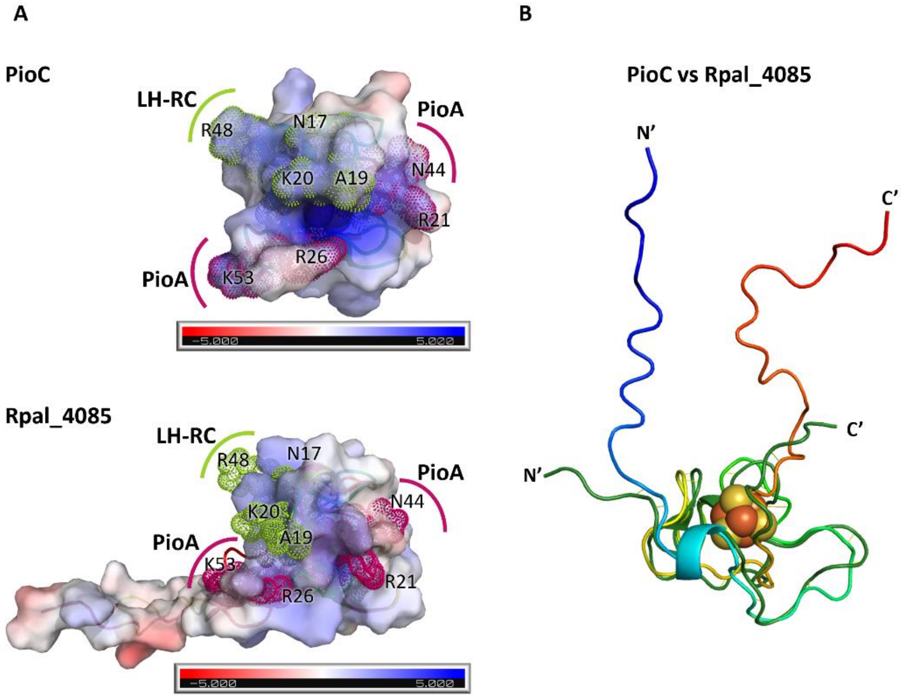

Figure VI-**6** Structural comparison of PioC and Rpal_4085. **A)** Top figure shows the electrostatic surface potential (−5 to +5 kT/e) of PioC (PDB ID 6XYV) highlighting residues that interact with PioA and LH-RC and bottom the electrostatic surface potential (−5 to +5 kT/e) of Rpal_4085 (AlphaFold model) highlighting PioC amino-acid residues that interact with PioA and LH-RC which are missing in Rpal_4085. **B)** Alignment of the structures of PioC and Rpal_4085. electrostatic surface potentials were calculated using the APBS plugin in PyMOL [32,37].

PioA: a jack of all trades that transfers electrons directly to the LH-RC

Given that Rpal_4085 cannot substitute PioC because of structural differences and unfavourable thermodynamic properties, we further investigated other alternatives for *R. palustris* to perform photoferrotrophic iron oxidation. It was previously observed that TIE-1 produces a 34-kDa holo-PioA that exists in two forms, a free soluble periplasmic protein, and a membrane-associated protein in complex with PioB [15]. This observation together with the observation that PioA was the most detrimental deletion for Fe(II) oxidation led to the hypothesis that soluble periplasmic PioA could directly reduce the LH-RC [13]. To test this hypothesis, reduced PioA was incubated with LH-RC in the anaerobic glovebox with NADP+, which functions as the final electron acceptor. No spectral changes were observed when reduced PioA and NADP+ were incubated alone, indicating that PioA did not transfer electrons to NADP+. Spectral changes in PioA were only observed upon the addition of catalytic amounts of LH-RC together with sample illumination (Figure 7). These were characterized by a shift in the Soret peak from ≈420nm to ≈409nm and the disappearance of the α and β peaks at 550 and 520nm, respectively. These changes indicate that PioA has been oxidised and electron transfer occurred to LH-RC.

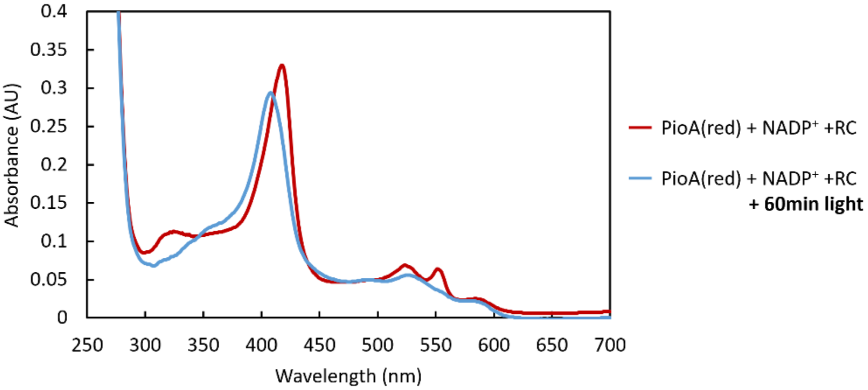

Figure VI-**7** PioA transfers electrons directly to LH-RC. UV-Visible spectral changes observed reflecting the oxidation of PioA in the presence of NADP+ and the RC upon sample illumination.

Conclusions

As previously proposed by Jiao and co-workers, PioABC proteins are essential for photoferrotrophic iron oxidation in *R. palustris* TIE-1 [13]. In this work, using paramagnetically-tailored NMR experiments we map the interactions of intermediate protein PioC with partners PioA and LH-RC. We also investigated the redox and electronic properties of PioC and Rpal_4085 to understand why Rpal_4085 despite being a HiPIP cannot interact nor transfer electrons from PioA to LH-RC. Rpal_4085 electrochemical properties are unfavourable for electron transfer to the LH-RC in the physiological pH range because of the redox-Bohr effect. Furthermore, paramagnetic NMR spectroscopy shows that in the reduced state, the protein exists in two conformations, unlike PioC, and that there are significant differences in the geometry of cluster ligands that interconvert in slow exchange. These two conformations may reflect the unknown function of Rpal_4085 and/or a by-product of protein production in conditions that dramatically differ from the physiological ones. By predicting the structure of Rpal_4085 with the use of AlphaFold, the most dramatic differences were found in the surface regions that superimpose with those of PioC responsible for the interactions with PioA and the LH-RC [37]. Therefore, the evidence collected here further supports the notion that this protein does not play a role in photoferrotrophism in *R. palustris* TIE-1. This reinforces the proposal that Rpal_4085 has a different functional role, likely related to the handling of divalent metals in the periplasm [14].

We also found that soluble PioA can transfer electrons directly to the LH-RC. Cytochromes *c* like PioA are assembled in the periplasmic space of Gram-negative bacteria by specialized maturation systems attached to the inner membrane [15,38]. Therefore, cytochromes that localize to the outer membrane like PioA are present in their final structural configuration in the periplasmic space. A clear precedent for this is reported in the literature for the

MtrA decaheme cytochrome from *Shewanella oneidensis*, which is homologous to PioA, and is found both in the membrane and the soluble fraction during purification [39]. The electron transfer between PioA and LH-RC provides an explanation for the previously observed retention of photoferrotrophic activity in the absence of PioC [13]. This observation is interesting given that in most purple bacteria the LH-RC includes a multiheme cytochrome which mediates electron transfer between soluble cytochrome *c* or HiPIP and the special pair of bacteriochlorophylls. In the case of *R. palustris* TIE-1 this multiheme cytochrome is absent, but the fact that PioA can also transfer electrons directly to the LH-RC suggests conservation of the latter towards the interaction with multiheme cytochromes [40]. Additionally, cytochrome c_2 and HiPIP can transfer electrons directly to the LH-RC in cyclic and non-cyclic photosynthesis, respectively. This diversity in the choice of physiological electron donors reveals an additional molecular aspect of the metabolic redundancy in this organism already notorious for its remarkable bioenergetic versatility [41].

Acknowledgements

The authors are grateful to Julea N. Butt who graciously made PioA expression system accessible. Financial support was provided by European EC Horizon2020 TIMB3 (Project 810856). This work was funded by national funds through FCT– Fundação para a Ciência e a Tecnologia, I.P. (FCT), Project MOSTMICRO-ITQB with refs UIDB/04612/2020 and UIDP/04612/2020. N-terminal sequencing service was provided by the ITQB Research facilities. The NMR data were acquired at CERMAX, ITQB-NOVA, Oeiras, Portugal with equipment funded by FCT, project AAC 01/SAICT/2016. IBT is financially supported by national funds through the FCT PT-NMR PhD Program via PD/BD/135187/2017.

References

[1] K.O. Konhauser, D.K. Newman, A. Kappler, The potential significance of microbial Fe(III) reduction during deposition of Precambrian banded iron formations, Geobiology. 3 (2005) 167–177.

[2] A. Camacho, X.A. Walter, A. Picazo, J. Zopfi, Photoferrotrophy: Remains of an ancient photosynthesis in modern environments, Front. Microbiol. 8 (2017) 1–17.

[3] M.S. Guzman, K. Rengasamy, M.M. Binkley, C. Jones, T.O. Ranaivoarisoa, R. Singh, D.A. Fike, J.M. Meacham, A. Bose, Phototrophic extracellular electron uptake is linked to carbon dioxide fixation in the bacterium *Rhodopseudomonas palustris*, Nat. Commun. 10 (2019) 1355.

[4] M. Ilbert, V. Bonnefoy, Insight into the evolution of the iron oxidation pathways, Biochim Biophys Acta. 1827 (2013) 161–175.

[5] I.H. Saraiva, D.K. Newman, R.O. Louro, Functional characterization of the FoxE iron oxidoreductase from the photoferrotroph *Rhodobacter ferrooxidans* SW2, J. Biol. Chem. 287 (2012) 25541–25548.

[6] B. Schink, Extracellular Redox Chemistry, in: Metals, Microbes, and Minerals - The Biogeochemical Side of Life, De Gruyter, 2021: pp. 33–58.

[7] L. Shi, H. Dong, G. Reguera, H. Beyenal, A. Lu, J. Liu, H.-Q. Yu, J.K. Fredrickson, Extracellular electron transfer mechanisms between microorganisms and minerals, Nat. Rev. Microbiol. 14 (2016) 651–662.

[8] D.J. Richardson, J.N. Butt, J.K. Fredrickson, J.M. Zachara, L. Shi, M.J. Edwards, G. White, N. Baiden, A.J. Gates, S.J. Marritt, T.A. Clarke, The “porin-cytochrome” model for microbe-to-mineral electron transfer, Mol. Microbiol. 85 (2012) 201–212.

[9] M.J. Edwards, D.J. Richardson, C.M. Paquete, T.A. Clarke, Role of multiheme cytochromes involved in extracellular anaerobic respiration in bacteria, Protein Sci. 29 (2020) 830–842.

[10] N.L. Costa, T.A. Clarke, L.A. Philipp, J. Gescher, R.O. Louro, C.M. Paquete, Electron transfer process in microbial electrochemical technologies: The role of cell-surface exposed conductive proteins, Bioresour. Technol. 255 (2018) 308–317.

[11] M.M. Faustino, B.M. Fonseca, N.L. Costa, D. Lousa, R.O. Louro, C.M. Paquete, Crossing the wall: Characterization of the multiheme cytochromes involved in the extracellular electron transfer pathway of *Thermincola ferriacetica*, Microorganisms. 9 (2021) 1–14.

[12] R.O. Louro, N.L. Costa, A.P. Fernandes, A. v. Silva, I.B. Trindade, B.M. Fonseca, C.M. Paquete, Exploring the molecular mechanisms of extracellular electron transfer for harnessing reducing power in METs: Methodologies and approaches, in: Biomass, Biofuels, Biochemicals: Microbial Electrochemical Technology: Sustainable Platform for Fuels, Chemicals and Remediation, Elsevier, 2018: pp. 261–293.

[13] Y. Jiao, D.K. Newman, The pio operon is essential for phototrophic Fe(II) oxidation in *Rhodopseudomonas palustris* TIE-1, J. Bacteriol. 189 (2007) 1765–1773.

[14] L.J. Bird, I.H. Saraiva, S. Park, E.O. Calcada, C.A. Salgueiro, W. Nitschke, R.O. Louro, D.K. Newman, Nonredundant Roles for Cytochrome c2 and Two High-Potential Iron-Sulfur Proteins in the Photoferrotroph *Rhodopseudomonas palustris* TIE-1, J. Bacteriol. 196 (2014) 850–858.

[15] D. Gupta, M.C. Sutherland, K. Rengasamy, J.M. Meacham, R.G. Kranz, A. Bose, Photoferrotrophs Produce a PioAB Electron Conduit for Extracellular Electron Uptake, MBio. (2019) 1–15.

[16] D.F.R. Doud, E.C. Holmes, H. Richter, B. Molitor, G. Jander, L.T. Angenent, Metabolic engineering of *Rhodopseudomonas palustris* for the obligate reduction of n-butyrate to n-butanol, Biotechnol. Biofuels. 10 (2017) 178

[17] Y. Jiao, A. Kappler, L.R. Croal, K. Newman, D.K. Newman, Isolation and Characterization of a Genetically Tractable Photoautotrophic Isolation and Characterization of a Genetically Tractable Photoautotrophic Fe(II) -Oxidizing Bacterium , *Rhodopseudomonas palustris* Strain TIE-1, Appl. Environ. Microbiol. 71 (2005) 4487–4496.

[18] A. Bose, E.J. Gardel, C. Vidoudez, E.A. Parra, P.R. Girguis, Electron uptake by iron-oxidizing phototrophic bacteria, Nat. Commun. 5 (2014) 3391.

[19] I.B. Trindade, M. Invernici, F. Cantini, R.O. Louro, M. Piccioli, 1H, 13C and 15N assignment of the paramagnetic high potential iron–sulfur protein (HiPIP) PioC from *Rhodopseudomonas palustris* TIE-1, Biomol. NMR Assign. 14 (2020) 211–215.

[20] M.L. Antonkine, M.S. Koay, B. Epel, C. Breitenstein, O. Gopta, W. Gärtner, E. Bill, W. Lubitz, Synthesis and characterization of de novo designed peptides modelling the binding sites of [4Fe-4S] clusters in photosystem I, Biochim Biophys Acta Bioenerg. 1787 (2009) 995–1008.

[21] Y. Saga, K. Hirota, Determination of the Molar Extinction Coefficients of the B800 and B850 Absorption Bands in Light-harvesting Complexes Derived from Three Purple Photosynthetic Bacteria *Rhodoblastus acidophilus*, *Rhodobacter sphaeroides*, and *Phaeospirillum molischianum* b y Extraction of Bacteriochlorophyll a, Anal Sci. 32 (2016) 801–805.

[22] D.B. Li, M.J. Edwards, A.W. Blake, S.E. Newton-Payne, S.E.H. Piper, L.P. Jenner, K.P. Sokol, E. Reisner, J.H. van Wonderen, T.A. Clarke, J.N. Butt, His/Met heme ligation in the PioA outer membrane cytochrome enabling

light-driven extracellular electron transfer by *Rhodopseudomonas palustris* TIE-1, Nanotechnology. 31 (2020) 354002.

[23] R.T. Francis, J.R. And, R.R. Becker, Specific Indication of Hemoproteins in Polyacrylamide Gels Using a Double-Staining Process, Anal. Biochem. 136 (1984) 509–514.

[24] V. Massey, The microestimation of succinate and the extinction coefficient of cytochrome c, Biochim Biophys Acta Bioenerg. 34 (1959) 255–256.

[25] V. Fourmond, QSoas: A Versatile Software for Data Analysis, Anal. Chem. 88 (2016) 5050–5052.

[26] E.P. Friis, J.E.T. Andersen, L.L. Madsen, N. Bonander, P. Moller, J. Ulstrup, Dynamics of *Pseudomonas aeruginosa* azurin and its Cys3Ser mutant at single-crystal gold surfaces investigated by cyclic voltammetry and atomic force microscopy, Electrochim. Acta. 43 (1998) 1114–1122.

[27] S. Ciofi-Baffoni, A. Gallo, R. Muzzioli, M. Piccioli, The IR-15N-HSQC-AP experiment: A new tool for NMR spectroscopy of paramagnetic molecules, J. Biomol. NMR. 58 (2014) 123–128.

[28] F.K. Yousafzai, R.R. Eady, Dithionite reduction kinetics of the dissimilatory copper-containing nitrite reductase of *Alcalegenes xylosoxidans*. The SO2.- radical binds to the substrate binding type 2 copper site before the type 2 copper is reduced, J. Biol. Chem. 277 (2002) 34067–34073.

[29] A. Bax, G.M. Clore, Protein NMR: Boundless opportunities, J. Magn. Reson. 306 (2019) 187–191.

[30] J.A. Purslow, B. Khatiwada, M.J. Bayro, V. Venditti, NMR Methods for Structural Characterization of Protein-Protein Complexes, Front. Mol. Biosci. 7 (2020) 1–8.

[31] I.B. Trindade, M. Invernici, F. Cantini, R.O. Louro, M. Piccioli, Sequence-specific assignments in NMR spectra of paramagnetic systems: A non-systematic approach, Inorganica Chim. Acta. 514 (2021) 119984.

[32] N.A. Baker, D. Sept, S. Joseph, M.J. Holst, J. Andrew McCammon, Electrostatics of nanosystems: Application to microtubules and the ribosome, Proc. Natl. Acad. Sci. U.S.A. 98 (2001) 10037-10041.

[33] I.B. Trindade, A. Coelho, F. Cantini, M. Piccioli, R.O. Louro, NMR of paramagnetic metalloproteins in solution: *Ubi venire, quo vadis*?, J. Inorg. Biochem. 234 (2022) 111871.

[34] R.O. Louro, T. Catarino, C.A. Salgueiro, J. LeGall, A. v Xavier, Redox-Bohr effect in the tetrahaem cytochrome c 3 from *Desulfovibrio vulgaris*: a model for energy transduction mechanisms, J. Biol. Inorg. Chem. 1 (1996) 34–38.

[35] D.R. Lloyd, D.H. Phillips, Oxidative DNA damage mediated by copper II, iron II and ž / nickel II Fenton reactions: evidence for site-specific mechanisms in the formation of double-strand breaks, 8-hydroxydeoxyguanosine and putative intrastrand cross-links, Mutat. Res. 424 (1999) 23–36.

[36] I.B. Trindade, M. Invernici, F. Cantini, R.O. Louro, M. Piccioli, PRE-driven protein NMR structures: an alternative approach in highly paramagnetic systems, FEBS J. 288 (2021) 3010–3023.

[37] J. Jumper, R. Evans, A. Pritzel, T. Green, M. Figurnov, O. Ronneberger, K. Tunyasuvunakool, R. Bates, A. Žídek, A. Potapenko, A. Bridgland, C. Meyer, S.A.A. Kohl, A.J. Ballard, A. Cowie, B. Romera-Paredes, S. Nikolov, R. Jain, J. Adler, T. Back, S. Petersen, D. Reiman, E. Clancy, M. Zielinski, M. Steinegger, M. Pacholska, T. Berghammer, S. Bodenstein, D. Silver, O. Vinyals, A.W. Senior, K. Kavukcuoglu, P. Kohli, D. Hassabis, Highly accurate protein structure prediction with AlphaFold, Nature. 596 (2021) 583–589.

[38] A.F. Verissimo, F. Daldal, Cytochrome c biogenesis system I: An intricate process catalyzed by a maturase supercomplex?, Biochim Biophys Acta Bioenerg. 1837 (2014) 989–998.

[39] K.E. Pitts, P.S. Dobbin, F. Reyes-Ramirez, A.J. Thomson, D.J. Richardson, H.E. Seward, Characterization of the *Shewanella oneidensis* MR-1 decaheme cytochrome MtrA: Expression in *Escherichia coli* confers the ability to reduce soluble FE(III) chelates, J. Biol. Chem. 278 (2003) 27758–27765.

[40] P.J. Jackson, A. Hitchcock, D.J.K. Swainsbury, P. Qian, E.C. Martin, D.A. Farmer, M.J. Dickman, D.P. Canniffe, C.N. Hunter, Identification of protein W, the elusive sixth subunit of the *Rhodopseudomonas palustris* reaction center-light harvesting 1 core complex, Biochim Biophys Acta Bioenerg. 1859 (2018) 119–128.

[41] K.& F.C. Nelson, Champions of versatility, Trends Microbiol. 12 (2004) 106–111.

“The irony is that the actual story starts
from the moment we think that everything had ended.”
Aaliya Mallick

VII. Chapter VII: Conclusions and Future Perspectives

Iron is a key element for life, and this is made evident by the fact that despite the unfavorable odds following the GOE, iron was kept as a vital element for virtually all forms of life [1]. Iron incorporates cofactors and these catalyze or enable some of the most important biological reactions. In biology, iron for the most part cycles between ferric and ferrous iron forms. Ferrous iron is the preferred cellular “coin-of-exchange”, however, given its instability/high reactivity, this is usually either bound transiently to dedicated small molecules or proteins or stored in ferritins in its oxidized form as ferric iron [2–4].

The relatively high need for iron, which contrasts with its low bioavailability, drove selective pressure on the development of sophisticated iron uptake systems for scavenging this essential element. Furthermore, it drove the development of tight iron sensing and regulation mechanisms in a way that prevents the hazardous effect of this precious metal in the presence of oxygen [5,6].

Siderophores are produced when iron levels are low and this is usually translated into two general scenarios: low iron levels in the environment, e.g., precipitated as ferric oxides in the soil or ocean, or the competition for iron is very high, e.g., host-pathogen interactions where nutritional immunity keeps iron away from pathogens [5,7,8].

Ferric-siderophore reductases, here including both FSRs and SIPs, catalyze the reduction of ferric-iron within Fe(III)-siderophores. This lowers the affinity of iron for these ligands and thus promotes complex dissociation and iron release in the ferrous form which is suitable for incorporating cellular metabolism. It is still unclear which are the immediate partners upon iron release, i.e.. labile iron pool, proteins from the heme or iron-sulfur maturation pathways or does it bind ferrous-iron sensors or iron chaperons? [8–13].

This work focused mainly on understanding how the biochemical and spectroscopic features of FhuF (archetypical FSR) tie in with the structural properties of this protein [12,14,15]. The structure of FhuF was determined using X-ray crystallography, and this is the first structure for the FSR family of proteins. FhuF has a novel cluster binding mode and in agreement with the concept of the rack-induced model, this is likely imposed by atypical cysteine binding motif (CC-x_{10}-C-X_2) which in turn gives rise to its peculiar spectroscopic properties. Altogether, these results position FhuF as a novel ferredoxin. Additionally, the 2Fe-2S coordination mode of FhuF also shows similarities with ferrochelatases, interestingly, proteins that are also involved in iron uptake [16,17]. Unfortunately, besides ensuring protein stability, the catalytic function of the 2Fe-2S cluster in those proteins remains unknown. Furthermore, as previously predicted in the Rosetta model of FhuF, the structure of FhuF resembles the catalytic domain of NIS, one of the siderophore synthetase families, arguing for the possibility of these enzymes playing a role in siderophore modification. It has been previously reported that ferrichrome is modified upon cellular uptake/reduction. The modified product of ferrichrome showed a significantly decreased affinity for ferric iron, questioning the proposed siderophore recycling hypothesis [18]. Thus, FhuF playing a role in siderophore modification would highlight the importance of these enzymes for competitive interactions for iron scavenging since hydroxamate siderophores are not known to be produced by *E. coli.* However, the fact that *E. coli* can compete for their acquisition and then modify them preventing further recycling of these compounds would be a very efficient competitive strategy that is yet to be proved.

This thesis opened the door for the investigation of FSR, with potential consequences for modulating the fitness of organisms in the environment and in infected hosts. Unfortunately, the instability of FSRs had hindered so far the characterization of these enzymes since their discovery [14,19]. In this line of thought, the structure and work developed for FhuF also paves the way for improving the stability of other FSRs so that their production and further characterization becomes feasible. In this aspect, we also showed that the production of these proteins is possible with the expression and purification of an FSR from *S. bicestrii* (*Sb*FSR). Unfortunately, this protein showed greater instability when compared to FhuF. A structural model using AlphaFold and comparison with FhuF, shows that *Sb*FSR contains a longer N-terminal loop which is missing in the structure of FhuF and the corresponding sequence has very low predictability confidence in AlphaFold. In similarity with the genome of *E. coli*, *S. bicestrii* also contains genes coding for both FSRs and SIPs. Thus, here we also produced and characterized the SIP from *S. bicestrii* (*Sb*SIP). This protein revealed novel biochemical features, including different affinities for NADH and NADPH and a lower activity for Fe(III)-siderophores. These results together with the structural properties of *Sb*SIP validate the putative binding pocket for NAD(P)H. Unfortunately, despite our efforts to obtain crystals with bound ligand, the binding pocket for the redox partners for both SIPs and FSRs remains open for discussion.

Regardless, this work revealed common features amongst SIPs and FSRs which extend from ferric-siderophore reduction. This includes the redox-Bohr effect, which increases the effective reduction potential of Fe(III)-siderophores easing their reduction but also ensuring a localized pH drop that enhances iron solubility. In agreement, the structure of these proteins also shows a common positively charged pocket that surrounds the catalytic center, which promotes proton transfer coupled with the transfer of electrons.

This work contributes to the development of strategies for interfering with the iron metabolism of Gram-negative bacteria, especially with the intent of controlling the unacceptable effects of antimicrobial resistance. Ferric-siderophore reduction, despite the apparent redundancy between SIPs and FSRs seems one of the narrowest and, almost unavoidable, funnel points of the siderophore pathway. However, further knowledge is necessary to understand the physiological requirements for the use of SIPs and FSRs and what drove the selection of one family of enzymes over the other in different microorganisms. It is also necessary to investigate if FSRs, in a similar manner to SIPs, play a role in the virulence of pathogens. So far, the mechanistic aspects of siderophore uptake have been highly explored. However, very little is known regarding the ecology and evolutionary aspects of these compounds for the microbial community [20]. It is of the utmost importance to understand the extent and impact of cheaters within the microbial community so that we can fully explore which Fe(III)-siderophores go through Fe(III)-siderophore reduction.

This work also features some of the caveats of studying proteins that contain and/or interact with metals. This includes sample instability and high sensitivity/variability to changes in temperature, pH, and buffer composition. Furthermore, redox-active metals contain unpaired electrons which for their highly reactive nature defy most conventional methods and techniques including NMR spectroscopy. On the other hand, the presence of unpaired electrons can represent unique opportunities to explore the unparallel properties of metal cofactors and their interactions in conditions that can mimic physiology [21,22]. Thus, we developed a novel strategy for determining the structure of metalloproteins using the model HiPIP PioC from *R. palustris*, having for the first time, determined a structure by NMR spectroscopy using exclusively paramagnetic constraints (PREs). This strategy was only possible due to the development of novel pulse sequences which allowed for the measurement of PREs which substituted for the lack of NOEs, caused by fast relaxation together with the small size of this protein [23–27]. The future beckons now for using this strategy for more challenging systems such as FhuF for e.g., where the backbone assignment of this protein will reveal key aspects regarding the interaction of this protein with redox partners or even possible inhibitors for these proteins. As proof of concept, we further used the assignment of PioC for studying the interaction of this protein with its physiological partners. We confirmed the previously proposed pio *o*peron pathway, where HiPIP PioC transfers electrons from PioA into the LH-RC [28,29]. We revealed interacting amino acid residues further explaining why Rpal_4085, another periplasmic HiPIP, cannot substitute for PioC, and instead, this is achieved by PioA which can also be soluble in the periplasm.

Overall, this work opened the door for a renaissance of the study of paramagnetic metalloproteins by NMR both with respect to their structure and their physiological function and interactions. Furthermore, it highlights that the investigation of biological problems requires the use of diverse methods to get to the bottom of it and that the realms of what can be investigated can be pushed further by developing new methods as the need arises.

VIII. Supplementary Information

Chapter II: Conjuring up a ghost: Structural and functional characterization of FhuF, a ferric siderophore reductase from *E. coli*

Table (II) **S1** SEC-SAXS data collection conditions.

	FhuF
Data acquisition	
Beamline – Facility	B21-DSL
Wavelength (Å)	0.91
Sample-to-detector distance (m)	2.7
s range ($Å^{-1}$)	0.0036-0.4396
Concentration ($mg\cdot mL^{-1}$)	~9
HPLC system / SEC column	Agilent 1200 HPLC / Shodex KW402.5-4F
Detector	Pilatus 2M
Temperature (K)	283.15

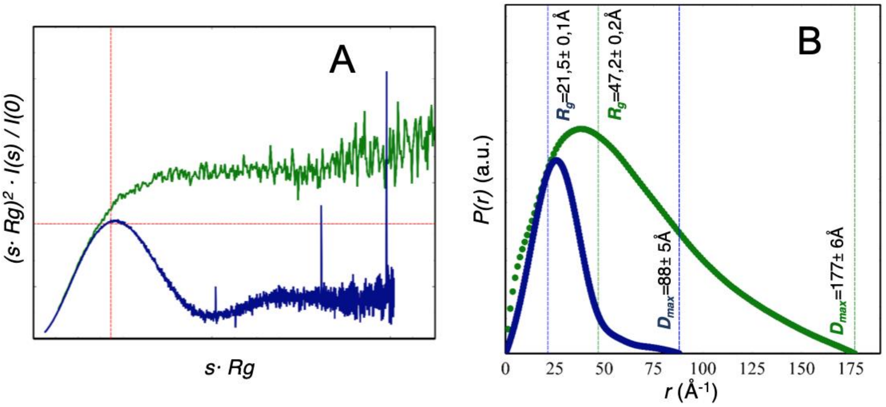

Figure (II) **S1** Comparative SAXS: FhuF versus an IDP-like protein of 29 kDa **A)** Kratky representations of the SAXS patterns of FhuF (blue) and N-CoR-NID (dark green) next to their respective P(r) versus r profiles, **B)** plotted using the same color code. Dashed lines indicate the Rg and Dmax values. The SAXS experimental set for the region spanning from residue Gln2059 to Glu2325 of the Nuclear Receptor Co-Repressor (N-CoR-NID).

.

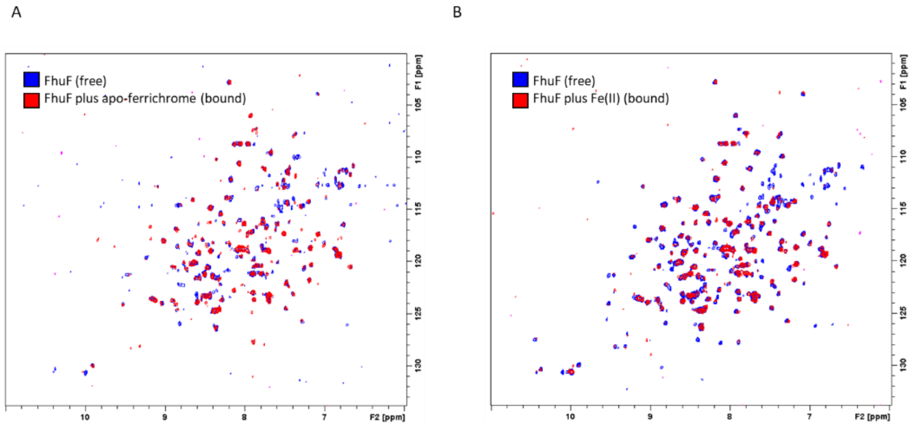

Figure (II) **S2 A)** 2D ^{1}H^{15}N TROSY-HSQC spectra of ^{15}N^{13}C-labeled FhuF portraying the spectral changes observed upon the addition of apo-ferrichrome. **B)** 2D ^{1}H^{15}N TROSY-HSQC spectra of ^{15}N^{13}C-labeled FhuF portraying the spectral changes observed upon the addition of Fe(II).

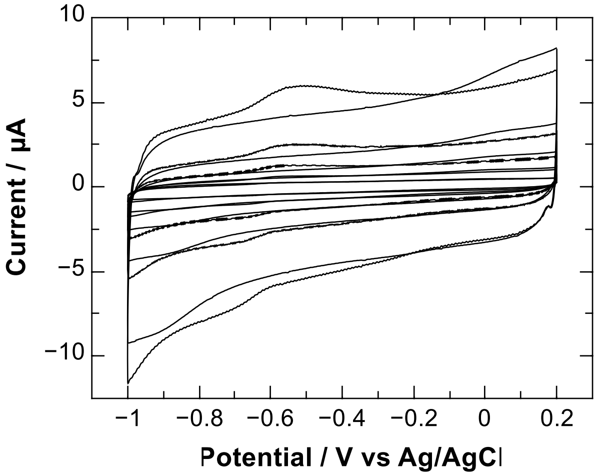

Figure (II) **S3** Raw voltammograms of unmodified (dashed line) and FhuF-modified (solid line) PGE recorded at different scan rates (20; 50; 100; 200; 500 mV/s) in 20 mM potassium phosphate buffer pH 7.9.

Chapter III: The structure of a novel ferredoxin – FhuF, a ferric-siderophore reductase from *Escherichia coli* K-12 with a novel 2Fe-2S cluster coordination

Table (III) **S1** List of amino-acid sequences of FhuF obtained and reported in the manuscript.

Sequence name	**Sequence**
FhuF WT (from gene)	MAYRSAPLYEDVIWRTHLQPQDPTLAQAVRATIAKHREHLLEFIRLDEPAPLNAMTLAQWSSPNVLSSLLAVYSDHIYRNQPMMIRENKPLISLWAQWYIGLMVPPLMLALLTQEKALDVSPEHFHAEFHETGRVACFWVDVCEDKNATPHSPQHRMETLISQALVPVVQALEATGEINGKLIWSNTGYLINWYLTEMKQLLGEATVESLRHALFFEKTLTNGEDNPLWRTVVLRDGLLVRRTCCQRYRLPDVQQCGDCTLK
FhuF WT expressed	MGHHHHHHHHHHSSGHIDDDDKHMMAYRSAPLYEDVIWRTHLQPQDPTLAQAVRATIAKHREHLLEFIRLDEPAPLNAMTLAQWSSPNVLSSLLAVYSDHIYRNQPMMIRENKPLISLWAQWYIGLMVPPLMLALLTQEKALDVSPEHFHAEFHETGRVACFWVDVCEDKNATPHSPQHRMETLISQALVPVVQALEATGEINGKLIWSNTGYLINWYLTEMKQLLGEATVESLRHALFFEKTLTNGEDNPLWRTVVLRDGLLVRRTCCQRYRLPDVQQCGDCTLK
FhuF WT cleaved	LQPQDPTLAQAVRATIAKHREHLLEFIRLDEPAPLNAMTLAQWSSPNVLSSLLAVYSDHIYRNQPMMIRENKPLISLWAQWYIGLMVPPLMLALLTQEKALDVSPEHFHAEFHETGRVACFWVDVCEDKNATPHSPQHRMETLISQALVPVVQALEATGEINGKLIWSNTGYLINWYLTEMKQLLGEATVESLRHALFFEKTLTNGEDNPLWRTVVLRDGLLVRRTCCQRYRLPDVQQCGDCTLK
FhuF- C143S expressed	MGHHHHHHHHHHSSGHIDDDDKHMMAYRSAPLYEDVIWRTHLQPQDPTLAQAVRATIAKHREHLLEFIRLDEPAPLNAMTLAQWSSPNVLSSLLAVYSDHIYRNQPMMIRENKPLISLWAQWYIGLMVPPLMLALLTQEKALDVSPEHFHAEFHETGRVACFWVDVSEDKNATPHSPQHRMETLISQALVPVVQALEATGEINGKLIWSNTGYLINWYLTEMKQLLGEATVESLRHALFFEKTLTNGEDNPLWRTVVLRDGLLVRRTCCQRYRLPDVQQCGDCTLK
FhuF- C143S cleaved	LQPQDPTLAQAVRATIAKHREHLLEFIRLDEPAPLNAMTLAQWSSPNVLSSLLAVYSDHIYRNQPMMIRENKPLISLWAQWYIGLMVPPLMLALLTQEKALDVSPEHFHAEFHETGRVACFWVDVSEDKNATPHSPQHRMETLISQALVPVVQALEATGEINGKLIWSNTGYLINWYLTEMKQLLGEATVESLRHALFFEKTLTNGEDNPLWRTVVLRDGLLVRRTCCQRYRLPDVQQCGDCTLK
FhuF- C143S as in structure	PQDPTLAQAVRATIAKHREHLLEFIRLDEPAPLNAMTLAQWSSPNVLSSLLAVYSDHIYRNQPMMIRENKPLISLWAQWYIGLMVPPLMLALLTQEKALDVSPEHFHAEFHETGRVACFWVDVSEDKNATPHSPQHRMETLISQALVPVVQALEATGEINGKLIWSNTGYLINWYLTEMKQLLGEATVESLRHALFFEKTLTNGEDNPLWRTVVLRDGLLVRRTCCQRYRLPDVQQCGDCTLK

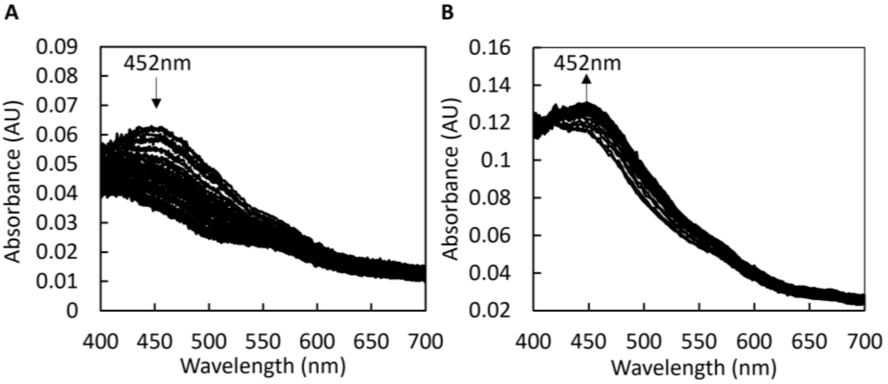

Figure (III) **S1 A)** Representative UV-visible spectral changes upon mixing sodium dithionite with FhuF. **B)** Representative UV-visible spectral changes upon mixing $\mathrm{FhuF_{red}}$ with Fe(III)-Ferrichrome.

Chapter IV: Ferric-siderophore reduction in *Shewanella bicestrii*: Structural and functional characterization of *Sb*SIP reveals an overlooked specificity of siderophore-interacting proteins

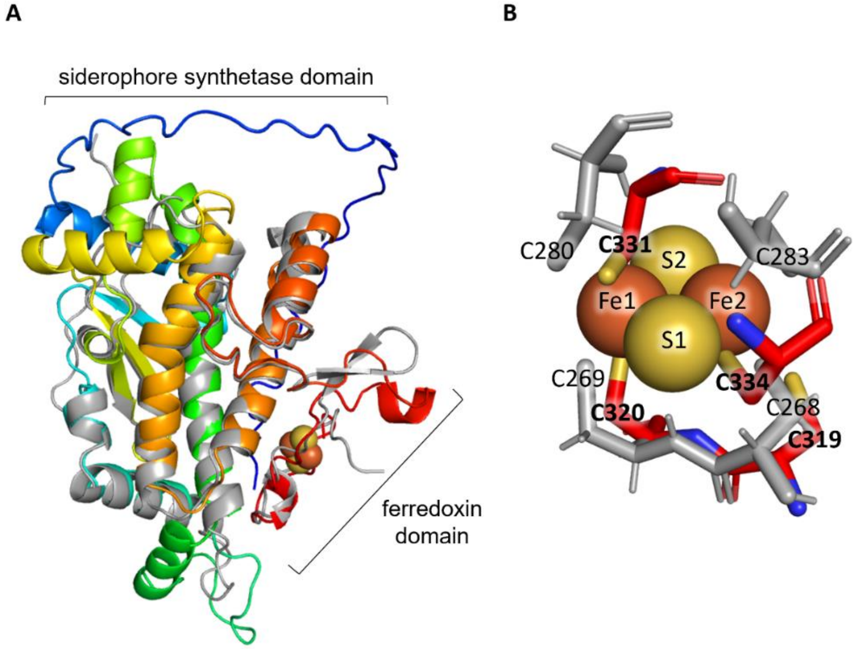

Figure (IV) **S1 A)** *Sb*FSR structural model vs the structure of FhuF from *E. coli* (PDB 7QP5). **B)** Close-up to the 2Fe-2S within the ferredoxin domain highlighting coordinating cysteines.

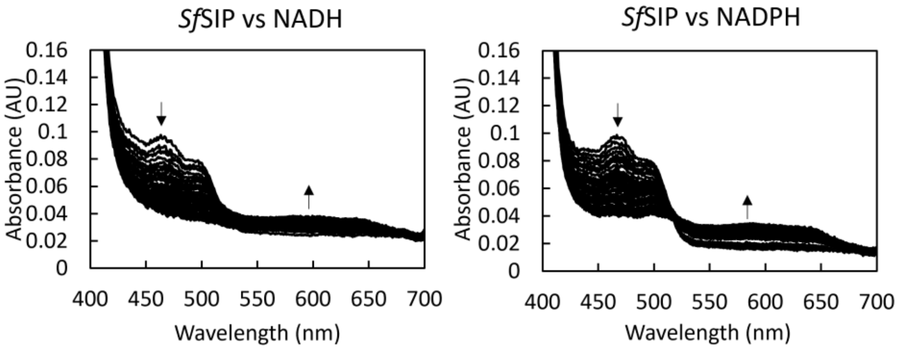

Figure (IV) **S2 A)** Representative UV-visible spectral changes upon mixing *Sf*SIP with NADH and **B)** NADPH. Arrows indicate the decrease at 470nm and increase at 600nm (formation of semiquinone state).

Chapter V: PRE-driven Protein NMR Structures - an alternative paradigm in Highly Paramagnetic Systems

Table (V) **S1** List of experiments collected to perform the sequence specific assignment and the structure calculations. Main parameters and magnetic fields used are reported.

Experiments	**Time Domain Data Size (points)**			**Spectral width (ppm)**			**ns**	**Delay time (s)**	**Magnetic field (MHz) (^{1}H Larm freq)**
	t_1	**t_2**	**t_3**	**F_1**	**F_2**	**F_3**			
[^{1}H-^{1}H]-NOESY	1024	2048		14.6 (^{1}H)	14.6 (^{1}H)		48	1.2	900
[^{1}H-^{1}H]-TOCSY	600	2048		14.0 (^{1}H)	14.0 (^{1}H)		48	2.0	600
^{1}H-^{15}N-HSQC	128	2048		40.0 (^{15}N)	13.2 (^{1}H)		2	1.5	500
^{1}H-^{13}C-HSQC	320	1024		80.0 (^{13}C)	13.0 (^{1}H)		20	2.0	600
CBCACONH	128	48	1800	80.0 (^{13}C)	40.0 (^{15}N)	13.2 (^{1}H)	8	1.3	900
CBCANH	128	48	1800	80.0 (^{13}C)	40.0 (^{15}N)	13.2 (^{1}H)	16	1.3	900

HNCO	72	48	1800	16.0 (^{13}C)	40.0 (^{15}N)	13.2 (^{1}H)	8	1.3	900
HNCACO	72	48	1800	16.0 (^{13}C)	40.0 (^{15}N)	13.2 (^{1}H)	24	1.3	900
HNCA	96	48	1800	40.0 (^{13}C)	40.0 (^{15}N)	13.2 (^{1}H)	16	1.3	900
HBHANH	128	40	2048	13.2 (^{1}H)	40.0 (^{15}N)	13.2 (^{1}H)	16	1.3	900
HNHA	48	128	2048	40.0 (^{15}N)	13.2 (^{1}H)	13.2 (^{1}H)	16	1.3	900
(H)CCH-TOCSY	128	64	1800	80.0 (^{13}C)	80.0 (^{15}N)	13.2 (^{1}H)	16	1.5	900
^{15}N-edited [^{1}H-^{1}H]-NOESY	128	40	2048	13.2 (^{1}H)	40.0 (^{15}N)	13.2 (^{1}H)	32	1.2	900
^{13}C-edited [^{1}H-^{1}H]-NOESY	192	64	2048	14.0 (^{1}H)	80.0 (^{13}C)	14.0 (^{1}H)	32	1.2	950
^{15}N R_1	128	1024		41.0 (^{15}N)	15.6 (^{1}H)		16	3.0	500
^{15}N R_2	128	1024		41.0 (^{15}N)	15.6 (^{1}H)		16	3.0	500
^{15}N- NOE	144	1024		41	15.6		56	5.0	500
^{1}HN R_1	220	1024		80.0 (^{15}N)	21.7 (^{1}H)		16	4.0	500
^{1}HN R_2	156	1024		80.0 (^{15}N)	21.7 (^{1}H)		64	4.0	500
^{1}HC R_1	320	1024		80.0 (^{13}C)	13.0 (^{1}H)		20	2.0	600
CON	128	1024		40.6 (^{15}N)	47.0 (^{13}C)		64	1.0	700

Table (V) **S2** List of experiments optimized to identify fast relaxing resonances. Main parameters and magnetic fields used are reported.

Experiments	**Time Domain Data Size (points)**		**Spectral width (ppm)**		**ns**	**Delays (s)**	**Magnetic field (MHz) (^{1}H Larm. freq)**
	t_1	**t_2**	**F_1**	**F_2**			
^{1}H-NOE	8192		80.0 (^{1}H)		400000	aq= 133 ms saturation=110ms	400
IR-^{15}N-HSQC-AP	220	1024	80.0	21.7 (^{1}H)	256	aq=47ms recyc=0.15s invrec=0.2s ⍰=700us	500
R_2-weighted ^{15}N HSQC-AP	256	1024	80.0 (^{15}N)	21.7 (^{1}H)	256	aq=47ms recyc=0.15s ⍰=2.0ms	500
^{1}H-^{13}C-HNCA	160	1024	100.0 (^{13}C)	25.0 (^{1}H)	512	aq=40ms Recyc=0.5s ⍰=2.0ms	500
^{1}H-$^{1\%}$N-HNCA	128	1024	70.0 (^{15}N)	25.0 (^{1}H)	512	aq=40ms Recyc=0.5s ⍰=2.0ms	500
1d-^{13}C	8192		245.6 (^{13}C)		32768	aq= 71ms recyc=73ms	900
[^{13}C-^{13}C]-COSY	500 (400)	2048 (1500)	258.2 (^{13}C)	258.2 (^{13}C)	480	aq=22ms recyc= 0.2s	700
IR-^{13}C-HSQC-AP	256	2048 (512)	136.0 (^{13}C)	60.2 (^{1}H)	1024	aq=34ms recyc=0.15s ⍰=2.0ms Invrec=30ms	500
IR-^{13}C HSQC $^{1}H_C$ R_1	320	1024	136.0 (^{13}C)	60.2 (^{1}H)	320	aq=17ms recyc=0.12s invrec=80ms ⍰=600us	500
IR-^{13}C HSQC-AP $^{1}H_C$ R_1	320	1024	136.0 (^{13}C)	60.2 (^{1}H)	1024	aq=17ms recyc=34ms invrec=80ms ⍰=600us	500

Table (V) **S3** Relaxation rates, measured at 298K, 500 MHz, of ^{1}H signals in PioC. Values measured in experiments optimized for the detection of fast relaxing signals are shown in bold italics.

Residues		**^{1}H$_{N}$ R$_{2}$ (s^{-1})**	**Err**	**^{1}H$_{N}$ R$_{1}$ (s^{-1})**	**Err**
VAL	1				
THR	2	11.1	0.4	12.9	0.5
LYS	3	15.4	1.3	15.9	0.8
LYS	4	19.1	1.5	3.83	0.1
ALA	5	23.4	0.8	5.41	0.17
SER	6	17.8	0.6	2.21	0.08
HIS	7	21.3	0.8	4.90	0.08
LYS	8	32.8	2.2	14.8	0.5
ASP	9	16.9	0.7	2.74	0.13
ALA	10	19.6	0.8	7.28	0.25
GLY	11	20.0	1.4	4.77	0.12
TYR	12	29.9	1.5	11.1	0.5
GLN	13	***53.2***	***4.1***	***16.6***	***0.6***
GLU	14	19.4	1.1	3.18	0.11
SER	15	21.6	1.0	3.19	0.18
PRO	16				
ASN	17	22.8	1.1	4.69	0.19
GLY	18	25.1	1.5	7.50	0.36
ALA	19	44.4	2.8	22.5	1.3
LYS	20	17.8	0.8	2.79	0.19
ARG	21	44.4	3.4	12.0	0.6
CYS	22	***311***	***18***	***116***	***32***
GLY	23	***60.4***	***6.8***	***19.0***	***0.6***
THR	24	42.0	2.8	14.6	0.3
CYS	25	***60.1***	***2.8***	***37.6***	***3.8***
ARG	26	***43.6***	***3.6***	***32.0***	***8.5***
GLN	27	***246***	***18***	***160***	***13***
PHE	28	***146***	***9***	***89.1***	***5.6***
ARG	29	***49.3***	***3.0***	***25.0***	***1.0***
PRO	30				
PRO	31				
SER	32	25.1	1.5	7.50	0.36
SER	33	24.2	0.8	5.75	0.27
CYS	34	42.5	4.0	17.6	0.5
ILE	35	***81.4***	***5.7***	***48.0***	***5.1***
THR	36	***107***	***9***	***100***	***7***
VAL	37	***156***	***16***	***129***	***12***
GLU	38	24.2	0.8	8.71	0.17

SER	39	19.7	1.0	3.89	0.10
PRO	40				
ILE	41	27.7	1.3	5.61	0.12
SER	42	42.8	2.4	13.9	0.4
GLU	43	19.2	0.5	5.18	0.06
ASN	44	27.4	1.5	5.62	0.11
GLY	45	***59.3***	***4.3***	***24.7***	***1.2***
TRP	46	***69.5***	***5.2***	***42.7***	***2.3***
CYS	47	***194***	***10***	***134***	***29***
ARG	48	***53.5***	***4.2***	***35.4***	***2.1***
LEU	49	***167***	***15***	***129***	***7***
TYR	50	***47.7***	***7.8***	***39.8***	***10.5***
ALA	51	***240***	***36***		
GLY	52	23.0	1.3	6.38	0.19
LYS	53	18.0	0.9	6.42	0.18
ALA	54	7.7	0.3	2.15	0.07
Trp sc	46	33.9	2.1		

Residues		**R$_1$ H$_\alpha$ (s^{-1})**	**R$_1$ H$_\beta$ (s^{-1})**	**R$_1$ H$_\gamma$ (s^{-1})**	**R$_1$ H$_\delta$ (s^{-1})**	**R$_1$ H$_\varepsilon$ (s^{-1})**	**R$_1$ other (s^{-1})**
VAL	1						
THR	2	2.50	2.66	2.73			
LYS	3	2.34	3.60	2.80	2.56	2.14	
LYS	4	3.79	3.93/4.41	4.40/6.36		3.94/4.25	
ALA	5	2.93	7.20				
SER	6	2.92	2.23/2.47				
HIS	7	10.2	4.06/4.13				
LYS	8	2.39	3.16/3.36	3.17/3.15	2.77/2.69	2.44	
ASP	9	1.96	2.72/2.80				
ALA	10	8.16	5.58				
GLY	11	5.01/3.09					
TYR	12	16.7	24.6/15.8		*56.7*		
GLN	13	3.22	2.78/3.41	5.03/5.09			
GLU	14	4.79	3.00/2.79	4.02			
SER	15	2.30	2.94/2.96				
PRO	16	4.99	4.04/3.61	3.10/6.02	2.46/2.58		
ASN	17	2.24	4.48/4.23				
GLY	18	1.37/2.14					
ALA	19	1.55	2.31				
LYS	20	5.78	6.90/8.35	4.60	3.67/4.27	2.35/2.32	
ARG	21	29.8	8.09/3.03	5.26/7.89	4.08/4.01		
CYS	22	***53.6***	***368/130***				***^{13}Cβ 67***
GLY	23	7.81/6.15					

THR	24		4.47	3.77			
CYS	25	***59.2***	***313/282***				***^{13}Cβ59 ^{13}Cα 13***
ARG	26	10.2	8.02/4.87	8.65/6.67	3.65/4.54		
GLN	27	29.6	1.61	1.76/2.03			
PHE	28	2.34	***45.1***		***44.5***		
ARG	29	4.94	5.32/6.11	5.96/5.40	4.22/4.39		
PRO	30	3.36	2.43/2.50	2.31/2.48	3.28/4.38		
PRO	31	2.15	1.64/1.97	4.79/2.02	1.77/1.42		
SER	32	4.67	3.45/3.44				
SER	33		5.89/5.72				
CYS	34	***69.3***	***164/588***				***^{13}Cβ65***
ILE	35	8.32	10.9	6.84/10.0/7.56	4.95		
THR	36	3.00	2.49	2.98			
VAL	37	21.6		59.9			
GLU	38	4.41	4.50/4.53	3.66/3.58			
SER	39	6.34	3.08/2.69				
PRO	40	3.62	2.12/2.79	4.69/4.24	1.88/1.87		
ILE	41	4.42	34.1	31.9/37.5/95.0	2.71		
SER	42	5.17	5.72/8.04				
GLU	43	16.2	4.91/4.19	4.03/3.26			
ASN	44	5.53	3.35/3.62				
GLY	45	14.9/10.9					
TRP	46		16.7/22.7		***36.4***	***84.3***	
CYS	47		***130/450***				***^{13}Cβ67***
ARG	48	13.8	4.23	7.25/6.63	3.10/4.39		
LEU	49	12.7		4.44	5.37		
TYR	50	2.70			***97.0***		
ALA	51	10.7	13.1				
GLY	52	4.12/7.56					
LYS	53	3.64	4.31	4.75	3.55		
ALA	54	2.56	2.08				

Table (V) **S4** Upper limit distances obtained from PREs used for structure calculations.

residues	**n.**	νυχλευσ	**metal center**[a]	**n.**	**upper limit (Å)**	**weight**[b]
LYS	8	H_N	Fe	4	9.60	2.00
GLY	11	H_N	Fe	4	10.0	
TYR	12	H_N	Fe	4	9.20	
TYR	12	H_δ	Fe	1	6.50	
GLN	13	H_N	Fe	1	7.50	2.00
ASN	17	H_N	Fe	1	8.80	
LYS	20	H_N	Fe	1	12.00	
ARG	21	H_N	Fe	1	9.00	2.00
CFS	22	H_N	Fe	1	4.90	2.00
GLY	23	H_N	Fe	1	6.70	2.00
THR	24	H_N	Fe	2	8.30	2.00
CFS	25	H_N	Fe	2	6.10	2.00
ARG	26	H_N	Fe	2	6.20	
GLN	27	H_N	Fe	2	5.00	2.00
PHE	28	H_N	Fe	2	5.50	2.00
PHE	28	H_N	Fe	3	5.80	2.00
PHE	28	H_δ	Fe	3	7.50	
PHE	28	H_δ	Fe	1	7.50	
ARG	29	H_N	Fe	3	7.00	
SER	33	H_N	Fe	3	9.00	
CFS	34	H_N	Fe	3	7.10	
ILE	35	H_N	Fe	3	6.00	2.00
THR	36	H_N	Fe	3	5.20	2.00
VAL	37	H_N	Fe	3	5.00	2.00
ILE	41	H_N	Fe	3	9.00	
SER	42	H_N	Fe	3	8.10	
ASN	44	H_N	Fe	1	9.00	
GLY	45	H_N	Fe	1	6.80	2.00
TRP	46	H_N	Fe	1	6.00	2.00
CFS	47	H_N	Fe	4	4.80	2.00
ARG	48	H_N	Fe	4	6.10	2.00

LEU	49	H_N	Fe	4	5.00	2.00
TYR	50	$H_{\varepsilon1}$	Fe	2	5.00	
TYR	50	H_N	Fe	4	6.20	2.00
ALA	51	H_N	Fe	2	5.40	
TRP	46	$H_{\varepsilon1}$	Fe	4	7.50	
TRP	46	$H_{\varepsilon1}$	Fe	1	7.40	
TRP	46	$H_{\delta1}$	Fe	4	6.30	
TRP	46	$H_{\delta1}$	Fe	1	6.00	
CFS	22	$H_{\beta3}$	Fe	1	3.74	
CFS	22	$H_{\beta2}$	Fe	1	4.46	
CFS	25	$H_{\beta3}$	Fe	2	3.91	
CFS	25	$H_{\beta2}$	Fe	2	3.84	
CFS	34	$H_{\beta2}$	Fe	3	4.20	
CFS	47	$H_{\beta2}$	Fe	4	4.30	
CFS	47	$H_{\beta3}$	Fe	4	3.62	
CFS	22	X_{β}	Fe	1	3.30	
CFS	25	X_{β}	Fe	2	3.20	
CFS	25	X_{α}	Fe	2	4.60	
CFS	34	X_{β}	Fe	3	3.20	
CFS	47	X_{β}	Fe	4	3.40	
CFS	22	H_{α}	Fe	1	5.21	
CFS	25	H_{α}	Fe	2	5.21	
CFS	34	H_{α}	Fe	3	4.76	
HIS	7	H_{α}	Fe	4	7.25	
ALA	10	H_{α}	Fe	4	7.68	
GLY	11	$H_{\alpha2}$	Fe	4	9.13	
TYR	12	H_{α}	Fe	4	6.49	
GLU	14	H_{α}	Fe	1	9.74	
PRO	16	H_{α}	Fe	1	9.15	
LYS	20	H_{α}	Fe	2	8.59	
ARG	21	H_{α}	Fe	1	5.90	
GLY	23	$H_{\alpha3}$	Fe	1	7.70	
GLY	23	$H_{\alpha3}$	Fe	1	8.30	
ARG	26	H_{α}	Fe	2	8.24	

GLN	27	H_{α}	Fe	2	6.90	
ARG	29	H_{α}	Fe	3	9.20	
SER	32	H_{α}	Fe	3	9.47	
ILE	35	H_{α}	Fe	3	7.64	
VAL	37	H_{α}	Fe	3	6.40	
GLU	38	H_{α}	Fe	3	9.82	
SER	39	H_{α}	Fe	3	8.55	
PRO	40	H_{α}	Fe	3	12.02	
ILE	41	H_{α}	Fe	1	9.80	
SER	42	H_{α}	Fe	1	9.00	
GLU	43	H_{α}	Fe	1	6.53	
ASN	44	H_{α}	Fe	1	8.74	
GLY	45	$H_{\alpha 2}$	Fe	1	6.64	
GLY	45	$H_{\alpha 3}$	Fe	1	7.13	
ARG	48	H_{α}	Fe	4	6.76	
LEU	49	H_{α}	Fe	4	6.89	
ALA	51	H_{α}	Fe	2	8.00	
ALA	51	H_{α}	Fe	2	7.00	
GLY	52	$H_{\alpha 2}$	Fe	2	10.32	
LYS	53	H_{α}	Fe	2	11.92	
LYS	4	$H_{\beta 2}$	Fe	3	10.73	
LYS	4	$H_{\beta 3}$	Fe	3	9.79	
ALA	5	H_{β}	Fe	3	8.00	
HIS	7	$H_{\beta 2}$	Fe	1	10.40	
HIS	7	$H_{\beta 3}$	Fe	1	10.26	
ALA	10	H_{β}	Fe	4	8.70	
TYR	12	$H_{\beta 2}$	Fe	1	6.01	
TYR	12	$H_{\beta 3}$	Fe	1	6.56	
PRO	16	$H_{\beta 2}$	Fe	1	10.45	
PRO	16	$H_{\beta 3}$	Fe	1	12.00	
ASN	17	$H_{\beta 2}$	Fe	4	9.69	
ASN	17	$H_{\beta 3}$	Fe	4	10.07	
LYS	20	$H_{\beta 2}$	Fe	2	9.00	
LYS	20	$H_{\beta 3}$	Fe	2	8.90	

ARG	21	$H_{\beta2}$	Fe	1	7.69	
THR	24	H_{β}	Fe	2	9.70	
ARG	26	$H_{\beta2}$	Fe	2	7.70	
ARG	26	$H_{\beta3}$	Fe	2	9.25	
PHE	28	H_{β}	Fe	3	5.50	
PHE	28	H_{β}	Fe	2	5.50	
ARG	29	$H_{\beta2}$	Fe	3	8.87	
ARG	29	$H_{\beta3}$	Fe	3	8.40	
SER	33	$H_{\beta2}$	Fe	3	8.52	
SER	33	$H_{\beta3}$	Fe	3	8.61	
ILE	35	H_{β}	Fe	3	7.12	
GLU	38	$H_{\beta2}$	Fe	3	9.86	
GLU	38	$H_{\beta3}$	Fe	3	9.82	
ILE	41	H_{β}	Fe	3	6.50	
SER	42	$H_{\beta2}$	Fe	1	8.61	
SER	42	$H_{\beta3}$	Fe	1	7.71	
GLU	43	$H_{\beta2}$	Fe	3	9.41	
GLU	43	$H_{\beta3}$	Fe	3	10.15	
ASN	44	$H_{\beta3}$	Fe	1	11.96	
TRP	46	$H_{\beta2}$	Fe	1	6.49	
TRP	46	$H_{\beta3}$	Fe	1	6.30	
ARG	48	H_{β}	Fe	4	10.08	
ALA	51	H_{β}	Fe	2	6.80	
LYS	53	H_{β}	Fe	2	9.94	
LYS	3	H_{δ}	Fe	3	13.52	
LYS	20	$H_{\delta2}$	Fe	2	10.40	
LYS	20	$H_{\delta3}$	Fe	2	9.80	
LYS	8	$H_{\delta2}$	Fe	4	12.34	
LYS	8	$H_{\delta3}$	Fe	4	12.73	
PRO	16	$H_{\delta2}$	Fe	1	14.48	
PRO	16	$H_{\delta3}$	Fe	1	13.37	
PRO	30	$H_{\delta2}$	Fe	3	10.98	
PRO	30	$H_{\delta3}$	Fe	3	9.71	
ARG	21	$H_{\delta2}$	Fe	1	9.96	

ARG	21	$H_{\delta3}$	Fe	1	10.03	
ARG	26	$H_{\delta2}$	Fe	2	10.00	
ARG	26	$H_{\delta3}$	Fe	2	9.3	
ARG	29	$H_{\delta2}$	Fe	3	10.00	
ARG	29	$H_{\delta3}$	Fe	3	9.71	
ARG	48	$H_{\delta2}$	Fe	4	11.36	
ARG	48	$H_{\delta3}$	Fe	4	9.71	
LYS	53	H_{δ}	Fe	2	10.56	
ILE	35	$H_{\delta1}$	Fe	3	9.34	
ILE	41	$H_{\delta1}$	Fe	3	12.61	
LEU	49	$H_{\delta2}$	Fe	4	9.11	
LYS	4	$H_{\gamma2}$	Fe	3	10.48	
LYS	4	$H_{\gamma3}$	Fe	3	9.02	
LYS	4	$H_{\varepsilon2}$	Fe	3	10.14	
LYS	4	$H_{\varepsilon3}$	Fe	3	9.85	
GLN	13	$H_{\gamma2}$	Fe	4	9.83	
GLN	13	$H_{\gamma3}$	Fe	4	9.78	
GLU	14	H_{γ}	Fe	1	11.08	
PRO	16	$H_{\gamma3}$	Fe	1	9.18	
LYS	20	$H_{\gamma2}$	Fe	2	9.99	
LYS	20	$H_{\gamma3}$	Fe	2	10.24	
ARG	21	$H_{\gamma2}$	Fe	1	9.65	
ARG	21	$H_{\gamma3}$	Fe	1	8.46	
THR	24	$H_{\gamma2}$	Fe	1	11.67	
ARG	26	$H_{\gamma2}$	Fe	2	8.26	
ARG	26	$H_{\gamma3}$	Fe	2	8.89	
ARG	29	$H_{\gamma2}$	Fe	3	9.21	
ARG	29	$H_{\gamma3}$	Fe	3	9.55	
ILE	35	$H_{\gamma12}$	Fe	3	8.82	
ILE	35	$H_{\gamma13}$	Fe	3	7.97	
ILE	35	$H_{\gamma2}$	Fe	3	8.56	
VAL	37	$H_{\gamma2}$	Fe	4	5.61	
ILE	41	$H_{\gamma12}$	Fe	3	6.28	
ILE	41	$H_{\gamma13}$	Fe	3	6.10	

ILE	41	$H_{\gamma 2}$	Fe	3	5.18	
GLU	38	$H_{\gamma 2}$	Fe	3	12.01	
GLU	38	$H_{\gamma 3}$	Fe	3	12.30	
GLU	43	$H_{\gamma 2}$	Fe	3	11.07	
ARG	48	$H_{\gamma 2}$	Fe	4	8.67	
ARG	48	$H_{\gamma 2}$	Fe	4	8.90	
LEU	49	H_{γ}	Fe	4	10.43	
LYS	53	H_{γ}	Fe	2	10.08	

[a] The numbering of iron ions follows the order of Cysteine residues bound to the cluster: Fe_1 is the iron ion bound to Cys 22, Fe_2 is bound to Cys 25, Fe_3 is bound to Cys 34 and Fe_4 is bound to Cys 47.

[b] Weighting factor 2 is given to those H_N for which both R_1 and R_2 have been measured.

Table (V) **S5** Summary of restraints and structure quality factors of the structure families obtained after molecular dynamics refinement (AMBER-16).

PioC	*full-set* [a]	*NOE-only**[a]*	*NOE-only***[a]*	*PRE-only*[a]
Total number of meaningful NOE upper distance constraints[b]**:**	**344**	**344**	**344**	
Intra-residue	136	136	136	
Inter-residue				
Sequential (|i-j| = 1)	103	103	103	
Medium-range (|i-j| < 4)	56	56	56	
Long-range (|i-j > 5)	49	49	49	
Total meaningful dihedral angle restraints:	51	51	51	
Phi	25	25	25	25
Psi	24	24	24	24
Total number of paramagnetic NMR Restraints:	**189**	**-**	**-**	**189**
Upper Distances constraints derived from $R_{1,2\ para}$	175	-	-	175
Cys ⍰CH_2 dihedral angle constraints ⍰$_2$	4	4	-	4

1D NOEs between Cys □CH2 and neighboring residues	7	7	-	7
H-bonds linking HN donor atoms to S□ of the preceding cluster-bound Cys	3	3	-	3
Cluster				
Geometrical parameters defining the cluster (upl)	26	26	26	26
Geometrical parameters defining the cluster (lol)	26	26	26	26
Residual restraint violations[c] :				
Average no. of distance viol/struct[d]				
Between 0.1 -0.2 Å	3.5	0	0	
Between 0.2 -0.5 Å	0.3	0	0	
> 0.5 Å	0	0	0	
RMS of Distances violations per meaningful distance constraint (Å):	0.02	0.002	0.002	
Maximum distance violation (Å)	0.33	0.04	0.07	
Average no. of Dihedral angle viol/ struct[d]				
1-10 °	3.0	0	0	2.85
> 10°	0	0	0	0.0
RMS violations per meaningful dihedral angle constraints (degree):	0.51	0.08	0.028	0.49
Maximum dihedral angle violation	5.40	0.89	0.37	4.22
Average no. of Residual PRE viol/struct [e]				
Between 0.1 -0.2 Å	7.55			2.65
Between 0.2 -0.5 Å	2.15			0.30
> 0.5 Å	0			0.05
RMS of Distances violations per meaningful distance constraint (Å):	0.04			0.025
Maximun distance restraint violation	0.44			0.58

residual CYANA Target Function (Å^2)	1.92±0.13	0.27±0.06	0.26±0.05	0.91±0.16
Structure Quality Factors - overall statistics[f]:	**Z-score[g]**			
Procheck G-factor e (phi / psi only)	-3.30	-3.34	-3.62	-4.13
Procheck G-factor e (all dihedral angles)	-4.91	-4.02	-4.20	-4.85
Verify3D	-4.01	-4.65	-4.33	-4.33
ProsaII (-ve)	1.24	0.0	-0.33	0.79
MolProbity clashscore	1.29	1.34	1.30	1.26
Ramachandran Plot Summary from Procheck [f]				
Most favoured regions	74.2%	71.4	69.6	65.1
Additionally allowed regions	20.9%	23.4	24.7	30.4
Generously allowed regions	3.40%	2.4	3.3	2.7
Disallowed regions	1.40%	2.7	2.4	1.7
Ramachandran Plot Statistics from Richardson's lab[f]				
Most favoured regions	84.6%	83.3	81.5	80.2
Allowed regions	12.4%	12.3	15.3	15.9
Disallowed regions	3.0%	4.4	3.1	3.8

*NOE-only** 344 meaningful NOEs + 26 geometrical parameters of the cluster + 14 constraints arising from cluster-bound residues (4 ⍰$_2$ dihedral angle constraints -7 NOEs + 3 Hbonds)

*NOE-only*** 344 meaningful NOEs + 26 geometrical parameters of the cluster without constraints arising from cluster bound residues.

full-set: 344 meaningful NOEs + 26 geometrical parameters of the cluster + 14 constraints arising from cluster-bound residues +178 PREs

PRE-only: 26 geometrical parameters of the cluster + 14 constraints arising from cluster-bound residues +178 PREs

[a] The data are calculated over the 20 conformers representing the NMR ensemble. The mean value and the standard deviation are given

[b] Number of meaningful restraints for each class.

[c] Analyzed for residues 1 to 54. The analysis has been performed on the ensembles derived from CYANA2.1, using the Pdbstat program (Tejero et al., 2013)

[d] The largest distance or dihedral angle average violations within the ensemble is reported. Average distance violations were calculated using the sum over r^{-6}

[e] The largest paramagnetic relaxation enhancement within the ensemble is reported. Average PRE violations were calculated using the sum over r^{-6}

[f] Selected residue ranges: 5-50. Calculated using PSVS 1.5 (Bhattacharya et al. 2007)

[g] With respect to mean and standard deviation for a set of 252 X-ray structures < 500 residues, of resolution <= 1.80 Å, R-factor <= 0.25 and R-free <= 0.28; a positive value indicates a 'better' score. Z-score generated using PSVS 1.5.

Table (V) **S6** Pairwise RMSD to the mean for PioC structures obtained with different sets of restraints.

Restraints used in Structure Calc.	***NOE-only****	***NOE-only*****	***full-set***	***PRE-only***
Backbone RMSD$^{\$}$ (residues 5-50)	1.04 ±0.29 Å	1.27±0.19 Å	0.62±0.11Å	1.31±0.27Å
All heavy at.RMSD$^{\$}$ (residues 5-50)	1.81±0.30 Å	1.95±0.22 Å	1.14±0.13Å	2.00±0.32Å

*NOE-only** 344 meaningful NOEs + 26 geometrical parameters of the cluster + 14 constraints arising from cluster-bound residues (4 ⍰$_2$ dihedral angle constraints -7 NOEs + 3 Hbonds)

*NOE-only*** 344 meaningful NOEs + 26 geometrical parameters of the cluster without constraints arising from cluster bound residues.

full-set: 344 meaningful NOEs + 26 geometrical parameters of the cluster + 14 constraints arising from cluster-bound residues +178 PREs

PRE-only: 26 geometrical parameters of the cluster + 14 constraints arising from *cluster-bound residues +178 PREs*

$ Data are related to the family of structure obtained upon CYANA calculation followed by 30 ps (15 000 steps with a time step of 2.0 fs) of restrained molecular dynamics at constant temperature and constant pressure (1.0 bar) using AMBER 16. RMSD is calculated over residues 5-50.

Supplementary Information Text

Definition of the cluster

The Iron sulfur cluster was inserted into structure calculation according to the procedure originally described [1]. A special residue, named CFS, was added to the CYANA library. The artificial residue, denoted CFS, consists of a cysteinyl residue in which the thiol hydrogen (Hγ) was replaced by an iron atom (Feδ) at the proper distance and by adding to the latter, through another covalent bond, the sulfur atom (Sε) constituting the inorganic sulfide of the cluster. Bond lengths and angles used in this construction were taken from previously reported structures [1-3]. Eight additional covalent bonds were added as link statements to the end of the sequence file between each iron atoms (Fe) and the two bonded sulfur atoms (*S*ε). This removes the van der Waals interactions between the Fe and the other ligands. Then, upper and lower distance limits are imposed along the eight edges of the cubane (the remaining four are defined within the four CFS residues), along the six edges of the tetrahedron described by the four iron atoms, six others along the edges of the tetrahedron described by the four inorganic sulfur atoms (*S*ε) and finally, among the six edges of the tetrahedron formed by cysteine *S*y atoms. A total of 26 upper and lower distances limits was used in the CYANA calculations. This construction allows us to define a rigid cluster while leaving undefined the chirality of the peptide folding around it. The summary of conformationally restricting constraints is reported in Table S4.

Structure calculations and refinement

Structure calculations were performed with the program CYANA 2.1 [4, 5]. A total of 2000 random conformers were subjected to 65000 steps of a simulated annealing process. The 20 conformers with the lowest target function constituted the final family. Each member of the family was subsequently submitted to refinement in explicit solvent with the Amber-16 package [6]. The force field parameters for the 4Fe-4S cluster were taken as in similar systems [7]. A value of 50 kcal mol-1 Ã$^{-2}$ was used as force constant for the NOE and paramagnetic NMR restraints whereas a value of 32 kcal mol^{-1}rad^{-2} was used for torsion angle restraints. The quality of the structure was evaluated in terms of deviations from ideal bond lengths and bond angles and through Ramachandran plots obtained using the programs with PSVS 1.5 program [8].

^{1}H R_1 and R_2 relaxation measurements and PRE constraints

Relaxation rates ^{1}H R_1 and ^{1}H R_2 were measured using a 11.7 T Bruker AVANCE 500 equipped with a triple resonance, inverse detection, cryoprobe (TXI) or a 14.0 T Bruker AVANCE NEO 600, equipped with a room temperature triple resonance inverse detection probe. For the H_N R_1 rates, two series of experiments were used to measure longitudinal relaxation rates. For slow relaxing signals, a standard ^{15}N-HSQC was edited with a non selective ^{1}H inversion recovery building block. Fifteen experiments were collected (See Table S1), using a recycle delay of 4 s and inversion recovery delays of 20 ms, 30 ms, 40 ms, 50 ms, 60 ms, 80 ms, 100 ms, 120 ms, 160 ms, 200 ms, 300 ms, 400 ms, 600 ms, 800 ms, 1s. In order to measure relaxation rates of signals severely affected by the hyperfine relaxation, R_1 H_N rates were measured also with an IR-^{15}N-HSQC-AP experiment [9]. Fourteen experiments were collected using a recycle delay of 150 ms, an INEPT transfer delay (formally 1/(4J)) of 710 us and inversion recovery delays of 2.0 ms, 4.0 ms, 6.0 ms, 10 ms, 15 ms, 20 ms, 25 ms, 30 ms, 40 ms, 50 ms, 60 ms, 80 ms, 120 ms, 200 ms. In both series of experiments, the intensities of the ^{15}N HSQC spectra fitted according to three parameter fitting $I(t)= I(0)*[1-2\exp(-t*R_1)]$.

Transverse relaxation rate ^1H_N-R_2, were also measured with two different approaches. For signals relatively far from the paramagnetic center, relaxation rates were measured using an experiment where a variable delay is inserted during the INEPT transfer of a ^{15}N HSQC experiment [10]. Fourteen experiments were recorded, using a 4s recycle delay, a 1200 us selective ^1H_N inversion pulse for $^3JH_NH_\alpha$ decoupling, relaxation delays of 8.0 ms, 12 ms, 16 ms, 28 ms, 40 ms, 52 ms, 64 ms, 76 ms, 88 ms, 112 ms, 136 ms, 160 ms, 200 ms and 240 ms. To measure ^{1}H R_2 rates of signals that are strongly affected by the hyperfine interaction, a new experiment, termed R_2-weighted ^{15}N-HSQC-AP has been used [11]. ^1H_N-R_2 measurements were obtained from a series of sixteen R_2-weighted ^{15}N-HSQC-AP experiments recorded using recycle delays of 150 ms and INEPT transfer periods of 0.1 ms, 0.2 ms, 0.3 ms, 0.4 ms, 0.6ms, 0.8 ms, 1.0 ms, 1.2 ms, 1.4 ms, 1.6 ms, 2.0 ms, 2.4 ms, 2.8 ms, 3.2 ms, 4.0 ms, 5.0 ms. All relaxation data were analyzed using the Bruker Topspin Dynamics Center.

The R_1 and R_2 rates obtained with the different methods were compared and, for each residue, the value with the lower standard deviation in the fitting was considered. As expected, slow relaxing ^{1}H resonances were better fitted using an in-phase ^{15}N HSQC as editing spectrum and experimental conditions typical of diamagnetic systems, i.e. a long recycle delay, and longer relaxation periods. Conversely, fast relaxing signals were better fitted using the IR-HSQC-AP and the R_2 weighted HSQC-AP sequences. We found that all signals having R_1 values faster than 30 s^{-1} (13 out of 48 total R_1 measurements) and R_2 values faster than 45 s^{-1} (18 out of 49 total R_2 measurements) were better fitted using the tailored sequences. The results are summarized in Table S6.

For ^{1}H signals observed in ^{13}C HSQC experiments, R_1 ^{1}H rates were measured by inserting a non-selective ^{1}H inversion recovery filter prior to a standard ^{13}C HSQC experiments and fitting the intensities of the ^{13}C HSQC spectra as described above. Seventeen experiments were collected using a 2s relaxation delay and inversion recovery delays of 1.0 ms, 5.0 ms, 10 ms, 20 ms, 30 ms, 40 ms, 60 ms, 70 ms, 90 ms, 120 ms, 200 ms, 300 ms, 400 ms, 600 ms, 800 ms, 1.2 s, 2.0 s. The results are reported in Table S3. ^{1}H relaxation rates of Cysteines Hβ and Hα protons were measured from an IR- ^{13}C HSQC-AP experiment. The experiments were performed using acquisition and recycle delays of 17 ms and 65 ms, respectively. An INEPT transfer dealy of 600 us was used throughout the series. Ten experiments were performed using inversion recovery delays of 500 us, 2.0 ms, 4.0 ms, 6.0 ms, 8.0 ms, 10 ms, 15 ms, 30 ms, 50 ms, 80 ms.

Supplementary Information Text References

1. Banci, L., Bertini, I., Eltis, L. D., Felli, I. C., Kastrau, D. H. W., Luchinat, C., Piccioli, M., Pierattelli, R. & Smith, M. (1994) The three dimensional structure in solution of the paramagnetic protein high-potential iron-sulfur protein I from *Ectothiorhodospira halophila* through nuclear magnetic resonance, *Eur J Biochem.* 225, 715-725.
2. Bertini, I., Donaire, A., Feinberg, B. A., Luchinat, C., Piccioli, M. & Yuan, H. (1995) Solution structure of the oxidized 2[Fe_4S_4] ferredoxin from *Clostridium pasteurianum*, *Eur J Biochem.* 232, 192-205.
3. Bertini, I., Eltis, L. D., Felli, I. C., Kastrau, D. H. W., Luchinat, C. & Piccioli, M. (1995) The solution structure of oxidized HiPIP I from *Ectothiorhodospira halophila*, can NMR probe rearrangements associated to electron transfer processes?, *Chemistry - A European Journal.* 1, 598-607.
4. Güntert, P. (2004) Automated NMR structure calculation with CYANA, *Methods Mol Biol.* 278, 353-378.
5. Guntert, P. & Buchner, L. (2015) Combined automated NOE assignment and structure calculation with CYANA, *J Biomol NMR.* 62, 453-71.
6. D.A. Case, I. Y. B.-S., S.R. Brozell, D.S. Cerutti, T.E. Cheatham, III, V.W.D. Cruzeiro, T.A. Darden, R.E. Duke, D. Ghoreishi, M.K. Gilson, H. Gohlke, A.W. Goetz, D. Greene, R Harris, N. Homeyer, S. Izadi, A. Kovalenko, T. Kurtzman, T.S. Lee, S. LeGrand, P. Li, C. Lin, J. Liu, T. Luchko, R. Luo, D.J. Mermelstein, K.M. Merz, Y. Miao, G. Monard, C. Nguyen, H. Nguyen, I. Omelyan, A. Onufriev, F. Pan, R. Qi, D.R. Roe, A. Roitberg, C. Sagui, S. Schott-Verdugo, J. Shen, C.L. Simmerling, J. Smith, R. Salomon-Ferrer, J. Swails, R.C. Walker, J. Wang, H. Wei, R.M. Wolf, X. Wu, L. Xiao, D.M. York and P.A. Kollman (2018) AMBER 2018.

7. Carvalho, A. T. & Swart, M. (2014) Electronic structure investigation and parametrization of biologically relevant iron-sulfur clusters, *Journal of chemical information and modeling.* 54, 613-20.

8. Bhattacharya, A., Tejero, R. & Montelione, G. T. (2007) Evaluating protein structures determined by structural genomics consortia, *Proteins: Structure, Function, and Bioinformatics.* 66, 778-795.

9. Ciofi-Baffoni, S., Gallo, A., Muzzioli, R. & Piccioli, M. (2014) The IR-N-15-HSQC-AP experiment: a new tool for NMR spectroscopy of paramagnetic molecules, *Journal of Biomolecular Nmr.* 58, 123-128.

10. Donaldson, L. W., Skrynnikov, N. R., Choy, W.-Y., Muhandiram, D. R., Sarkar, B., Forman-Kay, J. D. & Kay, L. E. (2001) Structural Characterization of Proteins with an Attached ATCUN Motif by Paramagnetic Relaxation Enhancement NMR Spectroscopy, *J Am Chem Soc.* 123, 9843-9847.

11. Invernici, M., Trindade, I. B., Cantini, F., Louro, R. O. & Piccioli, M. (2020) Measuring transverse relaxation in highly paramagnetic systems, *J Biomol NMR*.

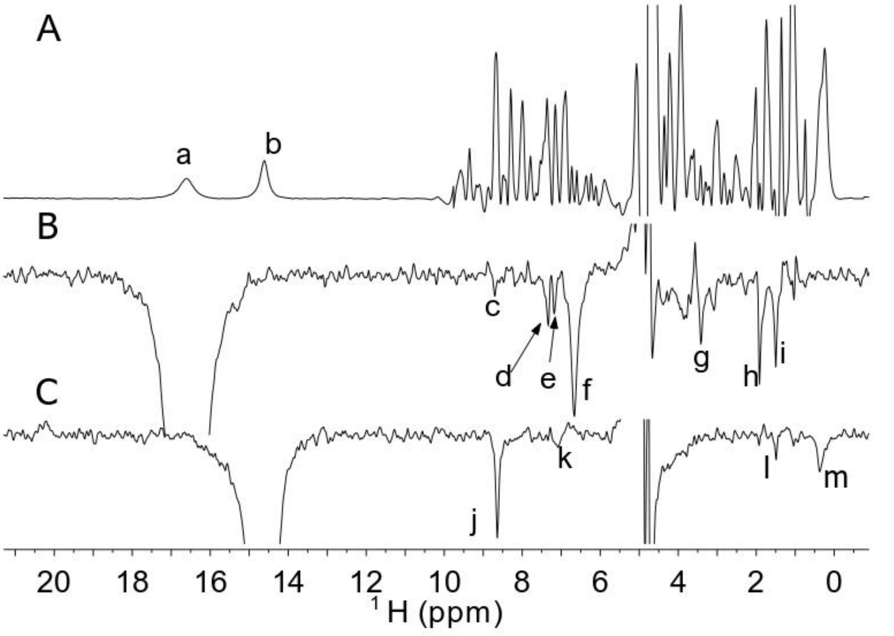

Figure (V) **S1 A)** 1D 1H NMR spectrum of PioC, optimized to observe hyperfine shifted and fast relaxing resonances. Two isolated peaks (labeled a-b) are observed. **B,C)** 1D NOE difference spectra obtained upon selective saturation of signals a-b. The NOE peaks observed in the difference spectra, labeled c-m, are used to perform the assignment of signals a and b.

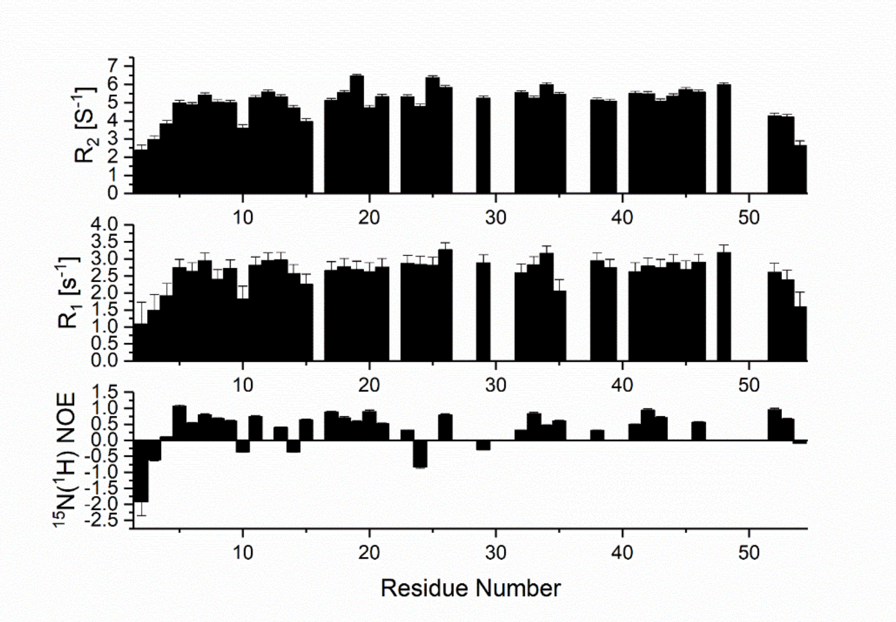

Figure (V) **S2** Experimental ^{15}N R_1, R_2 rates and heteronuclear NOEs as obtained from the 15N relaxation experiments performed at 500 MHz, 298K on a ^{15}N labelled PioC sample.

“…the holy curiosity of enquiry,
for this delicate little plant, aside from stimulation,
stands mainly in need of freedom,
without this it goes to wrack and ruin without fail….”
Albert Einstein

UNIVERSIDADE NOVA DE LISBOA
OMNIS CIVITAS CONTRA SE DIVISA NON STABIT

itqb nova

Oeiras, **November, 2022**

Ironing out ferric-siderophore reduction in Gram-negative bacteria

Inês B. Trindade